

ION AND PLASMA SYSTEMATICS
DURING THE FIRST KATRIN
NEUTRINO MASS MEASUREMENTS

Zur Erlangung des akademischen Grades eines

Doktors der Naturwissenschaften

von der KIT-Fakultät für Physik des

Karlsruher Instituts für Technologie

genehmigte

Dissertation

VON

M. Sc. Fabian Ruben Friedel

aus Karlsruhe

Referent: Prof. Dr. Guido Drexlin
Institut für Experimentelle Teilchenphysik, KIT
Korreferent: Prof. Dr. Kathrin Valerius
Institut für Astroteilchenphysik, KIT

Tag der mündlichen Prüfung: 13. November 2020

Erklärung der Selbstständigkeit

Ich versichere wahrheitsgemäß, die Arbeit selbstständig angefertigt, alle benutzten Hilfsmittel vollständig und genau angegeben und alles kenntlich gemacht zu haben, was aus Arbeiten anderer unverändert oder mit Änderungen entnommen wurde.

Karlsruhe, den 24.11.2020

.....

(Fabian Friedel)

Contents

Introduction	ix
1 Neutrino physics	1
1.1 Postulation and discovery	1
1.2 Three flavors	2
1.3 Neutrino properties within the standard model	3
1.4 Beyond the standard model: neutrino oscillations	4
1.4.1 Neutrino oscillations in vacuum	5
1.4.2 Neutrino oscillation experiments	8
1.5 Open questions	14
1.6 Absolute mass scale determination	16
1.6.1 Why is it important?	16
1.6.2 Supernova time-of-flight	17
1.6.3 Cosmology	18
1.6.4 Neutrinoless double beta-decay	20
1.6.5 Beta-decay	22
2 The KATRIN experiment	27
2.1 Measurement principle	27
2.1.1 Energy analysis via adiabatic collimation and electrostatic filtering	28
2.1.2 Tritium source	31
2.1.3 Response function	31
2.1.4 Fitting model for the beta-spectrum endpoint region	31
2.2 Anticipated neutrino mass sensitivity	34
2.3 Overview of hardware components	35
2.3.1 Windowless, gaseous tritium source	36
2.3.2 Rear section	39
2.3.3 Differential pumping section	41
2.3.4 Cryogenic pumping section	42
2.3.5 Pre-spectrometer	44
2.3.6 Main spectrometer	45
2.3.7 Focal plane detector	45
2.3.8 Monitor spectrometer	47
2.4 Overview of software components	47

3	Framework of this thesis	51
3.1	Ion- and plasma-related systematic effects on the KATRIN neutrino mass measurement	51
3.1.1	Tritium ion and secondary electron creation	51
3.1.2	Ion distribution inside the WGTS	54
3.1.3	Background contributions by tritium ions	54
3.1.4	Influence of ion blocking and removing beam line instrumentation	59
3.1.5	WGTS plasma effects	59
3.2	KATRIN timeline during development of this thesis	61
3.3	Objectives of this thesis	64
4	Gas flow and electromagnetic field simulations for the 2017 krypton commissioning	69
4.1	The krypton isotope $^{83\text{m}}\text{Kr}$	70
4.2	Technical implementation of the gaseous $^{83\text{m}}\text{Kr}$ source in July 2017	71
4.3	Gas flow simulations	72
4.3.1	MolFlow+	72
4.3.2	Simulation parameters	73
4.3.3	Results	74
4.4	Electromagnetic field simulations	75
4.5	Combination of simulation results	76
4.6	Comparison to the measurement	77
4.7	Summary	79
5	Minimization of ion-induced background for neutrino mass measurements	81
5.1	Beam line instrumentation	82
5.1.1	Beam line electrodes	82
5.1.2	Ion detection methods inside the spectrometer and detector section	85
5.2	Advances in ion detection using deuterium ions	89
5.2.1	Creation of inactive ions	90
5.2.2	Blocking with ring and dipole electrodes	92
5.2.3	Calibration of the pre-spectrometer current measurement	94
5.2.4	Calibration of the ICE detection method	96
5.2.5	Pressure-dependent ICE measurements with argon gas	101
5.2.6	Conclusion	103
5.3	Optimization of ion blocking electrodes for neutrino mass measurements	104
5.3.1	WGTS column density ramp-up	104
5.3.2	Measurement of the ion energy spectrum	107
5.3.3	Measurement of blocking electrode neutralization	109
5.3.4	Background from tritium decay inside the dipole electrodes	112
5.3.5	Optimum ring and dipole electrode voltage settings	117
5.3.6	Residual tritium ion flux into the pre-spectrometer	118
5.3.7	Conclusion	120
5.4	Summary	120

6	Experimental investigations of the WGTS tritium plasma	123
6.1	The plasma in the KATRIN tritium source	124
6.1.1	Key concepts of plasma physics	124
6.1.2	The WGTS plasma	128
6.1.3	Boundary conditions for the WGTS plasma potential	131
6.1.4	Systematic plasma effects for neutrino mass determination and objectives of the experimental investigations	135
6.2	Experimental methods for plasma investigation	136
6.2.1	PRO KATRIN	137
6.2.2	PRO KATRIN with ions	144
6.2.3	Characteristic current-voltage curves (I-U curves)	145
6.2.4	Search for high-frequency plasma instabilities with the egun .	147
6.2.5	High-frequency sinusoidal voltage modulation at the rear wall	148
6.3	Plasma investigations during the KATRIN neutrino mass runs 1 and 2	150
6.3.1	Plasma coupling to rear wall	151
6.3.2	Radial endpoint homogeneity: determination of the optimum rear wall set voltage for neutrino mass measurements	156
6.3.3	Measurement of characteristic I-U curves via rear wall voltage sweeps	158
6.3.4	Study of time dependencies of the RW voltage reference points	162
6.3.5	Influence of different WGTS operation modes on plasma measurement results	168
6.3.6	Measurements of the rear section egun transmission function width in order to investigate high-frequency plasma instabilities	173
6.3.7	Search for plasma eigenfrequencies in the FPD rate data . . .	176
6.3.8	Plasma potential change for a high-frequency sinusoidal voltage modulation at the rear wall	177
6.3.9	Influence of the DPS dipole electrode voltages on the plasma potential	182
6.3.10	Influence of the DPS infrared illumination on the plasma potential	185
6.4	Summary	186
7	Conclusion and outlook	191
8	Appendix: Calculation of correction factors for the determination of the background contribution by tritium decay inside the DPS dipole electrodes	195
	List of Acronyms	199
	List of Figures	201
	List of Tables	205
	Bibliography	207
	Acknowledgements	225

Introduction

Neutrinos were integrated as electrically neutral and massless fermions into the standard model of particle physics. To date, three different flavors of neutrinos are known: the electron [CRH⁺56], muon [DGG⁺62] and tau [KUA⁺01] neutrino. The observation of neutrino flavor oscillations [FHI⁺98, AAA⁺02] has shown that neutrinos in fact do possess a non-zero rest mass based on the measurements of their relative mass differences. Today, the absolute value of the neutrino mass is still unknown, but a direct measurement would significantly constrain models on large-scale structure formation in the early universe and mass generation models beyond the Higgs mechanism. The most stringent upper limit on the absolute mass of neutrinos of $m_{\bar{\nu}_e} < 1.1 \text{ eV}/c^2$ (90% C.L.) [AAA⁺19c] was set in 2019 by the Karlsruhe Tritium Neutrino (KATRIN) experiment.

The KATRIN experiment was designed for measuring the effective mass of the electron antineutrino $m_{\bar{\nu}_e}$ with an unprecedented sensitivity of $0.2 \text{ eV}/c^2$ (90% C.L.) within a total time of five calendar years [KAT05].

Antineutrinos and electrons are produced together in the β -decay of molecular tritium contained in a windowless, gaseous source [BBB⁺12] with an activity on the order of 10^{11} Bq. The β -electrons are magnetically guided along the 70 m long setup towards the main spectrometer, a large-scale MAC-E filter, where they are filtered according to their kinetic energy. Transmitted β -electrons are counted in a segmented silicon detector. The parameter $m_{\bar{\nu}_e}$ affects the shape of the β -spectrum close to the kinematic endpoint $E_0 = 18.6 \text{ keV}$ and is determined by applying a four-parameter fit of E_0 , $m_{\bar{\nu}_e}^2$, the signal amplitude A_{sig} and the background amplitude A_{bg} .

Systematic effects are of major importance in the calculation of the experimental sensitivity and thus either have to be minimized to be negligible or have to be characterized in sufficient detail in order to take them into account in the neutrino mass fitting model. The main topic of this thesis is related to systematic effects arising from the continuous creation of charged particles, i.e. ions and electrons, by β -decay and the ionization of gas molecules by inelastic scattering of β -electrons. These charged particles form a cold, magnetized plasma inside the gaseous tritium

source.

Tritium ions would be a significant source of background in case they would be transmitted all the way to the main spectrometer. A dedicated setup of hardware instrumentation for blocking, removal and detection of ions was installed and commissioned in previous works, especially in [Kle19]. In the course of this thesis the detection methods were calibrated in a commissioning campaign using inactive deuterium ions. Further, the settings of the blocking and removing electrodes were optimized and applied over the first two KATRIN neutrino mass measurement campaigns.

The space charge potential of the source plasma defines the starting potential of the β -electrons, which is the reference value for the energy measurement at the MAC-E filter. Thus, any spatial or temporal variation of the space charge potential distribution directly would distort the measured β -spectrum shape and thereby would introduce a shift of the best-fit neutrino mass result. Further, high-frequency plasma instabilities could change the kinetic energy of the β -electrons in flight. This thesis presents the first-ever experimental investigations of KATRIN-specific plasma phenomena performed over the course of the first two neutrino mass measurement campaigns.

The content of this thesis is divided into seven chapters and an appendix.

- In chapter 1 the history and current developments of neutrino physics are summarized.
- In chapter 2 the KATRIN experimental setup is described in detail.
- Chapter 3 is intended to serve as an overview for the following chapters 4 to 6. A detailed introduction into relevant systematic effects is given and the main objectives of this thesis are presented.
- In chapter 4 gas flow and electromagnetic field simulations for one of the first commissioning campaigns in July 2017 with gaseous krypton instead of tritium are described and the results are compared to the outcome of the measurements.
- Chapter 5 deals with ion-induced systematic effects. Results from three different measurement campaigns obtained with inactive and tritium ions are given.
- In chapter 6 a variety of plasma systematics is discussed. The results obtained in the first neutrino mass measurement campaigns by applying custom-made methods are presented.
- A conclusion and an outlook are given in chapter 7.

1. Neutrino physics

An evaluation of the KATRIN experiment and the work described in this thesis requires some understanding of the history and current status of neutrino physics. Therefore, a brief introduction based on [XZ11, Zub12, OO19] will be given in this chapter.

1.1 Postulation and discovery

Historically the neutrino is closely related to the dawn of nuclear physics. In 1914 it was found by J. Chadwick [Cha14] that the energy distribution of β -radiation is continuous. This finding gave rise to a long debate among the scientific community. From simple kinematic calculations a discrete energy spectrum was expected like it was found for both α - and γ -radiation. Subsequent calorimetric measurements [EW27, MO30] showed that the continuous energy distribution shown in Fig. 1.1 indeed can be assigned solely to the initially emitted beta-particle and is not the result of a secondary effect. If the fundamental principle of conservation of energy is fulfilled, the only logical explanation was the production of a yet undetected particle carrying the missing fraction of the decay energy. In addition, the conservation of the angular momentum required this hypothetical particle to carry a spin of $1/2$. This new particle was postulated by W. Pauli in his famous letter from 1930 [vM85] initially calling it the "neutron". Since then the β -decay is correctly described with three particles in the final state:

$$M(A, Z) \rightarrow D(A, Z + 1) + e^- + \bar{\nu}_e \quad (1.1)$$

with $M(A, Z)$ being the mother nucleus with the nucleon number A and the proton number Z , and $D(A, Z + 1)$ being the daughter nucleus. This inspired E. Fermi to develop a theory for β -decay in which he named the new particle "neutrino" for the first time [Fer34].

The experimental confirmation of the neutrino hypothesis turned out to be challenging. A neutral and only weakly interacting particle is not expected to produce a sizable number of signals to detect. An often used detection reaction is the inverse

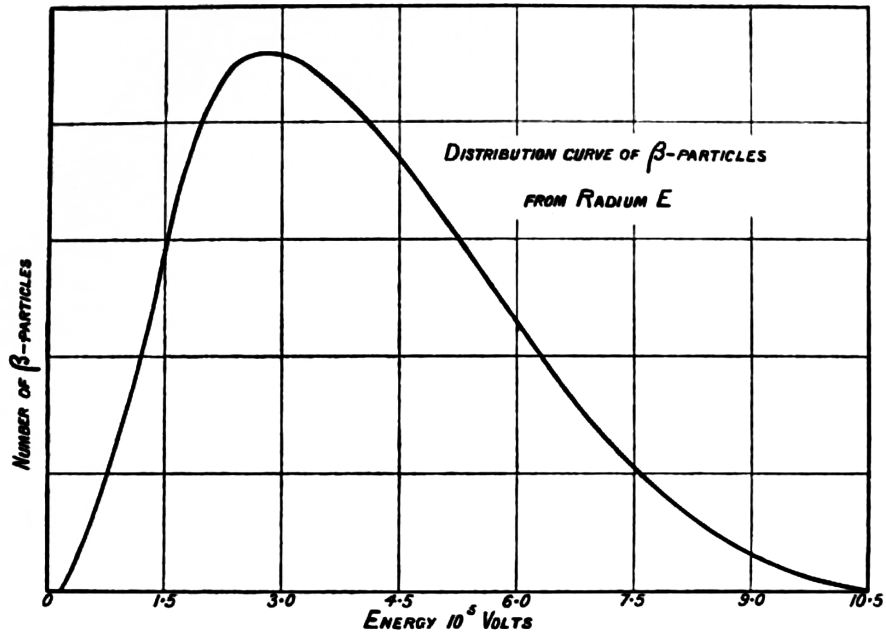
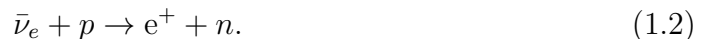


Figure 1.1: Historical measurement result for the β -decay energy spectrum of radium E (today known as bismuth-210). The curve has been measured in 1927 by C. D. Ellis and W. A. Wooster using energy-dependent magnetic deflection and an ionization chamber for detection. The figure is taken from [EW27].

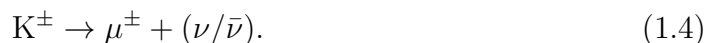
beta-decay where an antineutrino reacts with a free proton and produces a neutron and a positron:



Finally, C. L. Cowan and F. Reines succeeded in measuring this process [RC53, CRH⁺56]. They placed their detector next to a nuclear reactor producing antineutrinos via β -decay of fission fragments. In their final setup from 1956 a sandwich detector consisting of target (water and cadmium chloride) and liquid scintillator layers was used.

1.2 Three flavors

Neutrinos are not always created along with electrons in β -decay, but also in combination with muons in the decay of charged mesons like pions or kaons [DGG⁺62]:



Until 1962 it was unclear whether the final state neutrinos of those three processes are of the same type. One can differentiate between β -decay-neutrinos and meson-decay-neutrinos by measuring the final state of the inverse β -decay-like interaction



for either one [OO19, DGG⁺62]. Here, X and Y are hadrons and α is the charged lepton associated with the neutrino ν_α . A muon-like neutrino ν_μ would only produce

muons but no electrons. Indeed this was observed at the Alternating Gradient Synchrotron (AGS) at the Brookhaven National Laboratory [DGG⁺62]. High-energy protons accelerated on a beryllium target were producing a cascade of muons and kaons. These mesons decayed in flight via the processes described in Eqs. 1.3 and 1.4, providing a neutrino beam. Finally, the neutrinos crossed a spark chamber to undergo reaction 1.5. The number of muon-like events exceeded the electron-like events significantly, so the existence of two different types of neutrinos was verified. Yet, there was one more flavor to discover. Precision measurements of the decay width of the Z^0 boson at the Large Electron Positron Collider (LEP) and at the SLAC Linear Collider (SLC) yielded a result for the existing number of weakly interacting, light neutrino flavors [THH⁺18]:

$$N_\nu = 2.984 \pm 0.008. \quad (1.6)$$

The third generation neutrino was associated with the τ lepton detected in 1975 [PAB⁺75] and was directly discovered in 2000 by the DONUT experiment [KUA⁺01]. High-energy protons provided by the Fermilab Tevatron were creating a variety of mesons when hitting a tungsten target. Third generation neutrinos were primarily created by the decay of D_S mesons

$$D_S \rightarrow \tau + \nu \quad (1.7)$$

and various follow-up decays of the tau lepton [KUA⁺01]. Hitting a nuclear emulsion target and interacting via the process described in Eq. 1.5, charged leptons were created and identified measuring their tracks [KUA⁺08]. Several τ -like events were identified completing the number of particles in the standard model neutrino sector.

1.3 Neutrino properties within the standard model

The standard model of particle physics is an experimentally well confirmed combination of quantum field theories [PS95] describing all known elementary particles and their fundamental interactions. Neutrinos are classified as fermions and more specifically as leptons. While a fermion is defined as a particle with half-integral spin obeying Fermi-Dirac statistics, the name lepton implies that the respective particle is not taking part in the strong interaction.

There are three neutrino flavors: the electron neutrino ν_e , the muon neutrino ν_μ and the tau neutrino ν_τ , corresponding to their leptonic partner particles electron e^- , muon μ^- and tauon τ^- . Within the standard model description all three neutrinos have a spin of 1/2, zero mass and carry zero electric charge. Hence, they do not interact electromagnetically.

The only way neutrinos can interact with their environment is via the weak interaction. As the name indicates the coupling strength is comparably low, which results in a typical interaction range of $L \approx 2.5 \times 10^{-3}$ fm and small cross sections of e.g. $\sigma \approx 1.7 \times 10^{-41} \text{ cm}^2 \times E_\nu/\text{GeV}$ for neutrino-electron scattering, scaling linearly with the neutrino energy E_ν [PRS⁺15]. On average, a 1 MeV neutrino would need to traverse an approximately 30 light year long iron-based target material in order to experience only one scattering on an electron [PRS⁺15].

In quantum field theory the weak interaction of neutrinos is described within the electroweak theory developed by S. L. Glashow, S. Weinberg and A. Salam [Gla61, Wei67, Sal68]. The interaction is mediated via the exchange of three heavy bosons.

In a so-called charged current (CC) interaction a W^+ or a W^- boson is involved while in neutral current (NC) interactions the Z^0 boson is the mediator. Both possibilities are displayed in Fig. 1.2.

Another feature of the weak interaction is the violation of parity conservation. Parity transformation is the mathematical operation of spatial mirroring $x \rightarrow -x$. If parity is violated, a process runs differently from its mirrored equivalent. The weak interaction is the only one where this applies, a fact which was first discovered in the β -decay of polarized ^{60}Co by C. S. Wu [WAH⁺57]. Assuming conservation of parity, the β -electrons should be emitted isotropically. In this case the antineutrino's helicity $H = \frac{\vec{S} \cdot \vec{p}}{|\vec{S}| |\vec{p}|}$ [PRS⁺15] with spin \vec{S} and momentum \vec{p} could be both positive or negative with equal probability. In fact, in the standard model antineutrinos (neutrinos) are always right-handed (left-handed), which is equivalent to a helicity eigenvalue of $H = 1$ ($H = -1$) for massless particles. Consequently, it was found by C. S. Wu that the β -electrons are mostly emitted in opposite direction of the nuclear spin of ^{60}Co . Shortly afterwards, the helicities of the neutrino $H_\nu = -1$ and the antineutrino $H_{\bar{\nu}} = +1$ were measured [GGS58, BFL61].

Nowadays it is known that the description of neutrinos stated above has to be complemented by the perception that neutrinos do have a tiny but non-zero rest mass which is detailed in the next section.

1.4 Beyond the standard model: neutrino oscillations

In order to understand how physicists know that neutrinos have mass one has to understand neutrino oscillations. These are periodic flavor transitions $\nu_\alpha \leftrightarrow \nu_\beta$ while the neutrino ν is propagating in space and time. A brief introduction into the theoretical formalism will reveal how the oscillations depend on the neutrino mass. Afterwards, the Nobel prize awarded experimental research in this field will be discussed. Both subsections are based on [Zub12, OO19].

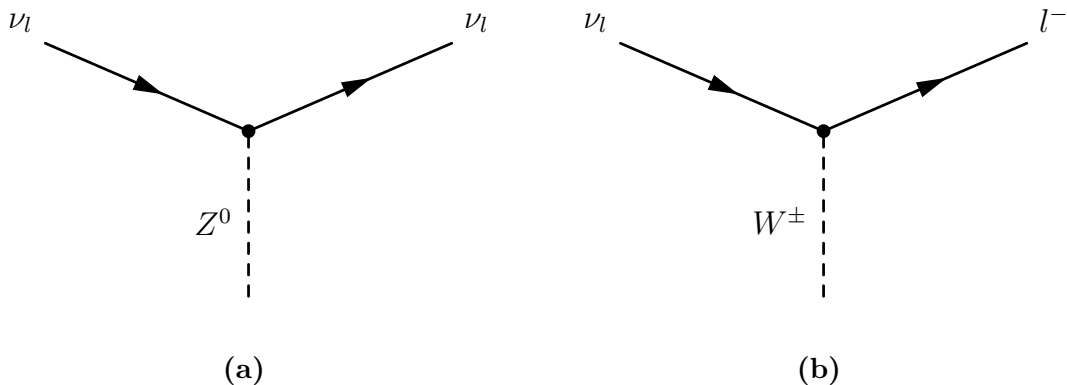


Figure 1.2: Weak standard model interactions of neutrinos. Both NC (a) and CC (b) interactions are illustrated by their corresponding Feynman diagram. The index l represents the lepton flavor e , μ or τ . The figure is inspired by [OO19].

1.4.1 Neutrino oscillations in vacuum

For describing neutrino propagation one needs an equation of motion and a wave function. In general, for fermions in vacuum the Dirac equation introduced in 1928 by P. A. M. Dirac [Dir28] is valid:

$$(i\gamma_\mu \frac{\partial}{\partial x_\mu} - m)\Psi(x) = 0. \quad (1.8)$$

It is given in natural units ($\hbar = c = 1$) with the index $\mu = 1, \dots, 4$ and the four-vector $x = (t, x_1, x_2, x_3)$ with time t and space x . The wave function is denoted Ψ , the mass m and the 4×4 Dirac matrices are defined as:

$$\gamma_0 = \begin{pmatrix} I & 0 \\ 0 & -I \end{pmatrix}, \gamma_k = \begin{pmatrix} 0 & \sigma_k \\ -\sigma_k & 0 \end{pmatrix}. \quad (1.9)$$

Here I is the 2×2 unit matrix and σ_k are the Pauli matrices [Pau27] with $k = (1, 2, 3)$:

$$\sigma_1 = \begin{pmatrix} 0 & 1 \\ 1 & 0 \end{pmatrix}, \sigma_2 = \begin{pmatrix} 0 & -i \\ i & 0 \end{pmatrix}, \sigma_3 = \begin{pmatrix} 1 & 0 \\ 0 & -1 \end{pmatrix}. \quad (1.10)$$

Solutions of the Dirac equation are given by eigenfunctions with well-defined masses m_j in the form of plane waves $\Psi(\vec{x}, t) = \nu_j(\vec{x}, t) = \nu_j(0, 0) \exp(i(\vec{p}_j \vec{x} - E_j t))$ with $j = 1, 2, 3$; energy E_j and momentum \vec{p}_j . These mass eigenstates are not necessarily identical with the flavor eigenstates ν_α with $\alpha = e, \mu, \tau$. Rather, they can be described as a quantum-mechanical superposition of the mass eigenstates connected by a 3×3 unitary mixing matrix U :

$$\begin{aligned} \nu_\alpha &= \sum_{j=1}^3 U_{\alpha j} \nu_j \quad \text{for neutrinos,} \\ \bar{\nu}_\alpha &= \sum_{j=1}^3 U_{\alpha j}^* \bar{\nu}_j \quad \text{for antineutrinos.} \end{aligned} \quad (1.11)$$

In an experiment only flavor eigenstates ν_α can be measured since they take part in the weak interaction. There is thus no single mass associated with an individual flavor. So a hypothetical high-resolution experiment measuring e.g. ν_e would not continuously measure the same mass but different masses m_j with a certain probability $|U_{ej}|^2$. The mixing matrix U is often referred to as PMNS matrix after the pioneering theorists B. Pontecorvo [Pon58], Z. Maki, M. Nakagawa and S. Sakata [MNS62] who developed the concept of neutrino oscillations. Explicitly it is defined as [THH⁺18]:

$$\begin{aligned} U &= \begin{pmatrix} 1 & 0 & 0 \\ 0 & c_{23} & s_{23} \\ 0 & -s_{23} & c_{23} \end{pmatrix} \cdot \begin{pmatrix} c_{13} & 0 & s_{13}e^{-i\delta} \\ 0 & 1 & 0 \\ -s_{13}e^{i\delta} & 0 & c_{13} \end{pmatrix} \cdot \begin{pmatrix} c_{12} & s_{12} & 0 \\ -s_{12} & c_{12} & 0 \\ 0 & 0 & 1 \end{pmatrix} \cdot \begin{pmatrix} e^{i\eta_1} & 0 & 0 \\ 0 & e^{i\eta_2} & 0 \\ 0 & 0 & 1 \end{pmatrix} \\ &= \begin{pmatrix} c_{12}c_{13} & s_{12}c_{13} & s_{13}e^{-i\delta} \\ -s_{12}c_{23} - c_{12}s_{13}s_{23}e^{i\delta} & c_{12}c_{23} - s_{12}s_{13}s_{23}e^{i\delta} & c_{13}s_{23} \\ s_{12}s_{23} - c_{12}s_{13}c_{23}e^{i\delta} & -c_{12}s_{23} - s_{12}s_{13}c_{23}e^{i\delta} & c_{13}c_{23} \end{pmatrix} \cdot \begin{pmatrix} e^{i\eta_1} & 0 & 0 \\ 0 & e^{i\eta_2} & 0 \\ 0 & 0 & 1 \end{pmatrix} \end{aligned} \quad (1.12)$$

with $c_{jl} = \cos(\theta_{jl})$, $s_{jl} = \sin(\theta_{jl})$, the mixing angle θ_{jl} , a Dirac CP violating phase δ and two Majorana CP violating phases $\eta_{1,2}$. CP transformation is the combination

of parity transformation P and charge conjugation C . The first one changes a right-handed into a left-handed neutrino and the second one transforms a neutrino into an antineutrino or vice versa $\nu \leftrightarrow \bar{\nu}$. CP violation is present if the transition probability for $\nu_\alpha \rightarrow \nu_\beta$ would be different to the one for $\bar{\nu}_\alpha \rightarrow \bar{\nu}_\beta$.

The PMNS matrix U is unitary, fulfilling $U^{-1} = U^\dagger = (U^*)^T$. Thus, one can inverse Eq. 1.11 receiving

$$\nu_j = \sum_\alpha U_{\alpha j}^* \nu_\alpha \quad \text{and} \quad \bar{\nu}_j = \sum_\alpha U_{\alpha j} \bar{\nu}_\alpha. \quad (1.13)$$

The transition probability $P(\nu_\alpha \rightarrow \nu_\beta)$ can be calculated as follows. It is assumed that neutrinos of flavor α are created at $t = 0$ at the position $x = 0$ which yields

$$\nu(x = 0, t = 0) = \nu_\alpha = \sum_{j=1}^3 U_{\alpha j} \nu_j(x = 0, t = 0). \quad (1.14)$$

In a time evolution of this equation, the plane wave solution as well as Eq. 1.13 is used, resulting in

$$\begin{aligned} \nu(x, t) &= \sum_j U_{\alpha j} \nu_j(x, t) \\ &= \sum_j U_{\alpha j} e^{i(\vec{p}_j \vec{x} - E_j t)} \nu_j(x = 0, t = 0) \\ &= \sum_{j, \beta} U_{\alpha j} U_{\beta j}^* e^{i(\vec{p}_j \vec{x} - E_j t)} \nu_\beta. \end{aligned} \quad (1.15)$$

The neutrino mass states ν_j are relativistic so $p_j \gg m_j$ and $p_j \approx E_j$ and $E_j = \sqrt{m_j^2 + p_j^2} \approx p_j + \frac{m_j^2}{2p_j}$. With the neutrino propagation distance $L = x = ct$ and $c = 1$ Eq. 1.15 becomes

$$\nu(x, t) = \sum_{j, \beta} U_{\alpha j} U_{\beta j}^* e^{-im_j^2 L / (2E_j)} \nu_\beta. \quad (1.16)$$

Finally, the transition probability is

$$\begin{aligned} P(\nu_\alpha \rightarrow \nu_\beta)(L) &= \left| \sum_j U_{\alpha j} U_{\beta j}^* e^{-im_j^2 L / (2E_j)} \right|^2 \\ &= \sum_{j, l} U_{\alpha j} U_{\alpha l}^* U_{\beta j} U_{\beta l} e^{-i\Delta m_{jl}^2 L / (2E)} \\ &= \delta_{\alpha\beta} - 4 \sum_{j>l=1}^3 \text{Re}(U_{\alpha j} U_{\alpha l}^* U_{\beta j} U_{\beta l}) \sin^2 \left(\frac{\Delta m_{jl}^2 L}{4 E} \right) \\ &\quad + 4 \sum_{j>l=1}^3 \text{Im}(U_{\alpha j} U_{\alpha l}^* U_{\beta j} U_{\beta l}) \sin \left(\frac{\Delta m_{jl}^2 L}{4 E} \right) \cos \left(\frac{\Delta m_{jl}^2 L}{4 E} \right) \end{aligned} \quad (1.17)$$

with $\Delta m_{jl}^2 = m_j^2 - m_l^2$. The Kronecker delta $\delta_{\alpha\beta}$ can be used because the flavor eigenstates are orthonormal. An analog treatment for antineutrinos starting from a modified version of Eq. 1.14 results in

$$P(\bar{\nu}_\alpha \rightarrow \bar{\nu}_\beta)(L) = \left| \sum_j U_{\alpha j}^* U_{\beta j} e^{-im_j^2 L / (2E_j)} \right|^2. \quad (1.18)$$

Evidently, if the PMNS matrix U is real with CP phases $\delta = \eta_1 = \eta_2 = 0$, both probabilities $P(\nu_\alpha \rightarrow \nu_\beta)$ and $P(\bar{\nu}_\alpha \rightarrow \bar{\nu}_\beta)$ would be identical and CP symmetry would be conserved. Moreover, it is obvious that the probabilities P are zero for vanishing differences of the mass squares $\Delta m_{jl}^2 = m_j^2 - m_l^2$. That is why an observation of neutrino oscillation is equivalent to at least one non-vanishing mass m_j or m_l . From an experimental point of view it is important to note the important role of the ratio L/E for the transition probability, since distance and energy can be specified in an experiment at least to some degree. In the simplified version of a two flavor oscillation the influence of this ratio can be seen more easily. In this case the PMNS matrix reduces to two dimensions:

$$\begin{pmatrix} \nu_e \\ \nu_\mu \end{pmatrix} = \begin{pmatrix} \cos \theta & \sin \theta \\ -\sin \theta & \cos \theta \end{pmatrix} \begin{pmatrix} \nu_1 \\ \nu_2 \end{pmatrix} \quad (1.19)$$

with only one mixing angle θ . Consequently, Eqs. 1.17 and 1.18 simplify to

$$\begin{aligned} P(\nu_e \rightarrow \nu_\mu) &= P(\bar{\nu}_e \rightarrow \bar{\nu}_\mu) \\ &= \sin^2(2\theta) \sin^2\left(\frac{\Delta m^2 L}{4 E}\right) \\ &= \sin^2(2\theta) \sin^2\left(\pi \frac{L}{L_0}\right) \end{aligned} \quad (1.20)$$

with $\Delta m^2 = m_2^2 - m_1^2$ and the oscillation length $L_0 = \frac{4\pi E}{\Delta m^2}$. This can also be written as [XZ11]:

$$P(\nu_e \rightarrow \nu_\mu) = \sin^2(2\theta) \sin^2\left(1.27 \frac{\Delta m^2}{\text{eV}^2} \frac{L}{\text{km}} \frac{\text{GeV}}{E}\right). \quad (1.21)$$

The transition probability is illustrated in Fig. 1.3a. The mixing angle θ defines the amplitude of the oscillation while the difference of the mass squares Δm^2 , the energy E and the propagation length L determine the frequency.

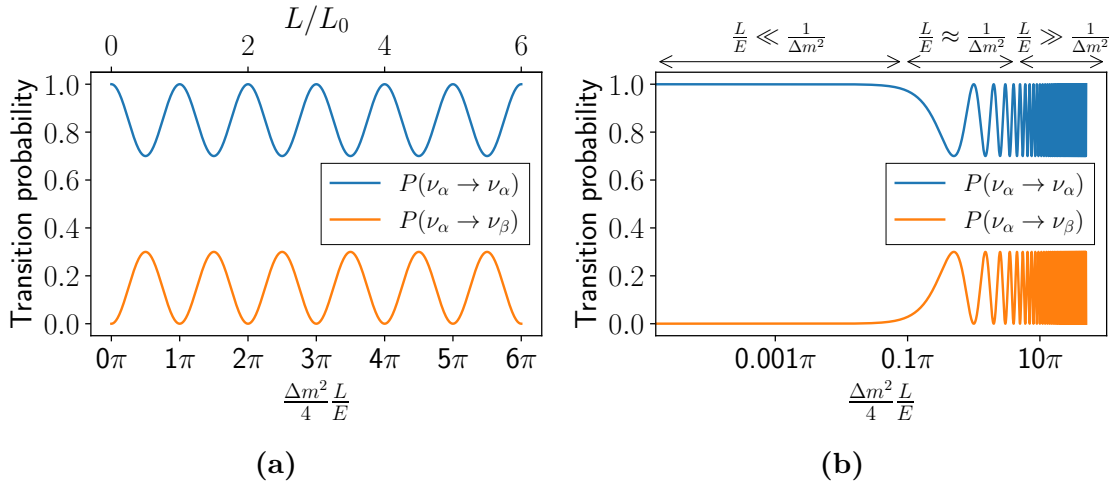


Figure 1.3: Transition probabilities for a two flavor oscillation. The transition probabilities of a flavor change $P(\nu_\alpha \rightarrow \nu_\beta)$ and of an unchanged flavor $P(\nu_\alpha \rightarrow \nu_\alpha) = 1 - P(\nu_\alpha \rightarrow \nu_\beta)$ are plotted for an amplitude $\sin^2(2\theta) = 0.3$ (a). The three characteristic regions of the L/E parameter are marked in an equivalent plot with logarithmic scale (b). Both figures are inspired by [Zub12].

1.4.2 Neutrino oscillation experiments

In general, neutrino oscillation experiments measure the flux of a specific neutrino flavor as a function of L/E . There are two different ways of doing so: in the appearance or the disappearance mode. If e.g. an oscillation $\nu_e \rightarrow \nu_\mu$ is considered, in the first case the flux of ν_μ while in the latter case the flux of ν_e would be measured. Considering Eq. 1.17 or the less complex two flavor version stated in Eq. 1.20, there are three characteristic regimes to be considered in order to evaluate the measurement sensitivity:

- $L/E \ll \frac{4}{\Delta m^2}$: In this case the propagation distance L is too short for the given energy E . The sine function is close to zero, so the probability of a flavor transition is negligible and no oscillation effect can be measured.
- $L/E \approx \frac{4}{\Delta m^2}$: Here, the chance is high that a flavor transition can be observed.
- $L/E \gg \frac{4}{\Delta m^2}$: The frequency of the oscillation is so high that a single cycle can not be resolved. Consequently, a measurement will yield only the average transition probability.

Graphically one can see the three different regions marked in Fig. 1.3b where the flavor transition probability is plotted on a logarithmic scale.

In order to be sensitive to all parameters of the PMNS matrix $\theta_{12}, \theta_{23}, \theta_{13}$ and to the mass splittings $\Delta m_{21}^2, \Delta m_{32}^2$ a multitude of experiments using different neutrino sources and baselines is needed. In the past years such experiments provided high-precision measurements of the PMNS matrix parameters as well as the mass differences. A combined analysis done in [THH⁺18] yields the recent results given in Tab. 1.1.

Solar neutrino experiments

The solar core continuously emits electron neutrinos with energies of up to ~ 19 MeV [Zub12] produced in the nuclear fusion reaction of hydrogen to helium:



A first detection of these solar neutrinos was achieved by the radiochemical Homestake experiment by R. Davis [Dav64, Dav94, CDD⁺98] for which he was awarded the 2002 Nobel prize in physics. In the Homestake gold mine in South Dakota, USA, a 615 ton C_2Cl_4 tank served as target for the inverse β -decay reaction



with a threshold energy of 814 keV. After an exposure time of several weeks the produced argon atoms were extracted from the target mass and put into proportional counters. The unstable ${}^{37}\text{Ar}$ isotope decays back via electron capture



with a half-life time of 35 d producing X-rays or Auger electrons from the excited ${}^{37}\text{Cl}^*$ which are detected. After more than 20 years of operation the data of 108 single measurement runs resulted in an average ${}^{37}\text{Ar}$ production rate of [CDD⁺98]

$$(2.56 \pm 0.16 \text{ (stat.)} \pm 0.16 \text{ (syst.)}) \text{ SNU} \quad (1.25)$$

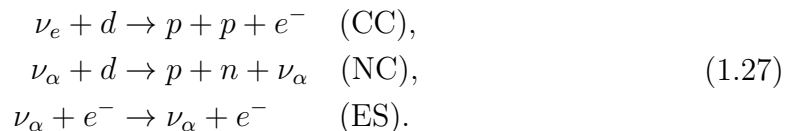
where the solar neutrino unit is defined as $1 \text{ SNU} = 10^{-36}$ captures per target atom per second. However, from the theoretical predictions of J. N. Bahcall a value of 7.5 SNU was expected [BBS68, Dav94].

Second-generation radiochemical experiments using gallium targets allow to detect solar neutrinos from proton-proton fusion (pp neutrinos) with energies of $E \ll 1 \text{ MeV}$. Neutrinos interact with gallium in the CC interaction



The final results of the experiments GALLEX [AHH⁺92, HHH⁺99], GNO [ABB⁺00, ABB⁺05] and SAGE [AVV02] again showed a deficit in solar neutrino flux with respect to the predictions of the solar model. Independently, this was confirmed by measurements with the (Super-)Kamiokande water Cerenkov detector [FHI⁺96, Suz01, BPB01]. This discrepancy is historically referred to as the "solar neutrino problem".

In fact, it was not a problem but an opportunity to discover new physics beyond the standard model. There are only two possible explanations for the solar neutrino problem. Either the solar model prediction is wrong or neutrino oscillations happen on the way between Earth and the center of the Sun. In the latter case, not all solar neutrinos arrive in the electron flavor state. Thus, experiments which are only sensitive to electron neutrinos measure a too low flux which seems not to match solar model prediction. In order to evaluate this hypothesis, a detector sensitive to all neutrino flavors is needed. Such a detector was realized with the Sudbury Neutrino Observatory (SNO) [AAA⁺01a, AAA⁺02, AAA⁺13], a 1000 ton heavy water (D₂O) target surrounded by an array of several thousand photomultiplier tubes. Neutrinos can initiate the following three reactions on the target material [AAA⁺01a]



Here, p stands for a free proton, n for a free neutron and d for the bound deuterium nucleus. While the CC interaction is only possible with electron neutrinos ν_e due to energy constraints, the NC and elastic scattering (ES) reactions are sensitive to all neutrino flavors ν_α . The complete set of measurements in all three channels provided insight about the individual flavor contributions to the overall flux [AAA⁺02]:

$$\begin{aligned} \phi_e &= (1.76 \pm 0.05 \text{ (stat.)} \pm 0.09 \text{ (syst.)}) \cdot 10^6 \text{ cm}^{-2}\text{s}^{-1}, \\ \phi_{\mu\tau} &= (3.41 \pm 0.45 \text{ (stat.)}_{-0.45}^{+0.48} \text{ (syst.)}) \cdot 10^6 \text{ cm}^{-2}\text{s}^{-1}. \end{aligned} \quad (1.28)$$

As can be seen only about one-third of the flux is originating from electron neutrinos. This strongly implies solar neutrino oscillation and is in excellent agreement with the results measured by R. Davis et al. For this finding the SNO director A. B. McDonald received the 2015 Nobel prize in physics.

However, there was still another puzzle to solve. Assuming neutrino oscillation in vacuum and considering Eq. 1.21, a baseline of $1.5 \times 10^8 \text{ km}$ equal to the distance between Earth and Sun and a neutrino energy of $\sim 10 \text{ MeV}$ implies a mass

splitting of $\Delta m^2 \approx 1 \times 10^{-10} \text{ eV}^2/c^4$. However, this parameter region was excluded by dedicated measurements of the KamLAND reactor neutrino experiment [EEF⁺03, AEE⁺05, A⁺08]. An alternative explanation was given by the Mikheyev-Smirnov-Wolfenstein (MSW) effect [Wol78, MS85]. This effect describes neutrino oscillations in matter. Neutrinos propagating through a medium like the solar plasma are undergoing a lot of coherent forward scattering processes with electrons. Electron neutrinos can perform CC as well as NC interactions, while the other two flavors are restricted to NC reactions only. This results in an extra potential $V = \sqrt{2}G_F n_e$ for electron neutrinos only, with the Fermi constant G_F and the electron density n_e . In section 1.4.1 neutrino mass eigenstates in vacuum were described as plane waves with the energy-momentum relation $E = \sqrt{p^2 + m^2}$ in natural units. Considering the extra potential originating from coherent forward scattering, an additional term has to be included in the energy-momentum relation, which can be interpreted as an increased effective mass $m_{\text{eff}}^2 = m^2 + A$ with $A \propto E\rho$ where ρ is the density of the medium and E is the neutrino energy. Different masses result in different Δm^2 and thus in different transition probabilities (cf. Eq. 1.20). Also, the mixing angle in matter θ_m and therefore the mixing amplitude $\sin^2(2\theta_m)$ has to be modified compared to the vacuum case:

$$\sin^2(2\theta_m) = \frac{\sin^2(2\theta)}{(\frac{A}{\Delta m^2} - \cos(2\theta))^2 + \sin^2(2\theta)}. \quad (1.29)$$

For the resonance condition $A = \Delta m^2 \cos(2\theta)$ the mixing is maximized. In the case of the Sun the electron density decreases radially. At some point the resonance condition for maximal mixing is fulfilled resulting in a maximum probability for a flavor transition. This is the reason why the electron neutrino flux measured on Earth is less than one would expect from considering only neutrino oscillations in vacuum (cf. Fig 1.3b).

In order to validate the predictions by the MSW effect one has to measure the oscillation parameters for different neutrino energies. The state-of-the-art experiment Borexino [ABB⁺08, AAA⁺19b] is able to detect solar neutrinos with sub-MeV energies via ν -e scattering in contrast to previous experiments which are only sensitive to higher energies. Considering Borexino measurements in the energy range from ~ 0.1 to ~ 10 MeV and KamLAND results, the so-called large mixing angle solution with $\sin^2(\theta_{12}) \approx 0.3$ and $\Delta m_{21}^2 \approx 7.5 \times 10^{-5} \text{ eV}^2/c^4$ was found to fit best to the data and is in good agreement with predictions by the solar model and the MSW effect [THH⁺18].

A combination of all solar neutrino oscillation experiments and the results from KamLAND give the current best-fit values for the parameters Δm_{21}^2 and $\sin^2(\theta_{12})$ which can be found in Tab. 1.1.

Atmospheric neutrino experiments

The Earth's upper atmosphere is constantly hit by high-energy cosmic ray particles which are mostly protons and helium nuclei. These primary particles interact with nitrogen and oxygen molecules to produce pions and kaons. These decay dominantly via the reactions described in Eqs. 1.3 and 1.4 producing muon neutrinos. Subsequently, electron and muon neutrinos are produced in the muon decay reactions

$$\mu^\pm \rightarrow e^\pm + (\nu_e/\bar{\nu}_e) + (\bar{\nu}_\mu/\nu_\mu). \quad (1.30)$$

The neutrino energy is typically in the GeV range and the oscillation baseline ranges from 10 km to the Earth's diameter of $\sim 12 \times 10^3$ km. Considering Eq. 1.21, measurements of atmospheric neutrino oscillation are sensitive to Δm^2 values between $\sim 1 \times 10^{-1} \text{ eV}^2/c^4$ and $\sim 1 \times 10^{-4} \text{ eV}^2/c^4$.

The first experiment to definitely observe neutrino oscillations with atmospheric neutrinos was Super-Kamiokande [FHI+98, ABH+18] in 1998. For this the 2015 Nobel prize in physics was awarded to T. Kajita. In Super-Kamiokande atmospheric neutrinos are detected via the CC interaction described in Eq. 1.5. Depending on the neutrino flavor, muons or electrons are produced in the final state. A cylindrical 50,000 ton water tank serves as target. The electrons or muons traversing the water volume produce Cerenkov radiation [Cer34], which can be detected by an array of more than 11,000 photomultiplier tubes mounted on the inner surface of the cylindrical tank. Electron neutrino (electron-like) and muon neutrino (muon-like) events can be differentiated by the shape of the detected Cerenkov light cone. The inner detector is surrounded by an additional veto detector with more than 1,800 photomultiplier tubes. Atmospheric neutrinos penetrate the target from all directions with an almost isotropic distribution. The incident direction is defined by its zenith angle Θ . For neutrinos coming from directly above it is $\cos(\Theta) = 1$, for neutrinos traveling through the Earth from the other side of the globe it is $\cos(\Theta) = -1$. In Super-Kamiokande the incident ν -direction can be reconstructed. The first pub-

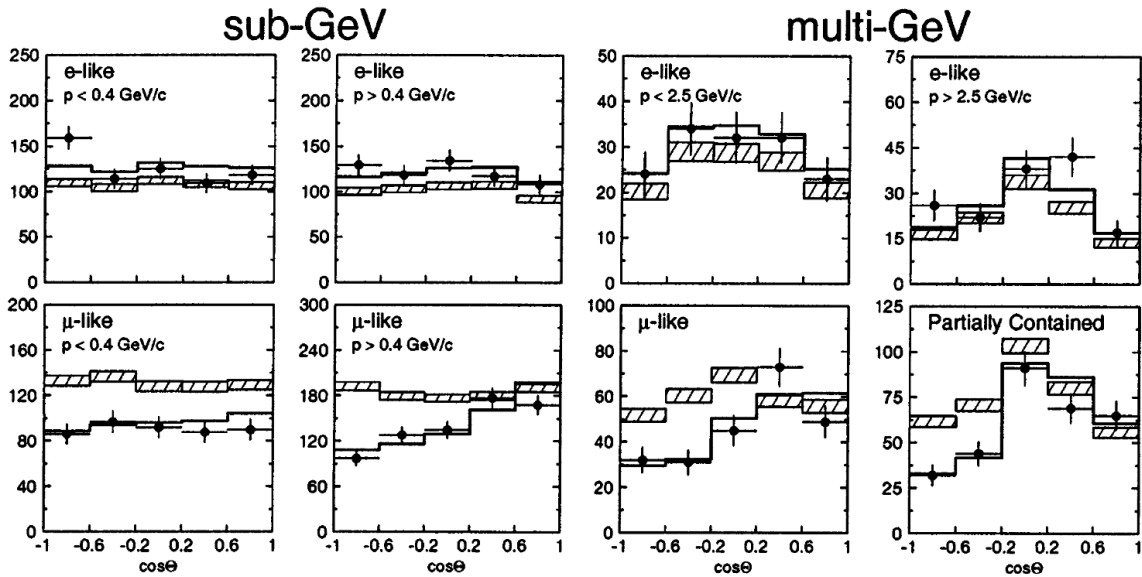


Figure 1.4: First Super-Kamiokande results of atmospheric neutrino zenith angle distributions. The plots are separated according to the neutrino energy with sub-GeV energies on the left and multi-GeV energies on the right. Electron-like events are shown on the top and muon-like events on the bottom. On the bottom right "partially contained" events are plotted. These are events which do not deposit their total energy in the fiducial volume of the inner target but parts of it in the outer veto detector. In each plot the reconstructed neutrino flux versus the zenith angle $\cos(\Theta)$ is shown. The hatched area represents the expectation for no neutrino oscillation from Monte Carlo simulations normalized to the experiment's data taking time. The bold line is the best-fit to the data points assuming $\nu_\mu \leftrightarrow \nu_\tau$ oscillations. The figure and its description are taken from [FHI+98].

lished results for a zenith angle-dependent measurement is shown in Fig. 1.4. A significant deficit of muon-like events when compared to Monte Carlo expectation can be seen. The deficit gets more pronounced for lower values of $\cos(\Theta)$, which are equivalent to longer traveling distances and thus longer oscillation baselines L/E . A reasonable explanation are multiple $\nu_\mu \leftrightarrow \nu_\tau$ transitions while traversing the Earth because of $L/E \gg 1/\Delta m^2$ (cf. Fig. 1.3b). Consequently, at the detector location only roughly half of the expected flux is measured. On the other hand, the Δm^2 values for $\nu_e \leftrightarrow \nu_\mu$ oscillations are comparably low, so in this case $L/E \ll 1/\Delta m^2$ and hence no deficit in electron-like events was measured.

After more than 20 years of operation and four different experimental phases, Super-Kamiokande has provided much more precise results of the Δm_{32}^2 and θ_{23} parameters [ABH⁺18]. Also, when using accelerator neutrinos, it is sensitive to the CP-violating phase δ . Nowadays, the values of $\sin^2(\theta_{23}) \approx 0.5$ and $|\Delta m_{32}^2| \approx 2.5 \times 10^{-3} \text{ eV}^2/c^4$ are well established and other experiments like IceCube [AAA⁺15] at the South Pole are sensitive to atmospheric neutrinos, too. However, the currently most precise values of atmospheric oscillation parameters are measured with the long-baseline accelerator neutrino experiments T2K and NO ν A in the disappearance channel [THH⁺18], which will be detailed later.

Nuclear reactor experiments

In nuclear reactors antineutrinos with an energy of up to 8 MeV are produced via the β -decay of fission products. The total isotropic neutrino flux emitted is

$$\phi_\nu = 1.9 \times 10^{17} \frac{P}{\text{MW}} \text{ s}^{-1} \quad (1.31)$$

with the reactor power P . In a detector with distance L to the reactor core positrons and neutrons are produced via inverse beta-decay on free protons (cf. Eq. 1.2) with a threshold energy of 1.8 MeV. The neutrino energy is not sufficient for producing heavy μ or τ leptons so the experiments measure in disappearance mode. The detection signal has a characteristic coincidence between a prompt and a delayed signal. The prompt signal is produced by the energy loss of positrons and their subsequent annihilation with electrons inside the detector material. Within 10-100 μ s neutrons are thermalized after multiple collisions in particular with hydrogen atoms of the scintillator. Finally, they are captured in a n/γ reaction by a nucleus, such as gadolinium or hydrogen. Typically, the detectors consist of several tons of scintillating liquid and a photomultiplier tube array surrounding it [THH⁺18].

Ideally, experiments use a combination of two detectors. One is located as close as possible to the reactor core for monitoring the antineutrino flux before oscillation effects can occur. The other one is located further away at a distance where the maximum sensitivity for the mixing parameter of interest is expected.

Reactor experiments with distances of $L \sim 100$ km between source and detector like KamLAND [A⁺08, G⁺13] in Japan are sensitive to θ_{12} mixing. For short baselines of $L \sim 1$ km the sensitivity for θ_{13} mixing is optimal. The three experiments Double Chooz [A⁺12a, A⁺16], RENO [A⁺12b, BCJ⁺18] and Daya Bay [A⁺12c, AAB⁺18] were the first to measure the smallest mixing angle $\sin^2(\theta_{13}) \approx 2 \times 10^{-2}$ for which the most current result is given in Tab. 1.1.

Accelerator neutrino beam experiments

Accelerator-based neutrino beams are produced by sending a high-energy proton beam onto a target producing pions and kaons which are focused and decay into neutrinos according to Eqs. 1.3 and 1.4. Predominantly, muon neutrinos are created. Both neutrino and antineutrino beams can be produced which allows studies of CP symmetry. One has to distinguish between short- ($L \ll 10$ km) and long-baseline ($L \gg 100$ km) experiments because each type is sensitive to different ranges of Δm^2 . [THH⁺18]

Long-baseline experiments employ a combination of near and far detector similar to reactor experiments. The first of its kind was the K2K experiment [AAA⁺01b] with a baseline of 250 km between the KEK proton synchrotron and Super-Kamiokande measuring at average neutrino beam energies of 1.3 GeV. It detected ν_μ disappearance consistent with measurements on atmospheric neutrinos [A⁺06]. Second-generation experiments were in addition capable of measuring $\nu_\mu \rightarrow \nu_e$ appearance. The MINOS experiment has provided high-precision measurements of the θ_{23} mixing by combining data of appearance and disappearance mode [A⁺13, AAA⁺14b]. The first ever detection of ν_τ appearance was accomplished by the OPERA experiment in the CERN to Gran Sasso neutrino beam (CNGS) [AAA⁺10, AAA⁺18c].

Currently, two state-of-the-art long-baseline experiments are pushing the precision frontier on the θ_{23} and Δm_{32}^2 parameters. The K2K successor experiment T2K [AAA⁺14a, AAA⁺18a] in Japan at 295 km baseline from the proton synchrotron J-PARC makes use of the Super-Kamiokande detector supplemented with multiple near detectors at a distance of a few hundred meters. In the US, Fermilab provides a neutrino beam for the NO ν A experiment [AAA⁺16, AAA⁺19a], which is located at a distance of 810 km. Both experiments are currently the dominant contributors to the θ_{23} and Δm_{32}^2 results given in Tab. 1.1. However, a high-precision measurement of the CP violating phase δ is still pending. Values for δ were published by Super-Kamiokande [ABH⁺18], MINOS [AAA⁺14b], T2K [AAA⁺18a] and NO ν A

Table 1.1: Current best-fit values for all neutrino oscillation parameters. The dominantly contributing experiments are the solar experiments for θ_{12} ; KamLAND for Δm_{21}^2 ; Daya Bay, Double-Chooz and RENO for θ_{13} and $|\Delta m_{13,23}^2|$; the long-baseline experiments K2K, Minos, T2K and NO ν A for θ_{23} and also for $|\Delta m_{13,23}^2|$ and the long-baseline experiments MINOS, T2K and NO ν A for δ . The octant defines whether $\theta_{23} < \pi/4$ (octant I) or $\theta_{23} > \pi/4$ (octant II) [BGG⁺12]. The terms "normal order" and "inverted order" refer to the $m_{1,2,3}$ mass ordering and will be explained in section 1.5. The values are taken from [THH⁺18].

Parameter	Measured value $\pm 1\sigma$
$\sin^2(\theta_{12})$	0.307 ± 0.013
$\sin^2(\theta_{23})$	$0.536_{-0.028}^{+0.023}$ (Inverted order)
$\sin^2(\theta_{23})$	$0.512_{-0.022}^{+0.019}$ (Normal order, octant I)
$\sin^2(\theta_{23})$	$0.542_{-0.022}^{+0.019}$ (Normal order, octant II)
$\sin^2(\theta_{13})$	$(2.18 \pm 0.07) \times 10^{-2}$
Δm_{21}^2	$(7.53 \pm 0.18) \times 10^{-5} \text{ eV}^2/c^4$
Δm_{32}^2	$(-2.55 \pm 0.04) \times 10^{-3} \text{ eV}^2/c^4$ (Inverted order)
Δm_{32}^2	$(2.444 \pm 0.034) \times 10^{-3} \text{ eV}^2/c^4$ (Normal order)
δ	$1.37_{-0.16}^{+0.18} \pi \text{ rad}$

[AAA⁺18b, AAA⁺19a]. But none of these results is significant enough to prove CP violation with $\delta \neq (0, \pi)$ at this moment. The best-fit value of a combined analysis is given in Tab. 1.1. Future accelerator neutrino experiments like DUNE [A⁺18a] and the Hyper-Kamiokande detector [Lod17] have the primary goal of demonstrating leptonic CP violation by measuring differences in $\nu_\mu \rightarrow \nu_e$ and $\bar{\nu}_\mu \rightarrow \bar{\nu}_e$. [THH⁺18] Short-baseline experiments probe higher scales of Δm^2 . In fact, evidences for neutrino oscillations with mass differences of $\Delta m^2 > 1 \times 10^{-2} \text{ eV}^2/c^4$ were reported in ν_e and $\bar{\nu}_e$ appearance mode by the experiments LSND [AAB⁺01] and MiniBooNE [AABB⁺18]. These findings, if genuine, can not be explained in the current three flavor model and would indicate the existence of a fourth flavor state, a sterile neutrino. Future projects like JSNS² [A⁺17] and a multi-detector approach at Fermilab [A⁺15] will evaluate the flavor oscillation in the $\Delta m^2 \sim 1 \text{ eV}^2/c^4$ region with increased sensitivity. [THH⁺18]

1.5 Open questions

The last decades have witnessed a tremendous progress in studies of fundamental neutrino properties. Three different flavors have been discovered and were successfully integrated in the electroweak theory of the standard model of particle physics. Beyond that, it was shown that neutrinos undergo the quantum-mechanical effect of periodic flavor transitions revealing that mass and flavor eigenstates are not identical and that at least two mass eigenstates have a non-vanishing rest mass. Most of the parameters describing these oscillations have been measured with high precision. Yet, neutrino physics is still a vivid field of modern research because of a large number of open questions. The most prominent ones will be discussed in the following.

What is the correct $m_{1,2,3}$ mass ordering?

The resonance condition of the MSW effect depends on the sign of Δm^2 . In solar neutrino experiments large mixing in agreement with the MSW effect was verified, so the resonance condition has to be fulfilled in the interior of the Sun which is only possible if $\Delta m_{21}^2 = m_2^2 - m_1^2 > 0$. On the other hand, the sign of Δm_{32}^2 is still unknown, leaving two possible scenarios for the correct neutrino mass hierarchy open:

- Normal mass hierarchy: $m_3 > m_2 > m_1$.
- Inverted mass hierarchy: $m_2 > m_1 > m_3$.

There are several possibilities for measuring the correct one. One would be the measurement of matter effects in atmospheric neutrino oscillations, which is one of the major goals of the PINGU upgrade of IceCube [A⁺14]. Also, long-baseline accelerator neutrino experiments like NO ν A have the prospect of measuring matter effects because their neutrino beam is traveling mostly underground. Another possibility is the detection of reactor neutrinos in a distance of ~ 60 km. For this baseline both Δm_{21}^2 and $\Delta m_{31}^2 \sim \Delta m_{32}^2$ oscillations are observable simultaneously. The JUNO detector as well as the RENO successor experiment RENO-50 are currently under construction and first data taking is expected in the 2020s [Men20, Kim15].

Is CP symmetry conserved in the neutrino sector?

The process of CP violation has been discussed in section 1.4.1. Yet, the CP phase δ of the PMNS matrix was not measured to be significantly different from $(0, \pi)$ and future long-baseline accelerator experiments have to provide a more precise result as detailed in section 1.4.2. The question of the existence of leptonic CP violation is not only relevant in the context of neutrino physics. Rather, it is a fundamental question about the origin of matter in the cosmos since cosmological structures only exist because of an imbalance between matter and antimatter on the 10^{-10} level in the early universe. In a full CP symmetric world any matter would have been annihilated with its antimatter counterpart.

Are neutrinos Majorana or Dirac particles?

If neutrinos are Dirac particles as charged leptons and quarks, they are a solution of the Dirac equation 1.8 in the form of a four-component spinor Ψ . The four components are left-handed neutrinos ν_l , right-handed neutrinos ν_r , left-handed antineutrinos $\bar{\nu}_l$ and right-handed antineutrinos $\bar{\nu}_r$. If they are Majorana particles, only ν_l and ν_r exist so there are no antineutrinos or, to put it in other words, the neutrino is its own antiparticle " $\nu = \bar{\nu}$ ". Experimentally, a differentiation has not been achieved yet. The most promising method to accomplish this is the search for neutrinoless double β -decay detailed in section 1.6.4.

Do more than three flavors exist?

In section 1.2 the results of the LEP and SLC measurements for the number of active neutrino flavors was given. It is important to note that these include only weakly interacting flavors with relatively small masses $m_\nu < m_Z/2 \approx 45.6 \text{ GeV}/c^2$ [THH⁺18]. So in principle, a right-handed neutrino flavor state not participating in the weak interaction could exist. These so-called sterile neutrinos interact only gravitationally, which makes their detection quite challenging. If they exist, they will take part in neutrino oscillations, so the mixing mechanism has to be extended at least to a four flavor formalism. Although there is no definite proof for the existence of sterile neutrinos, several experiments found deviations from the expected results for three active neutrinos.

In reactor neutrino experiments with baselines $L < 100 \text{ m}$ a several percent lower flux than expected from new theoretical calculations was measured [MFL⁺11]. A possible explanation for this so-called reactor antineutrino anomaly is the oscillation of parts of the electron antineutrino flux into sterile neutrinos with eV/c^2 masses. As already discussed in section 1.4.2, in the short-baseline accelerator experiments LSND and MiniBooNE an excess of signals was found in the appearance channel of their data that can be interpreted in terms of sterile neutrinos with a mass in the eV/c^2 range. The radiochemical gallium experiments GALLEX and SAGE placed artificial radioactive sources close to their detectors for calibration purposes [KHH⁺10, AGG⁺09, GL10]. This can be used to perform a short-baseline neutrino oscillation measurement. Again, compared to the expectation, a reduced flux was measured in the disappearance channel. However, according to a global analysis by Machado et al. [Mac20] there is some tension between the appearance and disappearance experiments at 4.7σ . The KATRIN experiment (see next chapter) will be able to probe part of the preferred parameter space.

Sterile neutrinos with masses of several keV/c^2 are possible dark matter candidates. The XMM-Newton satellite has measured an unknown X-ray line at an energy of

3.5 keV [BMF⁺14]. It could originate from a radioactive decay of a sterile neutrino ν_S into a standard model flavor ν_α and a photon γ .

A promising approach of measuring sterile neutrinos with keV/ c^2 masses is the detection of small distortions in the β -spectrum as is intended with the KATRIN experiment [MLG⁺15].

What is the absolute mass scale?

The neutrino oscillation measurements of the squared mass splittings Δm^2 allow to place lower bounds for the mass eigenvalues, depending on the mass hierarchy. For the normal mass hierarchy it is $m_2 \geq \sqrt{\Delta m_{21}^2} \approx 9 \text{ meV}/c^2$ and $m_3 \geq \sqrt{\Delta m_{31}^2} = \sqrt{\Delta m_{32}^2 + \Delta m_{21}^2} \approx 50 \text{ meV}/c^2$. For the inverted mass hierarchy the bounds are $m_1 \geq \sqrt{\Delta m_{13}^2} = \sqrt{-(\Delta m_{32}^2 + \Delta m_{21}^2)} \approx 50 \text{ meV}/c^2$ and $m_2 \geq \sqrt{-\Delta m_{32}^2} \approx 50 \text{ meV}/c^2$. However, the absolute mass scale remains unknown. The relevance of this parameter as well as the various approaches to determine it will be introduced in the next section.

1.6 Absolute mass scale determination

This section is meant to be a detailed overview over the current field of experimental neutrino mass determination. First, the search for the absolute mass scale will be motivated in section 1.6.1 by emphasizing the importance of the mass parameter to different physics branches based on [KAT05, Zub12, OO19]. Then, the different experimental techniques will be explained.

1.6.1 Why is it important?

There are two physics disciplines which would benefit most from a direct measurement of the neutrino mass: particle physics and cosmology. In the following, the implications of the mass parameter for both fields are discussed.

In particle physics the exceptional smallness of the neutrino mass compared to all other fermions is the rationale to explore alternative mass generation models beyond the well-established Higgs mechanism [EB64, Hig64, GHK64]. Many of them are based on the so-called seesaw mechanism. In the seesaw type I, heavy right-handed Majorana neutrinos are introduced. The heavier they are, the lighter the left-handed light flavors become. In seesaw type II scenarios, three novel Higgs bosons couple to the three light neutrino flavors generating their masses. The seesaw and other models each are predicting a specific type of $m_{1,2,3}$ pattern namely either the hierarchical ($m_3 > m_2 > m_1$ or $m_2 > m_1 > m_3$) or the quasi-degenerate ($m_3 \approx m_2 \approx m_1$) version. A measurement of the absolute mass scale would result in the falsification of multiple models and point towards the correct one.

A major aspect of cosmology is the study of the origin of large-scale structures. While the cosmological principle describes the universe as homogenous on the very large scale [Per09], in fact, at the size of galaxy clusters and superclusters the matter is grouped while in between large voids are present. If neutrinos held a non-negligible portion of the matter-energy budget of the universe, they would have a strong influence on the formation of matter clusters [BES80].

Structure formation is assumed to originate from matter density fluctuations in the early universe. After the initial perturbation, the self-gravity process will lead to a collapse of the matter if the mass and radius are below the Jeans mass and radius [UB02]. In the early universe massive neutrinos contributed to this critical mass and size. These primordial neutrinos decouple at $t = 1$ s after the Big Bang. Before that, they were in thermal equilibrium with photons, electrons and positrons via the reactions

$$\gamma + \gamma \leftrightarrow e^+ + e^- \leftrightarrow \nu_\alpha + \bar{\nu}_\alpha. \quad (1.32)$$

As the universe expanded its temperature T fell below a critical value of $k_B T \approx 1$ MeV leading to the so-called freeze-out of neutrinos at $t = 1$ s. Since then the "neutrino fireball" [Per09] streams freely through the universe not longer interacting with other particles. Today, it can be calculated that the temperature of this relic neutrino background should be $T_\nu = 1.95$ K with a number density $n_\nu = 336 \text{ cm}^{-3}$ [Zub12]. In the early universe these neutrinos were highly relativistic with velocities much higher than the escape velocities of galaxies or galaxy clusters, so they are referred to as Hot Dark Matter (HDM). Thus, for them it was possible to escape even high density areas. Small-scale structure formation was suppressed by this free streaming. The critical size and mass scales are [Zub12]:

$$\begin{aligned} \lambda &\approx 1230 \left(\frac{m_\nu}{\text{eV}} \right)^{-1} \text{ Mpc}, \\ M &\approx 1.5 \times 10^{17} \left(\frac{m_\nu}{\text{eV}} \right)^{-2} M_{\text{sol}} \text{ Mpc}. \end{aligned} \quad (1.33)$$

Here, the solar mass is defined as $M_{\text{sol}} = 2 \times 10^{30}$ kg and 1 Megaparsec is $1 \text{ Mpc} = 3.09 \times 10^{22}$ m [UB02]. This size and mass scale correspond to superclusters which are the first structures forming in a universe dominated by neutrinos [Zub12]. Smaller structures are damped out. It is obvious that Eq. 1.33 depends on the neutrino mass: Smaller neutrino masses lead to smaller structures.

1.6.2 Supernova time-of-flight

The final stage of a star's lifetime is marked by a cosmic explosion called supernova. Vast numbers of neutrinos are emitted in the core-collapse type supernovae. There, the core of massive stars with $M > 8M_{\text{sol}}$ reach high temperatures so that the fusion chain proceeds up to iron, which has the highest nuclear binding energy of all elements. No energy can be gained from fusion of iron. Therefore, the gravitational pressure inside the core is no longer counterbalanced by energy released in the fusion processes. Instead, electrons in the core build up a Fermi gas and provide a degeneracy pressure due to the Pauli principle working against gravity. As the fusion to iron nuclei evolves, at some point the core will reach the Chandrasekhar mass limit of $M > 1.4M_{\text{sol}}$ above which the reactions

$$p + e^- \rightarrow n + \nu_e \quad \text{and} \quad X + e^- \rightarrow Y + \nu_e \quad (1.34)$$

take place with free protons p and heavier nuclei X, Y [Zub12]. This reduces the number of electrons and thus the magnitude of the degeneracy pressure. The dominant gravitational force finally leads to the core collapse. During the contraction thermal neutrinos are produced via [OO19]

$$\gamma + \gamma \rightarrow e^+ + e^- \rightarrow \nu_\alpha + \bar{\nu}_\alpha. \quad (1.35)$$

As the collapse evolves, at some point a mean nucleon distance on the order of 1 fm [OO19] is reached where the strong interaction is getting repulsive, which leads to a rebound. The matter bounces back and builds up a shock wave eventually leading to the explosion of the star where the outer layers of the star are blown away. About 99% of the total energy is released via neutrinos [Zub12]. Finally, the core remains as either a neutron star or a black hole.

The neutrino mass can in principle be determined via the time-of-flight t_f from the supernova core to the Earth. For neutrinos travelling with speed v , energy E_ν and momentum p_ν over a distance L during the time between emission t_0 and arrival t , the time-of-flight is defined by [Zub12]:

$$t_f = t - t_0 = \frac{L}{v} = \frac{L}{c} \frac{E_\nu}{p_\nu c} = \frac{L}{c} \frac{E_\nu}{\sqrt{E_\nu^2 - m_\nu^2 c^4}} \approx \frac{L}{c} \left(1 + \frac{m_\nu^2 c^4}{2E_\nu^2} \right) \quad (1.36)$$

with the speed of light c . For two distinct neutrinos with energies E_1 and E_2 emitted at t_{01} and t_{02} , respectively with $\Delta t_0 = t_{02} - t_{01}$ the detection time difference on Earth is [Zub12]

$$\Delta t = t_2 - t_1 = \Delta t_0 + \frac{L m_\nu^2 c^3}{2} \left(\frac{1}{E_{\nu,2}^2} - \frac{1}{E_{\nu,1}^2} \right). \quad (1.37)$$

Measuring the energy and arrival time of at least two neutrino events from a supernova is therefore allowing a mass determination.

So far, the only opportunity to do this was the SN 1987A core-collapse supernova in the Large Magellanic Cloud. Four detectors published results on detected neutrino events: Kamiokande II [HKK⁺87], the Irvine-Michigan-Brookhaven detector [BBB⁺87], the Baksan Scintillator Telescope [AAKV88] and Mont Blanc [ABB⁺87]. From the most stringent analysis an upper electron antineutrino mass limit of

$$m_{\bar{\nu}_e} < 5.7 \text{ eV}/c^2 \quad (95\% \text{ C.L.}). \quad (1.38)$$

can be derived [LL02].

1.6.3 Cosmology

The minimal cosmological model describes the development and current state of the universe in the Λ CDM scenario assuming that the total density Ω_{tot} is a sum of the density of photons Ω_γ , neutrinos Ω_ν , baryons Ω_b , cold dark matter Ω_{CDM} and dark energy Ω_Λ . The electron contribution is comparatively small thus it is neglected. Concerning neutrinos, the density parameter in natural units is defined as [THH⁺18]

$$\Omega_\nu h^2 = \frac{\sum m_\nu}{93 \text{ eV}}. \quad (1.39)$$

The scaled dimensionless Hubble parameter is given by $h = H_0 / 100 \text{ km s}^{-1} \text{ Mpc}^{-1}$ with the Hubble constant $H_0 = 67 \text{ km s}^{-1} \text{ Mpc}^{-1}$ [A⁺18b]. This neutrino density influences cosmological observations in several ways. However, only in the two cases explained below the effect of m_ν is large enough to constrain the neutrino mass. [Won11, THH⁺18]

As already mentioned in section 1.6.1, the neutrino density affects today's matter

distribution in the cosmos. This distribution can be described by an autocorrelation function $\xi(r)$ giving the probability that at distance $x = r$ the same matter overdensity is found as at $x = 0$. In cosmology it is convenient to take the Fourier conjugate of the autocorrelation function called the matter power spectrum $P(k)$. Neutrinos wash out small-scale structures in the early universe due to their free streaming (cf. section 1.6.1). The formation of structure at very large scales is favored if the sum of neutrino mass eigenvalues $\sum m_\nu$ is larger.

A measurement of the matter power spectrum would reveal this influence which is illustrated in Fig. 1.5a. It can be seen that for a larger sum of neutrino mass eigenvalues the power spectrum decreases at high wavenumbers k corresponding to small sizes r . The effect is dominated by the neutrino mass sum, not by the individual masses. Measured data of the power spectrum are provided by large sky surveys essentially producing galaxy catalogs from which galaxy number densities can be derived. Prominent examples are the Sloan Digital Sky Survey (SDSS) and the 2dF Galaxy Redshift Survey (2dFGRS). [Won11, Zub12, THH⁺18]

The absolute neutrino mass also influences the cosmic microwave background (CMB) radiation. This is an isotropic radiation first detected in 1964 by A. A. Penzias and R. W. Wilson [PW65] for which they were awarded the Nobel prize in 1978. It originates from an epoch $t = 380000$ years after the Big Bang when radiation and matter decoupled. The CMB radiation perfectly agrees with radiation emitted by a black body at a temperature of $T = 2.7$ K [Per09]. Depending on the direction in the sky tiny temperature anisotropies ΔT occur on the order of 10^{-5} K. These anisotropies represent the matter fluctuations at the time of decoupling. Since it is an angular-dependent distribution it is convenient to expand the temperature fluctuations into spherical harmonics Y_{lm} with $l = [0, \infty]$, $m = [-l, l]$ and $l \approx \pi/\theta$ denoting the angle

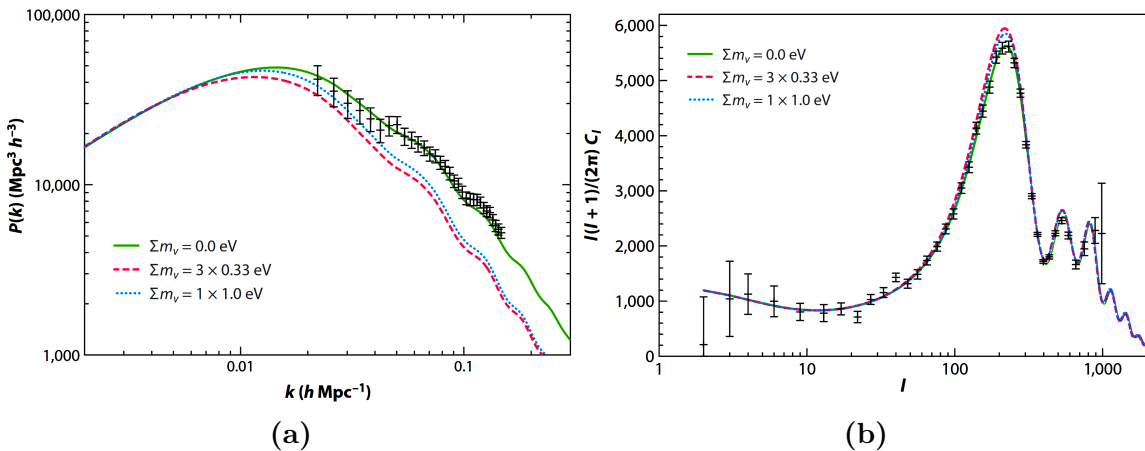


Figure 1.5: Models showing the influence of different sums of neutrino mass eigenvalues on cosmological spectra. In (a) models of the matter power spectrum $P(k)$ for different neutrino masses are shown. Large wavenumbers k correspond to small distances r . The data points originate from the 2dF sky survey in 2005 [CPP⁺05]. In (b) models of the cosmic microwave background temperature anisotropy spectrum are plotted for different neutrino masses. Large harmonic indices l represent small angles θ . The data points were provided by the first three years of observations by the WMAP satellite published in 2007 [HNB⁺07]. Both figures are taken from [Won11].

θ between two points in the sky. Using the correlation function $C(\theta)$ between two points the temperature anisotropy can be expressed as

$$\Delta T_l = \sqrt{C_l \frac{(l+1)}{2\pi}}. \quad (1.40)$$

In the temperature anisotropy spectrum usually ΔT^2 is plotted versus the harmonic index l . The spectrum shape is sensitive on the matter distribution at the time of decoupling, so different neutrino masses can change it as can be seen in Fig. 1.5b. A leading experiment of measuring CMB spectra is the Planck satellite. Combining these results with Galaxy Redshift Survey data leads to a current upper limit of [A⁺18b]

$$\sum m_\nu < 0.12 \text{ eV}/c^2 \quad (95\% \text{ C.L.}). \quad (1.41)$$

It is important to note that this limit is only valid in the Λ CDM framework and strongly depends on other free parameters of this model. [Per09, Won11, Zub12]

1.6.4 Neutrinoless double beta-decay

Some nuclei can undergo two simultaneous β -decays if the nucleus in between the parent and daughter nucleus has a higher mass than the other two nuclei. This double β -decay is a standard model weak interaction and the rarest ever observed decay process [EHM87]. The typical mean life times are rather long with $\tau > 10^{20}$ years since it is a second-order weak process [Per09]. Nevertheless, observations of double β -decay date back to the 1950s [IR50]. Hypothetically, if neutrinos were Majorana particles, it would be possible that this decay happens without neutrinos in the final state:

$$M(A, Z) \rightarrow D(A, Z + 2) + 2e^-. \quad (1.42)$$

Here, e^- represents an electron, M is the mother and D is the daughter nucleus with the nucleon number A and the proton number Z . It is feasible to consider this as a two-stage process. In a first step a right-handed neutrino is emitted which is absorbed as a left-handed neutrino in the second vertex. The probability of such a helicity flip is $P = (1 - v/c) \propto (m_\nu c^2)^2 / 2E^2$ with the neutrino velocity v and energy E [Per09]. In case of $m_\nu = 0$ the probability vanishes, so neutrinoless double β -decay ($0\nu\beta\beta$) does not occur. If it is observed, the decay rate will depend on the neutrino mass. Quantitatively, the decay rate can be derived starting from Fermi's Golden Rule resulting in [Zub12]:

$$R_{0\nu\beta\beta} / \ln(2) = (T_{1/2}^{0\nu\beta\beta})^{-1} = G^{0\nu\beta\beta}(Q, Z) \left| M_{GT}^{0\nu\beta\beta} - M_F^{0\nu\beta\beta} \right|^2 \left(\frac{\langle m_{\beta\beta} \rangle}{m_e} \right)^2. \quad (1.43)$$

Here $T_{1/2}^{0\nu\beta\beta}$ is the half-life time, $M_{GT}^{0\nu\beta\beta}$ is the Gamov-Teller and $M_F^{0\nu\beta\beta}$ is the Fermi transition matrix element. The phase space factor $G^{0\nu\beta\beta}(Q, Z)$ depends on the proton number Z and the Q -value. The latter parameter Q is defined as the total nuclear transition energy available as kinetic energy $Q = M_i - M_f - 2m_e$ with the masses of the initial and final state nuclei M_i and M_f and the electron mass m_e [BG15]. The effective Majorana neutrino mass $\langle m_{\beta\beta} \rangle$ is given by [Zub12]

$$\begin{aligned} \langle m_{\beta\beta} \rangle &= \left| \sum_i U_{ei}^2 m_i \right| \\ &= \left| m_1 c_{12}^2 c_{13}^2 e^{2i\eta_1} + m_2 c_{13}^2 s_{12}^2 e^{2i\eta_2} + m_3 s_{13}^2 e^{-2i\delta} \right| \end{aligned} \quad (1.44)$$

using the parametrization from Eq. 1.12. It is important to note that the two Majorana CP phases $\eta_{1,2}$ and the Dirac CP phase δ have to be considered, so the single terms might partly or fully cancel each other. [Per09, Zub12]

Using Eq. 1.44 and the well-known mixing parameters from Tab. 1.1, the effective Majorana mass $m_{\beta\beta}$ can be plotted as a function of the lightest neutrino mass m_{lightest} , which is m_1 or m_3 depending on the mass hierarchy. This can be seen in Fig. 1.6a. It is shown that for a normal mass hierarchy $m_{\beta\beta} = 0$ is possible because the complex phases in Eq. 1.44 lead to a cancellation of the individual terms. So neutrinoless double β -decay would never be observed although neutrinos might be Majorana particles. A schematic plot of the decay rate versus the energy for the sum of both electrons can be found in Fig. 1.6b. In the standard model double β -decay the decay energy is shared by two electrons and two neutrinos, so the summed electron spectrum is continuously distributed up to the endpoint which is equal to the Q-value. On the other hand, in the neutrinoless double β -decay the electrons carry all the energy and their spectrum is a peak at the position of the Q-value. An experimental challenge is the overlap of both spectra resulting from the broadening of both the $2\nu\beta\beta$ spectrum and the $0\nu\beta\beta$ peak, due to the finite energy resolution of the detector. [Zub12, BG15]

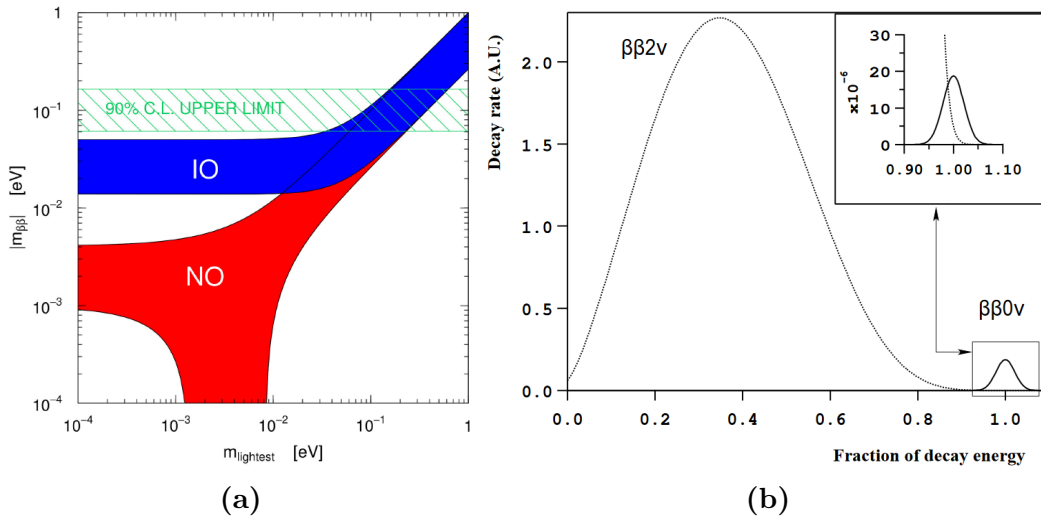


Figure 1.6: Effective Majorana mass constraints on the lightest neutrino mass and double β -decay energy spectra. In (a) the effective Majorana neutrino mass $m_{\beta\beta}$ is plotted versus the lightest neutrino mass m_{lightest} with 99.7% C.L. contours. In blue the inverted mass ordering (IO) with $m_{\text{lightest}} = m_3$ and in red the normal mass ordering (NO) with $m_{\text{lightest}} = m_1$ is displayed. The plot is only valid in a 3ν framework excluding additional sterile neutrinos. An upper limit for $m_{\beta\beta}$ represented by the 90% C.L. green hatched area was set by the KamLAND-Zen experiment in 2016 [GGH⁺16]. The figure and its description are taken from [dSGM⁺18]. In (b) a schematic of the electron sum energy spectra for the $2\nu_e$ and the $0\nu_e$ double β -decay case is given. The upper right part of the figure is a zoom into the endpoint region. The $2\nu_e$ spectrum intensity was increased to better illustrate the overlap between both spectra. The figure and its description are taken from [Cre03].

From the experimental point of view, a high $0\nu\beta\beta$ decay rate and low $2\nu\beta\beta$ decay rate are favored. Considering Eq. 1.43, isotopes with large phase space factors (scaling with Q^5) and large transition matrix elements are advantageous. On top of that, high-purity material enhances the sensitivity further. Even if these criteria are fulfilled, the count rates are still extremely small, so background minimization is of major importance which is why experiments typically are located deep underground. There are two groups of $0\nu\beta\beta$ experiments. In the first group, detector and source are identical while in the second they are separated. There are multiple experiments using different isotopes and detection techniques. Semiconductor detectors provide a high energy resolution for investigating the decay of ^{76}Ge which can be enriched to more than 85%. Other important approaches are cryogenic bolometers for ^{130}Te decay and time projection chambers with ^{136}Xe emitters.

The current world-leading limit on $m_{\beta\beta}$ was obtained with a modified setup of the already mentioned KamLAND reactor oscillation experiment called KamLAND-Zen. The KamLAND detector contains a photomultiplier tube array mounted on the inner surface of a spherical stainless steel vessel with 18 m diameter [A⁺08]. In the center a 3-m-diameter balloon encloses 13 t of low-activity liquid scintillator, loaded with 90% enriched ^{136}Xe [GGH⁺16]. A total of 534 days of data combined yields a lower limit for the half-life time and an upper limit for the Majorana mass of [GGH⁺16]

$$\begin{aligned} T_{1/2}^{0\nu\beta\beta} &> 1.07 \times 10^{26} \text{ yr} && (90\% \text{ C.L.}), \\ m_{\beta\beta} &< 0.061 - 0.165 \text{ eV}/c^2 && (90\% \text{ C.L.}). \end{aligned} \tag{1.45}$$

In order to deduce the limit on the Majorana mass, theoretical calculations of the nuclear transition matrix elements which are part of Eq. 1.43 are necessary. These calculations have rather high uncertainties. Also, the mass limits are valid only in a three flavor Majorana neutrino model. The existence of a fourth flavor sterile neutrino would change e.g. the plot shown in Fig. 1.6a significantly. [Zub12, dSGM⁺18, OO19]

1.6.5 Beta-decay

Neutrino mass measurements using nuclear β -decays do not depend on specific models. The parameter $m_{\bar{\nu}_e}$ is deduced purely from kinematic considerations like in the supernova time-of-flight approach. There are three very similar versions of β -decay [Zub12]:

$$\begin{aligned} M(A,Z) &\rightarrow D(A,Z+1) + e^- + \bar{\nu}_e && (\beta^- \text{-decay}), \\ M(A,Z) &\rightarrow D(A,Z-1) + e^+ + \nu_e && (\beta^+ \text{-decay}), \\ M(A,Z) + e^- &\rightarrow D(A,Z-1) + \nu_e && (\text{electron capture}). \end{aligned} \tag{1.46}$$

Here, e^- represents an electron, e^+ a positron, M is the mother and D is the daughter nucleus with the nucleon number A and the proton number Z . Neglecting the difference in atomic binding energies, the corresponding Q-values are [Zub12]

$$\begin{aligned} Q_{\beta^-} &= (m_M(A,Z) - m_D(A,Z+1) - m_{\bar{\nu}_e}) c^2, \\ Q_{\beta^+} &= (m_M(A,Z) - m_D(A,Z-1) - 2m_e - m_{\nu_e}) c^2, \\ Q_{\text{EC}} &= (m_M(A,Z) - m_D(A,Z-1) - m_{\nu_e}) c^2. \end{aligned} \tag{1.47}$$

The masses m_M and m_D refer to the atomic masses of mother and daughter atoms. The electron mass is given by m_e . It is important to note that the effective neutrino mass values fulfill $m_{\bar{\nu}_e} = m_{\nu_e}$ taking CPT (charge conjugation + parity + time reversal) symmetry for granted.

In the KATRIN experiment the super-allowed β^- -decay of tritium is used. In the following the focus will be on this specific version of β -decay. The energy spectrum is continuously distributed between 0 eV and the spectrum endpoint $E_0 = Q - E_{\text{rec}}$ with the daughter nucleus recoil energy E_{rec} . Starting from Fermi's Golden Rule the differential transition rate can be derived and is given in natural units by [AW03]

$$\frac{d^2 N_\beta}{dt dE} = \frac{G_F^2 \cos^2 \theta_C}{2\pi^3 \hbar^7} |M^2| \cdot F(E, Z + 1) \cdot p \cdot (E + m_e) \epsilon \sqrt{\epsilon^2 - m_{\nu_e}^2} \theta(\epsilon - m_{\nu_e}). \quad (1.48)$$

The constants are the Fermi constant G_F , the Cabibbo angle θ_C , the Fermi function F , the proton number Z and the nuclear transition matrix element M . Properties of the electron are its momentum p , its kinetic energy E and its mass m_e . The relative distance to the endpoint is given by $\epsilon = E_0 - E$ and the Heaviside function θ requires $\epsilon \geq m_{\nu_e}$.

It can be seen that the effective electron neutrino mass, which is small compared to the endpoint E_0 , affects the energy spectrum only close to E_0 changing its shape and reducing the maximum energy from E_0 to $E_0 - m_{\nu_e} c^2$. The β -spectrum shape and the influence of the neutrino mass are illustrated in Fig. 1.7.

Two effects are neglected in Eq. 1.48. The first one is neutrino mixing. If considered, the squared electron neutrino mass in Eq. 1.48 has to be substituted by the following sum:

$$m_{\nu_e}^2 = \sum_j |U_{ei}|^2 m_j^2. \quad (1.49)$$

The resulting spectrum is a sum of three spectra, each with a different maximum energy $E_0 - m_j c^2$. However, current experiments have not sufficiently large resolution to resolve mass differences as tiny as $|m_j - m_k|$, so that the spectrum can be

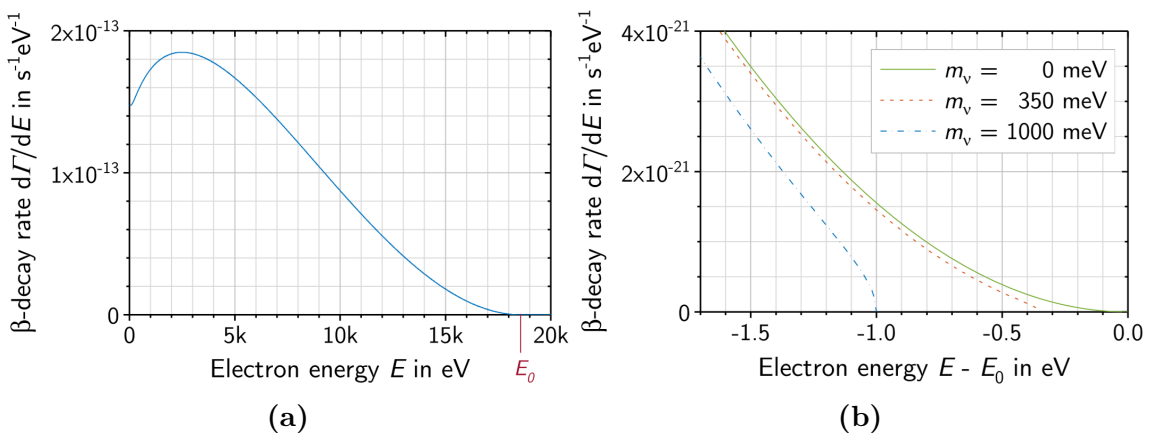


Figure 1.7: Energy spectrum of tritium β -decay and influence of the electron neutrino mass on the shape close to the endpoint. In (a) the differential β -spectrum is shown with an endpoint energy of $E_0 = 18.574$ keV. The decay rate values are given for a single tritium nucleus. The influence of different electron neutrino mass values can be seen in (b). Both figures and their descriptions are taken from [KBD⁺19].

analyzed only in terms of a single squared effective neutrino mass $m_{\nu_e}^2$. Secondly, atomic and molecular excitations of the daughter molecule have to be taken into account. Then, the electron spectrum described by Eq. 1.48 is shifted by the potential V_k for each of the different rotational, vibrational and electronic excitations of the molecule, which are occupied with probability W_k . Again, the resulting spectrum is a sum of k different spectra with maximum energies $E_0 - V_k$ and amplitudes proportional to W_k . This effect is only accessible through theoretical simulations, which pose an important systematic uncertainty that limits the sensitivity of experiments with molecular β -sources. [AW03, Zub12]

Some β -emitting isotopes are especially suitable for neutrino mass investigations. Ideally, those isotopes possess the following characteristics [KAT05].

- **A low endpoint energy E_0 :** The lower the absolute endpoint of the energy spectrum, the higher the fraction of β -electrons in close vicinity to E_0 .
- **A short half-life time $T_{1/2}$:** In order to gather enough statistics close to the endpoint, a source with a high count rate is required. A short half-life time reduces the necessary column density of the source material to reach such a high activity. Otherwise, the decay electrons would not be able to leave the source without interactions with the source material.
- **Simple atomic structure:** The complexity of quantum-mechanical calculations for higher order corrections of the spectral shape is reduced significantly. Also low Z values reduce inelastic scattering, which affects the energy of β -electrons.
- **Super-allowed nuclear transition:** The nuclear transition matrix element is energy-independent for super-allowed decays [Zub12].

The lowest endpoint value of all β -emitters is attributed to ^{187}Re with $E_0 = 2.47$ keV [DHMW13] decaying via



with an exceeding long half-life time of $T_{1/2}^\beta = 4.3 \times 10^{10}$ yr [DHMW13]. Neutrino mass limits from this decay stem from investigations with cryogenic microcalorimeters. In this approach the total decay energy, except the one carried away by the neutrino, is deposited in an absorber material, where it generates heat. An advantage of this approach is that many systematic effects, like those related to energy-losses, vanish. The temperature rise in the absorber $\Delta T = \Delta E/C_V$, which depends on the specific heat capacity C_V , is measured. Small heat capacities are favored for maximum sensitivity. As the specific heat scales with T^3 according to the Debye model [Deb12], the temperature should be as low as possible and thus be on the mK level. Currently, the best upper limit from ^{187}Re -decay was achieved by the MIBETA experiment [SAB⁺04] using AgReO_4 microcalorimeters:

$$m_{\bar{\nu}_e} < 15 \text{ eV}/c^2 \quad (90\% \text{ C.L.}) \quad (1.51)$$

The next stage of this technique, the MARE experiment, aimed for an ultimate neutrino mass sensitivity as low as $0.1 \text{ eV}/c^2$ [Nuc12]. However, due to technical challenges and the lack of funding this approach was discontinued.

A promising alternative is the calorimetric investigation of the electron capture

spectrum of ^{163}Ho pursued by the ECHo [GBD⁺14, GBC⁺17] and HOLMES [N⁺18] experiments. With a half-life time of $T_{1/2}^{\text{EC}} \approx 4600$ yr and a reasonably low Q-value of $Q \approx 2.6$ keV, the electron capture proceeds as follows [GBC⁺17]



The anticipated sensitivities are on the eV level in the first stage and ultimately expected to push into the sub-eV level [N⁺18, GBC⁺17].

However, the only isotope fulfilling all four criteria for a suitable β -emitter given above is tritium. As a hydrogen isotope its atomic structure is simple. Both the endpoint energy of $E_0 = 18.574$ keV [KBD⁺19] and the half-life time $T_{1/2}^{\beta} = 12.3$ yr [DHMW13] are reasonably low and the β -decay to helium



is super-allowed. Consequently, the world-leading upper limits from direct kinematic measurements of the neutrino mass result from tritium beta-decay experiments. In 1991 the Mainz [WPB⁺93, KBB⁺05] and in 1994 the Troitsk [BBG⁺95, ABB⁺11] experiment started data taking [DHMW13]. A combined analysis of the final results yielded an upper limit of $m_{\bar{\nu}_e} < 2.0$ eV/ c^2 (95% C.L.) [THH⁺18].

Currently, the worldwide lowest upper limit from β -decay measurements was achieved by the KATRIN experiment with a similar but much improved technique and a one order of magnitude larger setup than Troitsk and Mainz. During the work on this thesis the first KATRIN neutrino mass run (KNM1) took place in spring 2019 and ultimately resulted in an upper limit of [AAA⁺19c]

$$m_{\bar{\nu}_e} < 1.1 \text{ eV}/c^2 \quad (90\% \text{ C.L.}). \quad (1.54)$$

Details about the measurement principle and setup will be given in the following chapter.

2. The KATRIN experiment

The Karlsruhe Tritium Neutrino (KATRIN) experiment is targeted to measure the electron antineutrino mass $m_{\bar{\nu}_e}$ with an unprecedented sensitivity of $0.2 \text{ eV}/c^2$ (90% C.L.). It is located at the Campus North of Karlsruhe Institute of Technology (KIT) in Eggenstein-Leopoldshafen. Relevant details of the measurement principle and the experimental setup will be explained in this chapter, based on the design report [KAT05] and more recent publications on the first operation of the global setup [ABB⁺18a] and the methodology for fitting the endpoint region of the beta-decay spectrum of tritium [KBD⁺19].

At first, the basic measurement principle will be explained in section 2.1. Based on this approach, in section 2.2 the anticipated sensitivity on the neutrino mass is stated. Finally, it is illustrated how the measurement principle is realized by giving technical and operational details of each hard- and software component in sections 2.3 and 2.4, respectively.

2.1 Measurement principle

The beta-decay of molecular tritium, T_2 , is given by



The electron energy is continuously distributed between 0 keV and the β -endpoint $E_0 = Q - E_{\text{rec}} = 18.574 \text{ keV}$ where the molecular recoil energy reaches a maximum value $E_{\text{rec}} = 1.7 \text{ eV}$ [KBD⁺19]. Only at the endpoint the spectral shape is significantly influenced by $m_{\bar{\nu}_e}$. The imprint of the neutrino mass on the energy spectrum can be seen from Eq. 1.48 and in Fig. 1.7b.

KATRIN is an apparatus designed for high-precision studies of the β -electron spectral shape close to E_0 . Only a tiny fraction on the order of 10^{-13} of all β -decays take place within the last 1 eV below E_0 . In order to measure significant spectral modifications both a low background and a high-activity source are required. Furthermore, the electron antineutrino mass $m_{\bar{\nu}_e} < 1.1 \text{ eV}/c^2$ [AAA⁺19c] is small compared to E_0 , so a high energy resolution is essential. This is achieved with the method described in the next section.

2.1.1 Energy analysis via adiabatic collimation and electrostatic filtering

The energy analysis of the β -electrons is done using a MAC-E filter (magnetic adiabatic collimation with electrostatic filter) [BPT80, LS85, PBB⁺92] type spectrometer. In Fig. 2.1 the measurement principle is illustrated. The main concepts are described in the following.

Beta-electron transport along magnetic field lines

Superconducting magnets provide magnetic field lines for guiding β -electrons created in the tritium source. An electron performs a circular motion around a specific field line due to the Lorentz force [Jac06]. This is superimposed with a linear motion in the direction they were emitted in β -decay. Combining both movements results in a helix-like cyclotron motion around magnetic field lines as shown in Fig. 2.2a. Changes in the absolute magnetic field during one cyclotron cycle are small leading

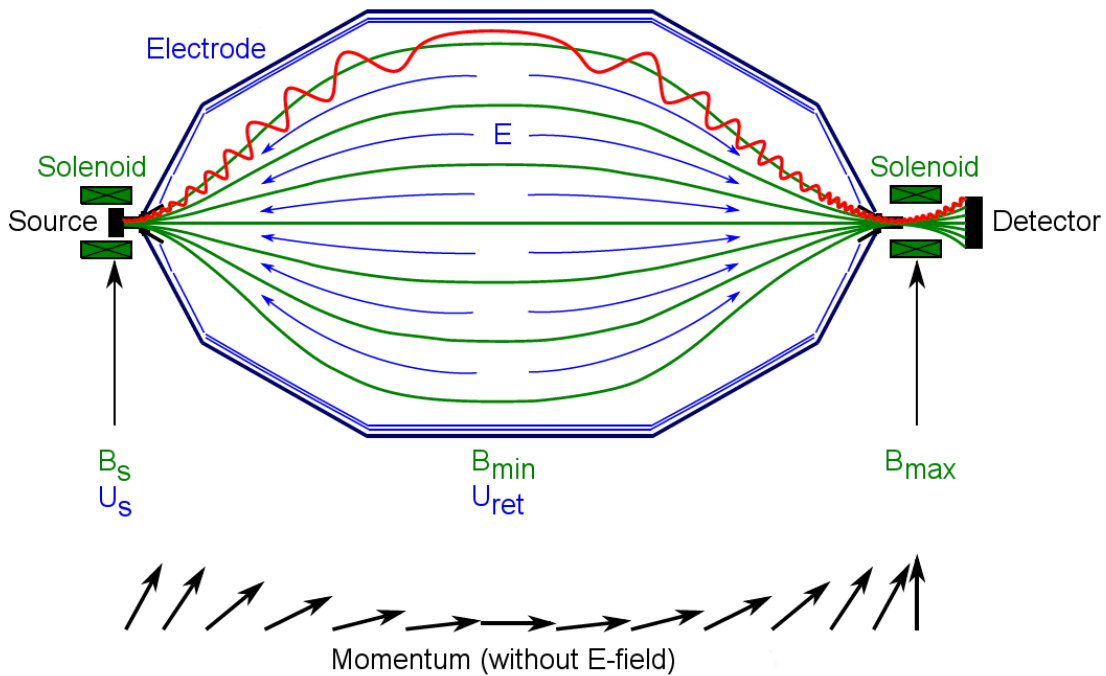


Figure 2.1: Illustration of the KATRIN measurement principle. Inside the tritium source β -electrons are emitted isotropically and guided along the magnetic field lines which are displayed in green. Two solenoid magnets provide the source magnetic field B_s and the maximum magnetic field in the setup B_{\max} . Towards the central analyzing plane the magnetic field strength diminishes to a minimum value B_{\min} . A negative retarding potential U_{ret} is put on the MAC-E filter vessel acting as an electrostatic barrier for the electrons starting inside the source potential U_s . The electric field lines are indicated in blue. The red colored track represents the movement of a negatively charged particle with sufficient longitudinal energy to overcome the potential and reach the detector. Below the MAC-E filter sketch the row of momentum vectors illustrates the translation of transversal into longitudinal momentum (= adiabatic collimation) and vice versa without including the retardation effect by the electric potential. The figure is taken from [Gro15] with minor adjustments.

to an adiabatic motion [Jac06]. In this context, adiabatic means that the electrons do not suffer from energy losses due to field inhomogeneities. For an adiabatic motion, the magnetic flux ϕ is conserved [Jac06]

$$\phi = \oint \vec{B} d\vec{A} = \text{const.} \quad (2.2)$$

Thus, regions with a higher magnetic field B come along with a smaller cross-section area A .

Integral measurement via electrostatic filtering

The β -electron movement is constrained by a negative retarding potential U_{ret} applied to the MAC-E filter vessel. It serves as an electrostatic barrier which can only be overcome by electrons with sufficient kinetic energy. Those with too low energies are reflected back into the tritium source while those with high enough energies are transmitted towards the detector where they are counted. As the electric potential is mirror symmetric to the central analyzing plane, after passing it, the electrons get longitudinally re-accelerated before their final detection. By consecutively applying several distinct retarding potentials and thereby recording the corresponding detector count rate, the integral β -spectrum is obtained. Since β -electrons are emitted isotropically in the tritium source, it is necessary to align their momentum vectors in longitudinal direction for maximizing the available energy for passing the filter potential. This process is called adiabatic collimation.

Adiabatic collimation

When traveling along a magnetic field line the electron momentum \vec{p} can be expressed as the sum of a parallel and a perpendicular part $\vec{p} = \vec{p}_{\parallel} + \vec{p}_{\perp}$. The angle in between is defined as the pitch angle θ which is illustrated in Fig. 2.2b. For an adiabatic motion, the ratio of the squared perpendicular momentum p_{\perp}^2 and magnetic field strength B is conserved [Jac06]:

$$\frac{p_{\perp}^2}{B} = \text{const.} \quad (2.3)$$

As electrons enter the MAC-E filter volume, the magnetic field strength decreases by several orders of magnitude to reach a minimum in the central analyzing plane. Consequently, p_{\perp}^2 is decreasing simultaneously along the way. The total momentum

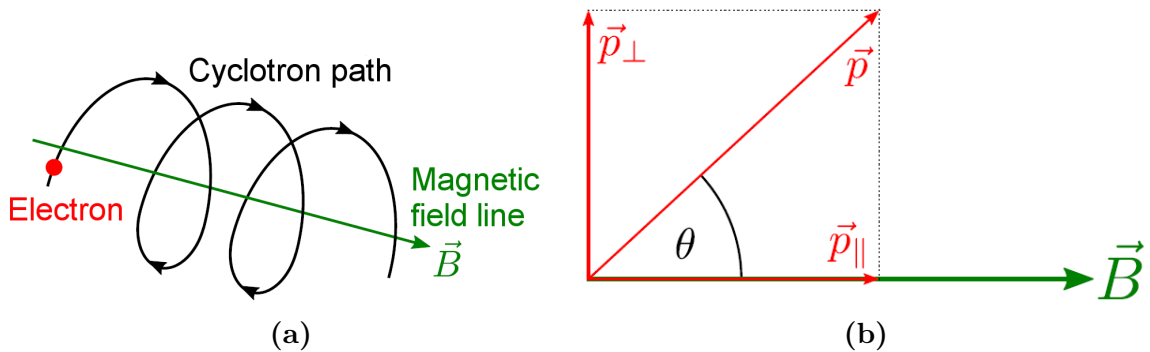


Figure 2.2: Electron movement along magnetic field lines (a) and the definition of the pitch angle θ (b). Both figures are taken from [Gro15].

p stays constant so that p_{\parallel} increases until it reaches its maximum value in the analyzing plane. The negative retarding potential U_{ret} is applied to the inner electrodes of the spectrometer vessel in such a way, that the most negative value of the electric potential coincides with the minimum value of the B-field strength in the analyzing plane, where the electrons are maximally collimated.

Transmission function

In reality, the transformation of p_{\perp} into p_{\parallel} can not be done with 100% efficiency because the analyzing plane magnetic field can not be infinitely small. The residual transversal energy ΔE , which can not be accounted for in the energy analysis is given by [KBD⁺19]

$$\Delta E = E \frac{B_A}{B_{\text{max}}} \frac{\gamma + 1}{2} \quad (2.4)$$

with the analyzing plane magnetic field B_A , the maximum magnetic field B_{max} along the considered field line, the total kinetic electron energy E and the relativistic γ factor $\gamma = E/m_e c^2 + 1$. This parameter ΔE is also referred to as the filter width. It is characteristic for each MAC-E filter and should be sufficiently small in order to enable the targeted measurement sensitivity.

The transmission properties of a MAC-E filter can be expressed analytically in the so-called transmission function [KBD⁺19]

$$T(E, U_{\text{ret}}) = \begin{cases} 0 & E - qU_{\text{ret}} < 0 \\ 1 - \sqrt{1 - \frac{E - qU_{\text{ret}}}{E} \frac{B_s}{B_A} \frac{2}{\gamma + 1}} & 0 \leq E - qU_{\text{ret}} \leq \Delta E. \\ 1 - \sqrt{1 - \frac{B_s}{B_{\text{max}}}} & E - qU_{\text{ret}} > \Delta E \end{cases} \quad (2.5)$$

Here, E is the electron kinetic energy, U_{ret} is the electrostatic retarding potential, $E - qU_{\text{ret}}$ is the electron surplus energy, ΔE is the filter width given in Eq. 2.4, B_s , B_A and B_{max} are the magnetic fields of the source, the analyzing plane and the maximum magnetic field along the respective field line. As can be seen, the electron surplus energy has to exceed the filter width ΔE for a maximum transmission probability. This maximum probability is not equal to one because of the magnetic mirror effect.

Magnetic mirror effect

In case of an electron moving from a lower into a higher magnetic field region, p_{\perp}^2 and thereby the pitch angle θ increase along with B , as described by Eq. 2.3. At some point the magnetic field is high enough that $\theta = 90^\circ$, so that the electron is reflected. This magnetic mirror effect leads to a maximum starting pitch angle inside the tritium source [KBD⁺19]:

$$\theta_{\text{max}} = \arcsin \left(\sqrt{\frac{B_s}{B_{\text{max}}}} \right) \quad (2.6)$$

which depends on the source magnetic field B_s and the maximum magnetic field realized in one position of the respective field line B_{max} . Electrons with higher starting angles are reflected at some high field region in the experiment and are not counted by the detector.

2.1.2 Tritium source

The source is a stable column of molecular tritium gas. It provides both a reference β -activity and a reference energy scale for KATRIN. In order to reduce systematic uncertainties of the reference activity, the density and temperature are stabilized and monitored on the per mill level. The reference energy scale is determined by the boundary surfaces and the formation of a plasma due to a variety of ionization processes creating tritium ions and secondary electrons. The electric potential of this plasma acts as a reference potential U_s for the experiment.

Beta-electrons can leave the gas column towards both ends. A strong magnetic field B_s is guiding the β -electrons outside of the source for energy analysis. Both B_s and the maximum magnetic field realized along a specific field line B_{\max} define the maximum pitch angle (cf. Eq. 2.6). Only β -electrons with $\theta \leq \theta_{\max}$ are transmitted all the way to the detector. Electrons with higher θ move on longer paths through the source gas resulting in higher probabilities for losing kinetic energy e.g. due to scattering with gas molecules. This systematic effect is limited by choosing θ_{\max} to be about 50° , which still gives good counting statistics. Analytically, the interactions between β -electrons and the gas column, as well as other energy loss mechanisms like e.g. cyclotron radiation, are described by the so-called response function.

2.1.3 Response function

The transmission function given in Eq. 2.5 results from an integral over all pitch angles between $\theta = 0$ and $\theta = \theta_{\max}$. The corresponding θ -dependent version can be extended by considering energy loss processes of β -electrons, which are mainly given by inelastic scatterings off gas molecules in the tritium source. It can be combined with the probability of n -fold scattering $P_n(\theta)$ and the energy loss function $f_n(\epsilon)$ giving the probability for an energy loss of ϵ during n scattering processes. For the narrow energy window analyzed in KATRIN, both can be considered as being independent of the electron energy E . Combining all three probability functions yields the response function [KBD⁺19]

$$R(E, U_{\text{ret}}) = \int_{\epsilon=0}^{E-qU_{\text{ret}}} \int_{\theta=0}^{\theta=\theta_{\max}} T(E - \epsilon, \theta, U_{\text{ret}}) \cdot \sin(\theta) \cdot \sum_j P_j(\theta) f_j(\epsilon) d\theta d\epsilon. \quad (2.7)$$

If $j = 0$, the electron leaves the source without scattering and the energy loss function is equal to the δ -distribution $f_0(\epsilon) = \delta(\epsilon)$. For s -fold scattering, $f_s(\epsilon)$ is the s -fold convolution of $f(\epsilon)$ with itself. The response function is illustrated in Fig. 2.3.

2.1.4 Fitting model for the beta-spectrum endpoint region

Ultimately, all β -electrons with sufficient starting energies and low enough pitch angles are transmitted through the MAC-E filter and are counted as individual events at the detector. Various processes taking place at the detector facing side of the MAC-E filter can lead to the generation of background electrons, which are counted at the detector in the same way as β -electrons. This background spectrum is added to the signal β -decay spectrum and potentially distorts the measurement. Therefore, it is of top priority to minimize this background contribution although it

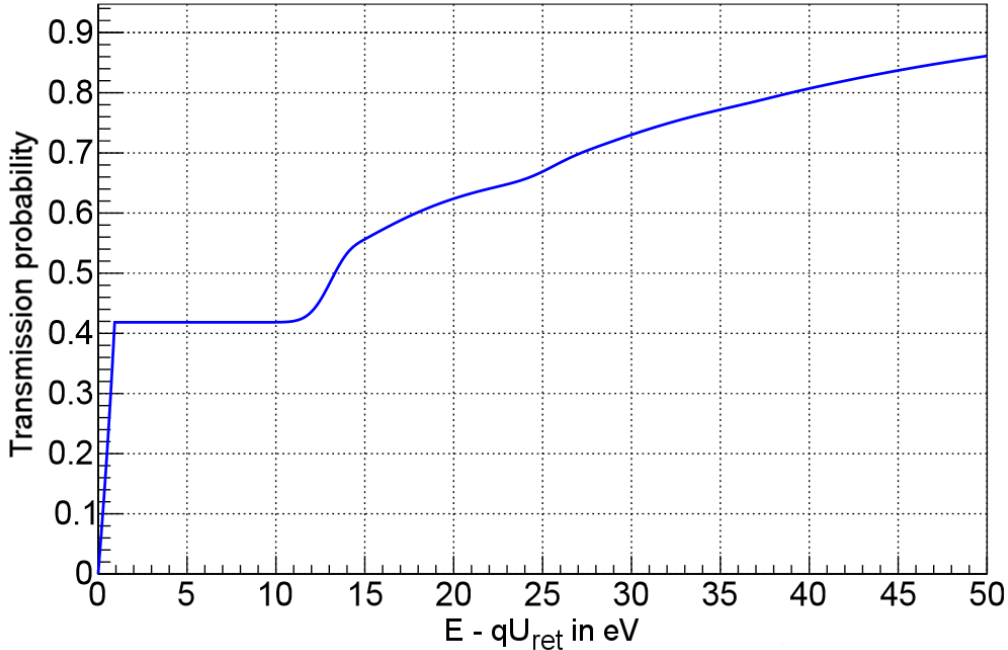


Figure 2.3: Illustration of the KATRIN response function. Shown is the response function $R(E, U_{\text{ret}})$ for a retarding potential $U_{\text{ret}} = 18.55$ kV and a maximum pitch angle $\theta_{\text{max}} = 50.8^\circ$ versus the surplus energy $E - qU_{\text{ret}}$. In this illustrative plot only about 42% of the β -electrons can leave the tritium source without losing energy due to inelastic scattering with gas molecules. The energy loss experienced in a single scattering amounts to roughly 10 eV. This corresponds to the additional surplus energy above the first transmission edge, where a second rise of the response function is evolving. The figure and its description are taken from [Gro15] with minor adjustments.

is not possible to fully eliminate it. The total rate measured by the detector is given by [KBD⁺19]

$$\frac{dN}{dt}(U_{\text{ret}}) = \frac{1}{2} \epsilon_{\text{det}} \cdot N_{\text{T}} \int_{qU_{\text{ret}}}^{E_0} \frac{d^2 N_{\beta}}{dt dE}(m_{\bar{\nu}_e}^2, E_0) \cdot R(E, U_{\text{ret}}) dE + \frac{dN_B}{dt} \quad (2.8)$$

with the theoretical decay rate of β -decay $d^2 N_{\beta}/dt dE$ from Eq. 1.48, the detection efficiency ϵ_{det} , the background rate dN_B/dt and N_{T} tritium atoms in the source. The response function $R(E, U_{\text{ret}})$ can be determined in dedicated measurements using an electron gun producing electrons with well-defined pitch angle and energy.

The measured spectrum is fitted with the model given in Eq. 2.8 containing four free parameters: the signal amplitude $A_{\text{sig}} \propto \epsilon_{\text{det}} \cdot N_{\text{T}}$, the endpoint E_0 , the background rate $A_{\text{bg}} = dN_B/dt$ and the squared neutrino mass $m_{\bar{\nu}_e}^2$. Because the imprint of $m_{\bar{\nu}_e}^2$ is strongest close to E_0 , the measurement range is restricted to ≤ 90 eV below the endpoint. The expected outcome of a KATRIN measurement in case of $m_{\bar{\nu}_e} = 0.350$ eV/ c^2 is illustrated in Fig. 2.4 for an energy interval up to 30 eV below the endpoint. In the top plot the influence of the four fit parameters on the integral β -spectrum is indicated. Below, the impact of $m_{\bar{\nu}_e}$ and A_{bg} on the deviation from the theoretical model expectation is shown. The maximum rate deficit due to the parameter $m_{\bar{\nu}_e}$ is observed only a few eV below the endpoint. A higher background rate is decreasing the magnitude of this deficit and shifts the peak towards lower energies. A significant amount of the measurement time should be devoted to this

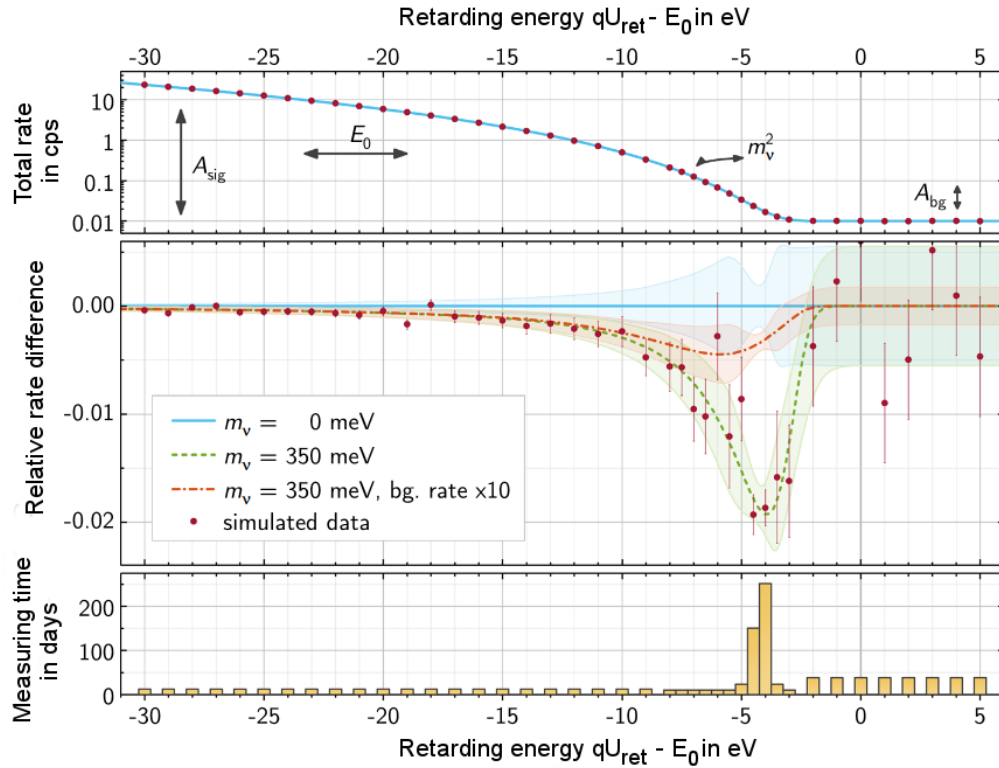


Figure 2.4: Simulation of the integral β -spectrum close to the endpoint for a neutrino mass of $0.350 \text{ eV}/c^2$ and comparison with the theoretical model expectations. The red data points are toy data compared to the theoretical model expectations for $m_{\bar{\nu}_e} = 0 \text{ eV}/c^2$ (blue solid line), $m_{\bar{\nu}_e} = 0.350 \text{ eV}/c^2$ (green dashed line), both with $A_{\text{bg}} = 10 \text{ mcps}$, and $m_{\bar{\nu}_e} = 0.350 \text{ eV}/c^2$ with $A_{\text{bg}} = 100 \text{ mcps}$ (orange dash-dotted line). On the top the integral β -spectrum is shown in a plot of the total detector count rate $dN/dt(U_{\text{ret}})$ versus the retarding energy qU_{ret} minus the endpoint E_0 . In the middle the relative rate difference between toy data and theoretical model expectation is plotted. The error bars of the toy data are purely statistical as well as the uncertainties of the model expectation which are indicated by the shaded bands. It can be seen that the background rate has a significant influence on the position and magnitude of the maximum rate deficit. On the bottom the distribution of the measuring time at each retarding potential $t(U_{\text{ret}})$ is illustrated. The error bars of the simulated toy data scale according to $\sigma(dN/dt) \propto 1/\sqrt{t}$. It should be noted that this specific measuring time distribution is similar but not exactly identical to the one actually applied in KATRIN neutrino mass measurements to date. The figure and its description are taken from [KBD⁺19] with minor adjustments.

region of maximum distortion as is depicted in the bottom plot.

Especially relevant for this thesis is the E_0 parameter. It is important to emphasize that there is a difference between the physical parameter $E_{0,\text{phys}}$ going into the theoretical decay rate defined in Eq. 1.48, and the fit parameter $E_{0,\text{fit}}$. The former is defined as the maximum energy of the β -spectrum for a neutrino mass of zero and no molecular excitation or other secondary effects. Thus, $E_{0,\text{phys}}$ is an intrinsic

property of β -decay and for T_2 there is only one true value¹. The fit parameter $E_{0,\text{fit}}$, however, is the best approximation of $E_{0,\text{phys}}$. Both parameters only converge if all relevant systematic effects are included in the fitting model. One of the main topics of this thesis are plasma effects (see sections 3.1.5 and 6) which are not yet implemented. Thus, as of now, the fit parameter $E_{0,\text{fit}}$ can be seen as an effective endpoint, possibly shifted to some extent by plasma or other as yet not considered effects. Whenever E_0 is mentioned hereinafter, it refers to the KATRIN-specific fit parameter $E_{0,\text{fit}}$.

2.2 Anticipated neutrino mass sensitivity

It is anticipated that the KATRIN experiment will be operated for five calendar years [KAT05]. This period includes maintenance breaks and dedicated measurements of systematic effects resulting in three net years of β -spectrum scanning [KAT05] over consecutive measurement runs. This long time is necessary to accumulate enough detector counts per retarding potential $N(qU_{\text{ret}})$ since those spread randomly according to a Poisson distribution with variance $\sigma^2 = \mu(qU_{\text{ret}})$, where $\mu(qU_{\text{ret}})$ is the arithmetic mean of the number of counts. The run-wise spectrum counts for each retarding potential are combined (e.g. by stacking) and fitted with the model in Eq. 2.8. The best-fit is found by minimizing the negative log-likelihood function for the parameter set $\theta = (m_{\bar{\nu}_e}^2, E_0, A_{\text{sig}}, A_{\text{bg}})$ [KBD⁺19].

Due to the random nature of the measured detector counts there is a statistical uncertainty σ_{stat} for each of the four best-fit results for the θ parameter set. With more measurement time t more counts N are measured and the statistical uncertainty on $m_{\bar{\nu}_e}^2$ decreases with $1/\sqrt{N}$ or $1/\sqrt{t}$, respectively [KBD⁺19].

On the other hand, the parameter $m_{\bar{\nu}_e}^2$ also has a systematic uncertainty σ_{sys} which is not decreasing with time. Any systematic uncertainty is arising from an imperfect understanding of the KATRIN apparatus and physics effects which are basically summarized in the response function $R(E, U_{\text{ret}})$ of Eq. 2.8. A thorough description of all systematic effects is given in [SM19]. Prominent examples are the energy loss of β -electrons leaving the tritium source, excitation of the molecular final states or - especially relevant for this thesis - spatial and temporal variations in the energy scale of the experiment. In the KATRIN design report a conservative estimate for the systematic uncertainty on $m_{\bar{\nu}_e}^2$ is given. Based on this value a net measurement time of three years was chosen, assuming an analyzed energy interval of $[E_0 - 30 \text{ eV}, E_0 + 5 \text{ eV}]$. After this time it is anticipated that the statistical and systematic uncertainty meet at a value of [KAT05]:

$$\sigma_{\text{stat}}(m_{\bar{\nu}_e}^2) \approx \sigma_{\text{sys}}(m_{\bar{\nu}_e}^2) \approx 0.017 \frac{\text{eV}^2}{c^4}. \quad (2.9)$$

The total uncertainty on $m_{\bar{\nu}_e}^2$ and the 90% C.L. sensitivity on an upper limit on $m_{\bar{\nu}_e}$ are then calculated via [KAT05, KBD⁺19]

$$\begin{aligned} \sigma_{\text{tot}}(m_{\bar{\nu}_e}^2) &= \sqrt{\sigma_{\text{stat}}^2(m_{\bar{\nu}_e}^2) + \sigma_{\text{sys}}^2(m_{\bar{\nu}_e}^2)} = 0.025 \frac{\text{eV}^2}{c^4}, \\ S(m_{\bar{\nu}_e}, 90\% \text{ C.L.}) &= \sqrt{1.64 \cdot \sigma_{\text{tot}}(m_{\bar{\nu}_e}^2)} = 0.2 \frac{\text{eV}}{c^2}. \end{aligned} \quad (2.10)$$

¹The β -spectra of other molecules or ions like T, T⁻, T₂⁺ etc. have different physical endpoints than T₂.

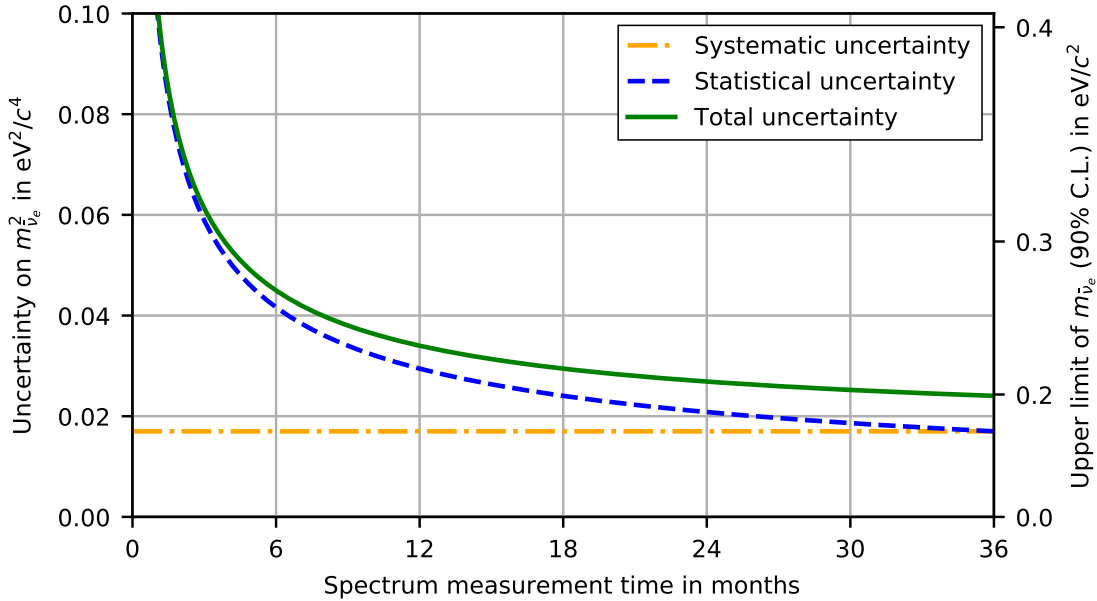


Figure 2.5: Anticipated uncertainties and sensitivity over time for a 36 months long measurement of the β -spectrum endpoint region. The 1σ uncertainties are given for the $m_{\nu_e}^2$ parameter and the 90% C.L. sensitivity for the upper limit of m_{ν_e} . The figure is inspired by [KBD⁺19].

The time-dependent evolution of all uncertainties and the 90% C.L. sensitivity can be seen in Fig. 2.5.

2.3 Overview of hardware components

The above explained principle is realized in a 70 m long apparatus. An engineering drawing can be found in Fig. 2.6. The setup consists of several components which are combined to an uniform beam line. Tritium gas is injected in the center of the windowless, gaseous tritium source (WGTS). At one end the rear section (RS) is connected to the source containing various calibration and monitoring devices. At the other end the WGTS is followed by two consecutive tritium pumping sections: the differential pumping section (DPS) and the cryogenic pumping section (CPS). Two MAC-E filter type spectrometers serve as energy filters for the β -electrons. The pre-spectrometer (PS) is a smaller version of the main spectrometer (MS) and acts as pre-filter. The actual energy analysis is done with the MS and afterwards the electrons are counted by the focal plane detector (FPD). For monitoring of the MS high voltage (HV) the monitor spectrometer (MoS), which is not part of the actual beam line, is attached to the MS. RS, WGTS, DPS and CPS are summarized in the source and transport section (STS) operated inside Tritium Laboratory Karlsruhe (TLK), whereas PS, MS and FPD constitute the spectrometer and detector section (SDS). All these components will be explained in detail in the following subsections. For orientation a right-handed coordinate system is used. The vertical y -axis is pointing upwards and the horizontal x -axis in west direction (from the MoS towards the MS). The z -axis is axial to the beam line. Positive z -direction is referred to as front (lower left to upper right in Fig. 2.6) and negative z -direction as rear (upper right to lower left in Fig. 2.6). Further, the direction of the tritium gas flow from

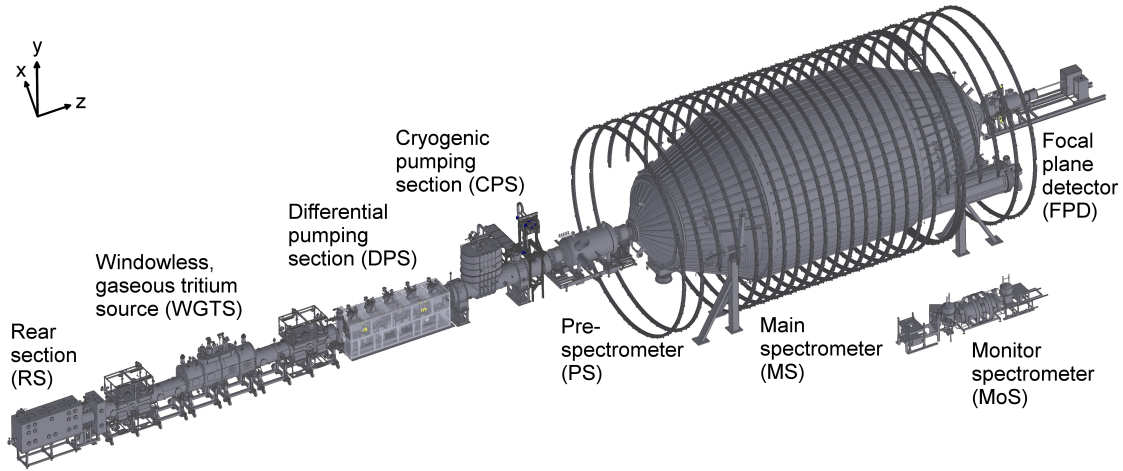


Figure 2.6: Engineering drawing of the global KATRIN setup. The individual hardware components as well as the right-handed coordinate system are explained in the text.

the center of the WGTS towards both ends defines the downstream (away from the center) and upstream (towards the center) direction.

2.3.1 Windowless, gaseous tritium source

The WGTS consists of a 10 m long cylindrical beam tube with a diameter of 90 mm in a homogenous magnetic field $B = 0.7 \times B_{\text{design}} = 2.52 \text{ T}$ with the design value $B_{\text{design}} = 3.6 \text{ T}$ provided by three superconducting solenoid magnets [BBB⁺12, ABB⁺18c]. From here, β -decay electrons start their journey towards the detector inside of a well-defined magnetic flux tube

$$\phi = 0.7 \times \phi_{\text{design}} = 134 \text{ T cm}^2. \quad (2.11)$$

with the design value $\phi_{\text{design}} = 191 \text{ T cm}^2$ [KAT05]. The source magnetic field and the maximum magnetic field at the KATRIN setup $B_{\text{max}} = 0.7 \times 6.0 \text{ T} = 4.2 \text{ T}$ (see section 2.3.6) define the maximum pitch angle according to Eq. 2.6:

$$\theta_{\text{max}} = 50.8^\circ. \quad (2.12)$$

It is a tradeoff between higher values for which the path through the WGTS gas column and thereby the probability of scattering is increased and lower values for which the number of β -electrons transmitted to the detector is decreased.

In the WGTS center tritium gas is injected with a nominal inlet flow rate of $1.8 \text{ mbar } \ell \text{ s}^{-1}$ corresponding to 40 g d^{-1} [PSB15] diffusing to both ends. At these ends the gas is pumped differentially by turbomolecular pumps (TMPs) in two pump ports each. Including these two differential sections, the overall length of the WGTS cryostat is 16 m. In the range of 8 m around the central gas inlet the pressure and gas flow according to simulations are reduced by factors of nearly 2000 and 400, respectively [KHD⁺18]. In total seven superconducting magnets are manufactured around the beam tube in a 27 t cryostat [HSM17], which can be seen in Fig. 2.7. They are cooled by a liquid helium vessel to a temperature of 4.5 K and provide magnetic fields of $B = 0.7 \times B_{\text{design}} = 3.92 \text{ T}$ with the design value $B_{\text{design}} = 5.6 \text{ T}$ in the front pumping section and $B = 0.7 \times B_{\text{design}} = 2.52 \text{ T}$ with the design value

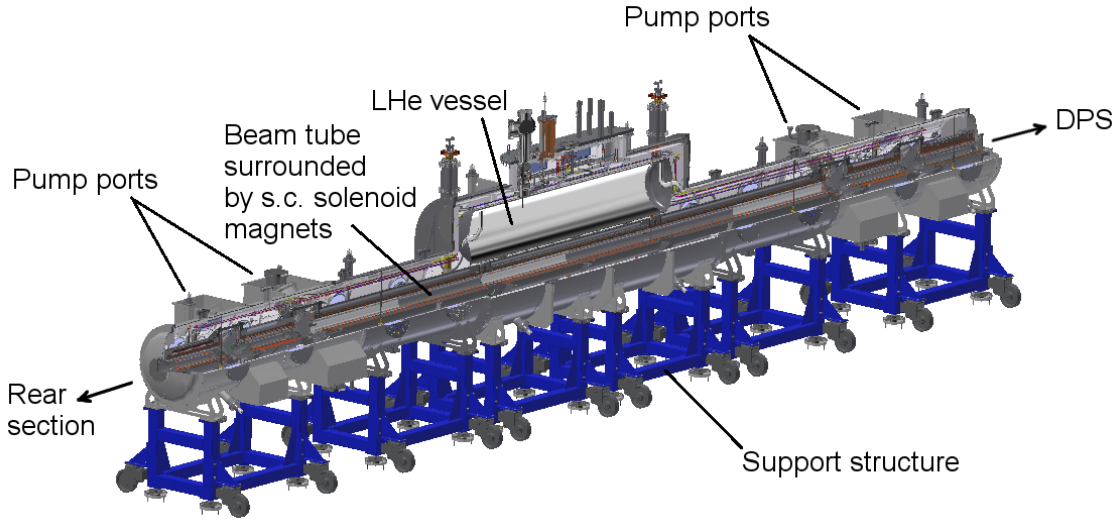


Figure 2.7: Engineering drawing of the 16 m WGTS cryostat in a three quarter section view.

$B_{\text{design}} = 3.6 \text{ T}$ in the center and at the rear end [ABB⁺18c].

In total the WGTS is expected to deliver a nominal activity of $1.7 \times 10^{11} \text{ Bq}$ at a tritium purity $\epsilon_{\text{T}} = 95\%$ per design [KAT05]. The corresponding column density of the tritium gas inside the beam tube is defined as [BBB⁺12]:

$$\mathcal{N}(p_{\text{in}}, p_{\text{out}}, T_{\text{BT}}) = \int_{-5\text{m}}^{+5\text{m}} n(\vec{r}, p_{\text{in}}, p_{\text{out}}, T_{\text{BT}}) dz \quad (2.13)$$

with the inlet and outlet pressure p_{in} and p_{out} , the molecular number density n , the position vector \vec{r} and the beam tube temperature T_{BT} . The design value is $\mathcal{N} = 5 \times 10^{17} \text{ molecules/cm}^2$ with a required precision and stability of $\Delta\mathcal{N}/\mathcal{N} = 0.1\%$ [BBB⁺12]. In order to meet this strict criterion, the inlet pressure, the outlet pressure and the temperature each have to be stabilized on a level of 0.1%.

In case of the nominal 30 K beam tube temperature this is done with a two-phase neon cooling system [GJBG⁺08, GBSS11, GBH⁺13] as it is schematically shown in Fig. 2.8. Two 16 mm evaporator tubes are brazed to the outside of the beam tube over the entire length. Inside, they are partly filled with liquid neon operated at its boiling point at 30 K. A heat load on this system does not induce a change in temperature but acts as latent heat for evaporation. The generated neon vapor flows through a condenser where it is liquefied again by cooling it down with $\sim 25 \text{ K}$ cold gaseous helium. In a closed loop the neon is fed back to the evaporator tubes. The WGTS beam tube can alternatively be operated at $T \approx 80 \text{ K}$ or $T \approx 100 \text{ K}$ by, instead of neon, using nitrogen or argon as cooling fluids, respectively.

The nominal absolute source temperature of 30 K is a tradeoff. At lower temperatures condensation and cluster formation of tritium isotopologues would initiate. At too high temperatures the Doppler broadening of the β -electron energy would be too high and, even more importantly, the tritium throughput necessary to reach the design column density value would be much higher.

The inlet pressure is stabilized by operating a loop system for gas circulation [PSB15].

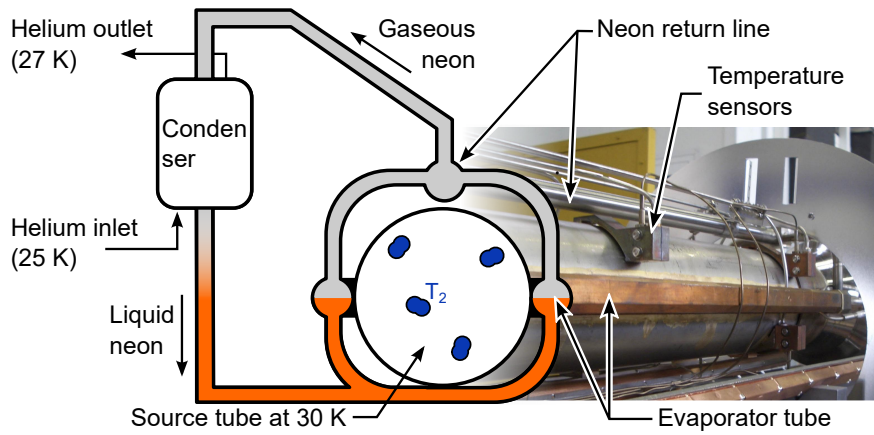


Figure 2.8: Schematic drawing of the WGTS two-phase neon cooling system. An explanation of the working principle is given in the text. The figure is taken from [BBB⁺12] with minor adjustments.

A simplified scheme can be found in Fig. 2.9. High-purity tritium gas provided by the TLK infrastructure [WSH⁺20] is fed into the WGTS center from a pressure and temperature controlled buffer vessel via an inlet capillary with constant conductance. In order to maintain the high and extremely stable β -activity inside the source, not only the pressure but also the tritium purity ϵ_T has to be precisely known and stabilized. Therefore, after the gas has been pumped by the TMPs it is re-circulated through a Pd/Ag permeator. All non-hydrogen molecules are removed there before the gas is re-injected into the pressure controlled buffer vessel. A small amount of tritium is thereby filtered out of the gas stream and is reprocessed by the TLK infrastructure. The purified gas is fed back into the loop system in order to

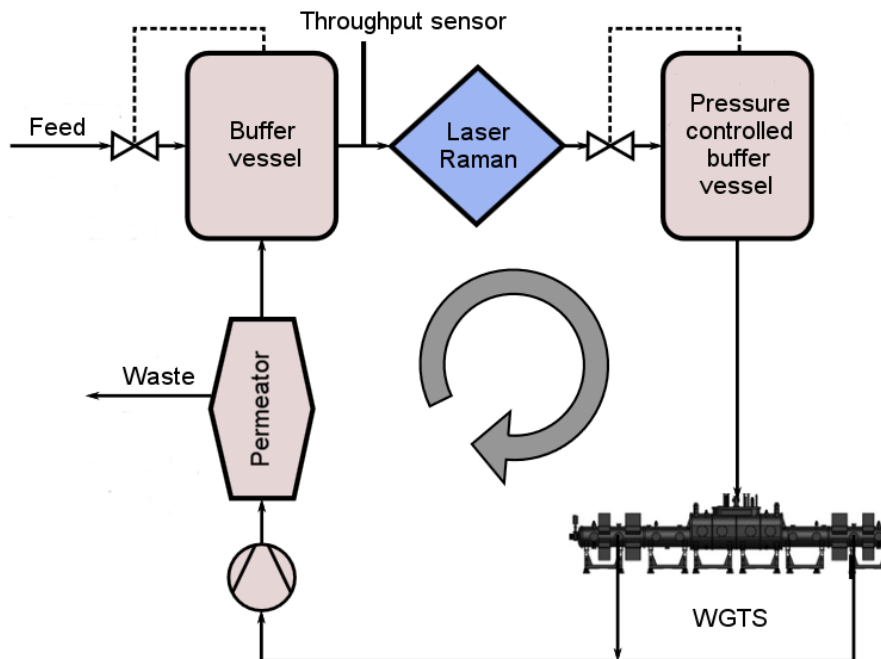


Figure 2.9: Simplified schematic drawing of the WGTS loop system. An explanation of the working principle is given in the text. The figure is taken from [BBB⁺12] with minor adjustments.

compensate the loss at the permeator. Before the pressure controlled buffer vessel a laser Raman (LARA) cell [Sch13, Fis14] is installed. Using Raman spectroscopy the isotopic composition of the tritium gas can be monitored in real-time providing the required design precision of 0.1%.

The WGTS column density is linearly dependent on the gas flow through the loop system, which is measured by a throughput sensor installed right before the LARA cell. This sensor is read out continuously and, after calibration, provides in-situ information about the column density during a measurement.

Due to the large number of β -decays and their subsequent ionization processes more than 1×10^{12} ions s^{-1} and an equal rate of secondary electrons are produced [KAT05] forming a cold, magnetized plasma. The systematic effects induced by this plasma and its charge carriers need to be understood for the neutrino mass measurements. These effects are the main topic of this thesis and are described in great detail in section 3.1 and the main chapters following it.

In order to characterize the WGTS plasma, a krypton operation mode at a temperature of $T \approx 80$ K or $T \approx 100$ K is possible. Gaseous ^{83m}Kr providing nearly mono-energetic conversion electrons is injected into the source tube without carrier gas or in combination with gaseous tritium [VSD⁺18]. The statistical analysis of the line shape of the discrete energy spectrum can be used to deduce important plasma parameters. The first ever WGTS operation in this mode was done in the krypton campaign in July 2017 [ABB⁺18a], for which simulation results of the gas density distribution along the beam line will be presented in chapter 4.

2.3.2 Rear section

The RS is terminating the KATRIN beam line at its rear end and is equipped with various calibration and monitoring devices. As shown in Fig. 2.10, it consists of two major components: the rear chamber and the electron gun (egun). In between both parts the RS magnet is providing a magnetic field $B = 0.857 \times B_{\text{design}} = 4.03$ T with the design value $B_{\text{design}} = 4.7$ T [ABB⁺18c].

The rear chamber is a vacuum vessel containing the rear wall (RW), a gold-coated, stainless steel disk with an outer diameter of 145 mm (see Fig. 2.11). In the center it has a 5 mm diameter hole where the egun beam can pass. It is mounted in a way that the 134 T cm^2 flux tube is mapped onto it. Thus, it serves as a boundary surface for electrons and ions. The magnetic field lines impinging on the RW surface are traversing the whole length of the WGTS beam line leading to a high longitudinal conductance for charged particles. Consequently, the WGTS plasma is kind of "short-circuited" to the electric potential of the RW [KAT05]. Its surface potential is therefore per design expected to be a major boundary condition for the starting potential of the β -electrons. The surface potential can be tuned by a bias voltage of up to ± 500 V applied to the RW and the current from electrons and ions collected onto it can be measured by a picoammeter. Also, it can be heated up to a temperature of 120 °C for bake-out. Detailed investigations about the RW influence on the WGTS plasma effects can be found in chapter 6. In order to be able to supply the source plasma with additional negative charge carriers, an UV light illumination of the RW can be used to produce electrons via the photoelectric effect. For this purpose a Cermax[®] xenon UV lamp [Ful20] is installed. An optical setup focuses

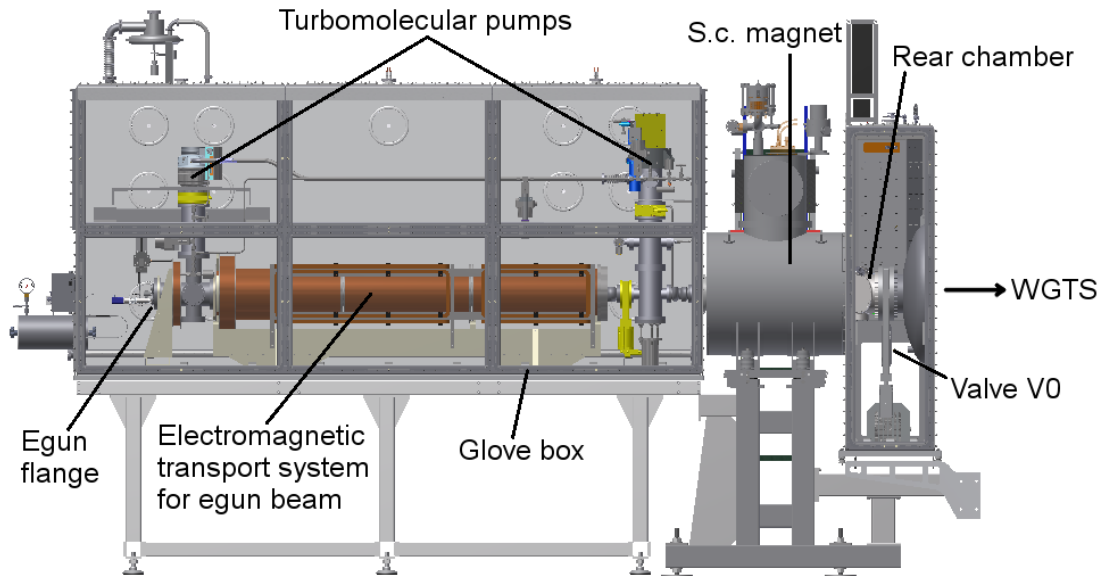


Figure 2.10: Engineering drawing of the rear section. The egun setup on the left is separated from the rear chamber on the right by a beam tube connecting part surrounded by the RS superconducting magnet. To the right the rear chamber is connected to the WGTS beam tube via the valve V0. The setup is contained in an underpressure glove box to prevent tritium contamination of the atmosphere.

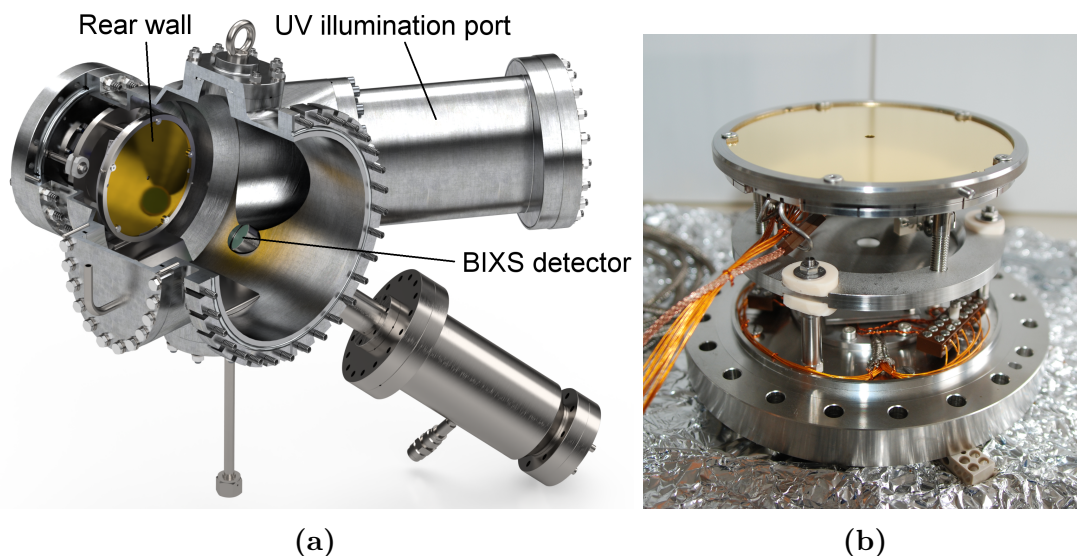


Figure 2.11: Engineering drawing of the rear chamber with a view inside (a) and photograph of the isolated rear wall mount (b). The figures are printed with permission from Y. Steinhauser (MPIK Heidelberg) and A. Jansen (KIT).

the light cone on the RW producing a large photo current on the order of $1 \mu\text{A}$ with a spatial homogeneity of $\pm 10\%$ over the whole surface.

In the rear chamber two silicon drift detectors are installed for in-situ WGTS activity monitoring via beta induced X-ray spectrometry (BIXS) [Röl15]. Beta-electrons continuously impinging on the RW generate X-ray bremsstrahlung with an intensity

$I \propto Z^2$ making gold ($Z = 79$) a suitable material. The BIXS detectors provide a statistical uncertainty of 0.1% on the WGTS tritium activity within a few tens of seconds.

In the egun setup photoelectrons are produced via the photoelectric effect by a point-like UV illumination of a gold-plated cathode. Currently, these electrons are accelerated by electric fields to kinetic energies of up to 20 keV² with an intrinsic energy spread of about 0.1 eV [Sac20]. An upgrade to reach kinetic energies of 35 keV is foreseen. The angular distribution can be adjusted by rotating electrode plates and is required to cover the full range of accepted pitch angles in KATRIN with a spread below 4°. Normal conducting magnets in the electromagnetic transport system provide the guiding field for the electrons towards the rear chamber, where they enter through the central RW hole and continue their way through the complete KATRIN beam line. To shift the beam in x - y -direction both electric and magnetic dipole fields in the electromagnetic transport system as well as magnetic dipole coils in the rear part of the WGTS can be used. With this narrow beam of nearly monoenergetic electrons various systematic effects can be measured. Most important are the measurements of the WGTS column density, the energy loss function and the main spectrometer transmission function which are indispensable for the calculation of the response function going into the final fit model in Eq. 2.8. [Bab14]

2.3.3 Differential pumping section

The 7.3 m long [FRS⁺19] DPS beam line is connected to the downstream end of the WGTS beam line via pump port 0 and to the upstream entrance of the CPS via pump port 5. An engineering drawing of the apparatus can be seen in Fig. 2.12. Overall, the DPS unit has three main purposes.

First, it is designed to reduce the gas flow of neutral tritium by at least five orders of magnitude. For this purpose, six TMPs are operated at five pump ports which connect five individual beam line elements. Each beam line part is tilted by 20° with respect to its neighbors to prevent tritium beaming in a direct line of sight. Since the gas flow entering the DPS has already been reduced by at least two orders of magnitude by the differential pumping at the WGTS front end, the gas flow out of the DPS is 10⁻⁷ or less relative to the WGTS center.

Second, the adiabatic transport of β -electrons has to be assured using five superconducting magnets which provide a magnetic field $B = 0.8 \times B_{\text{design}} = 4.0$ T with the design value $B_{\text{design}} = 5.0$ T [ABB⁺18c].

The third task is one of the central topics of this thesis. As already indicated in section 2.3.1, not only neutral tritium but also positive and negative charged tritium ions originate from the WGTS. Like β -electrons, ions propagate along the magnetic field lines eventually all the way to the spectrometer and detector section. To prevent this, two ring electrodes are mounted in the last beam line element 5 and in pump port 5, respectively. A positive electrostatic potential of several Volt is reflecting positive ions back in upstream direction. In order to remove them, three dipole electrodes are installed in the beam line sections 1 to 3, drifting out ions in a negative dipole field via $E \times B$ drift. Furthermore, negatively charged ions are blocked by the negative dipole electrode field. Initially, a fourth dipole element located in beam line section 4 was also foreseen to remove ions. However, since the

²Personal correspondence with R. Sack, 2020

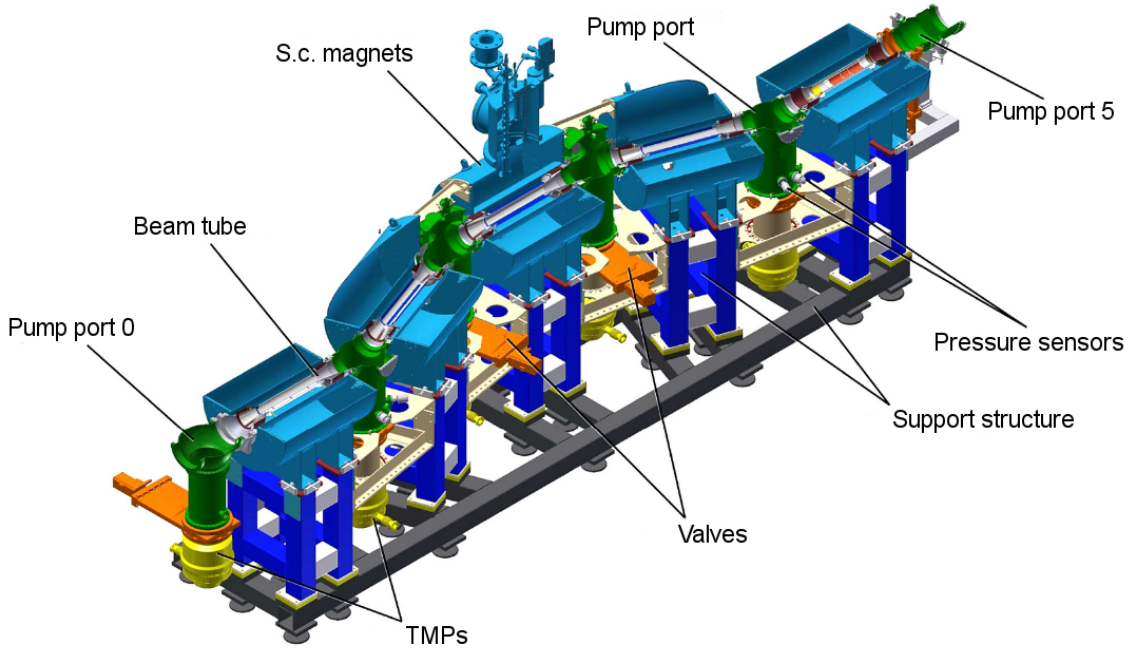


Figure 2.12: Engineering drawing of the DPS in a half to three-quarter section view. The single beam tube parts (gray) are connected to each other via vertical pump ports (green) where valves (orange) and TMPs (yellow) are attached to. Each beam tube element is surrounded by a superconducting solenoid magnet (blue). Pump port 0 and pump port 5 are the connecting parts to the WGTS and the CPS, respectively. Not explicitly shown is the beam line instrumentation for blocking and removing tritium ions. Due to the major importance for this thesis a dedicated illustration is given in chapter 5 in Fig. 5.1. The figure and its description are taken from [FRS⁺19] with minor adjustments.

first KATRIN neutrino mass measurement campaign in spring 2019 [AAA⁺19c], it is instead operated at a positive dipole field in order to block positive ions and remove secondary electrons potentially stored between DPS and PS. A more in-depth description and extensive studies of the DPS ion instrumentation performance during three KATRIN measurement campaigns are presented in chapter 5. Downstream of the first ring electrode in beam tube 5 an FT-ICR (fourier-transform ion cyclotron resonance) unit [UDRL⁺09] is mounted for measuring the abundancies of different ion species according to their charge-to-mass ratios. However, it is not operational due to technical issues. [Kle19]

2.3.4 Cryogenic pumping section

The CPS (see Fig. 2.13) is situated as next element in the beam line after the DPS. It has to provide a reduction of the gas flow by at least another seven orders of magnitude. A total of seven superconducting solenoid magnets provides a magnetic field of $B = 0.7 \times B_{\text{design}} = 3.92 \text{ T}$ with the design value $B_{\text{design}} = 5.6 \text{ T}$ [ABB⁺18c]. The pumping principle of the CPS is quite different to the DPS. It consists of seven beam tube parts with two additional pump ports resulting in a total length of 6.5 m in z -direction [Röt19]. The parts 2-5 are cooled down to a temperature between 3-4 K and tilted by 15° with respect to each other. On their gold-plated surfaces an argon

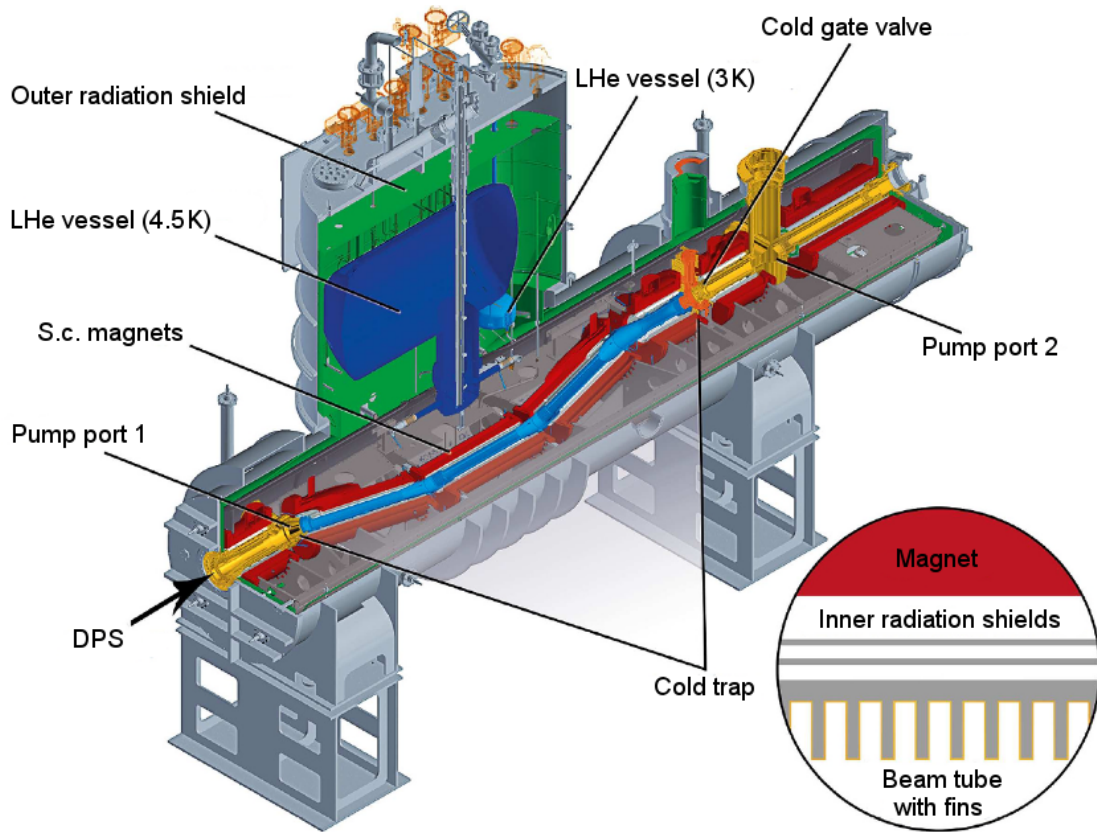


Figure 2.13: Engineering drawing of the CPS in a three-quarter section view.

In the center a gold-plated beam tube is located which is surrounded by seven superconducting solenoid magnets (red). Both are thermally decoupled by a radiation shield (gray) between them. Additionally, the 12 t cryostat is housing two liquid helium vessels (blue) to cool the magnets and beam tube as well as a radiation shield towards room temperature (green). The central cold trap section (light blue) is illustrated by the bottom right close-up view where the finned structure of the inner beam tube surface is indicated. The figure and its description are taken from [FRS⁺19] with minor adjustments.

frost layer is prepared on which tritium molecules are adsorbed via cryosorption [Röt19]. For increasing the effective pumping area the inner beam tube surface is equipped with circular fins [FRS⁺19]. After a duty cycle of 60 d the argon frost layer has to be removed by purging with helium gas with a closed cold gate valve (cf. Fig. 2.13) and a new clean layer is deposited [Röt19]. Combining the pumping power of WGTS differential pumping, DPS and CPS an overall reduction of the tritium gas flow by at least 14 orders of magnitude is required by design. Dedicated simulations [KHD⁺18, FRS⁺19] and measurements [Röt19, MBB⁺20] revealed that this requirement is actually exceeded by several orders of magnitude. An exact number can not be stated since for the CPS only a lower limit of the reduction $R_{\text{CPS}} \gg 10^{10}$ [Röt19] was measured with deuterium gas. For the combined differential pumping at the WGTS end and at the DPS a value $R_{\text{diff}} = (9.6 \pm 1.0) \times 10^7$ [MBB⁺20] was measured. Overall, this yields $R = R_{\text{diff}} \cdot R_{\text{CPS}} \gtrsim 10^{18}$.

Inside pump port 2 the forward beam monitor (FBM) is installed for monitoring the

WGTS β -activity with a precision of 0.1% in less than 100 s [Ell19]. Beta-electrons are measured by a seven-pixel silicon drift detector^{3,4} mounted on a detector board, which can be moved in x - y -direction to any position in the CPS beam line. During neutrino mass measurements the FBM is continuously taking data at the monitoring position located at the outer rim of the magnetic flux tube.

In pump port 2 also a condensed $^{83\text{m}}\text{Kr}$ source (CKrS) [Ful20] can be inserted vertically into the beam line. It provides nearly mono-energetic electrons for calibration purposes of the spectrometer section.

2.3.5 Pre-spectrometer

The PS is the first component located outside of the TLK as part of the SDS which is shown in Fig. 2.14. It is an ultra-high vacuum (UHV) stainless steel vessel with a length of 3.4 m, a diameter of 1.7 m and a total volume of $V = 8.5 \text{ m}^3$ [FBD⁺11]. It is a small version of the MS based on the MAC-E filter principle described in section 2.1.1 with a rather large filter width of $\Delta E = 70 \text{ eV}$ [ABB⁺16]. It was designed as a pre-filter for β -electrons at a retarding potential of -18.3 kV blocking the majority of electrons from reaching the MS where they might ionize residual gas and increase the background rate. Two superconducting solenoid magnets are operated at the vessel entrance and exit, respectively, both at a magnetic field $B = 0.7 \times B_{\text{design}} = 3.15 \text{ T}$ with the design value $B_{\text{design}} = 4.5 \text{ T}$ [ABB⁺18c]. At these positions also two ring electrodes are installed which block positive tritium ions [Kle19]. These units complement the ion blocking devices in the DPS described in 2.3.3. In order to reach ultra-low pressures on the order of 10^{-11} mbar , the vacuum tank is bakeable to a temperature of up to $350 \text{ }^\circ\text{C}$ and two pump ports are equipped with TMPs and a non-evaporable getter pump [GBB⁺18]. High voltage is applied to the vessel and to an inner electrode system. At one of these electrodes a current measurement is assembled for monitoring a possible tritium ion flux into the PS [Kle19]. If a

³K. Urban, Application of a TRISTAN Silicon Drift Detector as Forward Beam Monitor in KATRIN, master's thesis, Technical University of Munich (TUM), 2019.

⁴Before July 2019 two silicon p-i-n diodes were installed instead of the silicon drift detector.

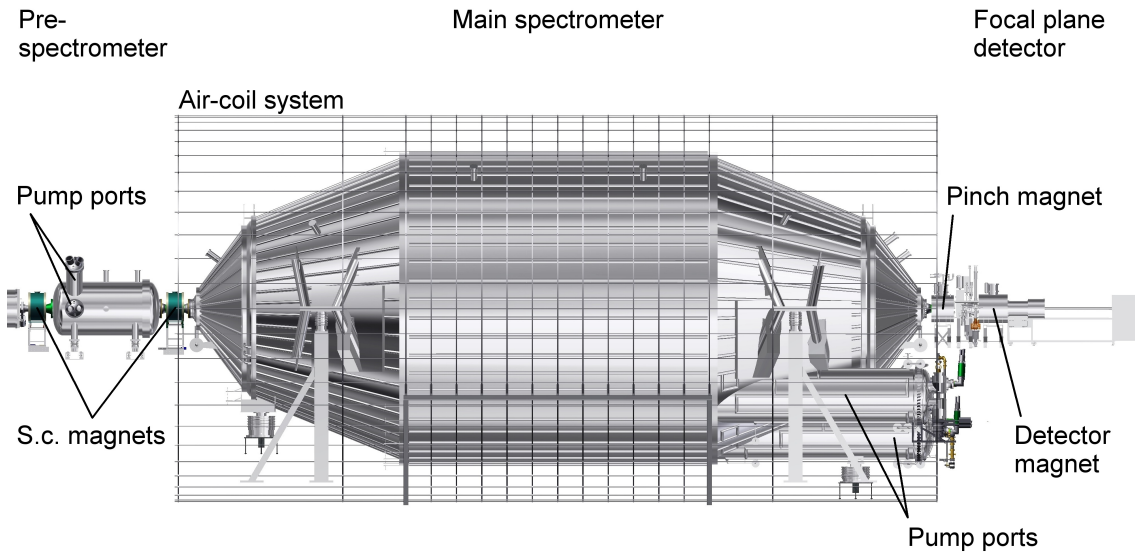


Figure 2.14: Engineering drawing of the spectrometer and detector section.

certain current threshold is exceeded, the valve between CPS and PS is closed. In section 5.1.2 a more elaborate description of the inner electrode system and the ion instrumentation will be given.

2.3.6 Main spectrometer

The MS (cf. Fig. 2.14) is a 1240 m³ stainless steel UHV vessel with a weight of 200 t, a diameter of 9.8 m and a length of 23.2 m [ABB⁺16]. There are two superconducting solenoid magnets located at its entrance and exit, respectively [ABB⁺18c]. The one at the entrance side is identical with the downstream PS magnet operated at $B = 3.15$ T. At the exit, the maximum field strength of the whole KATRIN setup $B_{\max} = 0.7 \times B_{\text{design}} = 4.2$ T with the design value $B_{\text{design}} = 6.0$ T [ABB⁺18c] is provided by the pinch magnet. Due to its large dimensions and strong magnets the MS is a high-resolution MAC-E filter. At a configuration with a minimum magnetic field $B_{\min} = 0.63$ mT in the central analyzing plane and $B_{\max} = 4.2$ T, it exhibits a filter width of $\Delta E = 2.8$ eV at the endpoint E_0 (cf. Eq. 2.4) [AAA⁺19c]⁵.

At the position of the pinch magnet the fifth and last ring electrode of the KATRIN beam line is mounted. Three horizontal pump ports are equipped with TMPs and getter pumps generating an ultimate vacuum pressure on the order of 10^{-11} mbar after a bake-out at temperatures⁶ of up to 350 °C [ABB⁺16]. The stainless steel vessel can be put to high voltage up to $U = -35$ kV [ABB⁺18c] and the retarding potential inside the volume is fine-tuned by an inner wire electrode system [Val11]. The wire electrode is set on a slightly more negative potential than the vessel, so that the UHV volume is shielded against secondary electron emission from the vessel surface. This emission is resulting from natural radioactivity or from cosmic ray interactions. A retarding potential stability on the ppm level is absolutely essential and monitoring at a precision level of 3 ppm at $U = -18.6$ kV is required for minimizing systematic effects on the neutrino mass fit result [ABB⁺18b]. This monitoring is realized in two redundant ways. First, the high voltage is scaled down to a voltage as low as 10 V with a high-precision voltage divider, which then can be measured with a commercially available digital multimeter [TMW09]. Secondly, it is done with the monitor spectrometer described in section 2.3.8.

Around the MS a normal-conducting air-coil system [EBB⁺18] is installed which allows fine-tuning of the magnetic field in the analyzing plane and also compensates the Earth's magnetic field. By operating the air-coils the minimum magnetic field in the analyzing plane can be varied over a range of about 0.1 mT to 1.1 mT⁷. The respective setting determines the boundary conditions for the β -electron transport through the vessel, e.g. the value of the MS energy resolution ΔE .

2.3.7 Focal plane detector

The last beam line component is the FPD, where the β -electrons are detected. It is located inside the detector magnet with a magnetic field of up to $B = 0.7 \times B_{\text{design}} = 2.52$ T with the design value $B_{\text{design}} = 3.6$ T [ABB⁺18c]. Accordingly, the

⁵The design configuration is $B_{\min} = 0.3$ mT and $B_{\max} = 6.0$ T, which results in $\Delta E = 0.93$ eV at the endpoint E_0 .

⁶Due to technical issues the actually applied bake-out temperature is 200 °C, rather than 350 °C.

⁷Up to the first KATRIN neutrino mass measurement in spring 2019 the highest applicable field was 1.45 mT. Due to technical reasons this number had to be reduced to 1.1 mT afterwards.

134T cm^2 flux tube is mapped onto the FPD sensitive area, which has a diameter of 90 mm [ABB⁺15]. Together with the MS exit pinch magnet the setup is shown in Fig. 2.15. Before reaching the FPD a post-acceleration electrode increases the longitudinal electron energy by 10 keV. This has the purpose to shift the electron energy in a region with low background originating from radioactivity in the nearby detector environment. The detector itself is a single silicon wafer with a 148 pixel p-i-n diode array [ABB⁺15]. All pixels have equal areas and are arranged in twelve rings with twelve pixels each and a central bull's-eye consisting of four pixels. This segmentation allows the study of radial and azimuthal effects. The energy resolution for each pixel is on the level of 2 keV and the combined detection efficiency is $\epsilon_{\text{det}} = 95\% \pm 1.8\%_{\text{stat.}} \pm 2.2\%_{\text{syst.}}$ ⁸ [ABB⁺15]. The detector housing beam tube part is protected against various background sources by a lead shield, a copper shield and a muon veto system [ABB⁺15]. For calibration purposes a ^{241}Am γ and a photoelectron source can be inserted into the beam line in front of the FPD. The electrons are produced via UV illumination of a Ti-disk, which can also be used as a Faraday cup measuring particle currents. The current meter used for this is referred to as PULCINELLA (precision ultra-low current integrating normalization electrometer for low-level analysis) [Mar17].

⁸This specific result for the detection efficiency was measured throughout the first SDS commissioning campaign. Since then the FPD wafer was swapped several times. Nevertheless, all of the installed wafers exhibit similar characteristics, so they should have comparable detection efficiencies.

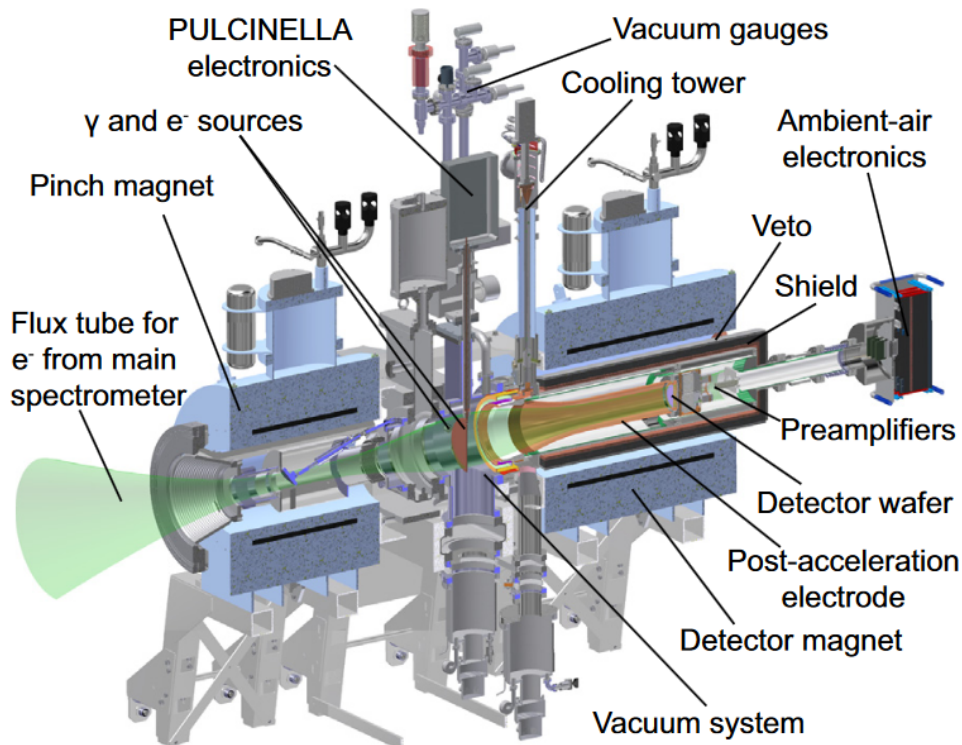


Figure 2.15: Engineering drawing of the focal plane detector system. The figure is taken from [ABB⁺15] with minor adjustments.

2.3.8 Monitor spectrometer

A ppm-precise monitoring of the MS high voltage fluctuations is achieved with the MoS using $^{83\text{m}}\text{Kr}$ as a nuclear standard. It is a third MAC-E filter type spectrometer, formerly used in the Mainz neutrino mass experiment with a length of 4 m and a diameter of 1 m [EBB⁺14]. The MoS is galvanically connected to the MS [EBB⁺14], so both are operated simultaneously at the same retarding potential. An implanted $^{83\text{m}}\text{Kr}$ source is emitting nearly mono-energetic electrons to the MoS detector. The ones originating from the K shell of the krypton atom have a sharp energy of 17.8 keV, which is not too far from the tritium endpoint energy of 18.6 keV. The MoS source can be set on a potential shifting the electron energy right to the current value of the MS retarding potential. At this position, small voltage deviations lead to a significant variation of the measured detector rate. With this principle the MS high voltage of -18.6 kV can be monitored with a precision below 60 meV (3 ppm) [EBB⁺14].

2.4 Overview of software components

There are different software components for hardware control, data acquisition, analysis and simulation.

Hardware control and data acquisition

There are two data types generated by the KATRIN apparatus, namely slow control and run-based data [Kle14]. Slow control refers to time series data continuously measured with a certain time interval of typically $\Delta t = 1$ s between two consecutive values. These could be values for temperature, pressure, electric current, voltage, magnetic field, and so on. In this way, the experiment's status is recorded nonstop also in between measurement runs, which plays a major role for safety and maintenance work. The slow control system can be both read out and controlled automatically. Mainly, this is done by the two software systems Siemens SIMATIC Process Control System 7 (PCS7) and Zentrale Datenerfassung und Steuerung (ZEUS) [LK05, ABB⁺15]. The data is stored in various local databases and collected by ADEI (Advanced Data Extraction Infrastructure) [CBKV10], a near real-time web interface [Kle14]. On the one hand, ADEI provides data visualization, some low-level analysis features and data output in various formats for further analysis. On the other hand, ADEI handles the storage of all data into a common MySQL database to which the KATRIN analysis infrastructure has access [Kle14].

The second data type is called run- or event-based data. It is produced whenever a measurement run is performed by the various detectors in KATRIN (FPD, muon veto, FBM, MoS detector). These runs are limited in time in contrast to slow-control data measured in a nonstop fashion. As for the FPD, the data can be collected either in histogram or in energy mode [ABB⁺15]. The latter is the standard mode for KATRIN measurements in which the individual energy and time information for each event is stored. For very high rates on the order of kilo- to mega-counts per second (cps) this would generate too large files. In this case one can switch to histogram mode where the events are not recorded individually but collected in an energy histogram. In histogram mode the rate data is stored in 1 s bins so information within shorter time scales is lost. This rather special mode was used for most of the high rate measurements described in section 6.3. The run-based software data

acquisition is done by ORCA (Object-oriented Real-time Control and Acquisition) [HCH⁺04] developed for operation on Mac OS. It is written in Objective-C and can be controlled via a drag and drop graphical user interface (GUI) or by self-written code scripts. Besides data acquisition ORCA provides run and hardware control.

Data analysis

The software framework KASPER is based on C++ and contains most of the analysis and simulation modules [Gro15]. Regarding data analysis especially the following two modules are relevant for this thesis.

- **KaLi** [Kle14]: This is a data library providing access to the KATRIN database. It can be operated via a web interface or by code scripts executed on KASPER.
- **BEANS** [Was14]: The Building Analysis Sequence (BEANS) primarily serves for analyzing FPD run data, but it can be used to access and analyze basically any data stored on the database. The analysis is done with a code based on individual one-line analysis elements. Each element represents one common procedure specified by configuration parameters. For example the element *KDEnergyEventReadout()* reads out run data collected in energy mode and *KDEnergyHistogram()* creates an energy histogram. BEANS output can be stored in graphic files or in ROOT [BR97] files for further processing. Most of the plots shown in chapters 5 and 6 are based on BEANS analysis in the first place.

Simulation

Within the simulation modules in KASPER the KATRIN hardware geometry and physical properties are implemented. For this thesis the simulation of electromagnetic fields as described in sections 4.4, 5.2.4 and 5.3.4 is of primary importance. Therefore, the relevant modules are described here, based on [Gro15].

- **KGeoBag**: This is the geometry module comprising geometrical shapes like cylinders, cubes and cones but also user-defined arbitrary shapes. Also, linear algebra methods e.g. for rotation are available. All hardware components described in section 2.3 are implemented in KGeoBag and combined to a global geometry.
- **KEMField**: The geometry files based on KGeoBag can be put into KEMField for calculation of electric and magnetic fields. The magnetic fields are computed in most cases using the zonal harmonic expansion method [Glü11]. This is a fast and accurate algorithm for axially symmetric fields. In this method an arbitrary point - called source point - located on the symmetry axis is chosen. The space around the source point is subdivided in three spherical regions. The innermost is called central region with a radial coordinate $0 < r < r_{\text{cen}}$. Then, a region with $r_{\text{cen}} \leq r \leq r_{\text{rem}}$ contains the magnet currents and magnetization. The last part is called remote region with $r > r_{\text{rem}}$. Based on the source point the axial and radial field at any point in the central and remote region can be calculated by expansion in Legendre polynomials and their derivatives. This method is applicable for all points within the KATRIN beam tube which covers most application cases. The required input parameter is the coil current of the solenoid magnets. Electric fields and potentials are calculated with the boundary element method requiring electric charge density distributions as input, which are generated considering the geometries and

voltages involved.

- **KASSIOPEIA** [FGT⁺17]: Both KGeoBag and KEMField are implemented in the particle tracking software package KASSIOPEIA. It calculates the trajectories of charged particles inside the KATRIN beam line by solving differential equations of motion. For a simulation run all input parameters can be defined in XML configuration files. Here the geometry, test particle properties, starting distributions, considered physical processes, tracking precision, termination conditions and the type of output can be specified. In the simulation both particle generation and tracking is done consecutively in a loop. A particle track consists of a certain number of steps. The distance between two consecutive steps can be defined by the user according to the required precision. A particle is generated and the single steps of the track are calculated until one of the termination conditions is fulfilled. Then the next loop iteration starts. After the last iteration has finished a ROOT output file is generated containing the results.

3. Framework of this thesis

The work described in this thesis was a central element of the recent measurement campaigns of the KATRIN experiment. It is about the investigation of effects induced by charged particles, i.e. ions and electrons, created inside the WGTS (and very few inside the DPS). In section 3.1 it will be presented what this means in detail by describing the entirety of possible systematic effects on the neutrino mass measurement. Afterwards, section 3.2 gives an overview of the KATRIN measurement campaigns from 2017 to 2019 in which all the measurements presented in this work have been performed. Finally, the specific challenges and objectives tackled in this thesis are listed in section 3.3.

3.1 Ion- and plasma-related systematic effects on the KATRIN neutrino mass measurement

The WGTS can be viewed as an ion factory. At the design β -activity of 10^{11} Bq more than 10^{12} tritium ions and an equal number of secondary electrons are created each second [Kle19]. This large number of charge carriers forms a cold, magnetized plasma inside the WGTS. Several contributions to the KATRIN design systematic uncertainty budget of $\sigma_{\text{sys}}(m_{\nu_e}^2) \leq 0.017 \text{ eV}^2/c^4$ [KAT05] arise. Some of these contributions can be minimized by dedicated countermeasures so that they can be neglected. The others have to be characterized in such detail that they can be taken into account in the neutrino mass analysis.

This section first describes how ions and secondary electrons are created and distributed inside the WGTS (sections 3.1.1 and 3.1.2). Afterwards, a detailed introduction into relevant systematic effects related to tritium ions and plasma phenomena is given (sections 3.1.3 to 3.1.5). As those effects are the central topic of this thesis a short overview list is given in Tab. 3.1.

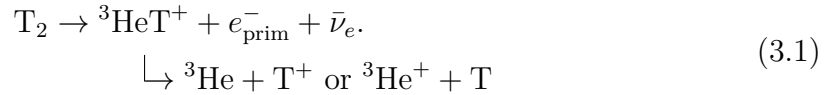
3.1.1 Tritium ion and secondary electron creation

Inside the WGTS tritium gas each T_2 β -decay will create a positively charged ${}^3\text{HeT}^+$ ion. With a probability of $(49.7 \pm 1.5)\%$ [Lin19], measured in the Tritium Recoil-Ion

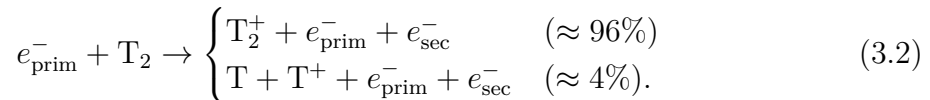
Table 3.1: Overview of the systematic effects on the neutrino mass determination induced by tritium ions and plasma effects. A detailed description of each effect is given in the sections 3.1.3 to 3.1.5.

Category	Systematic effect
Background	<ul style="list-style-type: none"> • MS background induced by tritium ions • β-decay of T^- • β-decay from the RW • β-decay from inside the DPS dipole electrodes
Influence of beam line instrumentation	<ul style="list-style-type: none"> • $E \times B$ drift of β-electrons in DPS dipole electrodes • High-frequency voltage noise at ring and dipole beam line electrodes
WGTS plasma effects	<ul style="list-style-type: none"> • Spatial plasma potential inhomogeneity • Time-dependent absolute plasma potential • Time-dependent spatial plasma potential inhomogeneity • Change of β-electron energy by high-frequency plasma instabilities

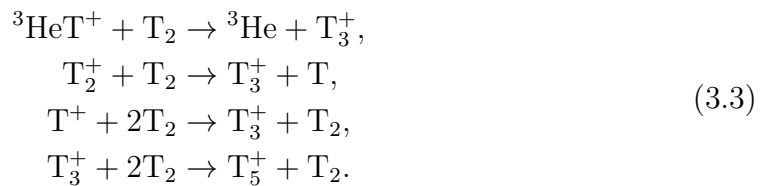
Mass Spectrometer (TRIMS) experiment, the daughter ion will dissociate according to [KAT05]:



The primary β -electron e_{prim}^- travels along the magnetic field lines through the gas column further ionizing molecules and thereby producing secondary electrons e_{sec}^- via impact ionization [KAT05]



At the design column density $\mathcal{N} = 5 \times 10^{17}$ molecules/cm², simulations by F. Glück indicate that each β -electron undergoes a total of 36 inelastic scattering processes on average¹. Subsequent collisions of ions with gas molecules lead to the creation of T_3^+ and positive ion clusters with higher masses. Some representative processes are [KAT05, Kle19]:



¹F. Glück, Longitudinal plasma simulations, talk at internal meeting, 2020.

Two T_2 molecules are required in the latter two interactions because of conservation of momentum and energy. Higher masses like T_7^+ , T_9^+ , T_{11}^+ and so on are also possible. Even atomic number cluster ions as well as T_2^+ react rather fast with neutral tritium molecules. Thus, the odd atomic number ions dominate inside the WGTS. Negative tritium ions are created via dissociative attachment [KAT05]:



with a rather small rate below 1% compared to positive ones.

All kinds of tritium ion species initially have energies in the range between meV and 10 eV. Due to multiple scattering processes with the 30 K cold gas they thermalize, which means that their energy distribution converges towards a Maxwell-Boltzmann distribution around the mean kinetic energy of $3/2k_B T = 3.9$ meV. However, in the KATRIN "first tritium" campaign [AAA⁺20] energies of up to 15 eV were measured for ions reaching the PS, when the ring electrode blocking potentials were intentionally lowered to a few volt [Kle19].

This observation can be explained by two considerations.

- In addition to the above described processes, there is a further ion creation mechanism associated to molecular dissociation [Kle19]. In the course of a β -decay (cf. Eq. 3.1) or an impact ionization (cf. Eq. 3.2), the ionized final state molecule can be excited to an anti-bonding electronic state. These states are repulsive leading to a weakening of the molecular bond and ultimately to a dissociation of the molecule. After dissociation the final state ion can have a comparably high energy of several tens of eV [Kle19]. Only a minor fraction of a few percent of all ions are created via molecular dissociation at impact ionization [SRL⁺96].
- Because of the differential pumping at both ends of the WGTS the neutral gas pressure decreases by several orders of magnitude over the length of 8 m towards the DPS. Simulation results [KHD⁺18] for the longitudinal density distribution can be seen in Fig. 3.1. Consequently, the fast thermalization via multiple scattering is most efficient in the central WGTS part. Charged molecules created further downstream in a lower pressure and collision-free region escape the gas column without losing significant amounts of their eV energies.

Thus, a small fraction of ions created via molecular dissociation exist and might leave the WGTS with eV or even 10 eV energies. However, those are suppressed by several orders of magnitude compared to the thermalized ions with meV energies.

Secondary electrons created in the reaction described in Eq. 3.2 also thermalize. Positive ions can recombine with these thermal electrons via [Kle19]



under emission of a photon γ or via dissociative recombination like [Kle19]



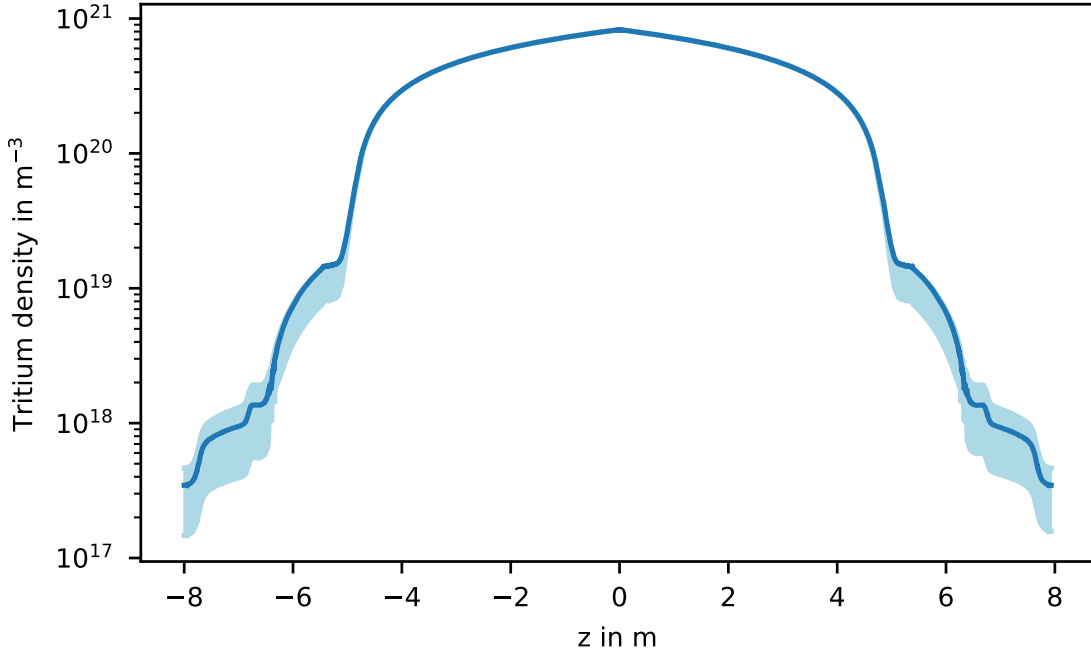
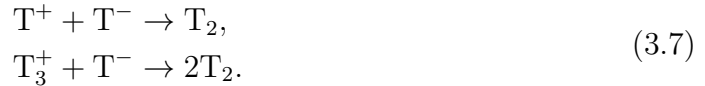


Figure 3.1: Simulated neutral gas density distribution along the WGTS z-axis. The simulation was done for the design column density $\mathcal{N} = 5 \times 10^{17} \text{ cm}^{-2}$. At the center ($z = 0 \text{ m}$) the gas is let in. The figure is based on simulation results from [KHD⁺18].

Furthermore, a recombination of positive and negative ions is possible e.g. via [Kle19]:



3.1.2 Ion distribution inside the WGTS

The longitudinal gas profile (cf. Fig. 3.1) is symmetric to the central gas inlet with an effective flow direction from the center towards the rear and front end, respectively. As for charged tritium molecules, this has an important implication. Once created, charged molecules and atoms move effectively with the gas flow. If they move in opposite direction, they are reflected back by multiple scatterings. Shortly after the start of tritium injection a steady state of ion creation and flow is maintained. This steady distribution has been simulated by F. Glück for the central 10 m of the WGTS which can be seen in Fig. 3.2 for the front part. While the gas flow distributes the ions quite homogeneously in the inner four meters, the densities then start to diminish significantly because of the dropping pressure. Due to the effective movement of ions with the gas flow away from the center at $z = 0$, the ion density is strongly reduced there. The most abundant species are T_3^+ and T_5^+ .

3.1.3 Background contributions by tritium ions

Both positive and negative tritium ion species can cause significant contributions to the background rate dN_B/dt (cf. Eq. 2.8). Higher background levels directly

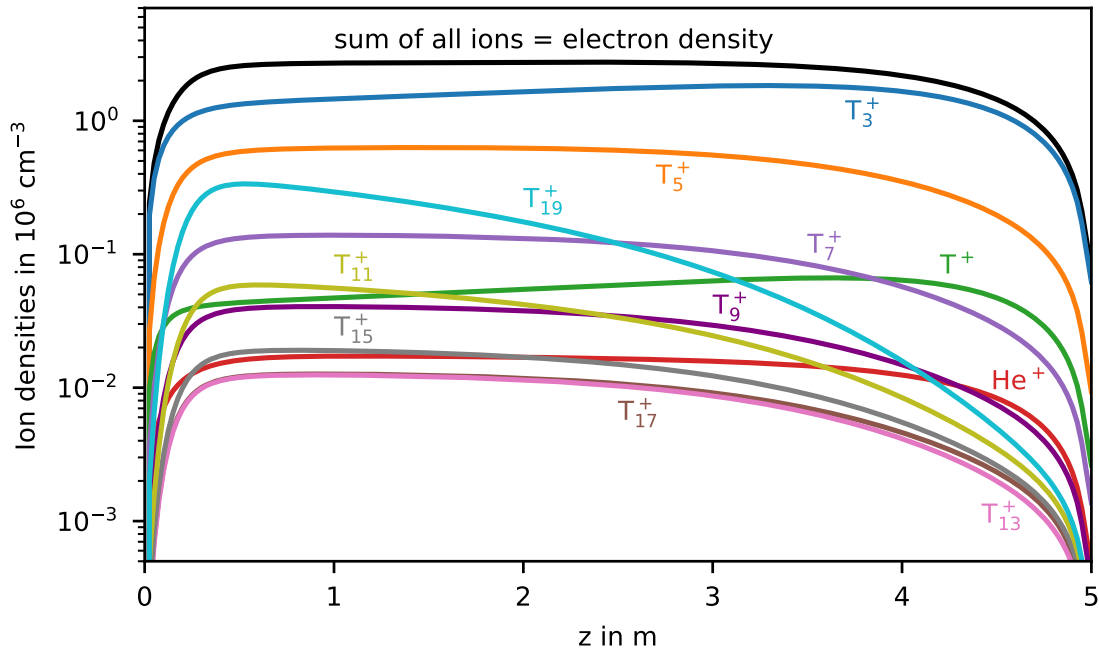


Figure 3.2: Simulated longitudinal ion density distribution in the front half of the WGTS. The simulation was done by F. Glück for a column density $\mathcal{N} = 4.2 \times 10^{17} \text{ cm}^{-2}$. It includes ion species up to T_{19}^+ and is done for the central 5 m up to the first WGTS pump port entrance. Assuming quasi-neutrality, the sum of densities over all ion species is equal to the total density of electrons inside the source. The WGTS center is at $z = 0 \text{ m}$ where the tritium gas inlet is located.

worsen the neutrino mass sensitivity as it was shown in toy Monte Carlo simulations [Kle14]. An energy-independent background rate $dN_B/dt(qU_{\text{ret}}) = \text{const.}$ increases the statistical fluctuations of the measured FPD count rates, which propagates into a higher statistical uncertainty on the neutrino mass [KAT05, Kle14]. On top of that, an energy-dependent background rate $dN_B/dt(qU_{\text{ret}})$ would change the shape of the β -spectrum and influence the deduced $m_{\bar{\nu}_e}^2$ parameter, ultimately leading to a systematic shift of the squared neutrino mass best-fit result.

Tritium ion-induced background in the main spectrometer

If not blocked, both positive and negative tritium ions would follow the magnetic field lines from their point of production in the WGTS up to the spectrometer section. Negative ions would be repelled by the PS negative high voltage and move back in upstream direction. Positive ions would be accelerated by the negative voltage out of the 134 T cm^2 flux tube and hit the surfaces of the PS vessel and inner electrodes.

From ion tracking simulations by F. Glück and with KASSIOPEIA it is known that the probability for positive ions to reach the MS is below 10^{-4} [Kle19]. However, this value depends on the ion species, energy, pitch angle, location and the PS electric and magnetic configuration. So it is not impossible that some ions might be transmitted through the PS directly into the MS.

Ions hitting the inner surfaces will neutralize and subsequently either will be directly reflected back into the UHV at a rather small rate of roughly 5% or implanted into

the surface [Kle19]. Assuming T_3^+ surface implantation, over the long term about 50%² of the neutral tritium atoms are expected to diffuse back to the surface and to be released again into the gas phase via desorption [Kle19]. In case of direct reflection and desorption from the surface they enter the PS volume as neutral particles and eventually diffuse into the MS volume. The diffusion speed is proportional to the conductance between PS and MS, $C_{PS \rightarrow MS}$, which is much lower than the PS effective pumping speed for tritium molecules [Kle19]. It is therefore estimated that only a few percent of the neutral tritium particles will reach the MS [Kle19]. In short, only positive tritium ions are able to invade the PS and from 100 ions only about 1 is effectively transmitted to the MS in the long term.

Inside the MS these migrated ions could result in an elevated background level due to two mechanisms: β -decay and subsequent ionization of residual gas. Beta-decays inside the analyzing volume of the MS produce keV-scale electrons. A few of them are transmitted to the FPD after gaining energy via acceleration in z -direction by the electric field between the MS and FPD potentials. Consequently, most of these events have a quite different energy from source β -electrons, so that they can be distinguished by the intrinsic FPD energy resolution. However, about 15% of all β -decays are accompanied by low-energy shake-off electrons. If they are produced downstream of the MS analyzing plane, they will be accelerated and detected at the FPD with an energy close to the retarding potential energy qU_{ret} [KAT05].

The second and more dominant effect increasing the background count rate is a direct follow-up of tritium β -decay inside the MS volume. This is because the MS - as any spectrometer of MAC-E filter type - stores β -electrons born in its own volume [MDF⁺13] if their pitch angles θ satisfy [Har15]

$$\theta > \theta_{\text{max}} = \arcsin \left(\sqrt{\frac{qU_{\text{ret}}(\vec{x}_s)}{E(\vec{x}_s)} \cdot \frac{B(\vec{x}_s)}{B_{\text{max}}}} \right) \quad (3.8)$$

due to the magnetic mirror effect described in section 2.1.1. Here, B_{max} is the maximum magnetic field along the electron's path, $E_{\text{kin}}(\vec{x}_s)$ is the kinetic energy, $qU_{\text{ret}}(\vec{x}_s)$ the retarding potential energy and $B(\vec{x}_s)$ the magnetic field at the electron's starting position \vec{x}_s . Because of the high magnetic fields at the MS entrance and exit regions of up to 4.2 T and the low magnetic field below 1 mT in the center, a large fraction of β -electrons is trapped inside this magnetic bottle. As they move back and forth they lose their keV energies via repeated ionizations and excitations of residual gas molecules [Wan13]. The secondary electrons created inside the 134 T cm² flux tube on the downstream side of the analyzing plane are accelerated towards the FPD and contribute to the background count rate. In the symmetric design setting of the MS magnetic field about half of the secondary electrons will do so. An asymmetric setting where the analyzing plane is shifted closer to the FPD is foreseen for future KATRIN operation in order to reduce the overall background level.

In order to limit the background contribution of neutral tritium inside the MS to a level of 1 mcps, a gas flow rate of T_2 and HT molecules into the PS of smaller than 1×10^{-14} mbar ℓ /s corresponding to 2.5×10^5 molecules/s is required in [KAT05].

²This number is by no means accurate since it is strongly dependent on the conditions of the solid and surface and on the desorption rate with respect to the diffusion speed.

To be conservative, 10% of this budget could be assigned to tritium ions. It has to be noted that the most abundant ion species is T_3^+ which has a higher activity than HT or T_2 . From these considerations an upper limit for the T_3^+ flux from the CPS into the PS was derived in [Kle19]:

$$\phi_{\text{CPS} \rightarrow \text{PS}} = 1 \times 10^4 T_3^+ \text{ ions/s.} \quad (3.9)$$

This corresponds to a MS background count rate of 0.1 mcps.

Energy-dependent backgrounds from RS, WGTS and DPS

There are three different sources of energy-dependent background. All of them originate from β -decays in regions with different starting properties than the dominant β -decay of gaseous T_2 inside the WGTS. For illustration, let us consider a background β -spectrum with endpoint energy $E_{0,2} > E_{0,1}$ compared to the original WGTS β -spectrum endpoint energy $E_{0,1}$ as shown in Fig. 3.3. Experimentally, it can not be distinguished between these two spectra because only the sum of both

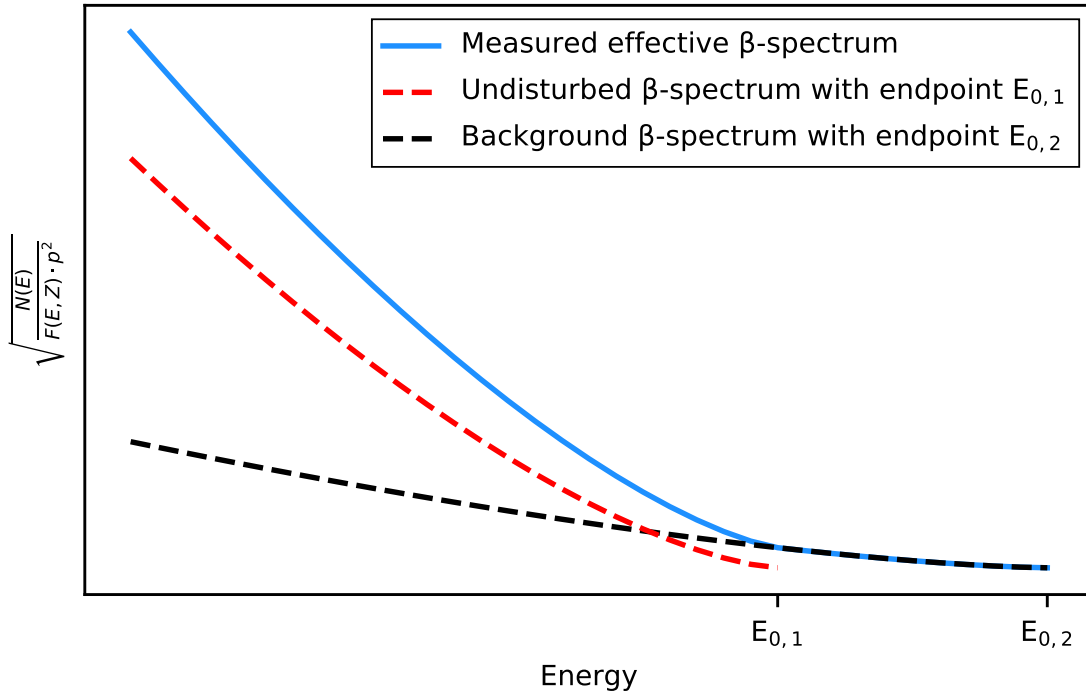


Figure 3.3: Illustrative plot showing the influence of an exemplary energy-dependent background β -spectrum on the effectively measured spectrum. The integral spectra are given in a Kurie-plot with $\sqrt{N(E)/(F(E,Z) \cdot p^2)}$ plotted against the energy. Here, $N(E)$ is the number of counts per energy E , $F(E,Z)$ is the Fermi function with the atomic number Z of the β -decay daughter molecule and p is the momentum of the β -electron. The undisturbed β -spectrum (red dashed line) is the WGTS signal spectrum from gaseous T_2 molecules modeled with an endpoint energy $E_{0,1}$. It is superimposed with a background β -spectrum (black dashed line), which has a 30 times lower amplitude and a higher endpoint energy $E_{0,2}$. Both spectra were approximated by the formula $N(E) = C \cdot (E_0 - E)^3$ with the number of counts N , the constant C , the endpoint E_0 and the energy E . In a measurement the sum of both (blue line) effectively will be obtained.

is measured. This effective sum spectrum will be distorted in its shape compared to the undisturbed spectrum, which ultimately leads to a systematic shift of the best-fit neutrino mass result if this is not accounted for in the analysis. Here, three different sources of such energy-dependent background spectra are discussed.

The β -decay final states of ionized tritium molecules or atoms differ from T_2 [KAT05]. For example, T^- decays into ${}^3\text{He}$ and T_2^+ into ${}^3\text{He}T^{++}$. Different final state atoms or molecules have different masses m , recoil energies E_{rec} , excitation energy levels V_k and population probabilities W_k ³. Consequently, depending on the analyzed energy interval, β -electrons originating from any species s can be interpreted as a background contribution to the T_2 β -spectrum with a different spectral shape and a different endpoint E_{0s} . Fortunately, except for T^- , all the endpoint energies are lower than for T_2 , which makes their impact on the endpoint region rather small [KAT05].

The gold-plated rear wall disc mounted in the RS terminates the 134 T cm^2 flux tube at the rear end. Roughly half of the WGTS tritium ions impinge on it and either get implanted, reflected or adsorbed at the surface. After some exposure time the RW will itself be a β -emitter with its own characteristic spectrum. First measurements show that the RW activity is increasing with the accumulated exposure time to the WGTS tritium gas. Up to now, two measurement campaigns with 22% and 84% of the design tritium column density, respectively, have been conducted (see section 3.2) and the RW activity is still several orders of magnitude lower than the WGTS T_2 signal rate [Ake]. However, at some point it will reach scales where it can not be neglected anymore. Then, this effect either has to be taken into account in the neutrino mass analysis or the RW activity has to be reduced by dedicated actions like baking or UV illumination.

In order to minimize the tritium ion-induced background in the MS, two ring and one dipole electrode to block positive ions, as well as three dipole electrodes to remove them via $E \times B$ drift are installed along the DPS beam line (cf. section 2.3.3, for an engineering drawing see Fig. 5.1 in section 5.1.1). Each electrode is operated at a certain electrical voltage. Depending on the selected polarity, β -electrons born inside of these potentials gain or lose energy when they leave them. The resulting β -spectrum will therefore be shifted by $\Delta E = -qU_e$ for an electrode voltage U_e . All the ring electrodes are operated at positive voltages so the β -spectrum endpoint will be lower than the one from the WGTS. Furthermore, they are mounted at the downstream end of the DPS where the tritium density is already decreased by more than seven orders of magnitude compared to the central WGTS. Therefore, the background contribution from ring electrodes can be neglected.

On the other hand, three of the four dipole electrodes are operated with a negative dipole field in the first three beam line elements of the DPS. In [Kle19] upper limits for the applied dipole voltages were derived theoretically in order to constrain the effect to an acceptable level. Back then, the fourth dipole electrode was also foreseen to be operated at a negative field. The resulting values for the half-shell voltages are -5 V/-15 V (dipole 1), -5 V/-35 V (dipole 2), -5 V/-85 V (dipole 3) and

³The influence of the four parameters m , E_{rec} , W_k and V_k on the β -spectrum is explained in section 1.6.5.

-5 V/-175 V (dipole 4). Between two consecutive dipole electrodes the tritium density decreases by a factor of 10 according to gas flow simulations and pressure gauge measurements. So the further downstream a dipole electrode is mounted, the higher its absolute voltage can be.

3.1.4 Influence of ion blocking and removing beam line instrumentation

The beam line instrumentation for blocking and removing of tritium ions in turn can introduce systematic effects. Besides the background contribution described above there are two more possible effects.

The DPS ring and dipole electrodes as well as the SDS ring electrodes are supplied by a DC voltage. In case there are high-frequency variations in this DC voltage, a β -electron traversing the electrode could experience a de- or acceleration. For this effect, the electrode voltage has to change during the transit time of the electron which corresponds to a time scale of roughly 10 ns for a 18.6 keV electron moving with a speed of approximately $v = 1/4c$. Thus, the voltage noise frequency has to be on the order of $f = 100$ MHz. As a countermeasure, highly stable iseg[®] voltage supplies of type DPr 05 are used for all ring and dipole electrodes and the DPS electrode circuits additionally were equipped with low-pass filters.

Three of the four DPS dipole electrodes have the purpose of drifting positive tritium ions out of the beam line. Negative ions are not influenced by this drift since they can not enter the negative dipole field due to electrostatic repulsion. On the other hand, β -electrons experience an $E \times B$ drift. In [Kle19], assuming all four dipole electrodes to be operated in drifting mode at equal polarity, the shift in x -direction after traversing all electrodes was calculated to be only 43 μm which is considered to be negligible.

3.1.5 WGTS plasma effects

The ions and secondary electrons produced continuously inside the source tube lead to the formation of a plasma [KAT05]. A plasma is a state containing neutral particles as well as significant amounts of free ions and electrons [Str18]. It behaves quite differently compared to a purely neutral gas. One of the main differences is the simultaneous and collective response of particles to electric or magnetic fields [Bit04]. The density of ion-electron pairs in the WGTS amounts to a few times 10^6 cm^{-3} [KAT05], which is rather low compared to common plasmas [Kuc16]. Due to the strong axial magnetic field inside the WGTS the perpendicular mobility of all charged particles is very low, although not zero. In first approximation, the plasma can be referred to as quasi-neutral⁴. Quasi-neutrality is given if the equation $n_e \approx \sum Z_i \cdot n_i$ with the number density of electrons n_e , ions n_i and their charge numbers Z_i is fulfilled [Str18].

In case that space charges build up locally in the WGTS beam tube this would have a direct impact on the β -electron energy. The energy of a β -electron born in a space

⁴Under certain boundary conditions this approximation is not valid for the WGTS plasma. This was found in plasma simulations by L. Kuckert (see section 6.1.3).

charge potential U_s will be shifted by $\Delta E = -qU_s$ when it leaves the potential. Consequently, in this case the effectively measured β -spectrum is a superposition of many individual β -spectra originating from many different locations inside the WGTS. In some way, this is analog to the effect induced by the DPS dipole electrodes described in section 3.1.3. The effectively measured β -spectrum will be distorted compared to an energy spectrum resulting from a homogeneous plasma potential. Assuming a gaussian variation σ of the space charge potentials the squared neutrino mass best-fit result will be shifted by $\Delta m_{\bar{\nu}_e}^2 = -2\sigma^2$ [RK88]⁵. It is important to note that a gaussian fluctuation of the MS retarding potential would result in exactly the same shift. In [KAT05] an upper limit for the systematic shift of the squared neutrino mass of

$$\Delta m_{\bar{\nu}_e}^2 < 2 \times 10^{-4} \frac{\text{eV}^2}{c^4} \quad (3.10)$$

was required. This would correspond to a plasma potential variation of about 10 meV. The effects of potential variations can occur in space and time.

Spatial plasma potential inhomogeneity

In longitudinal direction, plasma potential inhomogeneities are assumed to be on the order of a few mV only because space charge imbalances can be compensated efficiently due to the high longitudinal conductivity [KAT05]. This assumption is supported by results of dedicated simulations based on a fluid plasma model [Kuc16]. In order to control the longitudinal plasma potential, the gold-plated RW is mounted in the RS to terminate the sensitive magnetic flux tube at the rear end of KATRIN. It provides a well-defined surface potential with small inhomogeneities, which governs the plasma potential inside the magnetic flux tube. The surface potential has two contributions: the intrinsic work function of the gold material and an externally applied bias voltage. Any radial or azimuthal variation of the work function might directly propagate to the plasma potential. Fortunately, this can be resolved at least to some degree by the pixel-wise segmentation of the FPD, which makes it possible, in principle, to analyze 148 different β -spectra at different radial and azimuthal positions at once. Also, the RW work function was measured with a Kelvin probe before it was built into the RS. The result was a spatial variation on the order of $\sigma = 10$ meV [Sch16]. Repeating this measurement within the scope of this thesis however gave much higher results on the order of $\sigma = 70$ meV. Ultimately, the RW work function and the plasma potential distribution have to be characterized in-situ because any external test setup will inevitably have different basic conditions regarding vacuum, tritium exposure, electrical setup, temperature, UV illumination and surface treatment history in general. The in-situ measurement is done using gaseous $^{83\text{m}}\text{Kr}$ as a nuclear probe for potential variations. Further diagnostic methods are investigated in this work.

⁵According to recent calculations by M. Machatschek this formula can not be applied for the special case of considering plasma effects. The reason is that it does not take into account that β -electrons born in a plasma potential from the rear part of the WGTS lose on average more energy on their way to the FPD than the ones born in the front part. Thus, not only the gaussian variance σ^2 of the plasma potential distribution is important but also its longitudinal shape. Details can be found in the forthcoming PhD thesis by M. Machatschek [Mac]. However, the formula stated in the text is still valid for low column densities and is sufficient for a qualitative understanding of the influence of an inhomogeneous plasma potential on the neutrino mass result.

Time-dependent plasma potential

KATRIN will run for five years with a net measurement time of three years. The measured FPD count rates will ultimately be combined (e.g. by stacking) in order to minimize the statistical uncertainty. If unaccounted, a time-dependency of the absolute value or the spatial profile of the plasma potential would introduce a systematic uncertainty to the combined data. The time-dependency could either be a fluctuation or a directed drift. Repeated measurements of the plasma parameters are necessary for monitoring these trends.

The underlying physical phenomena either could be variations in the plasma boundary conditions, like e.g. the RW surface potential, or plasma instabilities. Plasma instabilities are small perturbations in e.g. density, temperature, electromagnetic fields etc. leading to growing perturbations and ultimately to the change of the equilibrium state [Str18]. Basically, all kinds of time scales can have a significant impact on the neutrino mass result. Furthermore, for the specific case of high-frequency plasma instabilities a second effect occurs.

Change of β -electron energy by high-frequency plasma instabilities

High-frequency (\gtrsim MHz) plasma instabilities can be induced by fast turbulent motion of electrons. This can lead to time-varying electric potentials on a very short time scale. If the time scale is of a similar order than a β -electron's time-of-flight needed for traversing the instability region, the electron will gain or lose energy. Basically, this effect is analog to voltage fluctuations at the beam line electrodes. An important countermeasure would be the removal of positive ions by drifting them out with the DPS dipole electrodes. Due to the quasi-neutrality condition, this in turn leads to a lower density of electrons inside the plasma and therefore to lower high-frequency plasma instability amplitudes. However, if high-frequency plasma instabilities really occur in the source plasma, it is not possible to entirely eliminate them a priori, which is why dedicated measurements have to be undertaken for characterization.

3.2 KATRIN timeline during development of this thesis

The KATRIN collaboration has performed various measurement campaigns and reached important milestones during the development of this thesis in the period from June 2017 to November 2020. All measurements described in chapters 4 to 6 were conducted within the scope of one of these campaigns and contributed to the successful operation and the final results. One major milestone - the first tritium operation of KATRIN in May and June 2018 with a reduced tritium activity of 0.5% of the nominal design value of 1.7×10^{11} Bq - will not be covered here because of its minor importance for this thesis. The interested reader is referred to [AAA⁺20].

Krypton campaign (July 2017)

The conversion electrons emitted in the course of the 32.2 keV transition of $^{83\text{m}}\text{Kr}$ possess a discrete energy spectrum with energies between 17.8 keV and 32.1 keV and narrow line widths on the order of 1 eV [VSD⁺18] (more details will be given in section 4.1). In the July 2017 commissioning milestone these conversion electrons were successfully transmitted through the complete KATRIN beam line from the

source to the FPD for the first time ever.

Gaseous $^{83\text{m}}\text{Kr}$ was injected into the WGTS which was operated in krypton mode at $T = 100\text{ K}$. All TMPs along the beam line were switched off so the CPS cold trap was the only active pump in the system. The rear section was not installed yet. Instead, at the rear side the WGTS was terminated by a flange with a single BIXS detector mounted axially.

In chapter 4 a simulation of the longitudinal gas distribution for this special hardware configuration will be presented including a comparison with measured data. After one week of measurements with the gaseous source the valve between DPS and CPS was closed and the condensed krypton source was inserted into the CPS flux tube for another week of measurements. The main objectives of this commissioning campaign were:

- the first WGTS operation in krypton mode with an isotropic electron source and adiabatic guiding of the emitted electrons to the FPD,
- high-precision spectroscopy of the $^{83\text{m}}\text{Kr}$ lines,
- evaluating the long-term stability of the experiment's energy scale and of important operational parameters like the MS high voltage and the WGTS temperature,
- testing the overall performance of the hardware components and analysis chains.

All these goals have been achieved and the results were published in dedicated papers. In [ABB⁺18a] the full beam line transmission and stability investigations are described. A calibration of the MS high voltage divider with a precision of 5 ppm using the line position difference of the K-32 and L₃-32 line was done in [ABB⁺18b]. On top of that, the krypton spectrum line widths were measured with an unprecedented precision of $\sim 1\%$ using the high MS energy resolution [AAB⁺19b].

STSIIIa campaign (September & October 2018)

This campaign was part of the "five phases to standard tritium operation of KATRIN" [BBS⁺17] from the arrival of the very first STS hardware components towards standard operation with tritium at nominal design density. The main goal was to commission the loop circulation system and the full beam line with inactive D₂ gas before reaching the point of no return of "contaminating" the system with large amounts of tritium.

The rear section and the loop system⁶ were attached beforehand as the last missing parts, so this was the first campaign with all main components in place. However, the Cermax[®] UV illumination of the RW was not yet ready and instead substituted by two miniZ UV lamps from RBD instruments[®].

One major achievement was the successful commissioning of the rear section egun with first measurements of the WGTS energy loss and column density. Also, D₂ carrier gas was used for producing inactive deuterium ions, which allowed sensitivity studies and the calibration of multiple ion detectors which is detailed in section 5.2. Especially in the SDS part this would not have been possible with radioactive tritium ions because of the resulting increase of the MS background level.

⁶The loop system has been integrated already in spring 2018 and was successfully operated during the "first tritium" campaign [AAA⁺20] a few months before the start of STSIIIa.

KATRIN neutrino mass runs KNM1 & KNM2 (March - May 2019 & September - November 2019)

In spring 2019 the first KATRIN neutrino mass measurement was performed during the KNM1 campaign with the aim of obtaining a new world-leading sensitivity on $m_{\bar{\nu}_e}$. Surprisingly, a large drift of the column density was observed during the initial ramp up of the source [Mar]. This was due to radiochemical reactions of tritium gas with the inner metal walls of the loop system. Subsequent adsorption of the reaction products at cryogenic temperatures was causing a reduction of the inlet capillary diameter, which in turn reduced the gas throughput and thereby the column density. The magnitude of the drift could be minimized by operating the WGTS at reduced levels of the column density $\mathcal{N} = 1.1 \times 10^{17}$ molecules/cm², which corresponds to 22% of the nominal design value. For almost five weeks the beta-spectrum endpoint region was scanned repeatedly accumulating statistics equivalent to a measurement of about five days at the design column density. The results were published in [AAA⁺19c]. In Fig. 3.4 the measured beta-spectrum can be seen together with the best-fit by the model from Eq. 2.8. A best-fit value of $m_{\bar{\nu}_e}^2 = -1.0_{-1.1}^{+0.9}$ eV² [AAA⁺19c] was found from which an upper limit of $m_{\bar{\nu}_e} < 1.1$ eV/c² (90% C. L.) [AAA⁺19c] was derived using the Lokhov and Tkachov method [LT15].

Before the start of the actual β -spectrum measurement various investigations of systematic effects took place including many ion- and plasma-related studies. In fact, this was the first opportunity to perform dedicated plasma measurements at KATRIN because it was the first time the WGTS was operated at a significant fraction of the design tritium column density. One of the major results of these plasma investigations was the determination of the optimum voltage at which the RW was operated over the entire β -spectrum measurement. Furthermore, the ion instrumentation of the DPS and the PS was operated over the course of several months providing safe and stable operation conditions. Ion- and plasma-related measure-

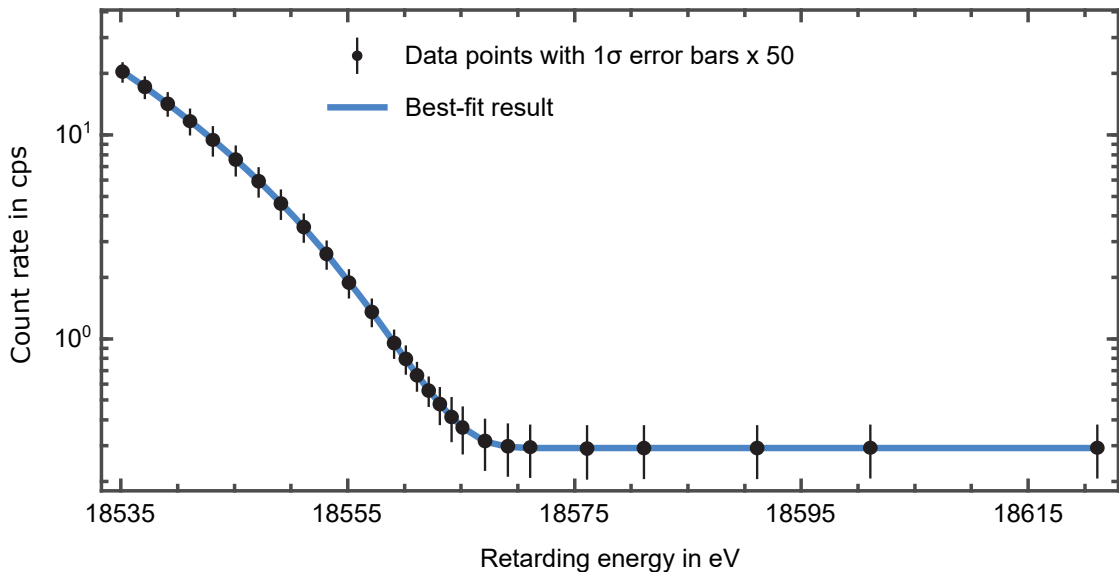


Figure 3.4: KNM1 measurement and best-fit result of the integral beta-spectrum. The stacked FPD count rate versus the MS retarding energy is shown. Each 1σ uncertainty bar is increased by a factor 50 for better visibility. The figure is taken from [AAA⁺19c] with minor adjustments.

ment results are given in section 5.3 and 6.3, respectively. After the measurement of the β -spectrum at the end of May a one week $^{83\text{m}}\text{Kr}$ campaign at $T_{\text{WGTS}} = 100\text{ K}$ was conducted including measurements both with and without tritium gas inside the WGTS.

After the summer maintenance break the KNM2 campaign took place with the goal of accumulating more statistics for neutrino mass determination. This time, the WGTS was operated at $\mathcal{N} = 4.2 \times 10^{17}$ molecules/cm², which equals 84% of the nominal design column density. A high priority was assigned to systematic plasma investigations before the start of the actual neutrino mass measurement. In order to perform dedicated plasma measurements, the β -spectrum scan was interrupted several times enabling long-term monitoring of plasma observables. The insights gained from these investigations (see section 6.3) had a major impact not only on the understanding of the influence of plasma effects on the neutrino mass result, but also for the subsequent measurement campaign KNM3, for which it was afterwards decided to change the WGTS operational temperature from 30 K to a higher temperature on the order of 80 K. For high-precision plasma investigations a $^{83\text{m}}\text{Kr}$ campaign took place right after the end of KNM2 β -scanning.

3.3 Objectives of this thesis

The overall objective of this thesis is to minimize and experimentally investigate ion- and plasma-related systematic effects on the KATRIN neutrino mass determination. An overview of these effects is shown in Tab. 3.1. This rather general goal can be subdivided into three different tasks, which are described below and then pursued in the three main chapters following.

1. Contributions to the $^{83\text{m}}\text{Kr}$ July 2017 measurements

The WGTS plasma effects stated in Tab. 3.1 can be investigated with $^{83\text{m}}\text{Kr}$ spectroscopy. One major problem with this method is that it is only applicable above beam tube temperatures of $\sim 80\text{ K}$ whereas the neutrino mass is measured at 30 K. In this work the focus therefore lies on alternative methods for plasma characterization applicable in-situ at 30 K. Nevertheless, contributions to the first KATRIN $^{83\text{m}}\text{Kr}$ campaign in July 2017 have been made, answering the following question.

- **Are the results of the krypton measurements in July 2017 in agreement with the beam line and electromagnetic field models of KATRIN?**

For the special hardware configuration of the July 2017 krypton campaign the spatial beam line distribution of krypton atoms has been simulated using a Test Particle Monte Carlo (TPMC) gas flow simulation code based on the KATRIN beam line geometry. In addition, the magnetic flux tube mapped on the FPD and the DPS dipole electrode electric potential have been simulated with KASSIOPEIA and KEMField, respectively. The combined results are compared to the measurement results of a specific line in the krypton energy spectrum. A good agreement between the results would confirm the validity of the KATRIN models implemented in the simulation tools.

2. Minimization of ion-induced background

In order to prevent tritium ions from entering the spectrometer section, a system of beam line hardware instrumentation has been established. Ring electrodes and one dipole electrode along the beam line block positive ions electrostatically, the other dipole electrodes block negative ions and remove positive ones via $E \times B$ drift. For measuring the residual ion flux into the PS the current of impinging ions is measured at one of its inner electrodes. Also, positive ions can be measured via the removal current of the DPS dipole electrodes or with the FPD using a special method called ion conversion to electrons (ICE). All these hardware devices and methods have been developed and commissioned by former works, especially by M. Klein [Kle19]. However, open points remained.

- **What are the calibration factors and sensitivities of the KATRIN ion detectors?**

The PS current and ICE ion detection method had to be calibrated. Explicitly, this means the determination of the conversion factor between the measured current or FPD rate and the corresponding ion flux into the PS. The size of a measured signal can not be interpreted without this factor. Also, knowing the conversion factor directly leads to the sensitivity of the method since the factor is basically equivalent to the efficiency of a conversion of ions into a measurable signal. In the end it is of major importance that the method is sensitive enough to detect an ion flux on the order of the allowed upper limit of $1 \times 10^4 \text{ T}_3^+$ ions/s, as stated in Eq. 3.9. The calibration needs to be done with high rates of inactive ions since tritium ions would "contaminate" the spectrometer section. Deuterium ions are especially suitable because of their similar mass. Consequently, the calibration factors and sensitivities were determined in the course of the STSIIIa campaign.

- **What are the optimum settings of ring and dipole electrodes in a nominal neutrino mass run?**

For both the ring and dipole electrodes one has to find and apply the optimum operation voltages. In both cases this is a tradeoff between lower and higher voltages. At lower ring electrode voltages high-energy positive ions from the source can pass. At higher voltages the ring electrode acts as a deep Penning trap for low-energy electrons producing Penning ions in turn. The same applies to the dipole electrode operated as a blocking electrode at positive polarity in the fourth DPS beam line section. As for the other three DPS dipole electrodes, lower dipole fields result in a slower drift of positive ions. On the other hand, if the absolute voltage U is too high, the background rate from β -decays inside the dipole increases approximately with $(E_0 + qU - E)^3$ with the electron kinetic energy E and the tritium endpoint E_0 . The ring electrode voltage characteristics have been measured both in STSIIIa and in the first neutrino mass measurement campaigns KNM1 and KNM2 at high WGTS tritium column densities. In KNM1 and KNM2 also the effect of the negative DPS dipole voltages was measured.

- **Are ions effectively stopped from entering the spectrometer section during a high column density neutrino mass run?**

In order to meet the strict requirements for a low MS background level, tritium

ions have to be stopped from entering the PS. This needs to be validated under nominal KATRIN conditions with the WGTS operated at a high tritium column density. It was successfully done both in KNM1 and KNM2 with 22% and 84% of the nominal design column density, respectively.

- **Is the ion retention, removal and detection system stable over long-term operation under nominal conditions?**

A KATRIN neutrino mass run is scheduled to last 60 days [KAT05]. It was never tested before if the hardware system for ion blocking, removal and detection can be safely operated for such a long time without any major incidents. The KNM1 and KNM2 campaign provided the first opportunity to do so.

3. Experimental investigations of the WGTS plasma effects

In the scope of this thesis the first KATRIN plasma measurements have been performed. The topmost goal was to measure the influence of the RW on the plasma. In particular, the following questions had to be answered.

- **What is the influence of different hardware configurations on the WGTS plasma?**

Besides the RW two more hardware devices along the beam line might have a direct influence on the plasma parameters. In the DPS, the first three dipole electrodes remove positive ions, which reduces the number of charge carriers. At the first DPS pump port an infrared illumination was mounted right before the beginning of KNM2, to allow for the neutralization of T^- ions. All these hardware devices were never operated with a high WGTS tritium column density before KNM1 and KNM2. Especially interesting is the influence of different RW and dipole electrode voltages on the plasma.

- **Is the plasma potential coupled to the rear wall surface potential?**

Due to the high longitudinal conductance of the plasma the RW potential is expected to define the plasma potential over the whole length of the source beam tube. A change of the RW bias voltage should therefore lead to a change of the WGTS potential and to a shift of the β -spectrum endpoint. Simulations based on a fluid model indicate that this assumption might only be valid over a certain RW voltage range [Kuc16]. Outside of this range, the RW could be "decoupled" from the plasma. Measurements of the β -spectrum at different RW bias voltages were done within the KNM1 and KNM2 campaign.

- **What is the optimum rear wall bias voltage for the neutrino mass measurement?**

The results of the simulations in [Kuc16] also imply an optimum RW bias voltage at which the spatial plasma potential inhomogeneity should be minimized. For both KNM1 and KNM2 optimum values were experimentally determined and applied during neutrino mass measurements.

- **How are plasma observables evolving over time?**

In KNM2 the first opportunity arose to repeat measurements of plasma observables in order to investigate time-dependent effects. The results are of major importance for long-term KATRIN measurements and have a significant impact on the future operation.

- **Are plasma instabilities observed in-situ?**

A method for measuring plasma instabilities was applied in KNM2 at different RW bias voltages.

4. Gas flow and electromagnetic field simulations for the 2017 krypton commissioning

In this chapter contributions to the July 2017 krypton campaign are presented. The main goals and a description of the hardware configuration for this commissioning campaign were given in section 3.2. For the one week measurement with gaseous krypton, gas flow and electromagnetic field simulations were performed in order to compare the results with measured data and thereby validate the model of the beam line and the electromagnetic field implemented in the simulation framework. The explicit goal of the simulations is to determine the ratio R of conversion electrons from krypton decays, measured by the FPD, originating from the WGTS and from the regions of the DPS dipole electrodes, respectively.

Experimentally, this ratio can be assessed by performing two independent measurements of the krypton L₃-32 line. First, this line is measured with the DPS dipole elements operated in monopole mode with a positive voltage $U = +U_{\max}$ applied to both half-shells. Here, $U_{\max} = +350$ V is the maximum allowed voltage for the electrodes. To first order, the energy of krypton decay electrons born inside this potential is shifted by a value $-eU_{\max}$. Thus, their energy drops below the pre-set filter potential of the MAC-E filter for the undisturbed L₃-32 energy interval, so that they are no longer counted by the FPD. The measured detector counts therefore originate mostly from conversion electrons starting in the WGTS. In a second measurement the dipole electrodes are operated in the same mode but at a voltage $U = -U_{\max}$, which shifts the corresponding electrons to higher energies. By increasing the absolute MS retarding potential accordingly, conversion electrons originating from the WGTS are now rejected, counting only electrons from the dipole regions. The ratio R is finally calculated by taking the ratio of detected count rates. In the simulation this special configuration is implemented and the final outcome is cross-checked with the measurement. The results were published in [ABB⁺18a].

This chapter is structured as follows. First, details about the conversion electrons from ^{83m}Kr-decays and their energy spectrum will be given in section 4.1. In the

following chapter 4.2, it will be explained how the implementation of the gaseous krypton source was realized in July 2017. Then, the gas flow and electromagnetic field simulations will be presented in sections 4.3 and 4.4, respectively. The results will be combined in section 4.5 and compared to the measured data in section 4.6. A concluding summary will be given in section 4.7.

4.1 The krypton isotope $^{83\text{m}}\text{Kr}$

The metastable $^{83\text{m}}\text{Kr}$ isotope is produced by electron capture decay of the mother isotope ^{83}Rb with a half-life time of $T_{1/2} = 86.2\text{ d}$ [McC15]. More than 95% of the decays end up in an excited metastable state of $^{83\text{m}}\text{Kr}$ at an energy of 41.6 keV above the ground state [McC15]. The ground level is reached via a cascade of a first 32.2 keV transition with a half-life time of 1.83 h and a second 9.4 keV transition with a half-life time of 155 ns [VSD⁺18]. The decay processes are illustrated in Fig. 4.1.

Both $^{83\text{m}}\text{Kr}$ transitions can either happen as γ -decays or via internal conversion where an electron of one of the inner atomic shells electromagnetically interacts with the nucleus and receives energy from it. The electron then has enough kinetic energy to leave the atomic shell and is emitted isotropically. The electron receives all the available energy of the nuclear transition minus the recoil energy. This is why the energy spectrum of $^{83\text{m}}\text{Kr}$ is a discrete spectrum with monoenergetic lines. Every line corresponds to a conversion electron emitted from a certain atomic shell $s \in (\text{K}, \text{L}, \text{M}, \text{N}, \dots)$ in a certain nuclear transition t . Neglecting the recoil energy of the nucleus, the line energies can be calculated according to [VSD⁺18]

$$E_{\text{line}} = E_t - E_B. \quad (4.1)$$

with the transition energy E_t and the atomic shell binding energy E_B . In the following only the 32.2 keV transition is considered. The lines are named according to the conversion electron's original atomic shell and the transition energy: K-32, L₁-32, L₂-32, L₃-32 and so on. The indices represent the atomic subshells. Due to Heisenberg's uncertainty principle each line has an intrinsic Lorentzian width Γ ranging from 0.03 eV to 3.75 eV [VSD⁺18]. In Tab. 4.1 an overview of important

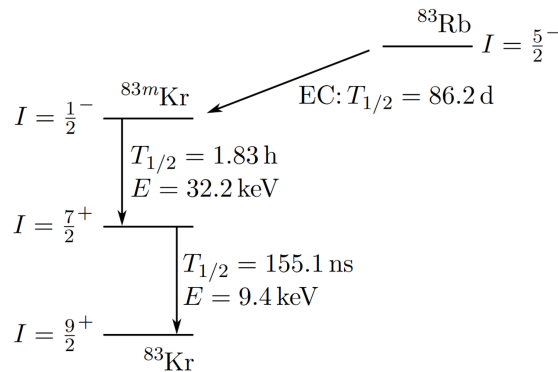


Figure 4.1: Decay scheme of $^{83\text{m}}\text{Kr}$. The $^{83\text{m}}\text{Kr}$ isotope is produced via electron capture (EC) of ^{83}Rb and decays in two consecutive transitions to the ground state. Nuclear spin quantum numbers I of every state, transition energies E and half-life times $T_{1/2}$ are given. The figure is taken from [SM19].

Table 4.1: Overview of important conversion electron properties of the $^{83\text{m}}\text{Kr}$ 32.2 keV transition. Each line s_i -32 of the krypton energy spectrum corresponds to conversion electrons emitted from a specific atomic shell s with a subshell i . A line is characterized by its mean energy E_{mean} , internal conversion coefficient α , relative intensity I_{ce} per decay and natural line width Γ . The internal conversion coefficient for a line s_i -32 is defined by the ratio of the emitted conversion electron rate to the emitted gamma photon rate $\alpha = R_{\text{ce}}/R_{\gamma}$. For a single 32.2 keV transition, the probability of an emission from s_i -32 is given by the relative intensity I_{ce} per decay. The natural line width Γ represents the full width at half maximum. The values are taken from [VSD⁺18].

Line	E_{mean} in eV	α	I_{ce} per decay in %	Γ in eV
K-32	17824.2 ± 0.5	478.0 ± 5.0	24.8 ± 0.5	2.70 ± 0.06
L ₁ -32	30226.8 ± 0.9	31.7 ± 0.3	1.56 ± 0.02	3.75 ± 0.93
L ₂ -32	30419.5 ± 0.5	492.0 ± 5.0	24.3 ± 0.3	1.165 ± 0.069
L ₃ -32	30472.2 ± 0.5	766.0 ± 7.7	37.8 ± 0.5	1.108 ± 0.013
M ₁ -32	31858.7 ± 0.6	5.19 ± 0.05	0.249 ± 0.004	3.5 ± 0.4
M ₂ -32	31929.3 ± 0.5	83.7 ± 0.8	4.02 ± 0.06	1.230 ± 0.061
M ₃ -32	31936.9 ± 0.5	130.0 ± 1.3	6.24 ± 0.09	1.322 ± 0.018
M ₄ -32	32056.4 ± 0.5	1.31 ± 0.01	0.0628 ± 0.0009	0.07 ± 0.02
M ₅ -32	32057.6 ± 0.5	1.84 ± 0.02	0.0884 ± 0.0012	0.07 ± 0.02
N ₁ -32	32123.9 ± 0.5	0.643 ± 0.006	0.0255 ± 0.0004	0.40 ± 0.04
N ₂ -32	32136.7 ± 0.5	7.54 ± 0.08	0.300 ± 0.004	0.03
N ₃ -32	32137.4 ± 0.5	11.5 ± 0.1	0.457 ± 0.006	0.03

line parameters for the 32.2 keV transition is given. The narrow line widths are the reason why $^{83\text{m}}\text{Kr}$ is ideally suited as a nuclear standard for energy calibrations and to investigate processes, such as plasma effects, that can affect the energy of electrons down to the meV scale.

4.2 Technical implementation of the gaseous $^{83\text{m}}\text{Kr}$ source in July 2017

For a constant supply of gaseous $^{83\text{m}}\text{Kr}$ during this specific campaign a dedicated source setup has been developed by the Nuclear Physics Institute (NPI) of the Czech Academy of Science in Řež [SDL⁺18]. The ^{83}Rb mother isotope was bound in 30 small zeolite beads each with a diameter of 2 mm. The total ^{83}Rb activity was 1.0 GBq at the first day of the measurement campaign [ABB⁺18a]. Inside a vacuum setup more than 80% of the created $^{83\text{m}}\text{Kr}$ daughter molecules are emanated into the UHV. The krypton source setup was connected to the WGTS beam line at the second pump port of the front part (cf. Fig. 2.7).

From this point, the krypton gas could disperse freely in the beam line. As already mentioned in section 3.2, the KATRIN setup was operated in a different configuration than in the common neutrino mass measurement mode. The differing settings are listed in the following.

- The loop system for tritium circulation was not connected. All WGTS and DPS TMPs were shut off, so only the CPS cold trap was pumping the krypton gas.
- Also, the RS was not yet attached to the apparatus. There was no rear wall, no magnet, and no egun.
- Except for the missing RS magnet all other magnets were operated at 70% of the design field strengths.
- The source beam tube was operated in krypton mode at $T = 100$ K.

In this special configuration, the krypton gas distribution in the beam line deviates significantly from the nominal tritium gas profile that is shown in Fig. 3.1.

4.3 Gas flow simulations

In nominal tritium operation the pressure profile of the beam tube covers three different flow regimes, each requiring its specific numerical approach [KHD⁺18]. As for krypton operation in July 2017, the pressure in the entire beam tube was low enough to assume free molecular flow for the description of the gas dynamics. In molecular flow the mean free path of the molecules is large compared to the dimensions of the beam tube and molecules only interact with the walls of the vacuum chamber but not with each other [Jou18]. In this environment, the Test Particle Monte Carlo (TPMC) package MolFlow+ is applicable.

4.3.1 MolFlow+

MolFlow+ [KP09] is a simulation code for gas particle tracking in UHV chamber setups. The chamber geometry is approximated by a three-dimensional mesh of two-dimensional polygons, whose elements are called facets. Particle tracks are straight lines extending from one surface element to another. Changes in direction only occur if a particle is reflected at a facet. Therefore, particle tracks are following a zigzag path through the geometry. Every facet features counters for particle hits, adsorptions and desorptions. The number of hits per unit area is proportional to the pressure. When a particle hits a facet with a finite sticking probability $\alpha \in [0,1]$, it can be adsorbed, thus ending the tracking. The properties of a facet are defined by various parameters. It can be a part of the chamber surface (opacity = 1), a pump ($\alpha > 0$), a gas source (desorption rate > 0) or a so-called virtual facet (opacity = 0). Virtual facets do not belong to the physical geometry but are included in the simulation either for providing additional counting information as virtual pressure gauges or subdividing the model into different regions to speed up the simulation.

To simulate the propagation of $^{83\text{m}}\text{Kr}$ the radioactivity of the gas particles has to be implemented. In the original version of MolFlow+ this process is not included. However, the source code has been modified previously by the KATRIN collaboration in order to be able to simulate radioactive radon particles in the MS [DHJ⁺17]. In this modified version particles can decay within the UHV geometry and the spatial decay coordinates are saved to an output file. The resulting density map of decays can be used in a second step to simulate the trajectories of $^{83\text{m}}\text{Kr}$ conversion electrons with KASSIOPEIA (see section 4.4). Furthermore, a particle adsorbed on a facet

can either stick to it permanently or it can be desorbed after a mean sojourn time τ .

4.3.2 Simulation parameters

A geometry mesh was created based on the design engineering drawings of the STS beam line. The final MolFlow+ beam line model can be seen in Fig. 4.2. It consists of a total of 109338 facets. Each facet is assigned different parameters.

- **Temperature:** The WGTS beam tube and pump port facets are assigned a temperature of $T = 100$ K. At the rear and front end the transition to 293 K room temperature takes place along the beam line bellows (cf. Fig. 4.2) assuming a linear temperature gradient. The DPS beam line is operated at room temperature. The first beam tube element and pump port of the CPS are operated at 80 K liquid nitrogen temperature. Finally, the CPS cold trap is cooled down to 4.5 K.
- **Particle reflection:** For every facet diffuse reflection according to the cosine law [Jou18] is assumed. The temperature of a facet is used to simulate the velocity distribution of diffusely reflected particles according to the Maxwell distribution.
- **Sticking factor:** The WGTS and DPS beam tubes are made of stainless steel while the CPS inner surface is gold-plated. For neither material the pumping parameters for krypton could be found in the literature. Therefore, surfaces with temperatures $T \geq 150$ K are assumed to have no pumping capability ($\alpha = 0$) and surfaces with $T < 150$ K are assumed to have maximum pumping probability ($\alpha = 1$)¹.
- **Mean sojourn time:** Once a particle sticks on a surface it stays there for a certain time, with a mean sojourn time τ . The desorption probability over time

¹In order to investigate the impact of this assumption, simulations have been performed with $\alpha = 0$ for all WGTS facets. The results for the final gas distribution do not deviate significantly from the $\alpha = 1$ case. Far more important than the choice of α are the free diffusion in the beam line and the CPS cold trap pumping. The value of the WGTS sticking coefficient is considered to be of minor importance since the particles desorb again after a rather short sojourn time in contrast to the CPS cold trap where they stick permanently.

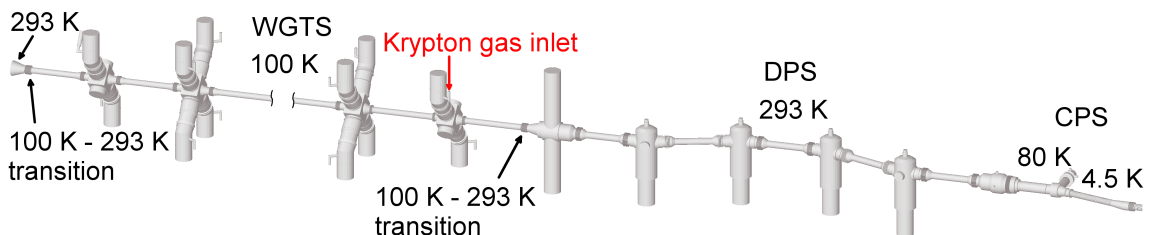


Figure 4.2: MolFlow+ beam line geometry model for krypton gas flow simulations. The surface mesh of the STS beam line is shown together with the respective temperature regimes. The simulation starts at the gas inlet marked in red and extends up to the CPS where the krypton is pumped with 100% efficiency at the 4.5 K cold trap.

follows an exponential law, similar to radioactive decays. The mean sojourn time τ is given by $\tau(T) = \tau_0 \exp(E_{\text{des}}/(RT))$ with $\tau_0 = 10^{-13}$ s, the desorption energy E_{des} , the ideal gas constant R and the temperature T [Jou18]. Values of $E_{\text{des}} = 18.0$ kJ/mole for krypton sticking on gold [WABHS75] and $E_{\text{des}} = 16.15$ kJ/mole for krypton sticking on stainless steel [TW71] were found. With these values mean sojourn times of $\tau(\text{WGTS}, 100 \text{ K}) = 2.7 \times 10^{-5}$ s and $\tau(\text{CPS}, 80 \text{ K}) = 5.7 \times 10^{-2}$ s are calculated and assigned to the corresponding facets². The mean sojourn time on the CPS cold trap is set to $\tau(\text{CPS}, 4.5 \text{ K}) = \infty$.

In addition to these facet parameters also the gas particle properties have to be defined. The half-life time of $^{83\text{m}}\text{Kr}$ atoms is set to $T_{1/2} = 1.83$ h and the mass to $m = 82.914$ g mol⁻¹ [AW93]. The simulation is started by desorbing test particles from a facet of the final downstream WGTS pump port at the location marked in Fig. 4.2.

4.3.3 Results

The simulation was mostly carried out on a 128 Gigabyte RAM server using 16 cores in parallel for several weeks. On average, a krypton particle will hit the beam line facets around 62000 times before it either decays or is pumped in the CPS, which is why the simulation is rather CPU-intensive.

The final results for the most important numbers are given in Tab. 4.2. In section 4.5 the longitudinal decay distribution is graphically shown in Fig. 4.4 (blue histogram). The majority of 98% of the krypton atoms are pumped by the CPS cold trap. Only 1.6% decay inside the beam line volume. From these around 80% take place

²These values are not expected to be precisely correct for the simulation scenario. However, as explained before the impact on the final result of the krypton beam line distribution is considered minor compared to more important boundary conditions like the CPS cold trap pumping.

Table 4.2: MolFlow+ simulation results for the krypton July 2017 campaign.

Shown are the most important absolute and relative numbers. A systematic uncertainty arises from leaks in the MolFlow+ mesh. After a particle track passes a leak it is terminated and does not contribute to the decay or pumping statistic. It can be seen from the numbers that this is an effect on the per mill level.

Parameter	Notation	Simulated number in units of 10^6
Particles started	N_{start}	9.12
Particle facet hits	N_{hit}	5.65×10^5
Particles pumped in CPS	N_{CPS}	8.94 (= 98% · N_{start})
Particle beam line decays	N_{BLD}	0.142 (= 1.6% · N_{start})
Particles escaped through leaks in geometry	N_{leak}	0.0356 (= 0.4% · N_{start})
Particle decays in WGTS beam line	$N_{\text{BLD}}^{\text{WGTS}}$	0.113 (= 80% · N_{BLD})
Particle decays in DPS beam line	$N_{\text{BLD}}^{\text{DPS}}$	0.0288 (= 20% · N_{BLD})
Particle decays in CPS beam line	$N_{\text{BLD}}^{\text{CPS}}$	0.000206 (= 0.1% · N_{BLD})

in the WGTS and 20% in the DPS, which leads to a beam line decay ratio of $N_{\text{BLD}}^{\text{WGTS}}/N_{\text{BLD}}^{\text{DPS}} = 4$. However, this ratio can not be measured directly in KATRIN. Only the decays located inside the volume of the sensitive magnetic flux tube can be assessed in a FPD rate measurement. Furthermore, in order to differentiate between DPS and WGTS decays, the only possibility is to use the DPS dipole electrodes. These can be operated at a certain negative voltage which allows to shift the energy of conversion electrons born inside this potential above the undisturbed krypton line originating from grounded beam line elements. So, simulations for both the sensitive magnetic flux tube and the DPS dipole electrode potential distribution are required. Those can then be combined with the MolFlow+ decay distribution.

4.4 Electromagnetic field simulations

The simulation of the 134 T cm^2 flux tube size is done with KASSIOPEIA. Twelve test particles are tracked along the magnetic field lines through the complete KATRIN setup starting at the outer edge of the twelve outermost FPD pixels and ending at the rear side of the WGTS. At each tracking step the x -, y - and z -position and the magnetic flux density B is determined. The cyclotron motion of electrons is not implemented so these positions are equivalent to the outer rim positions of the magnetic flux tube. All magnet currents are set to 70% of their nominal design values. The RS magnet is not implemented since it was not in place for the krypton campaign. The results for the magnetic field line tracks can be seen in Fig. 4.3. In addition, a second tracking simulation is performed with 148 magnetic field lines starting in the center of the 148 FPD pixels. This gives more precise information about the magnetic field B at every decay position, which is used later to calculate the pitch angles θ of decay electrons.

The DPS dipole electrode potential distribution is simulated with the KEMField

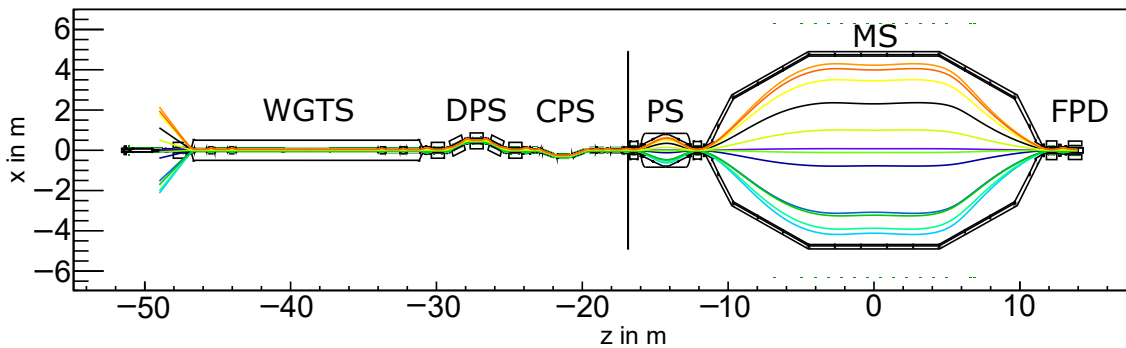


Figure 4.3: KASSIOPEIA simulation results for the outermost field lines of the sensitive magnetic flux tube mapped onto the FPD in the July 2017 krypton campaign. Shown is a top view on the x - z -coordinates of twelve magnetic field line tracks along the complete KATRIN setup. As defined in chapter 2.3, the x - and z -axis are horizontally aligned pointing in west and north direction, respectively. The field lines represent the outer rim of the sensitive magnetic flux tube. Each line starts at the outer edge of one of the twelve outermost FPD pixels and is tracked until the rear part of the WGTS. There, the field lines expand because the RS magnet was not installed back in July 2017.

module. As already described in section 2.3.3, four dipole electrodes are operated in the DPS beam line sections 1-4 and two ring electrodes in beam line section 5 and pump port 5. In the simulation the two half-shells of the electric dipole elements are set to -350 V. The ring electrode in beam line element 5 is set to $+250$ V while the pump port 5 ring electrode is not included. Beam line and pump port elements are set to 0 V as they are grounded in the setup. From this configuration a charge density map for the DPS is calculated by KEMField. Based on this map the electric potential at all locations inside the beam line can be calculated analytically. The results are given in the next section.

4.5 Combination of simulation results

The blue histogram in Fig. 4.4 represents the longitudinal decay distribution inside the beam line vacuum as simulated with MolFlow+. It features some characteristic peaks occurring at certain z -positions. These are the pump port locations in the beam line where the krypton gas expands due to the larger volume compared to the more narrow beam tube elements. Closer to the CPS the number of decays decreases significantly.

In a next step, this distribution has to be combined with the magnetic flux tube distribution obtained by the corresponding KASSIOPEIA simulation. Decays located outside of the 134 T cm^2 flux tube are rejected and only the ones located inside are considered for further analysis. The result of this selection is that only 23.6×10^3 decays take place inside the sensitive magnetic flux tube volume, which equals 0.26% of all simulated particles and 16.6% of all beam line decays. This affects the longitudinal decay distribution significantly as can be seen from the orange histogram in Fig. 4.4. Since the flux tube widens in the pump port regions due to the lower magnetic field the characteristic peaks are still present although their amplitude is considerably smaller.

However, this is still not the true distribution measured by the FPD. Some of the decay electrons are reflected on their way to the detector due to the magnetic mirror effect once their pitch angle θ is larger than the maximum acceptance angle θ_{\max} (cf. section 2.1.1). Using the results of the second KASSIOPEIA simulation with 148 field lines, the pitch angle can be calculated for all locations a conversion electron is born in. The probability of this electron to reach the FPD from a location \vec{x} without getting reflected magnetically is given by

$$P(\vec{x}) = \frac{1 - \cos(\theta_{\max}(\vec{x}))}{2} = \frac{1 - \cos\left(\arcsin\left(\sqrt{\frac{B(\vec{x})}{B_{\max}(\vec{x})}}\right)\right)}{2}. \quad (4.2)$$

Here, $\theta_{\max}(\vec{x})$ is the maximum acceptance angle (cf. Eq. 2.6), $B(\vec{x})$ is the magnetic flux density at the decay location \vec{x} and $B_{\max}(\vec{x})$ is the maximum magnetic field along the corresponding magnetic field line. In order to assess the krypton decay distribution actually measured by the FPD, the probabilities $P(\vec{x})$ can be used as weighting factors resulting in the green histogram in Fig. 4.4. After all, the peaks are compensated by the magnetic mirror effect. Most of the decay electrons originate from the WGTS, but also the DPS and the first part of the CPS contribute.

In a last step, these results have to be combined with the KEMField generated electric potential map for the DPS dipole electrodes when operated in monopole

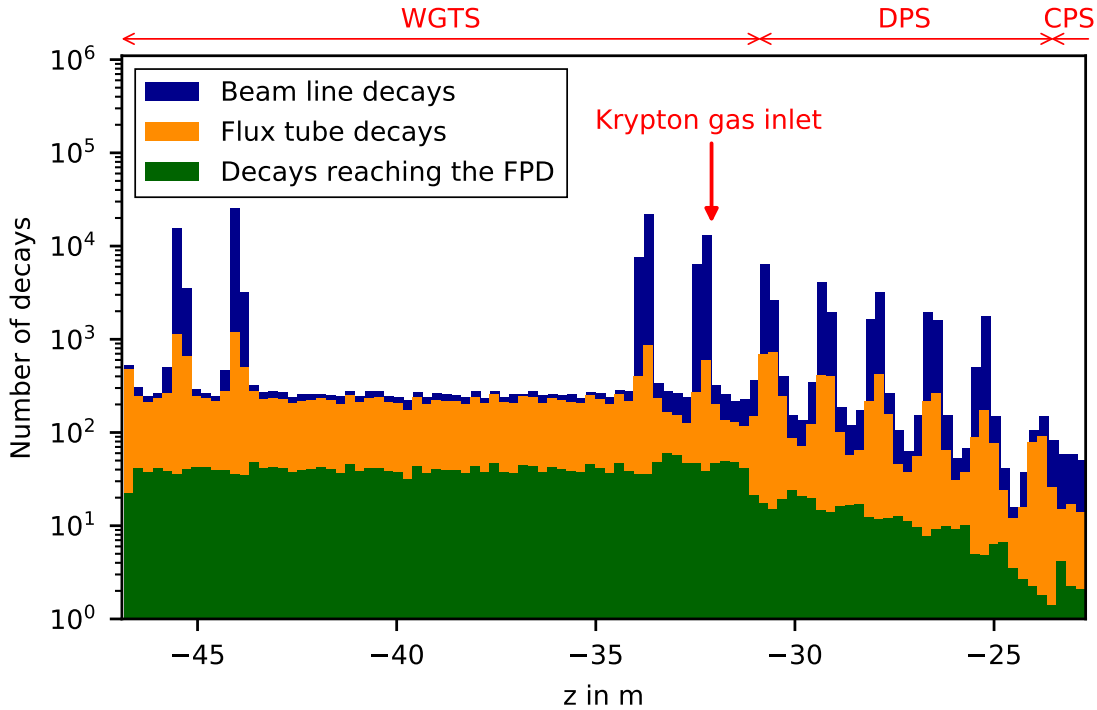


Figure 4.4: Simulated longitudinal distributions of $^{83\text{m}}\text{Kr}$ decays in the July 2017 campaign. The blue histogram illustrates the beam line decay distribution as simulated with MolFlow+. Decays located inside of the sensitive magnetic flux tube volume are represented by the orange histogram. Each peak can be assigned to a pump port with one exception at $z < 46.6$ m where the missing RS magnet is responsible for the excess. A weighting of the orange colored histogram with the transmission probability $P(\vec{x})$ for electrons created at \vec{x} results in the green distribution. This is the distribution of electrons contributing to a count rate measurement at the FPD. The z -values are given in KATRIN coordinates with the origin in the center of the MS analyzing plane.

mode at -350 V. At each decay position inside the sensitive magnetic flux tube the electric potential is calculated and plotted in Fig. 4.5 for the DPS. Obviously, for electrons to be affected by an energy shift strongly depends on their starting position. If they are emitted from inside the dipole electrodes, they are maximally shifted. On the other hand, the effect is minimal inside the beam line pump ports. The potential distribution is rather broad. Consequently, the electron energies are not shifted by exactly 350 eV but by a broad range of energies below 347 eV, the highest absolute potential value inside the sensitive magnetic flux tube according to the simulation.

4.6 Comparison to the measurement

In July 2017 the krypton spectrum was measured by the integrating MS filter. When measuring a specific line, the absolute MS electric retarding potential is first set above the line energy and is then reduced step-wise. At each step the FPD count rate is measured for a certain time at a stable retarding potential. During such a step-wise scan the count rate rises steeply as more and more electrons can overcome

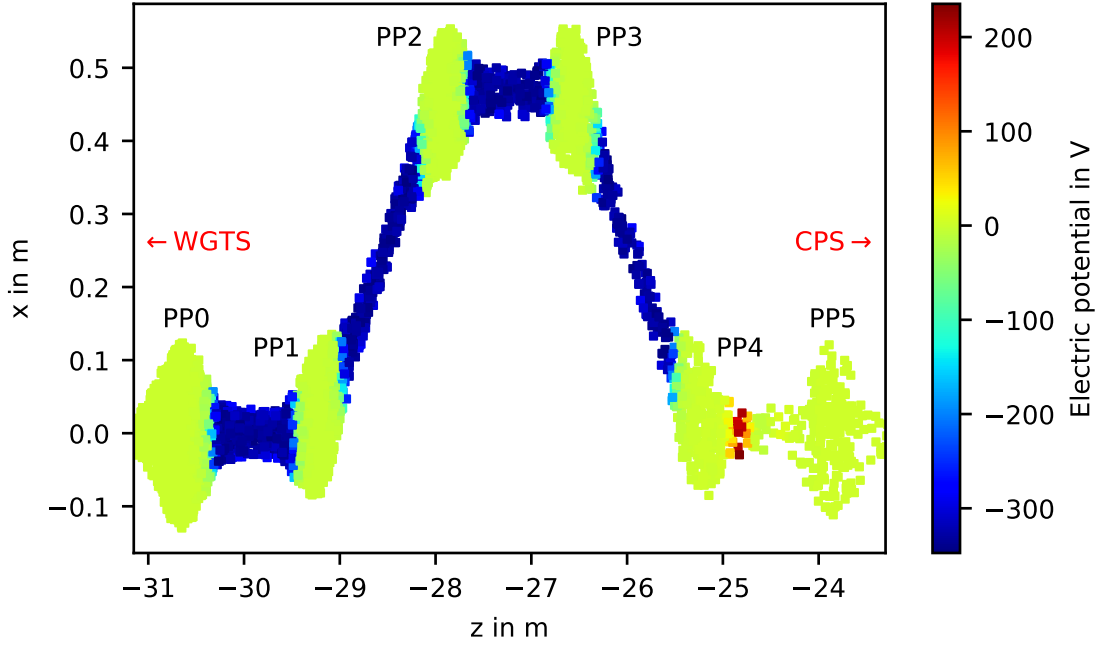


Figure 4.5: Simulated electric potential distribution at the DPS $^{83\text{m}}\text{Kr}$ decay locations for all four dipole electrodes operated in monopole mode at $U = -350$ V. Only decay locations within the 134 T cm^2 flux tube are considered. Inside the beam line pump ports PP0-5 the potential decreases to 0. In between the four dipole electrodes are operated. In the last beam line element the ring electrode is operated at $+250$ V. The z -values are given in KATRIN coordinates with the origin in the center of the MS analyzing plane. As the z -values increase towards the CPS the number of decays drops, which can be seen from the lower density of data points.

the filter potential. A plateau is reached when the line scan is completed. The differential line shape can be modeled by a Lorentzian function [AAB⁺19b]

$$L(E) = A/\pi \frac{\Gamma/2}{(E - E_{\text{mean}})^2 + \Gamma^2/4}. \quad (4.3)$$

Here, E is the energy, A is the amplitude, E_{mean} is the line position in energy and Γ is the full width at half maximum. Both the unshifted and the shifted L_3 -32 line were measured separately.

In case of the unshifted line the MS high voltage scan range has a lower absolute limit of $U_{\text{low}} = 30\,465.3$ V and an upper absolute limit of $U_{\text{high}} = 30\,480.4$ V. As for the shifted L_3 -32 line, the electrons experience a broad range of energy shifts leading to a line broadening of several tens of eV. However, the scan range is restricted because the L_2 -32 line is located 52.7 ± 0.7 eV below the L_3 -32 line (cf. Tab. 4.1). In order to avoid an interference, the analysis of the measured data is constrained to a voltage interval in between the absolute limits $U'_{\text{low}} = 30\,769.7$ V and $U'_{\text{high}} = 30\,820.9$ V. The ratio R_{meas} of the unshifted to the shifted L_3 -32 line can be calculated from the measured integral count rates N_{meas} via

$$R_{\text{meas}} = \frac{N_{\text{meas}}^{\text{L}_3-32}(U_{\text{low}}) - N_{\text{meas}}^{\text{L}_3-32}(U_{\text{high}})}{N_{\text{meas}}^{\text{L}_3-32}(U'_{\text{low}}) - N_{\text{meas}}^{\text{L}_3-32}(U'_{\text{high}})}. \quad (4.4)$$

The output of the simulation has to be treated in a way that it is comparable with this result. In a first step, the simulated electric potential distribution from Fig. 4.5 has to be weighted with the transmission probability stated in Eq. 4.2. Then, the resulting distribution $N(E_{\text{pot}})$ is convolved with the Lorentzian L_3 -32 line profile $L(E)$ from Eq. 4.3 according to

$$N_{\text{sim}}^{\text{L}_3-32}(E) = N(E_{\text{pot}}) \otimes L(E) = \int_{-\infty}^{\infty} N(\epsilon)L(E - \epsilon)d\epsilon. \quad (4.5)$$

Here, $L(E)$ is parametrized with $E_{\text{mean}} = 30\,472.6$ eV and $\Gamma = 1.15$ eV [AAB⁺19b]. The amplitude A is irrelevant since it cancels out in the final ratio result. A modified energy distribution $N_{\text{sim}}^{\text{L}_3-32}(E)$ is obtained by this convolution. It can be compared to the actually measured distribution by extracting R_{sim} via integrating the number of simulated events per energy $N_{\text{sim}}^{\text{L}_3-32}(E)$ over the respective voltage ranges:

$$R_{\text{sim}} = \frac{\int_{U_{\text{low}}}^{U_{\text{high}}} N_{\text{sim}}^{\text{L}_3-32}(eU)dU}{\int_{U'_{\text{low}}}^{U'_{\text{high}}} N_{\text{sim}}^{\text{L}_3-32}(eU)dU}. \quad (4.6)$$

The results for the measured and the simulated ratio are³

$$\begin{aligned} R_{\text{meas}} &= 14.6 \pm 0.5, \\ R_{\text{sim}} &= 15.2 \pm 0.6. \end{aligned} \quad (4.7)$$

Both results are comparable within their uncertainties which are purely statistical. As for the simulation, the uncertainty is estimated using the bootstrapping method. Decay events for calculating R_{sim} are randomly sampled from the basic population. The sample standard deviation of the resulting R_{sim} distribution is equal to the statistical uncertainty.

4.7 Summary

The July 2017 krypton commissioning campaign was a major milestone for the KATRIN experiment. It was one of the first steps on a path towards regular krypton measurements to characterize the tritium plasma. The setup was operated in a quite different hardware configuration than the one used for the neutrino mass measurement. These special conditions have been implemented into a vacuum and electromagnetic field model, which have allowed to simulate the effective spatial distribution of krypton decays. The results agree with the experimentally obtained data, which supports the correctness of the underlying models. Systematic uncertainties of the simulation arise from the unknown parameters of krypton-surface interaction in UHV and any deviation between built-in and true beam line geometry, which should prevent a perfect agreement between simulated and measured data on the level of a few percent or lower.

³The numbers slightly differ from the ones published in [ABB⁺18a] since the analysis has been refined since then.

5. Minimization of ion-induced background for neutrino mass measurements

Following the objectives defined in section 3.3, the minimization of the ion-induced background count rate will be pursued in this chapter. Two superior goals have to be achieved. First, tritium ions have to be stopped from entering the spectrometer and detector section during nominal operation of the KATRIN experiment. This has to be guaranteed over the entire duration of a measurement campaign which can be up to three months. Optimum operational settings for ion blocking electrodes have to be found and the effectiveness of ion retention has to be verified by performing high-sensitivity measurements of the residual ion flux into the PS. Second, the systematic background contribution of tritium decaying inside the volume of the negatively biased DPS dipole electrodes has to be determined.

Measurement results of the three different measurement campaigns STSIIIa, KNM1 and KNM2 (cf. section 3.2) will be presented. All measurements have been planned and executed as a part of the KATRIN ion team consisting of F. Glück, A. P. Vizcaya Hernández, M. Klein and M. Schlösser. It will be denoted whenever an explicit contribution from one of them is depicted in the text. Also, the calibration in section 5.2.4 has been done over the course of the bachelor thesis by E. Weiss¹ who was supervised by the author.

The creation processes and systematic effects induced by tritium ions were already described in chapter 3 (see sections 3.1.1 to 3.1.4). This chapter is subdivided into an introductory part in section 5.1 where the beam line instrumentation is described in detail and the two sections 5.2 and 5.3 describing the insights gained from measurements with deuterium and tritium ions, respectively. As one of the main results, optimum ring electrode voltage settings - which will presumably be applied over the entire KATRIN live-time - are stated in section 5.3.5. At these settings it was verified that the residual ion flux into the PS during long-term nominal operation is

¹E. Weiss, Determination of the Ion Conversion to Electron efficiency of the KATRIN Pre-Spectrometer, bachelor's thesis, Karlsruher Institut für Technologie (KIT), 2019.

well below the required upper limit, as will be presented in section 5.3.6.

5.1 Beam line instrumentation

The instrumentation for tritium ion handling and diagnostics consists of two types of beam line electrodes as well as of various detection devices for a direct measurement of the tritium ion flux in real-time.

5.1.1 Beam line electrodes

Tritium ions have to be prevented from entering the PS so as to minimize their contribution to the background of the neutrino mass measurement. A maximum flux of $\phi_{\text{CPS} \rightarrow \text{PS}} = 1 \times 10^4 \text{ T}_3^+$ ions/s (cf. Eq. 3.9) into the PS must not be exceeded in order to restrict the ion-induced MS background rate to below 0.1 mcps. For this reason, ring electrodes are operated at a positive DC bias voltage so that positive tritium ions are blocked electrostatically.

Ring electrodes

In total, five ring electrodes are mounted in the beam line, but only three of them are located upstream of the PS where they can be used for blocking ions from entering the SDS. In this thesis the ring electrodes are referred to as DPSa, DPSb and PS1. Important parameters of these electrodes can be found in Tab. 5.1. Also, engineering drawings are displayed in Fig. 5.1 together with the locations in the KATRIN beam line.

DPSa and DPSb are placed in the most downstream DPS beam line element and inside DPS pump port 5, respectively. PS1 is mounted inside the warm bore of the superconducting solenoid magnet upstream from the PS. The ring electrodes are not built as rings but as stainless steel cylinders. These cylinders are split at one spot in order to prevent magnetic induction of circular currents in case of a magnet quench. All ring electrodes are fed by iseg[®] DPr 05 106 24 5_SHV-THQ-EPU power supplies, which provide a voltage of up to 500 V with a maximum peak-to-peak noise of 7 mV according to the data sheet. Both positive and negative voltages can be applied. In the DPS low-pass filters remove high-frequency noise. They are installed in between the power supplies and the ring electrodes. Redundant connections equipped with low-pass filters are used to monitor the working voltages with Knick Elektronische Messgeräte[®] VariTrans P29000P2/00 isolating amplifiers. The low-pass filters in these redundant cables lead to a reduction of the effective ring electrode voltage to $(81 \pm 4)\%$ [Kle19] of the set value at the iseg[®] power supply.

The blocking principle may appear straightforward in the first place, but some difficulties arise from the fact that the ring electrodes act as a Penning trap for low-energy electrons (see section 5.2.1). In order to find the optimum values for the operating bias voltages, these effects are investigated both with deuterium (see sections 5.2.1 and 5.2.2, and the forthcoming doctoral thesis of A. P. Vizcaya Hernández [VH] for details) and tritium ions (see section 5.3.2). Ultimately, optimum voltage set points are found and stated in section 5.3.5.

Dipole electrodes

After a positive ion gets reflected at the potential hill of a ring electrode it travels back upstream into the WGTS along the magnetic field lines. There, it scatters

Table 5.1: Overview of important parameters of the ring electrodes DPSa, DPSb and PS1. Shown are the beam line location, width, inner radius and the effective fraction of the potential in the center of the electrode ($x = y = 0$) compared to the applied voltage on the metal ring.

Ring electrode	DPSa	DPSb	PS1
Location	DPS beam tube 5	DPS PP5	PS entrance
Length	60 mm	60 mm	50 mm
Inner radius	45 mm	143.5 mm	82 mm
Potential fraction in center [Kle19]	84%	40%	46.5%

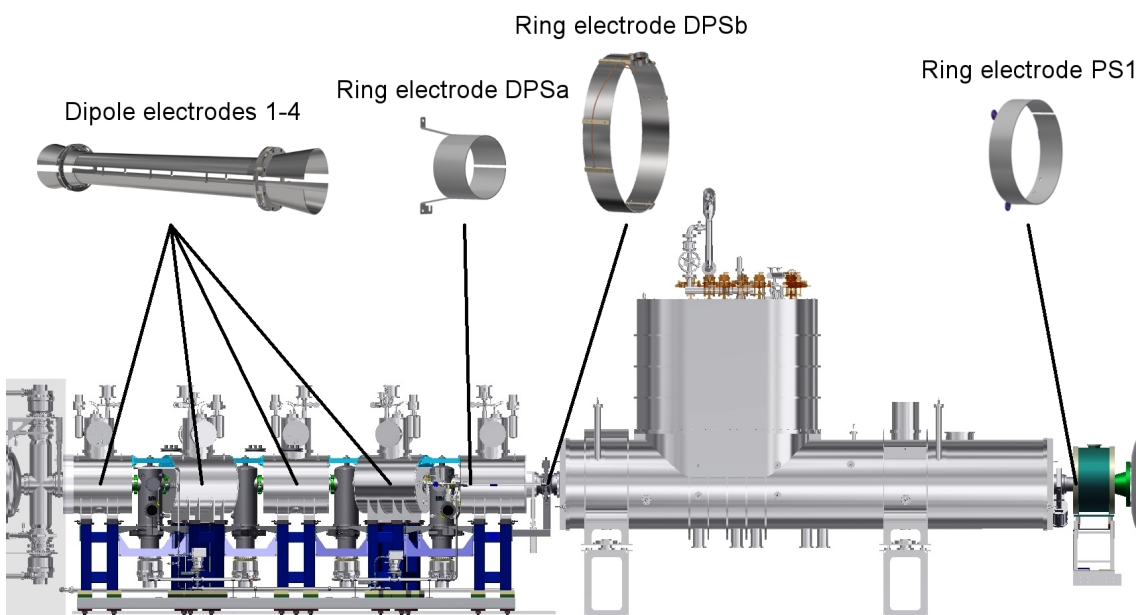


Figure 5.1: Locations of the beam line electrodes for tritium ion blocking and removing. From left to right: The four dipole electrodes each consist of two half-shells located inside the first four beam tube elements of the DPS. Six small lobes are attached to one of the two electrode halves (the one set on the higher absolute bias voltage). Positive ions are drifted via $E \times B$ drift until they neutralize at one of these lobes. In the fifth and last DPS beam tube section, the smallest ring electrode DPSa is installed. DPSb and PS1 are mounted in PP5 and inside the warm bore of the superconducting magnet in between CPS and PS, respectively.

multiple times with the molecules of the gas column until it is reflected back in the downstream direction of the gas flow. Effectively, the ion is trapped between the blocking electrode and the WGTS gas column, traveling back and forth. New ions are continuously created and contribute to the amount of trapped particles, which are only slowly removed by recombination with secondary electrons. Without any intervention, a large positive space charge would build up, leading to a higher tritium plasma density possibly giving rise to plasma instabilities. Furthermore, negative tritium ions are not retained by the positive blocking potentials in the first place. In order to solve these two problems, four identically constructed dipole electrodes are operated in the beam line sections 1 to 4 of the DPS. However, the fourth

one is currently operated as a blocking electrode like the ring electrodes, because this provides the unique opportunity to block with a dipole field which cannot be neutralized over time by accumulation of low-energy electrons inside. This effect of neutralization will be discussed more elaborately in section 5.3.3. Furthermore, the positive dipole field removes secondary electrons potentially stored between the DPS and PS negative potentials. Otherwise, those electrons might contribute to the neutralization process.

An engineering drawing of all four dipole electrodes can be found in Fig. 5.1. They consist of two stainless steel half-shells. On each half-shell a bias voltage can be applied via an iseg[®] DPr 05 106 24 5_SHV-THQ-EPU power supply. Similar to the ring electrodes, low-pass filters are interconnected to filter high-frequency ripples. As for the dipole electrodes 1 to 3, both half-shells are operated at a negative polarity in order to block negative ions and drift positive ones via an $E \times B$ drift.

The $E \times B$ drift process of a charged particle follows from the laws of classical electrodynamics [Jac06] in the special configuration of orthogonal electric (E) and magnetic (B) fields. In addition to the helix-like cyclotron motion, the particle experiences a perpendicular motion with velocity [Jac06]

$$\vec{v} = \frac{\vec{E} \times \vec{B}}{B^2}. \quad (5.1)$$

In a negatively biased DPS dipole electrode the top half-shell is set on a higher absolute potential than the lower half-shell. Thus, the electric field points upwards in positive y -direction while the magnetic field points in negative z -direction². Positive ions are consequently drifted towards the beam tube surface in negative x -direction. They can leave the dipole element radially by moving through the gap in between both half-shells. Outside the dipole electrode tube the drift direction is reversed. Either the ions hit some obstacle in the beam tube and are neutralized there, or they are drifted around the top half-shell and re-enter the interior of the dipole electrode on the opposite side.

In order to make sure that the ions are removed rigorously, 6 mm broad lobes are welded to the top half-shell. Those can be seen in the dipole electrode engineering drawing in Fig. 5.1. In total, six lobes are attached. By chance, an ion will hit one of the lobes during the radial drift movement. In this case the ion is neutralized which induces a current. At the fourth dipole electrode negative particles are drifted instead of positive ions, but the principle is the same. Four identical 9103 picoammeters from RBD instruments[®] are used for measuring the neutralization current at each dipole element. Each is interconnected between the power supply and the lobe carrying half-shell.

The ion removal currents of the dipole elements 1 to 3 are important observables measured in-situ during neutrino mass runs. A monitoring of the voltage applied to the electrode would influence the trueness of the current measurement. Therefore, only the power supply output voltage is monitored, not the voltage at the electrode itself which would require an isolating amplifier at a redundant cable connection, like at the ring electrodes.

The drifting ions hit one of the lobes only by chance, not inevitably. It might happen that their drift distance in between two consecutive lobes is larger than the lobe width. Then they are eventually neutralized at a connecting part or a cable within

²The KATRIN coordinate system was described in section 2.3.

the beam tube, not at the lobe surface. A measured current value can therefore not be translated directly into the total number of positive ions removed from the system. The larger the dipole field, the bigger the deviation between both numbers will be.

Another reason to keep the absolute bias voltages applied to the dipole electrodes 1 to 3 rather low is the effect of background counts originating from tritium molecules decaying inside these dipole elements, as described in section 3.1.3. In [Kle19] upper limits for each dipole element have been derived theoretically in order to constrain the impact on the neutrino mass sensitivity to an acceptable level. These maximum values are $(-5\text{ V}/-15\text{ V})$, $(-5\text{ V}/-35\text{ V})$ and $(-5\text{ V}/-85\text{ V})$ for dipole electrodes 1, 2 and 3, respectively. The first number denotes the lower and the second number the upper half-shell voltage. These voltages were applied both in the KNM1 and KNM2 measurement campaigns to the first three dipole electrodes. Measurement results for the background count rate in this configuration are stated in section 5.3.4. Dipole element number 4 is operated at opposite polarity with voltage settings $(+25\text{ V}/+20\text{ V})$.

5.1.2 Ion detection methods inside the spectrometer and detector section

In section 3.1.3 the disruptive nature of a tritium ion flux into the PS on the targeted neutrino mass sensitivity was described. Therefore, several techniques for ion detection are available. First and foremost, these techniques are used for in-situ verification that the ion flux into the PS is minimal. Moreover, they can also be used to obtain the source ion energy spectrum and to investigate the blocking electrode performance during neutrino mass or commissioning campaigns.

- **Pre-spectrometer current measurement:** The current measurement at the PS downstream cone electrode is a real-time monitoring method developed in order to take data continuously during neutrino mass measurements. However, due to different systematic effects and a rather high electronic noise, the sensitivity for short-term measurements on the time scale of seconds or minutes is rather low. The Gaussian dispersion of the current values exhibits a standard deviation on the order of $\sigma \approx 1\text{ pA}$ which is far above the required sensitivity for measuring currents of $\sim 1\text{ fA}$ corresponding to the quoted upper limit of 1×10^4 ions/s into the PS.
- **Ion conversion to electrons:** A much faster approach with a more than one order of magnitude higher sensitivity is the ion conversion to electrons (ICE) process in the PS. On the other hand, ICE has the drawback to require a special high voltage setting which makes it impossible to make use of the ICE method during neutrino mass runs at nominal settings.
- **PULCINELLA current measurement:** Both of the previous methods need calibration in order to assess absolute numbers for the ion flux from the measured data. The PULCINELLA picoammeter connected to the Ti-disk in the FPD setup (cf. section 2.3.7) is utilized in a calibration measurement for the ICE method.

Pre-spectrometer current measurement

In a neutrino mass run the pre-spectrometer is operated at a negative high voltage

of several kV (typically -10.5 kV) applied to various electrodes which can be seen in Fig. 5.2. With this setup it is possible to measure ion-induced current signals. Voltages can be applied to the UHV vessel U_{vessel} , the upstream cone electrode $U_{\text{cone,up}}$, the central wire electrode U_{wire} and the downstream cone electrode $U_{\text{cone,down}}$. During a neutrino mass run the voltages are $U_{\text{vessel}} = -10$ kV and $U_{\text{cone,up}}/U_{\text{wire}}/U_{\text{cone,down}} = -10.5$ kV/ -10.5 kV/ -10.5 kV (PS nominal setting)^{3,4}. Positive ions entering the PS are accelerated by these negative voltages and move non-adiabatically out of the magnetic flux tube towards the stainless steel UHV surfaces where they are neutralized. A subset of these ions hits the downstream cone electrode to which a Keithley[®] 6514 picoammeter is connected in combination with a low-pass filter for high-frequency noise filtering.

Monitoring the flux of radioactive ions at KATRIN is not only important for background minimization, but also necessary from the radiation protection point of view. A maximum flux of 2×10^8 T_3^+ ions/s from the CPS into the PS can be derived from the required exemption limit of 1 GBq [Kle19]. The Keithley[®] picoammeter read-out is used during operation of beam line valve V4 in between the CPS and

³The inner electrodes are operated at a 500 V more negative potential than the vessel because of two reasons. At first, the sensitive magnetic flux tube is shielded from low-energy background electrons ejected from the vessel wall [FBD⁺11]. Furthermore, the ignition of a Penning discharge inside the PS is prevented.

⁴It was decided to apply these voltages at the beginning of KNM1 in order to decrease the depth of the PS-MS Penning trap [AAB⁺19a]. Before, the anticipated set values were $U_{\text{vessel}} = -17.8$ kV and $U_{\text{cone,up}}/U_{\text{wire}}/U_{\text{cone,down}} = -18.3$ kV/ -18.3 kV/ -18.3 kV.

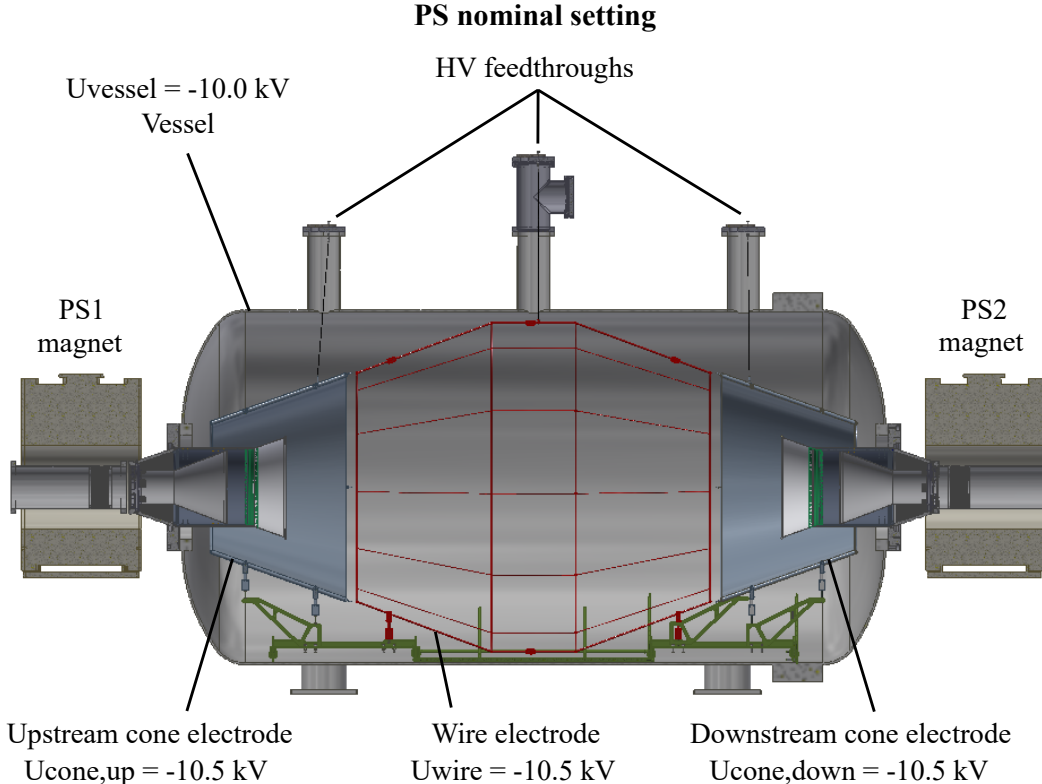


Figure 5.2: Engineering drawing of the pre-spectrometer inner electrode system in nominal setting during neutrino mass measurements in a half section view. The vessel and the three axially symmetric inner electrodes can each be set on an individual voltage.

PS. If a current threshold of 5 pA is exceeded for three consecutive measurements at a sampling rate of 1 s, the valve will be closed automatically [Kle19].

Every second a total of 14 current values are recorded, and the arithmetic mean and sample standard deviation are stored in the KATRIN data base. The data is recorded continuously over the years of operation, enabling in-situ monitoring of the flux of positive ions into the PS throughout the neutrino mass runs and in between. According to the data sheet of the Keithley® 6514 picoammeter, 3 fA is the minimal systematic uncertainty.

The sensitivity is worsened by several systematic effects, which were already observed in the first commissioning measurements [Kle19]. For a 1 s data sampling rate a Gaussian noise on the order of 1 pA is present. Furthermore, large spikes of unknown origin, ranging from several pA to up to 10^{37} A, occur randomly in time. This happens on a time scale of several minutes to hours in between two spikes. On top of that, the current data is strongly correlated to the temperature in the spectrometer hall, which is unstable on the level of ± 1 °C. This in turn leads to fluctuations of the current on the order of a few times ± 10 fA. This can be overcome by averaging over long enough time periods during which the temperature fluctuation averages out. These three systematic effects reduce the short-term sensitivity to roughly ~ 1 pA. However, on a time scale of hours, currents below 10 fA are measurable.

Besides these effects directly related to the current measurement itself, two more systematic effects influence the sensitivity on the estimate of ion flux from the CPS into the PS $\phi_{\text{CPS} \rightarrow \text{PS}}$ from the measured data.

- **Ion detection probability $C_{\text{cone,down}}$:** The first effect is that not all of the ions entering the PS actually hit the downstream cone electrode. The fraction of detected ions can be quantified by the calibration factor $C_{\text{cone,down}}$ linking the measured neutralization current $I_{\text{cone,down}}$ and the actual ion flux from the CPS into the PS $\phi_{\text{CPS} \rightarrow \text{PS}}$. Tracking simulations have been performed at a PS voltage setting of $U_{\text{vessel}} = -18.6$ kV and $U_{\text{cone,up}}/U_{\text{wire}}/U_{\text{cone,down}} = -19.1$ kV/ -19.05 kV/ -19.0 kV (PS ICE setting, see next paragraph "Ion conversion to electrons"). Two different simulation approaches yield $C_{\text{cone,down}} \approx 21\%$ (simulation with a self-developed C++ code by F. Glück) and $C_{\text{cone,down}} \approx 15\%$ (simulation with KASSIOPEIA by A. P. Vizcaya Hernández). The discrepancy could not be finally resolved, so the true value is estimated to be $C_{\text{cone,down}} \approx (18 \pm 3)\%$.
- **Secondary electron emission factor C_{see} :** Another calibration factor arises from the charge multiplication process at the stainless steel surface of the cone electrode. It is well known from literature (see e.g. [RB71]) that ions with keV energies bombarding a stainless steel surface eject secondary electrons, which leads to an amplification of the measured positive current. Again, a calibration factor C_{see} is necessary in order to take this secondary electron emission (see) effect into account.

From a measured current $I_{\text{cone,down}}$ ultimately the positive ion flux from the CPS into the PS $\phi_{\text{CPS} \rightarrow \text{PS}}$ can be calculated via

$$\phi_{\text{CPS} \rightarrow \text{PS}} = \frac{I_{\text{cone,down}}}{e \cdot C_{\text{cone,down}} \cdot C_{\text{see}}} \quad (5.2)$$

with the elementary charge e . The higher the product $C_{\text{cone,down}} \cdot C_{\text{see}}$ is, the higher is the sensitivity on $\phi_{\text{CPS} \rightarrow \text{PS}}$ because the same ion flux will produce a higher current signal.

Ion conversion to electrons

The ion conversion to electrons (ICE) method is a supplementary approach to measure $\phi_{\text{CPS} \rightarrow \text{PS}}$ with a high sensitivity over a period of a few seconds. The basic idea is that positive ions entering the PS will produce secondary electrons either by ionizing residual gas in the volume or via a surface-driven mechanism. Those secondary electrons can then be detected by the FPD. From the electron count rate the ion flux into the PS can be inferred.

This method requires special settings of the SDS components. The PS electrode system is operated at $U_{\text{vessel}} = -18.6 \text{ kV}$ and $U_{\text{cone,up}}/U_{\text{wire}}/U_{\text{cone,down}} = -19.1 \text{ kV}/-19.05 \text{ kV}/-19.0 \text{ kV}$ (PS ICE setting, see Fig. 5.3). Before this setting is applied, in order to provide stable measurement conditions, the PS vessel has to be "conditioned" for a few minutes at a higher absolute voltage of e.g. -25 kV . Without this preconditioning, the measured FPD count rate might be elevated for a time of several hours.

In order to provide an adiabatic transport of the ICE electrons to the FPD, the MS retarding voltage is put on a lower absolute value of -10 kV . Furthermore, the magnetic field in the analyzing plane is set to the highest possible value in a range between 1.1 mT to 1.45 mT by maximizing the currents at the MS air-coil system. From the measured FPD count rate R_{ICE} the positive ion flux into the PS $\phi_{\text{CPS} \rightarrow \text{PS}}$

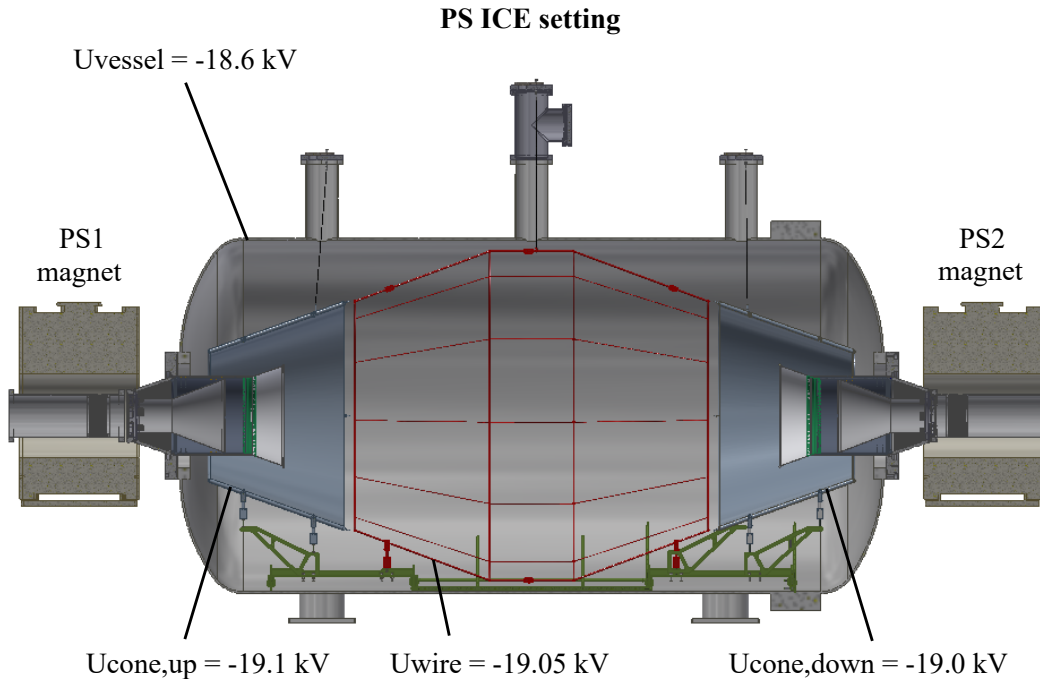


Figure 5.3: Engineering drawing of the pre-spectrometer inner electrode system in the ICE setting in a half section view. The absolute voltages applied to the inner electrodes are decreasing in downstream direction permitting secondary electron transport towards the FPD.

can be calculated via

$$\phi_{\text{CPS} \rightarrow \text{PS}} = \frac{R_{\text{ICE}}}{C_{\text{ICE}}}. \quad (5.3)$$

Again, an absolute calibration is necessary in order to determine C_{ICE} . The higher C_{ICE} , the higher is the sensitivity on the ion flux into the PS for a given FPD count rate. Comparing this approach to the PS cone current measurement described before, there are two advantages but also one drawback.

- As will be described later in sections 5.2.3 and 5.2.4, the ICE sensitivity obtained with deuterium ions is more than one order of magnitude higher.
- Also, the statistical uncertainty can be reduced to the limit of systematic uncertainties in much less time. It only takes a few seconds in the ICE mode to measure a flux $\phi_{\text{CPS} \rightarrow \text{PS}}$ on the level of 10^3 ions/s. This corresponds to a current of ~ 0.1 fA measured at the PS downstream cone electrode. As for the PS cone current, a time period ranging from minutes to hours is necessary to reach the maximum sensitivity.
- On the other hand, the ICE measurements require a special setting of the SDS part, so data taking is only possible in between neutrino mass runs whereas the PS current measurement provides results continuously.

PULCINELLA current measurement

The Ti-disk to which the PULCINELLA picoammeter is connected can be inserted into the beam line upstream of the FPD. In its final position it completely shadows the sensitive FPD area. In the context of this thesis it is used as a Faraday cup measuring the absolute current of deuterium ions for the determination of C_{ICE} in a dedicated STSIIIa calibration measurement described in section 5.2.4. For this special measurement both PS and MS have to be operated on a positive voltage so as to enable the transport of positive ions through the spectrometers. A positive bias voltage of about 100 V applied to the Ti-disk prohibits secondary electron emission. Thus, there are no charge multiplication effects and the measured current is identical to the absolute ion current. Technically, it was possible to measure absolute currents of up to 600 pA in the STSIIIa campaign.⁵

5.2 Advances in ion detection using deuterium ions

In the KATRIN STSIIIa campaign (cf. section 3.2) various calibration and commissioning measurements have been performed with inactive ions in order to characterize the ion blocking, removal and detection setup in preparation for the first neutrino mass measurement campaign KNM1. The use of inactive ions provides a unique opportunity to perform measurements without the risk of increasing the background in the spectrometer and detector section. Consequently, a high flux of ions into the PS can be permitted in the course of dedicated calibration measurements of the PS current and the ICE detection methods. Also, the STSIIIa measurements were the final opportunity for a test of the beam line ring and dipole electrode instrumentation before tritium operation at high column density. In contrast to nominal tritium operation, where tritium ions are self-created from β -decay and subsequent impact ionization by β -electrons (cf. section 3.1.1), in STSIIIa the ions were created in

⁵Personal correspondence with E. L. Martin, 2020.

a completely different way. Most important was the process of impact ionization by photoelectrons, which were generated at the rear wall and magnetically guided through the beam line. For each of the measurements described in this chapter it will be explicitly stated which ion source was used. Once created, the ions were transported within the 134 T cm^2 flux tube through the beam line.

In section 5.2.1 the three different STSIIIa ion creation routines are described. Some basic measurements with the ring and dipole electrodes are presented in section 5.2.2. The PS current and ICE ion detection methods were calibrated in dedicated measurements. The results can be found in the sections 5.2.3 and 5.2.4. Finally, the ICE measurement has been performed at different argon gas pressures (see section 5.2.5) yielding important insights about the underlying mechanism. A conclusion of the STSIIIa ion investigations can be found in section 5.2.6.

5.2.1 Creation of inactive ions

For the STSIIIa ion measurements three different procedures were utilized in order to create several different ion species.

- **Helium ions** were produced inside the MS at the beginning of the campaign in order to perform some basic tests of the beam line electrodes.
- **Deuterium ions** were created from the WGTS deuterium gas column.
- **Penning ions** both from deuterium and residual gas were created via the Penning mechanism at the DPS electrodes.

Helium ion creation inside the Main Spectrometer

A Light Hammer 6 Mark II irradiation system from Heraeus Noblelight[®] mounted at the downstream end of the MS was used to illuminate a part of the inner MS vessel surface with high-intensity UV light (for details see [Bae17]). Photoelectrons were produced and emitted from the surface while simultaneously a continuous flux of gaseous helium was introduced into the vessel. The MS air-coil system was operated at a special setting in order to guide photoelectrons into the volume where they created He^+ ions via impact ionization. A positive voltage of a few tens of V was applied to the MS inner electrode system to drive the He^+ ions out of the spectrometer while the PS voltage was reduced to 0 V. The MS vessel itself was set on a negative voltage in order to accelerate the photoelectrons into the volume for subsequent ionization.

At a MS helium gas pressure on the order of 10^{-8} mbar a He^+ rate of the level of 10^9 ions/s was achieved. This was determined by dedicated PS downstream cone electrode current measurements at a special PS electrode setting.

Deuterium ion creation inside the WGTS

At the other end of KATRIN - the rear section - two MiniZ UV lamps from RBD instruments[®] were utilized for creation of photoelectrons by illuminating the RW disk. In one exceptional case, instead of the MiniZ lamps, a light fiber normally mounted at the e-gun was used for illumination (see section 5.2.2). The RW bias voltage was set to a negative polarity in order to accelerate the photoelectrons away from the RW towards the WGTS. In this configuration a photocurrent on the order of 40 nA was measured which corresponds to around 2×10^{11} photoelectrons/s. In

order to alter the number of created ions, the cross section of $e^- - \text{D}_2$ scattering could be controlled via changing the RW bias voltage. D_2 gas with small traces of HD and H_2 was circulated in the loop system providing a highly-stable column density inside the WGTS. Photoelectrons were used to ionize the gas, producing D_2^+ and D^+ via impact ionization and molecular dissociation (cf. section 3.1.1), respectively. During ion investigations the deuterium column density was kept constant at about 1×10^{15} molecules/cm², which corresponds to 0.2% of the design column density at nominal tritium operation.⁶

Penning ion creation in beam line electrodes

Some of the photoelectrons traverse the WGTS gas column and find their way up to the DPS where the D_2 pressure is reduced by several orders of magnitude compared to the WGTS center. If deuterium gas particles are ionized in the environment of a positively biased dipole or ring electrode, the secondary electrons might be trapped inside the electrode potential. This is because a positive potential in combination with the magnetic guiding field acts as a Penning trap for low-energy electrons. These electrons gain energy by moving deeper into the trap and they lose energy by ionizing deuterium gas. This leads to a cascaded production of secondary electrons trapped in the potential well.

In each interaction a deuterium ion is produced and accelerated out of the trap. The ion's energy corresponds to the Penning trap depth i.e. to the applied electrode voltage. This allows to adjust the energy according to the requirements of the individual measurement.

Also, the rate of produced Penning ions increases with the voltage as can be seen in Fig. 5.4. Two cases for Penning ion creation at the first DPS dipole electrode are shown. In both settings the dipole electrode is operated in monopole mode with equal voltage applied to its half-shells and the ions are detected with the ICE method. First, Penning ions are created from residual gas only (see Fig. 5.4a). The rate linearly depends on the applied voltage. In the second case, deuterium gas is circulated in the WGTS loop system. In this configuration, a stable D_2 gas column is maintained in the WGTS beam line extending up to the DPS dipole electrodes (see Fig. 5.4b). A higher order dependence between the rate and the voltage is established which is indicated by the parabolic fit. It should be noted that the obtained rates are much higher than with residual gas only.

An ultimate explanation for the observed rate-voltage dependencies can not be given as of now since it would require dedicated numerical simulations. For a cascaded production of particles in principle an exponential dependence is expected. However, the energy of a secondary electron available for further ionization decreases if it is created deeper in the potential well. Thus, the number of ionizations per secondary electron depends on the location where it is created, which could be a possible explanation for the observed lower order dependencies. Further, the different rate-voltage dependencies observed for residual gas and D_2 Penning ions could be due to the different types of target molecules, which exhibit different ionization cross sections and angular distributions of the scattered electrons.

In any case, using the Penning mechanism provides ions with a well-defined rate and energy for multiple commissioning measurements.

⁶Personal correspondence with A. Marsteller, 2020.

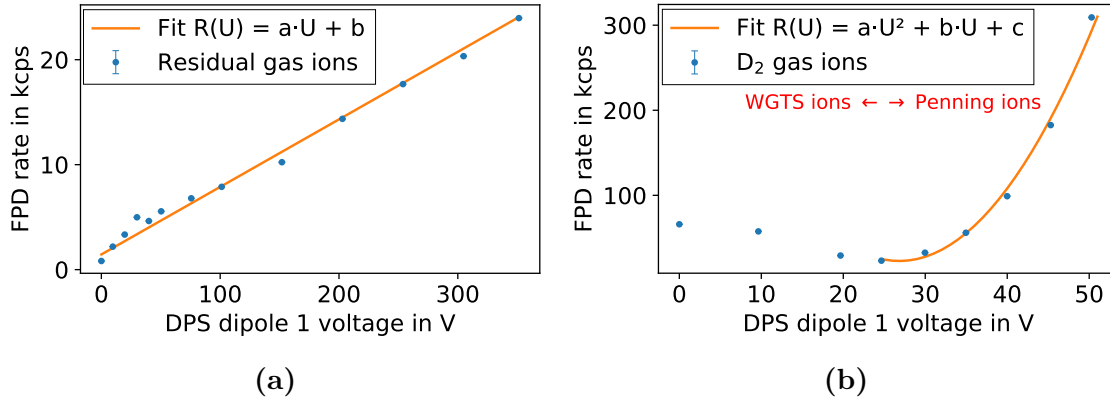


Figure 5.4: STSIIIa Penning ion creation at DPS dipole electrode 1. The Penning ion rate as measured by the ICE method versus the Penning trap voltage is shown. Dipole electrode 1 is operated in monopole mode at positive polarity for Penning ion creation. Another beam line electrode downstream of dipole electrode 1 is operated at negative polarity in order to prevent RW photoelectrons from reaching the PS. In (a) only residual gas is used. The ionization is done by photoelectrons emitted from the RW which is operated at $U_{RW} = -100$ V. In (b) a stable D_2 gas column is established in the beam line and the RW is put to $U_{RW} = -200$ V. Below a dipole electrode voltage of around 25 V the spectrum is dominated by deuterium ions originating from the WGTS gas column. For higher voltages the WGTS ions are blocked completely and the Penning ion spectrum appears.

5.2.2 Blocking with ring and dipole electrodes

For the KATRIN experiment, a proof-of-principle investigation of ion blocking was indispensable before nominal WGTS tritium operation could start. In fall 2018 it was especially critical because in the "first tritium" campaign, which was conducted about three months before STSIIIa, the DPS dipole electrode 2 had some technical issues and was not working properly [Kle19].

A STSIIIa proof-of-principle measurement with RW photoelectrons is shown in Fig. 5.5. The electrons were created via photoemission, induced by illuminating the RW inner surface with a light fiber borrowed from the egun setup. Thus, the light intensity is dominant in the RW center and does not cover the complete RW surface. A bias voltage of $U_{RW} \approx -71$ V accelerated them away from the rear section. There was no active loop circulation, so the beam line only contained residual gas which allowed an undisturbed transport of electrons through the complete KATRIN setup until they were detected by the FPD. Applying negative bias voltages to one of the beam line electrodes should repel the electrons leading to a drop of the FPD count rate. This was observed in three individual measurements each with a different electrode. The voltages of rings DPSa, DPSb and of the first dipole were ramped step-wise.

An intrinsic width of the measured transmission functions is observed due to the inhomogeneity of the effective potential inside the magnetic flux tube. Besides the different widths, also the absolute position differs although the energy of the blocked particle is the same in all three cases. This is most pronounced for DPSb where the applied voltage necessary for blocking is much higher than the actual electron energy. This can be attributed to its large dimensions (cf. Tab. 5.1), which lead to

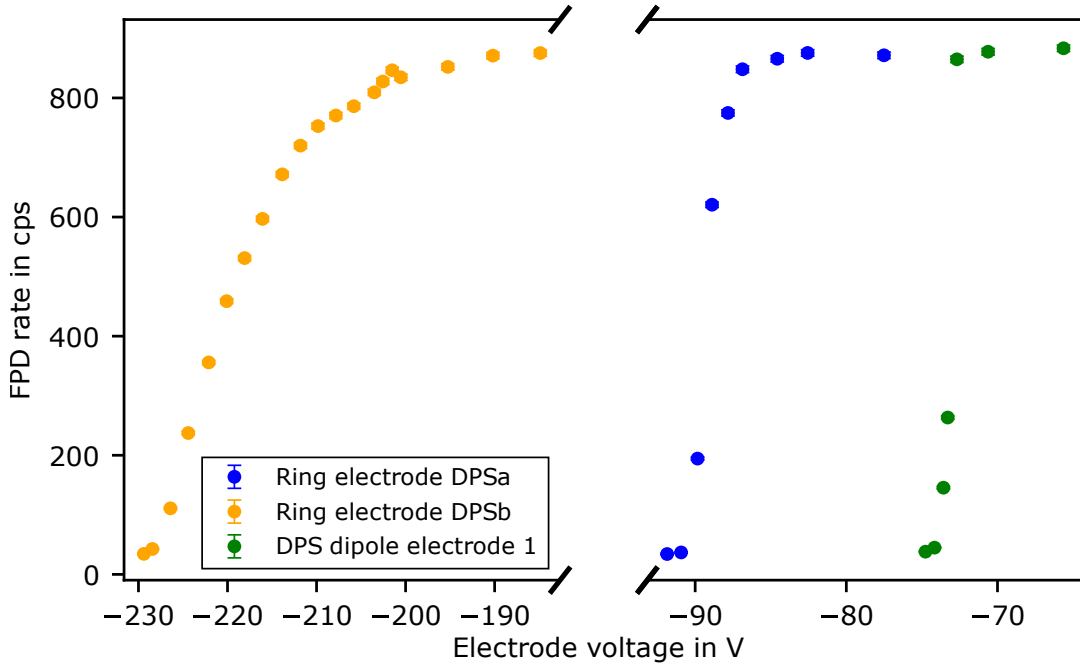


Figure 5.5: Blocking of photoelectrons from the RW with negative voltages applied to different beam line electrodes. As the blocking voltage is set to higher absolute values, the FPD rate drops as expected. The photoelectrons are produced by illuminating the central part of the RW with UV light from a fiber of the egun setup. The photoelectron energy is defined via a RW bias voltage of $U_{RW} \approx -71$ V. However, the power supply used in this specific measurement suffers from a drift on the 1 V level, which directly translates to the effective electron energy. The device has been replaced afterwards. Nevertheless, it is obvious that the blocking electrodes have different transmission functions, which is due to their different geometries which result in different effective potentials in the center.

a much smaller effective electric potential in the center. The dipole electrodes 2, 3 and 4 were tested likewise by blocking He^+ ions from the MS, which resulted in an increase of the ion current measured at the PS downstream cone electrode.

The blocking electrodes can also be used in a measurement of the integral energy spectrum of deuterium ions generated inside the WGTS (see the part of Fig. 5.4b where $U_{\text{dipole1}} \lesssim 25$ V). The spectral shape provides some insights about what to expect in the first neutrino mass run where similar measurements were performed. Although the ion creation mechanisms are different in tritium operation, the basic processes of impact ionization and molecular dissociation are present in both configurations. Thus, the ion energy spectra are comparable to some degree. Dedicated measurements at multiple deuterium column densities were analyzed and are going to be published in [VH].

The main result from these investigations is that a DPSa bias voltage around 25 V is the minimum voltage necessary in order to block the entire deuterium ion flux. No dependence of this minimum voltage on the column density is found for the analyzed range of 0% to about 0.2% of the design value. It is a first estimate for the optimum DPSa operational voltage during neutrino mass runs or at least its lower limit.

5.2.3 Calibration of the pre-spectrometer current measurement

In section 5.1.2 the PS current method was introduced. Positive ions entering the PS are neutralized on its downstream cone electrode with probability $C_{\text{cone,down}}$ and induce a current $I_{\text{cone,down}}$ measured by a Keithley[®] 6514 picoammeter. From simulations, $C_{\text{cone,down}} \approx (18 \pm 3)\%$ can be estimated for the ICE setting at the PS. However, a second calibration factor C_{see} is needed for deriving the absolute flux of positive ions $\phi_{\text{CPS} \rightarrow \text{PS}}$ into the PS (cf. Eq. 5.2). This factor arises from secondary electron emission induced by ions hitting the electrode surface. It was measured using deuterium ions.

Both factors, $C_{\text{cone,down}}$ and C_{see} , depend on the PS voltage setting. An overview of the relevant settings is given in Tab. 5.2. At first, a dedicated calibration measurement was carried out at the ICE setting in order to determine $C_{\text{see}}(\text{ICE})$. However, the calibration factors are mainly required for the PS nominal setting which is applied during neutrino mass runs, but which was redefined after STSIIIa. The results of a second STSIIIa measurement can be used in order to determine the overall calibration factor $C(\text{nominal}) = e \cdot C_{\text{cone,down}}(\text{nominal}) \cdot C_{\text{see}}(\text{nominal})$ for the PS nominal setting.

Calibration at the ICE setting

The basic idea is to compare the currents at the PS downstream cone electrode at two different settings: one time measured at the ICE setting and one time at a low voltage (LV) setting, where secondary electron emission is negligible. The ion flux into the PS is the same for both settings, but the simulated detection probability $C_{\text{cone,down}}$ is different. This has to be taken into account in the analysis.

An appropriate LV setting has been proposed by F. Glück (cf. Tab. 5.2). At this setting a more positive voltage with respect to the vessel is applied to the PS downstream cone electrode enabling back reflection of possibly emitted secondary electrons.

For the measurement, deuterium Penning ions were created in the first DPS dipole electrode operated in monopole mode at a positive voltage of 40 V. Photoelectrons were provided by the RW at a bias voltage of -100 V. The electrons were blocked

Table 5.2: Overview of PS high voltage settings. Shown are the voltages applied to the PS vessel U_{vessel} , the upstream cone electrode $U_{\text{cone,up}}$, the wire electrode U_{wire} , the downstream cone electrode $U_{\text{cone,down}}$ and the simulated detection probability of positive ions at the downstream cone electrode $C_{\text{cone,down}}$. All parameters are given for the low voltage (LV), the ICE and the nominal setting, respectively. It should be noted that the nominal setting applied during neutrino mass measuring mode is defined by all inner electrodes set to -10.5 kV, which is slightly different from the setting stated in this table.

Setting	LV	ICE	(Close to) nominal
U_{vessel} in V	-450	-18600	-10000
$U_{\text{cone,up}}$ in V	$+30$	-19100	-10500
U_{wire} in V	$+30$	-19050	-10450
$U_{\text{cone,down}}$ in V	-400	-19000	-10400
$C_{\text{cone,down}}$ in %	70 ± 9	18 ± 3	Not simulated

from entering the PS by a negatively biased dipole electrode 4.

In both settings, LV and ICE, the PS downstream cone signal current $I_{\text{cone,down}}^{\text{signal}}$ can be determined by subtracting the background current $I_{\text{cone,down}}^{\text{background}}$ from the measured total current $I_{\text{cone,down}}^{\text{tot}}$. The background currents were measured while the entire ion flux was blocked with the DPSa ring electrode. The results are

$$\begin{aligned} I_{\text{cone,down}}^{\text{background}}(\text{LV}) &= (-0.28 \pm 0.04) \text{ pA}, \\ I_{\text{cone,down}}^{\text{signal}}(\text{LV}) &= (7.67 \pm 0.04) \text{ pA}, \\ I_{\text{cone,down}}^{\text{background}}(\text{ICE}) &= (0.52 \pm 0.03) \text{ pA}, \\ I_{\text{cone,down}}^{\text{signal}}(\text{ICE}) &= (75.17 \pm 0.06) \text{ pA}. \end{aligned} \tag{5.4}$$

Based on these current values, the calibration factor $C_{\text{see}}(\text{ICE})$ at the ICE setting can be determined:

$$C_{\text{see}}(\text{ICE}) = \frac{I_{\text{cone,down}}^{\text{signal}}(\text{ICE})}{I_{\text{cone,down}}^{\text{signal}}(\text{LV})} \cdot \frac{C_{\text{cone,down}}(\text{LV})}{C_{\text{cone,down}}(\text{ICE})} = 38.1 \pm 8.0. \tag{5.5}$$

Thus, the ion flux into the PS can be inferred from the measured cone current according to Eq. 5.2, by dividing through the overall calibration factor

$$C(\text{ICE}) = e \cdot C_{\text{cone,down}}(\text{ICE}) \cdot C_{\text{see}}(\text{ICE}) = (1.10 \pm 0.30) \times 10^{-18} \text{ C}. \tag{5.6}$$

Consequently, in the ICE setting a signal current of $I_{\text{cone,down}}^{\text{signal}} = 1 \text{ fA}$ corresponds to a flux of $\phi_{\text{CPS} \rightarrow \text{PS}} = (910 \pm 244) \text{ ions/s}$.

Calibration at the nominal PS setting

At the beginning of the first neutrino mass measurement campaign KNM1 it was decided to operate the PS vessel at a reduced voltage of -10 kV instead of the anticipated design value of -17.8 kV , in order to decrease the depth of the Penning trap in between PS and MS. At this reduced nominal setting the calibration factors stated above are not valid anymore. Fortunately, in STSIIIa the PS cone current was measured once at a setting close to the nominal one (cf. Tab. 5.2) using residual gas Penning ions produced at the first dipole electrode. Immediately after this, the corresponding current was measured in the ICE setting. Subtracting the respective background currents results in

$$\begin{aligned} I_{\text{cone,down}}^{\text{signal}}(\text{nominal}) &= (0.79 \pm 0.01) \text{ pA}, \\ I_{\text{cone,down}}^{\text{signal}}(\text{ICE}) &= (4.13 \pm 0.01) \text{ pA}, \\ \frac{I_{\text{cone,down}}^{\text{signal}}(\text{nominal})}{I_{\text{cone,down}}^{\text{signal}}(\text{ICE})} &= (0.190 \pm 0.003). \end{aligned} \tag{5.7}$$

Using the result from Eq. 5.6, the overall calibration factor for the nominal PS setting is given by

$$\begin{aligned} C(\text{nominal}) &= C(\text{ICE}) \cdot \frac{I_{\text{cone,down}}^{\text{signal}}(\text{nominal})}{I_{\text{cone,down}}^{\text{signal}}(\text{ICE})} \\ &= (2.09 \pm 0.56) \times 10^{-19} \text{ C}. \end{aligned} \tag{5.8}$$

Thus, a signal current of $I_{\text{cone,down}}^{\text{signal}} = 1$ fA measured during a nominal neutrino mass run corresponds to a flux of $\phi_{\text{CPS}\rightarrow\text{PS}} = (4.8 \pm 1.3) \times 10^3$ ions/s. An unknown systematic uncertainty arises from the use of Penning ions from residual gas, which is mainly composed of H_2 . These Penning ions have different masses than deuterium or tritium ions. Thus, the downstream cone calibration factors of these ions might have different PS voltage-dependencies. So, in case the above stated numerical result is applied to tritium ions, a systematical error is introduced.

5.2.4 Calibration of the ICE detection method

The ICE method described in section 5.1.2 refers to a special HV setting of the spectrometers, where positive ions entering the PS are converted to secondary electrons, which then are accelerated to the FPD where they are counted. In order to determine the absolute flux of positive ions $\phi_{\text{CPS}\rightarrow\text{PS}}$ into the PS from the measured FPD count rate R_{ICE} , the calibration factor C_{ICE} has to be known. According to Eq. 5.3, it is given by

$$C_{\text{ICE}} = \frac{R_{\text{ICE}}}{\phi_{\text{CPS}\rightarrow\text{PS}}}. \quad (5.9)$$

This factor can be determined in a dedicated calibration measurement by introducing a well-defined flux of deuterium ions into the PS and measure the corresponding ICE rate with the FPD. The final result was obtained in a thorough analysis described in the bachelor thesis of E. Weiss⁷. In the following a detailed summary will be given.

Measurement

The calibration measurement was split into two parts in order to measure the ICE rate R_{ICE} and the ion flux $\phi_{\text{CPS}\rightarrow\text{PS}}$ separately.

- **Measurement of R_{ICE} :** The ICE rate was measured by the FPD with the PS operated in ICE mode (cf. Fig 5.3).
- **Measurement of $\phi_{\text{CPS}\rightarrow\text{PS}}$:** The Ti-disk of the detector section connected to the PULCINELLA picoammeter (cf. section 5.1.2) was inserted into the beam line for measuring the ion flux. It completely shielded the FPD. In order to enable the transmission of the positive deuterium ions through the spectrometers towards the Ti-disk, both PS and MS were operated at positive retarding voltages $U_{\text{ret}} > 0$ V.

In both measurements the STS hardware settings were identical⁸. Deuterium Penning ions were created in dipole electrode 1 of the DPS, which was operated at a positive voltage of ~ 203 V applied to both half-shells. The RW photoelectrons were blocked from SDS via a negative retarding voltage of -352 V applied to both half-shells of dipole electrode 4. In the SDS, the maximum analyzing plane magnetic field of 1.45 mT was provided by the MS air-coil system in order to maximize the adiabaticity of the secondary electrons.

The SDS HV settings were significantly different for both measurements. In the R_{ICE} measurement, the PS HV system was operated at the ICE setting and the

⁷E. Weiss, Determination of the Ion Conversion to Electron efficiency of the KATRIN Pre-Spectrometer, bachelor's thesis, Karlsruher Institut für Technologie (KIT), 2019.

⁸The only exception was the RW bias voltage as will be detailed in the following paragraph "Correction factors to incorporate systematic effects of the measurement".

MS HV was turned off. In the $\phi_{\text{CPS}\rightarrow\text{PS}}$ measurement, a voltage of +185 V was applied to the PS inner electrodes and the MS inner electrodes were operated at different voltages between +180 V and +200 V. Both the PS and MS vessel were set to $U_{\text{vessel}} = 0$ V. In this special SDS mode positive deuterium ions were transmitted through the spectrometers towards the detector section and neutralized on the Ti-disk inducing a current I_{PUL} . It was biased on a positive voltage of 90 V in order to prevent the ejection of secondary electrons when ions hit the disk. The voltage of the DPSa ring electrode was increased to block the ions from the SDS and to allow determination of the background current. Thus, the total current measured by PULCINELLA $I_{\text{PUL,tot}}(U_{\text{ret}})$ at a certain retarding voltage U_{ret} minus its background current $I_{\text{PUL,background}}$ yields the signal current $I_{\text{PUL,signal}}(U_{\text{ret}})$, which can directly be converted into the absolute ion flux into the PS via

$$I_{\text{PUL,signal}}(U_{\text{ret}}) = I_{\text{PUL,tot}}(U_{\text{ret}}) - I_{\text{PUL,background}} = \phi_{\text{CPS}\rightarrow\text{PS}} \cdot e \cdot f(U_{\text{ret}}) \cdot f_{\text{RW}} \quad (5.10)$$

with the elementary charge e and the correction factors $f(U_{\text{ret}})$ and f_{RW} which are necessary in order to take the systematic effects of the measurement into account.

Correction factors to incorporate systematic effects of the measurement

The first correction factor f_{RW} arises from the fact that the RW bias voltage was mistakenly changed in between the two parts of the measurement. First, the RW was operated at $U_{\text{RW}} = -100$ V during the $\phi_{\text{CPS}\rightarrow\text{PS}}$ measurement and then at $U_{\text{RW}} = -200$ V during the R_{ICE} measurement. This is a systematic error since a different RW voltage results in a different electron energy, a different ionization cross section and ultimately into a different ion flux $\phi_{\text{CPS}\rightarrow\text{PS}}$. In the analysis this is taken into account by a simulated correction factor $f_{\text{RW}} = 0.9540 \pm 0.0008$.

The second factor $f(U_{\text{ret}})$ incorporates various systematic effects which influence the measurement result and need to be modeled in dedicated simulations.

- **Broad energy spectrum of the measured ions:** In case of monoenergetic ions the interpretation of the current measurement is rather straightforward with $f(U_{\text{ret}}) = 1$. At a high enough MS retarding potential the ions are blocked completely and the background current can be measured. When lowered below a certain threshold corresponding to the ion energy, the absolute current jumps to a higher value in a single step. However, in reality the energy spectrum is rather broad. There are three main reasons for this. First, around 9% [SRL+96] of the deuterium ions are produced via molecular dissociation in the first place, possessing Gaussian-like distributed energies of up to 15 eV more than their non-dissociative counterparts [DK63]. Second, ions are born at different locations inside the sensitive magnetic flux tube of the first dipole electrode, so they experience different electric starting potentials. Third, the pressure along the z -axis inside the dipole electrode decreases by almost one order of magnitude due to differential pumping in the DPS. This affects the longitudinal ionization profile because the e^- -D₂ scattering probability is determined by $p_{\text{scat}} = \sigma(E_e) \cdot n \cdot l$ [Gil72] with the cross section σ , the electron energy E_e , the number density n and the path length l . Ultimately, the raw deuterium ion energy spectrum has to be convoluted with the starting potential distribution and the ionization profile in order to determine the energy spectrum of the ion flux into the spectrometers.

- **Imperfect transmission through the spectrometers:** Deuterium ions have a several thousand times higher mass than electrons, which are usually transmitted through the spectrometers during nominal operation. This might lead to deviations from the desired adiabatic motion at magnetic fields as low as 1.45 mT [GBB⁺05]. Some of the ions move non-adiabatically on rather chaotic trajectories and will not reach the Ti-disk, so they do not contribute to the measured current. Consequently, the measured signal current $I_{\text{PUL,signal}}$ would be lower than the true ion current into the PS. The impact of non-adiabatic effects increases with the surplus energy which is defined as the kinetic ion energy minus the MS retarding energy eU_{ret} .

Combining both systematic effects leads to an effective voltage-dependent correction factor $f(U_{\text{ret}}) < 1$ for the retarding voltages U_{ret} of interest.

Simulations

The numbers for $f(U_{\text{ret}})$ are determined by combining results of three different simulation frameworks.

1. The starting potential distribution of the ions was determined by simulating the electric potential distribution inside the sensitive magnetic flux tube volume of dipole electrode 1. The magnetic field line tracks were simulated with KASSIOPEIA for a magnetic field $B = 3.5$ T provided by the first DPS superconducting solenoid. At each tracking position on the field lines, the corresponding electric potential value was simulated with KEMField. The results can be seen in Fig. 5.6.
2. The longitudinal pressure profile was simulated with MolFlow+. The concept of MolFlow+ was introduced in section 4.3.1. It provides tracking of test particles inside a vacuum chamber for free molecular flow. A stand-alone model of the DPS beam line was used for the simulation. The TMPs attached to the DPS pump ports are each implemented by a surface with a sticking probability $\alpha = 0.195$ corresponding to the pumping speed for D_2 according to a model developed by O. B. Malyshev [Mal07]. Two virtual (i.e. transparent) facets extending from PP0 to PP1 are included for measuring the longitudinal pressure profile via counting of particle hits. They are aligned horizontally (x - z plane) and vertically (y - z plane), respectively. The longitudinal pressure distribution is simulated along the central z -axis, as it is assumed that there is no radial dependence. The result can be seen in Fig. 5.7. In order to combine the results of the horizontally and vertically aligned facets, both curves are averaged.
3. The non-adiabatic effects of deuterium ions inside the PS and MS have to be taken into account. Therefore, the transmission probability of deuterium ions through the spectrometers towards the PULCINELLA Ti-disk had to be simulated. The simulations were done by E. Weiss based on a self-developed C++ code provided by F. Glück. The ion tracking starts inside the PS1 magnet at the PS entrance and is terminated once the particle either hits the Ti-disk or is neutralized on the vessel or inner electrode surface. A storage of particles inside the spectrometer volume due to the magnetic mirror effect can be excluded since dedicated simulations showed that for long enough time scales the stored ions are ultimately transmitted to the Ti-disk. Interactions

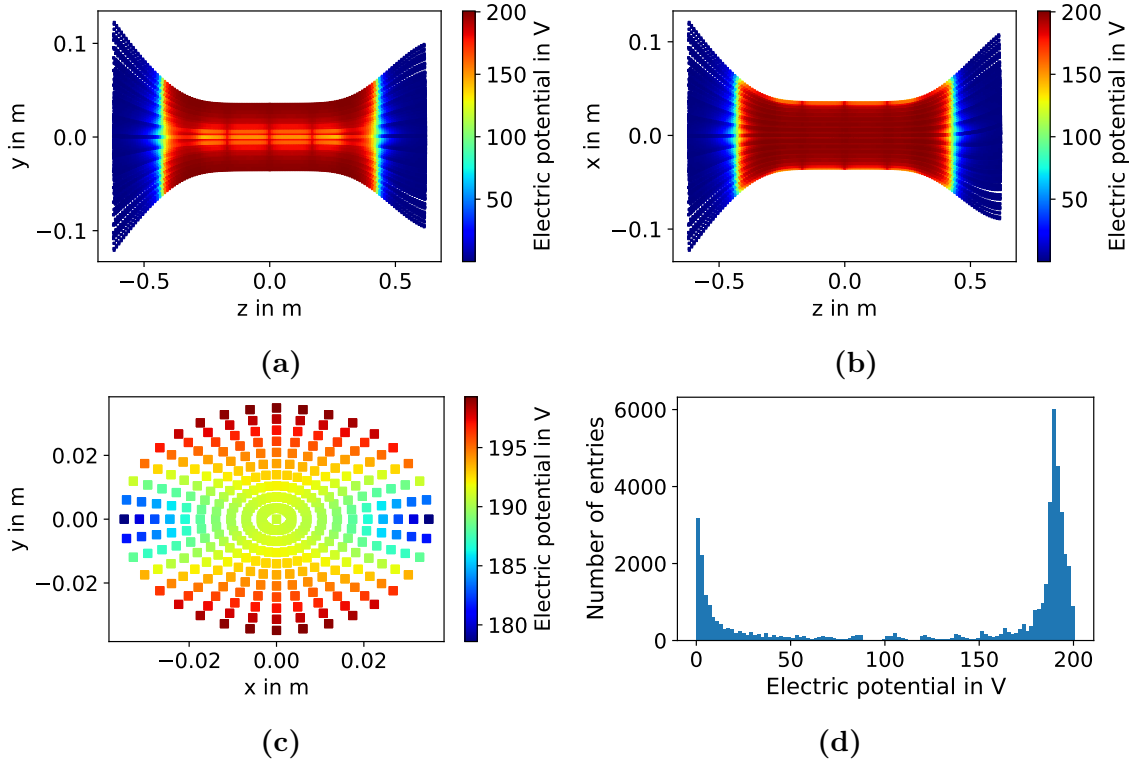


Figure 5.6: KEMField simulation of the electric potential distribution inside the sensitive magnetic flux tube volume of the first DPS dipole electrode. In the simulation the dipole electrode is operated in monopole mode at a positive voltage of 202.5 V applied to both half-shells. The spatial distribution of the magnetic field lines is simulated with KASSIOPEIA. Shown are the y - z (a), the x - z (b) and the $z = 0$ (c) distribution of the resulting electric potential inside the sensitive magnetic flux tube of 134 T cm². A histogram of the electric potential is given in (d).

with neutral gas molecules are not considered due to the rather short ion path lengths and the ultra-low pressure on the order of 10^{-11} mbar in the MS. The transmission probability is simulated for different starting positions, pitch angles, ion energies and retarding potentials.

Analysis

The simulations of the various systematic effects can eventually be used to correct the measurement result. The analysis of the FPD rate measurement yields $R_{\text{ICE}} = (2.230 \pm 0.003)$ Mcps after applying a pile-up correction, taking into account that two events can possibly not be differentiated in case of a too short interarrival time. The corresponding ion currents were determined with the PULCINELLA picoammeter yielding $I_{\text{PUL,background}} = (15.45 \pm 0.02)$ pA for the background current. Finally, the combination of all simulation results gives the correction factor $f(U_{\text{ret}})$ for each retarding voltage. The relevant retarding voltage-dependent results are summarized in Tab. 5.3. Five different results are obtained for the current into the PS, $I_{\text{CPS} \rightarrow \text{PS}} = I_{\text{PUL,signal}}(U_{\text{ret}})/f(U_{\text{ret}})$. However, the true value should not depend on the MS retarding voltage. As the best estimate of the true value, a weighted arithmetic mean $\bar{I}_{\text{CPS} \rightarrow \text{PS}} = (129 \pm 4)$ pA is calculated. Plugging this number into Eq. 5.10 and taking the correction factor $f_{\text{RW}} = 0.9540 \pm 0.0008$ into account yields

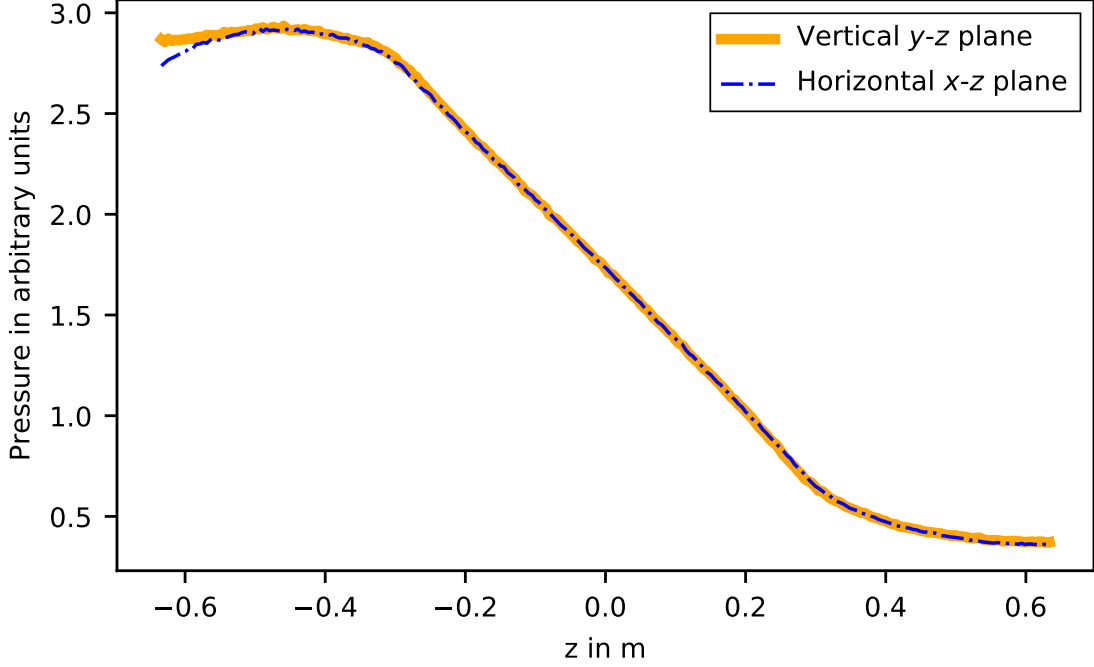


Figure 5.7: MolFlow+ simulation of the longitudinal D_2 pressure profile in the first DPS beam tube element. Shown is the pressure along a vertically and a horizontally aligned virtual facet. The origin ($z = 0$ m) is located at the center of the first DPS beam tube element which is identical to the center of the first dipole electrode. Inside PP0 at around $z = -0.6$ m a significant difference can be observed between the horizontal and the vertical plane. This is due to the vertically aligned TMPs which introduce an azimuthal asymmetry in the setup.

the ion flux $\phi_{\text{CPS} \rightarrow \text{PS}}$. Finally, the ICE calibration factor can be determined to be

$$C_{\text{ICE}} = \frac{R_{\text{ICE}}}{\phi_{\text{CPS} \rightarrow \text{PS}}} = (2.771 \pm 0.095) \times 10^{-3} \text{ counts/ion}. \quad (5.11)$$

It can thus be concluded that a single FPD count measured via the ICE method corresponds to a number of (361 ± 12) ions entering the PS.

Table 5.3: STSIIIa measurement and simulation results for determining the deuterium ion flux into the PS as measured by PULCINELLA in dependence of the MS retarding voltage. Shown are the measured signal currents $I_{\text{PUL,signal}}(U_{\text{ret}})$, the simulated correction factors $f(U_{\text{ret}})$ and the deuterium ion current into the PS $I_{\text{CPS} \rightarrow \text{PS}} = I_{\text{PUL,signal}}(U_{\text{ret}})/f(U_{\text{ret}})$ for the different MS inner electrode retarding voltages U_{ret} . The values were determined by E. Weiss in the context of his bachelor thesis.

U_{ret} in V	$I_{\text{PUL,signal}}(U_{\text{ret}})$ in pA	$f(U_{\text{ret}})$	$I_{\text{CPS} \rightarrow \text{PS}}$ in pA
180	64.97 ± 0.06	0.4840 ± 0.0004	134.2 ± 0.2
190	59.8 ± 0.1	0.4010 ± 0.0004	149.0 ± 0.4
195	37.8 ± 0.1	0.2608 ± 0.0004	145.0 ± 0.5
198	18.08 ± 0.08	0.1570 ± 0.0003	115.2 ± 0.6
200	11.32 ± 0.06	0.0955 ± 0.0002	118.5 ± 0.7

5.2.5 Pressure-dependent ICE measurements with argon gas

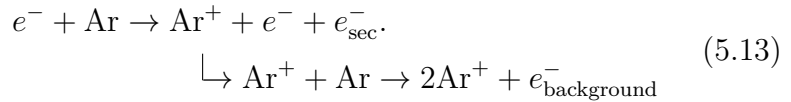
The sensitivity of the ICE method scales with the efficiency of converting ions into secondary electrons, which is quantified by the calibration factor C_{ICE} . Given that the dominant mechanism of the ion to electron conversion inside the PS is impact ionization of residual gas particles, the calibration factor should be a function of the residual gas pressure $C_{\text{ICE}} = C_{\text{ICE}}(p)$. Thus, it should be possible to increase the sensitivity of the measurement by increasing the pressure inside the PS.

In fact, pressure-dependent FPD rates have been measured in the "first tritium" campaign by M. Klein [Kle19]. In this specific campaign the tritium activity in the WGTS was only 0.5% of the design value [AAA⁺20]. The pressure dependence was investigated by introducing argon gas into the PS vessel. It was found that the FPD rate increases with the argon pressure, although the pressure dependence could not be explained.

The idea of the underlying mechanism was that positively charged tritium ions (e.g. T_3^+) entering the PS are accelerated by the negative high voltage and ionize argon gas particles on their way, while secondary signal electrons e_{signal}^- are produced via



The signal electrons are subsequently measured by the FPD. This is a single-stage process, so the obtained count rate should be a linear function of the argon pressure p . However, there is a second reaction producing background electrons $e_{\text{background}}^-$. A certain fraction of the argon gas will diffuse from the PS into the CPS where it is ionized by the β -electrons from tritium decay. The thus created Ar^+ ions are then attracted by the negative PS voltage and accelerated through the PS argon gas cloud producing background electrons. The reaction is referred to as Ar^+ background and can be written as follows:



Here, the background count rate should scale with p^2 as it is a two-stage process. During tritium operation it is not possible to distinguish between the reactions of Eqs. 5.12 and 5.13 because both β -electrons and tritium ions are simultaneously transported to the PS. The superposition of both effects allows no clear observation of either the linear or the quadratic scaling of the rates with the pressure. In STSIIIa however, the β -electrons are replaced by RW photoelectrons. These photoelectrons have sufficiently low energy so they can be blocked by applying a negative voltage at one of the beam line electrodes. This allows to perform two distinct measurements.

- **Exclusive measurement of the ion-induced signal:** If all photoelectrons are blocked, only signal electrons according to Eq. 5.12 (T_3^+ is replaced by D_2^+ or H_2^+) are measured.
- **Exclusive measurement of the Ar^+ background:** On the other hand, if there is no circulation of D_2 gas and if no beam line electrode is operated at a positive voltage, there are no ions produced at all. Letting the RW photoelectrons pass up to the PS enables an exclusive measurement of the background reaction described in Eq. 5.13.

Thus, in the specific settings of the STSIIIa campaign it is indeed possible to measure background and signal of the ICE method independently.

However, the measurement results as shown in Fig. 5.8 disagree with the expectation. In both measurements, the observed pressure dependence was one order of magnitude smaller than predicted.

- The first measurement (see Fig. 5.8a) was performed with only residual gas in the beam line. All beam line electrodes were switched off and the RW photoelectrons reacted according to Eq. 5.13. The FPD rate linearly rises with the argon pressure. A quadratic dependence as it is expected from first principle is not observed.
- In the second measurement (see Fig. 5.8b), Penning ions were created from the residual gas inside the first DPS dipole electrode while the RW photoelectrons were blocked. No dependence is found between FPD rate and argon pressure. A similar behavior is observed when D₂ gas is introduced into the WGTS (see other data sets in Fig. 5.8b). The rate stays constant for different gas pressures.

These findings shed a new light on the investigations during the "first tritium" cam-

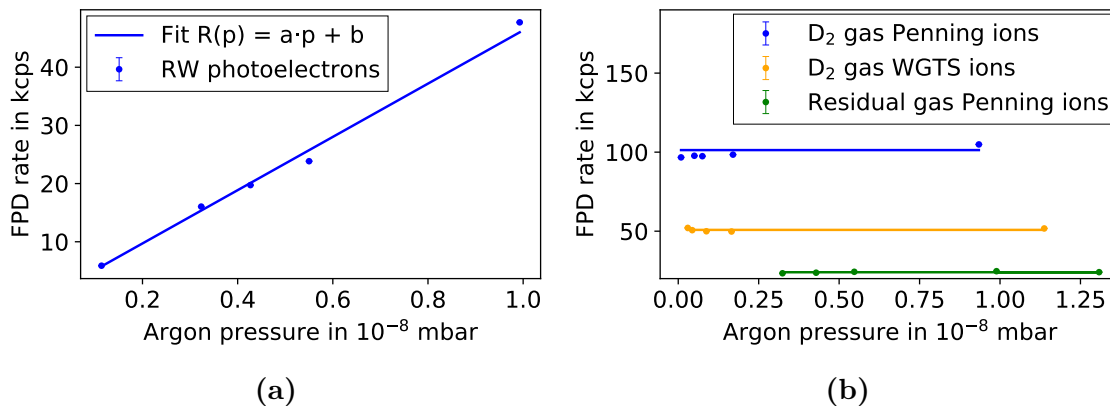


Figure 5.8: Pressure dependence of the ICE method. Shown is the FPD count rate measured with the ICE method versus the argon gas pressure in the PS. An exclusive measurement of the Ar⁺ background rate induced by RW photoelectrons (cf. Eq. 5.13) with energies of approximately 100 eV shows a linearly rising rate (a). On the other hand, measurements for different types of ions (cf. Eq. 5.12 with H₂⁺ and D₂⁺ instead of T₃⁺) reveal that the gas pressure has no significant influence on the measured ion-induced signal rate (b). Three distinct measurements are performed each with a different ion source while the RW photoelectrons are blocked by a negatively biased beam line electrode. Penning ions from dipole electrode 1 are created both with and without a D₂ gas column inside the WGTS. Without D₂, the Penning ions are created from residual gas inside the electrode volume at a voltage of +350 V (monopole mode) by photoelectrons from the RW which is operated at $U_{RW} = -100$ V. With D₂, the Penning ions are produced at a dipole electrode voltage of +40 V (monopole mode) with the RW set to $U_{RW} = -200$ V. In the third case, all beam line electrodes are switched off or put on a negative bias voltage and the RW setting is $U_{RW} = -100$ V. Thus, ions generated inside the WGTS D₂ gas column are able to pass all the way to the PS where they produce signal electrons.

campaign published in [Kle19]. Apparently, the measured pressure-dependent rate increase can be solely attributed to the β -electron-induced Ar^+ background. So introducing argon gas into the PS does not improve the sensitivity of the ICE method. Rather, it is getting worse because the background increases. Two conclusions can be drawn from this.

- Introducing argon gas into the PS for ICE measurements is counterproductive and should be avoided for future campaigns.
- The impact ionization processes stated in Eqs. 5.12 and 5.13 are expected to scale linearly and quadratically with the gas pressure, respectively. However, these dependencies were not observed in the measurements. Hence, impact ionization seems not to be the dominant mechanism producing the signal electrons in the ICE mode.

An alternative explanation of the underlying mechanism was formulated by F. Glück. It might be that the positive ions entering the PS sputter off neutral particles from the inner surfaces which then enter the sensitive magnetic flux tube volume seen by the FPD. Some of these particles are highly excited Rydberg atoms and can be ionized by a tiny energy impact e.g. from photons of the thermal black body radiation of the spectrometer vessel. Based on years of dedicated studies (see e.g. [Tro19]), a similar process was identified as a promising candidate for explaining the MS background characteristics. In the MS, Rydberg atoms are sputtered off the inner surfaces by ions produced in the α -decays of implanted nuclei [Tro19]. It is likely that analog processes could take place in the PS, converting ions into signal electrons.

5.2.6 Conclusion

In the STSIIIa campaign helium, residual gas and deuterium ions were successfully produced in the MS, the DPS beam line electrodes and the WGTS. It was possible to control both the ion creation rate and energy. The resulting ion flux has allowed to validate the ion blocking capabilities of the DPS ring electrodes, as well as the successful application of voltages to all DPS dipole electrodes. Further, detailed investigations of the PS current and the ICE detection method were performed. Both methods were calibrated by determining the corresponding calibration factor, which enables the conversion of the measured current or FPD rate into the flux of positive ions into the PS. This is especially important regarding the subsequent KNM1 campaign in which high amounts of tritium ions had to be blocked from entering the spectrometers and even tiny ion rates as low as 1×10^4 ions/s into the PS would be harmful for the FPD background rate.

It was found that the sensitivity of the ICE method, which scales with the calibration factor, is high enough to detect ion fluxes on the level of 10^3 ions/s. However, the STSIIIa studies have revealed that introducing argon gas into the PS is unfavorable for the ion detection. It is even counterproductive since the electron-induced Ar^+ background rate scales linearly with the argon pressure while the ion-induced signal rate is pressure-independent.

5.3 Optimization of ion blocking electrodes for neutrino mass measurements

In spring and fall 2019 the first KATRIN neutrino mass measurement campaigns KNM1 and KNM2 took place (cf. section 3.2). During these periods, the WGTS was exposed to high amounts of tritium gas, constituting a crucial test for the ion beam line instrumentation. Column densities of 22% (KNM1) and 84% (KNM2) of the design value of $\mathcal{N} = 5 \times 10^{17}$ molecules/cm² at a tritium purity of above 95% were established and kept stable for several months.

Before and in between the neutrino mass runs several ion characterization measurements were performed. Different beam line settings were used, especially many different WGTS column densities. For each of the different investigations described in the following sections the relevant settings of the KATRIN apparatus will be stated. Unless otherwise noted, column density values are calculated from data of the throughput sensor measuring the inlet flow rate into the WGTS beam line (cf. Fig. 2.9 in section 2.3.1) based on a model from [Hei19] provided by A. Marsteller. However, it suffers from a systematic uncertainty of +3%/-4% [Hei19]. More precise values can be derived from dedicated egun calibration measurements performed by F. Block, C. Köhler and A. Marsteller, which is done in section 5.3.4.

The characterization measurements described in this section are the following. Measurements of the DPS dipole electrode current are undertaken during the ramp-up procedure of the tritium column density (see section 5.3.1). In sections 5.3.2 to 5.3.4 the ring and dipole electrodes are characterized in various studies and finally optimum voltage settings for their long-term operation are identified in section 5.3.5. With these settings applied, it is verified that the ion flux into the PS $\phi_{\text{CPS} \rightarrow \text{PS}}$ is low enough to meet the stringent KATRIN requirements (see section 5.3.6).

5.3.1 WGTS column density ramp-up

On March 4, 2019 the KNM1 tritium injection into the WGTS started. In several steps the column density was ramped up first to about 7% of the nominal design value of $\mathcal{N} = 5 \times 10^{17}$ molecules/cm². On March 7 a value of 16% was reached and another three days later - on March 10 - a value of about 42% was achieved. Due to radiochemical reactions in the loop system (see section 3.2 for details) column density instabilities were observed from this point on, so the analysis presented in this section does not include higher column density values⁹.

From first principle, the tritium ion flux - consisting mainly of T₃⁺ - from the WGTS into the DPS can be calculated from the column density and the tritium purity via [Kle19]:

$$\phi_{\text{WGTS} \rightarrow \text{DPS}}(\epsilon_{\text{T}}, \mathcal{N}) = \lambda_{\text{T}} \cdot A_{\text{WGTS}} \cdot p_{\text{trans}}^{\text{DPS}} \cdot (1 - p_{\text{recom}}) \cdot \epsilon_{\text{T}} \cdot \left(\mathcal{N} + \frac{m_{\beta}(\mathcal{N}_{\text{nom}})}{\mathcal{N}_{\text{nom}}} \mathcal{N}^2 \right). \quad (5.14)$$

The first term in the bracket can be attributed to tritium decay and the second term to impact ionization by β -electrons. Here, $\lambda_{\text{T}} = \ln(2)/T_{1/2} = 1.78 \times 10^{-9} \text{ s}^{-1}$ is the decay constant of tritium and $A_{\text{WGTS}} = 63.6 \text{ cm}^2$ is the WGTS cross section

⁹This issue could be resolved in the course of KNM1, so for KNM2 and beyond higher column density values with a stability on the per mill level were realized.

area corresponding to the maximum radius of the WGTS beam tube $r = 4.5$ cm and a magnetic flux tube of $\phi = 229$ T cm² at the design field $B = 3.6$ T [Kle19]. Further, $p_{\text{trans}}^{\text{DPS}} = 95.5\%$ is the fraction of field lines transmitted to the DPS according to dedicated KASSIOPEIA simulations by M. Deffert, $\epsilon_{\text{T}} > 95\%$ is the tritium purity, \mathcal{N} is the column density and $m_{\beta}(\mathcal{N}_{\text{nom}}) = 36$ is the average number of ions created by a single β -electron at the nominal design column density \mathcal{N}_{nom} [Kle19]. Furthermore, the probability for the ion to recombine with a secondary electron before it is able to leave the WGTS, p_{recom} , has to be taken into account. According to simulations by F. Glück in the case of T_3^+ at the nominal design column density of $\mathcal{N} = 5 \times 10^{17}$ molecules/cm² about 80% of the ions recombine, so only 20% finally leave the WGTS. At lower column densities on the other hand, the probability of recombination p_{recom} is minimal and almost all T_3^+ molecules persist long enough to be transmitted to the DPS. Thus, the higher \mathcal{N} is, the lower is the ion flux $\phi_{\text{WGTS} \rightarrow \text{DPS}}$ relative to the actual creation rate.

This is important in studies of the drift currents at the DPS dipole electrodes. A negative dipole field is applied to the first three units in order to drift out positive ions via $E \times B$ drift. The ions are drifted radially out of the magnetic flux tube until they are neutralized on one of the metal lobes attached to the upper half-shell (cf. Fig. 5.1). Thereby, a current is induced which is measured via a 9103 picoammeter from RBD instruments[®]. For the start-up of KNM1 the voltages of the lower/upper half-shell were set to $(-5$ V/ -15 V), $(-5$ V/ -35 V) and $(-5$ V/ -85 V) for the dipole electrodes 1, 2 and 3, respectively. Dipole number 4 was operated in positive ion blocking mode at $(+25$ V/ $+20$ V) (see sections 5.3.2 and 5.3.3 for details). This configuration leads to a blocking of negative ions directly at the first electrode and a drift of positive ions at the first three electrodes.

During the column density ramp-up, negative currents were measured corresponding to the removal of positive ions. A strong correlation between current and column density can be seen from the data in Fig. 5.9, where the step-wise ramp-up from about 16% to 42% of the design column density is shown. The highest current was measured at the third dipole electrode and the lowest current at the first dipole electrode, corresponding to their respective dipole fields. The currents measured throughout the complete ramp-up procedure, which lasted from March 4 to March 10, are plotted in Fig. 5.10. Also, the current measured by the RW picoammeter at a bias voltage of $U_{\text{RW}} = 0$ V is shown. It provides additional insight since the current was measured at the rear end of the KATRIN beam line and besides positive ions also negative ions, secondary electrons and β -electrons did contribute to the measured signal. Positively charged particles induce negative currents (analog to the dipole electrodes) and negatively charged particles induce positive currents. Several findings from these measurements are given below.

- The sign of the RW and the dipole electrode current is different, which means that at the RW the negatively charged particles dominate.
- Also the absolute current values are higher at the RW for the applied voltage of $U_{\text{RW}} = 0$ V. At this point, it is important to note that both the RW and the dipole electrode currents strongly depend on U_{RW} . This will be shown in more detail in chapter 6.3.3.
- The column density dependence at the RW and at the DPS show different behavior. As for the RW, the current rises quadratically with \mathcal{N} . At the dipole

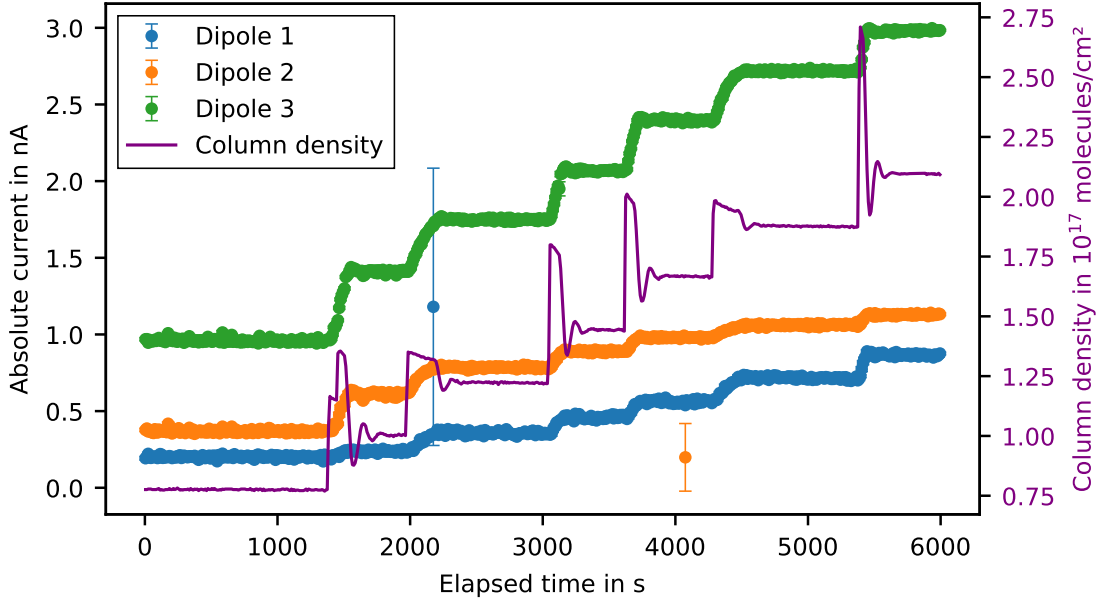


Figure 5.9: KNM1 measurement of the DPS dipole electrode currents during step-wise tritium column density ramp-up. Dipole electrode current data and a column density ramping curve is shown over time. The column density values are derived from the throughput sensor measuring the inlet flow rate into the WGTS with the model from [Hei19]. At the beginning of each step rather large spikes are observed which are artifacts caused by over-regulation of the throughput sensor. The data was taken at March 10, 2019 during step-wise ramping from $\mathcal{N} = 7.8 \times 10^{16}$ molecules/cm² ($\triangleq 16\%$ of the design value) to $\mathcal{N} = 2.1 \times 10^{17}$ molecules/cm² ($\triangleq 42\%$ of the design value) at a mean tritium purity of $\epsilon_T = 97.3\%$.

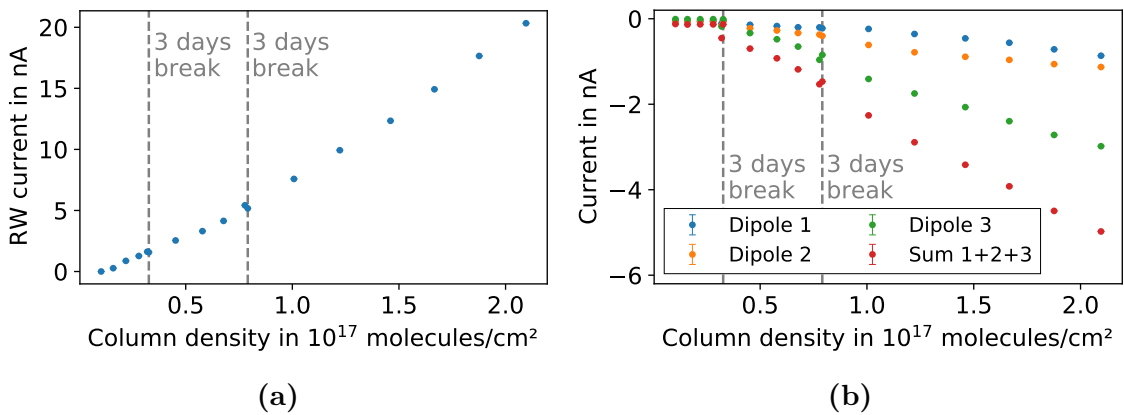


Figure 5.10: KNM1 measurement of the RW and DPS dipole electrode currents versus the column density during step-wise ramp-up. The RW data (a) and the dipole electrode data (b) were measured simultaneously from March 3 to March 10, 2019 with two three-day breaks in between. A maximum column density of $\mathcal{N} = 2.1 \times 10^{17}$ molecules/cm² ($\triangleq 42\%$ of the design value) was reached. The mean tritium purities at the three measurement days were $\epsilon_T = 97.4\%$, $\epsilon_T = 97.5\%$ and $\epsilon_T = 97.3\%$, respectively.

electrodes a rather linear dependence is observed, which can be explained by recombination processes as described previously.

- At the first day of ramp-up, when the targeted column densities were rather low in the range between $\mathcal{N} = 0$ and 3.3×10^{16} molecules/cm² (\triangleq 7% of the design value), the dipole electrode current did not change at all. Only the respective dark currents were measured. Three days later, on March 7, the current value was significantly different at similar column density. Continuous measurements reveal that over the course of these three days the current drifted from the dark current towards the increased value. This delayed response is only observed at very low column densities and is not present in the RW current which immediately rises as soon as tritium is introduced into the WGTS. Probably, these observations are caused by inadvertent positive blocking potentials due to work function differences between the WGTS and the DPS beam tube. Those positive potentials are slowly neutralized by low-energy secondary electrons. Such phenomena were already observed in the course of the ion investigations of the "first tritium" campaign [Kle19].

Further ramp-up procedures were performed during KNM1 and KNM2 due to maintenance breaks, systematic investigations and technical issues. Further measurements of the dipole electrode currents at special source and voltage settings will be discussed in detail in [VH].

Besides continuous current measurements in the DPS, the ion flux into the PS $\phi_{\text{CPS} \rightarrow \text{PS}}$ is measured both via the ICE and the PS current method during various WGTS rampings and throughout the whole campaigns. The results are presented in section 5.3.6.

5.3.2 Measurement of the ion energy spectrum

At the beginning of KNM1 it was decided to operate the fourth DPS dipole electrode at a positive dipole field in order to block ions instead of drifting them out like the first three dipole electrodes do. The reason is that a dipole electrode operated in dipole mode cannot be neutralized by accumulation of low-energy electrons because they are constantly drifted out (see the next section 5.3.3 for details about the effect of neutralization). Also, the ring electrode DPSb was set to a low voltage of +5 V because of the large amounts of Penning ions created by it.

Consequently, the three major blocking electrodes in nominal KATRIN operation constitute the fourth DPS dipole electrode and the ring electrodes DPSa and PS1. The ion-induced rate measured with the ICE method does not continuously decrease if the blocking potential increases. Instead, there is a minimum, as shown in Figs. 5.11 and 5.12. The measured FPD rate $R(U)$ as a function of the electrode voltage U can be described as the sum of an exponential term, a linear term and a constant offset:

$$R(U) = a_1 \cdot \exp(-a_2(U - a_3)) + a_4 \cdot U + a_5 \quad (5.15)$$

with the free parameters a_1 , a_2 , a_3 , a_4 and a_5 . This is a phenomenological description as a quantitative understanding of the underlying mechanisms is currently pending and would require dedicated numerical simulations.

Below a certain electrode-dependent threshold voltage the exponential term is dominating. In this low-voltage region, tritium ions from the front part of the WGTS with the highest energies are able to pass the blocking potential and reach the PS.

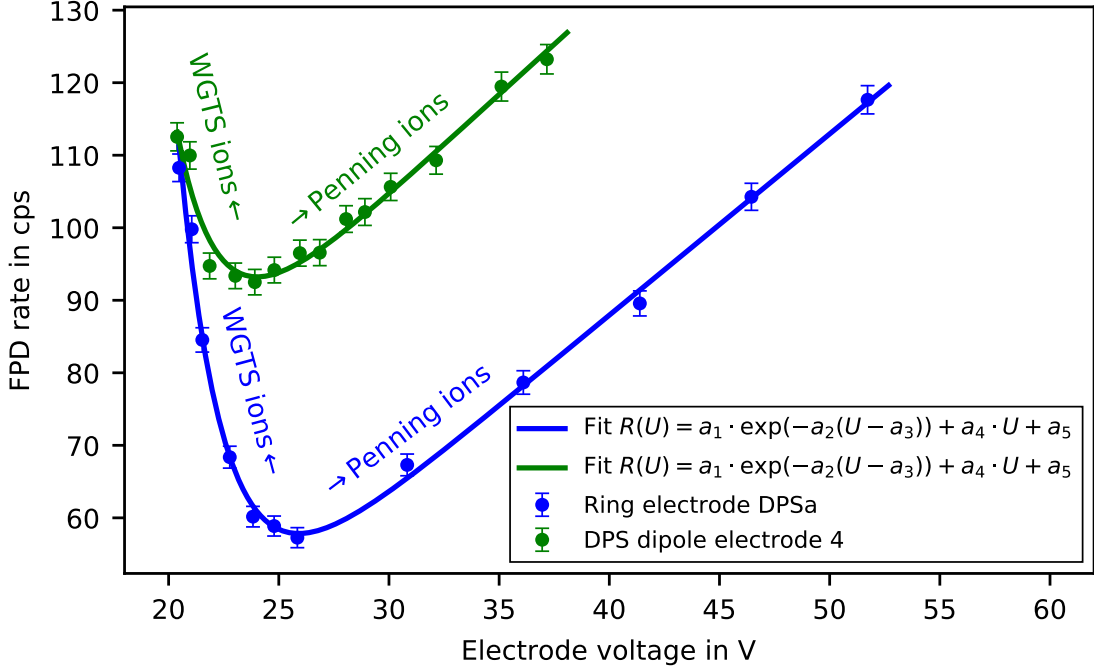


Figure 5.11: KNM1 ion energy spectrum measurements with DPS electrodes during tritium operation. The ion flux into the PS as measured by the ICE method versus the respective electrode voltage is shown. As for dipole electrode 4, the plotted voltage is the one of the lower half-shell while the upper half-shell voltage is always 5 V lower. The ring electrode measurement was performed at a tritium column density of $\mathcal{N} = 3.3 \times 10^{17}$ molecules/cm² (\triangleq 66% of the design value) and the dipole electrode measurement at $\mathcal{N} = 3.2 \times 10^{17}$ molecules/cm² (\triangleq 64% of the design value).

Those are non-thermal ions from molecular dissociation (cf. section 3.1.1). Above the threshold voltage where the WGTS ion flux is completely blocked the observed rate is solely caused by Penning ions produced by trapped electrons inside the blocking electrode potential¹⁰. These trapped electrons are in turn produced via impact ionization of gas molecules by β -electrons passing through. For the Penning ions a linear voltage dependence of the rate is observed.

These characteristics are similar to the observations for residual gas and deuterium ions during STSIIIa (cf. Fig. 5.4). It is expected that the Penning ions from the DPS electrodes are mostly residual gas ions because the tritium fraction of the gas composition is rather low there, although not zero as indicated by residual gas analyzer measurements. PS1 is located downstream of the CPS so at this position only non-tritium residual gas will contribute to the creation of Penning ions. Both assumptions are supported by the observed linear voltage-dependencies, which fit to the STSIIIa results for residual gas Penning ions before the first major tritium operation (see Fig. 5.4a). As the process is pressure-dependent, the PS1 Penning ion creation rates are roughly one order of magnitude lower than the ones from the DPS electrodes corresponding to the different residual gas pressure regimes.

The minima of the fit function given in Eq. 5.15 are 24 V (dipole 4 lower half-shell),

¹⁰The basic principle of the Penning trap ion creation mechanism is explained in section 5.2.1 for deuterium ions.

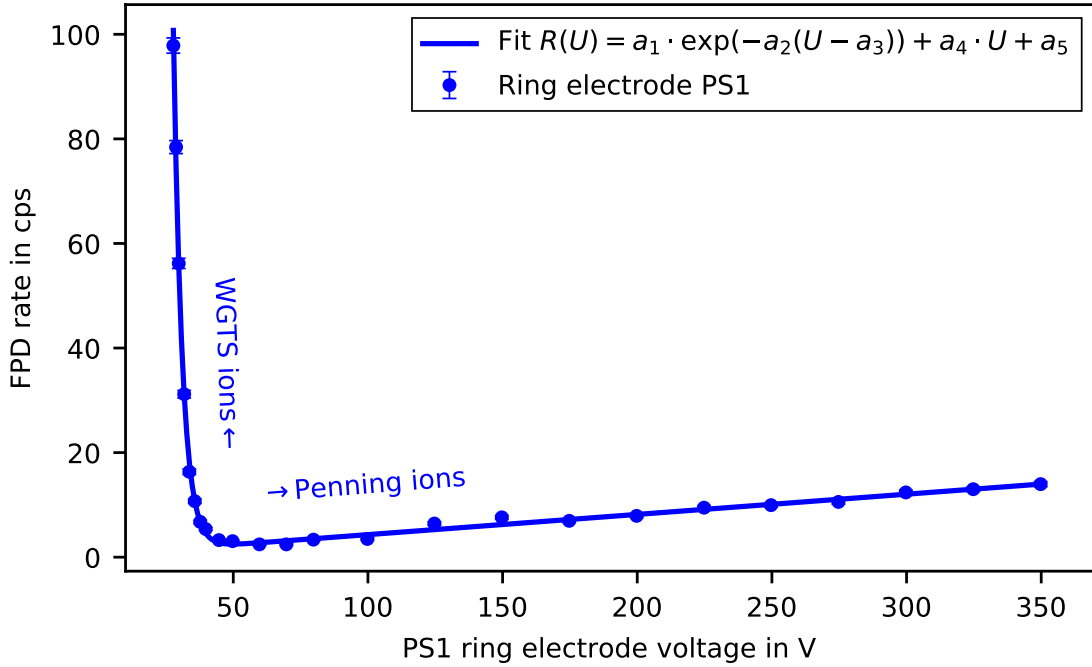


Figure 5.12: KNM1 ion energy spectrum measurement during tritium operation with ring electrode PS1. The ion flux into the PS as measured by the ICE method versus the PS1 ring electrode voltage is shown. Compared to the fourth dipole and the DPSa ring electrode (cf. Fig. 5.11), the obtained Penning ion-induced rates are significantly lower, which can be attributed to the lower pressure between CPS and PS. The data set was obtained at a tritium column density of $\mathcal{N} = 2.9 \times 10^{17}$ molecules/cm² (\triangleq 58% of the design value).

26 V (DPSa) and 50 V (PS1) for tritium column density fractions of 64%, 66% and 58% of the nominal design value, respectively. As it is shown in measurements with the DPSa ring electrode in Fig. 5.13, the minimum is stable to a few Volts for different column density values. So, in principle, these minima are the optimum operational voltages due to their perfect tradeoff between blocking the WGTS ion flux while minimizing the Penning ion production rate. However, Penning ions from the DPS beam line are blocked by the PS1 electrode anyway and those originating from PS1 itself are not tritiated and therefore not harmful for the MS background. Furthermore, neutralization (see next section 5.3.3) could lower the effective blocking voltage. Consequently, it is advisable to operate the blocking electrodes at voltages above their respective minimum.

5.3.3 Measurement of blocking electrode neutralization

The KNM1 campaign offered the first-ever opportunity of long-term operation of the system of blocking electrodes along the beam line with a high source activity. A rather critical point as to the long-term performance is the possibility of a neutralization of the blocking electrode voltages. The underlying concept is that secondary electrons will accumulate inside the potential well of the electrode, where they are trapped via the Penning mechanism.

In the first place, secondary electrons at these spots are created from residual or

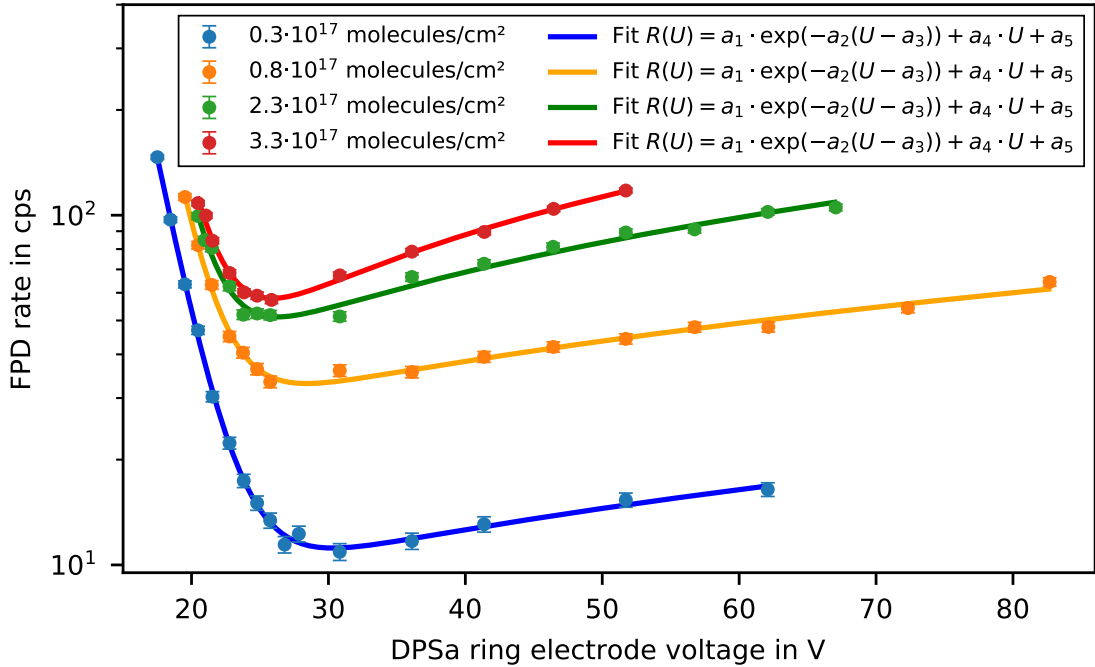


Figure 5.13: KNM1 ion energy spectrum measurements with ring electrode DPSa for different tritium column densities. The ion flux into the PS as measured by the ICE method versus the DPSa ring electrode voltage is shown for different tritium column densities ranging from 6% to 66% of the design value.

tritium gas ionizations by passing β -electrons. Once trapped, a single electron in turn will ionize further gas molecules which leads to an increased amount of accumulated secondary electrons while the positive ions will leave the trap. As more and more low-energy electrons are created, the potential well is filled up gradually with negative charge carriers. Over time the effective blocking voltage will thus be reduced (i.e. neutralized).

In the worst case, this effect would lead to a significant neutralization of all blocking electrodes, allowing tritium ion transmission towards the spectrometer section. From monitoring of the operational electrode voltages alone, this subliminal process would remain unnoticed. Consequently, dedicated measurements are required to determine the time scales of neutralization for each electrode.

Measurements were performed before the start of KNM1 with RW photoelectrons and residual gas Penning ions as well as in-situ during KNM1 and KNM2 tritium operation. The corresponding analysis has been carried out by A. P. Vizcaya Hernández which is why a detailed description will be given in [VH]. Within this section, only a brief overview of the measurements and the most important results will be given.

Test measurements before the start of KNM1

On February 28, 2019, a few days before the initial KNM1 WGTS ramp-up, the first measurement of blocking electrode neutralization was performed. As no tritium was circulating, ions were created from residual gas in analogy to STSIIIa (cf. section

5.2.1). Photoelectrons were provided by the negatively biased RW, which was illuminated by the Cermax[®] UV setup yielding a photocurrent of 1 μ A corresponding to 6×10^{12} photoelectrons/s. This is more than one order of magnitude above the photoelectron rate obtained with two MiniZ lamps during STSIIIa. The ion flux into the PS was measured via the ICE method.

In this configuration the blocking performance of ring electrode PS1 was measured twice: once while blocking the RW electrons with a negatively biased beam line electrode upstream of PS1 and once without blocking them. In both cases, applying a sufficiently high positive voltage to PS1 resulted in an immediate drop of the ICE count rate, as expected for a properly working blocking electrode. However, without blocking the electrons, the rate was rising again after a rather short time $\tau < 1$ min until saturating at an increased level. This can be interpreted as a neutralization process of the PS1 blocking voltage. When blocking the RW photoelectrons, they cannot reach PS1 so they cannot ionize residual gas and thereby produce secondary electrons which fill up the blocking potential well. When the electrons are not blocked, they are transmitted to PS1 which permits neutralization.

An analog investigation with the fourth DPS dipole electrode at a positive dipole field did not yield any difference between the two cases. This observation is in agreement with the expectation that neutralization processes of dipole electrodes do not occur. Inside a positive dipole field, electrons are removed within a short time and cannot accumulate.

These test measurements show that neutralization can happen within the time scale of seconds at the corresponding conditions. It should be emphasized that the measurements were performed with low-energy photoelectrons and not with high-energy β -electrons. During neutrino mass measurements, both the cross sections for residual gas impact ionization and the electron flux through the blocking electrodes are much lower than during these first test measurements. Thus, a several orders of magnitude larger neutralization time can be expected for nominal tritium operation.

In-situ monitoring during KNM1 and KNM2

In the course of the KNM1 and KNM2 campaigns, the process of neutralization has been investigated in-situ and the main blocking electrodes DPSa, PS1 and dipole electrode 4 were characterized. The basic idea is that a voltage neutralization of ΔU should shift the measured ion energy spectrum (cf. section 5.3.2) by $e\Delta U$. Neutralization can be reversed by removing the trapped electrons via the application of a negative voltage to the respective electrode.

The measurement procedure is thus as follows. After some waiting time t_{neut} during which neutralization should take place, the ion energy spectrum can be measured for the first time. Then, the electrode is emptied and afterwards the energy spectrum is measured again. Determining the shift $e\Delta U$ between both spectra yields the neutralization of the blocking voltage per time $\Delta U/t_{\text{neut}}$.

In the first days of tritium operation rather short t_{neut} on the order of hours to days were investigated in order to prevent unrecognized neutralization. Later, t_{neut} was increased to a few weeks. The most significant results were obtained in KNM2 at a high column density of 84% of the design value where neutralization tends to be faster than at lower tritium activity.

It was found that none of the three main blocking electrodes is neutralized on a time scale of hours, days or even weeks. Rather, within one week the voltages were neutralized by less than 1%. Thus, an operation over months would be possible

without any drawback.

The results are quite encouraging but nevertheless countermeasures against neutralization have been applied. First, the fourth DPS dipole electrode was continuously operated at a positive field with voltages of (+25 V/+20 V) applied to its lower and upper half-shell, respectively. In this configuration it can not be neutralized and secondary electrons which are created and trapped between the negative DPS and PS voltages are removed. Furthermore, the blocking electrodes are routinely emptied once per week in between the β -scanning runs. These countermeasures have enabled a safe operation of KATRIN over the term of several months during KNM1 and KNM2, without interruption of the ion blocking.

5.3.4 Background from tritium decay inside the dipole electrodes

Tritium gas decaying inside the electric potential of the negatively biased DPS dipole electrodes is a potential source of background for the neutrino mass determination as described in detail in section 3.1.3. Beta-electrons born inside the dipole electrode potential experience an energy shift which ultimately leads to a distortion of the original WGTS T_2 β -spectrum. This effect can be quantified in a dedicated measurement.

Measurement procedure

The β -electrons originating from the dipole electrodes are shifted to higher energies. This allows to measure the energy spectrum of those electrons by putting the MS retarding potential U_{ret} above the endpoint of the undisturbed WGTS T_2 β -spectrum. If the dipole electrode of interest is operated in monopole mode at the maximum set voltage of $U_{\text{max}} = -350$ V, its β -spectrum is shifted by $\Delta E = e|U_{\text{max}}|$ and will dominate the FPD signal rate above the T_2 endpoint. From the measured count rate the tritium activity inside the dipole electrode volume can be determined.

Since the partial pressure of tritium in the DPS is rather low and gets gradually further reduced by about a factor of 10 between two consecutive pump ports, the effect is on the order of 100 mcps, 10 mcps and 1 mcps for the three dipole electrodes, respectively. The sensitivity on measuring such low rates is reduced by the intrinsic MS background rate which is of the order of 100 mcps. Maximum sensitivity can be reached by setting the MS retarding potential as close as possible above the WGTS T_2 endpoint since the DPS signal rate increases to first order with $(E_{0,\text{DPS}} - E)^3$, where $E_{0,\text{DPS}}$ is the DPS β -spectrum endpoint.

KNM1 and KNM2 results

Measurements have been performed exclusively with the first dipole electrode in KNM1 and KNM2 because the beta-rate from the other electrodes was too small. Throughout the measurements the dipole electrodes 2 to 4 were kept stable at low voltages in order to avoid a systematic influence. A retarding voltage of $-18\,577$ V was applied to the MS and the air coils were set to the maximum field setting in order to ensure adiabatic transport of the β -electrons. The voltage of dipole electrode 1 was alternated between its minimum and maximum value. In the minimum voltage setting the MS background rate was measured, while in the maximum voltage setting the sum of the MS and the DPS dipole 1 background rate was measured. The results are plotted in Fig. 5.14.

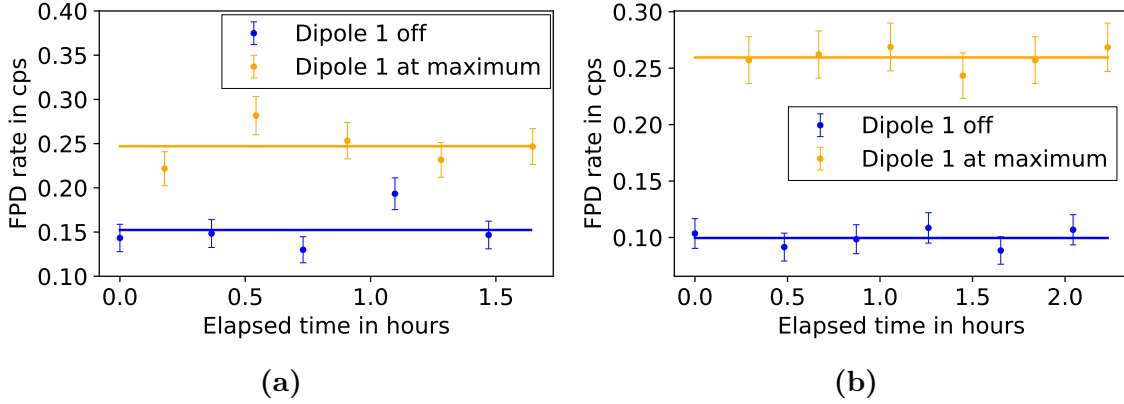


Figure 5.14: KNM1 and KNM2 measurements of the FPD background rate originating from tritium inside the first DPS dipole electrode. The FPD rate versus time is shown. Each data point is obtained in a 10 min run. The voltage setting of dipole electrode 1 is alternated between the maximum set point $U_{\max} = -350$ V and no voltage applied to both half-shells while the other dipole electrodes are kept stable at low voltages. As for KNM1 (a), the mean rates are determined to (152 ± 7) mcps (no voltage) and (247 ± 9) mcps (maximum voltage) at a mean column density of 2.5×10^{17} molecules/cm² ($\hat{=}$ 50% of the design value) and a mean tritium purity of $\epsilon_T = 95.9\%$. In KNM2 (b) the mean rates are (100 ± 5) mcps (no voltage) and (260 ± 8) mcps (maximum voltage) at a mean column density of $(4.22 \pm 0.01) \times 10^{17}$ molecules/cm² ($\hat{=}$ 84% of the design value) and a mean tritium purity of $\epsilon_T = 98.4\%$.

In order to determine the background rate from the tritium decay inside the first dipole electrode R_{dipole1} at the maximum electrode voltage U_{\max} , one has to subtract the measured rates from each other yielding:

$$\begin{aligned} \text{KNM1: } R_{\text{dipole1}}(U_{\max}) &= (95 \pm 12) \text{ mcps}, \\ \text{KNM2: } R_{\text{dipole1}}(U_{\max}) &= (160 \pm 10) \text{ mcps}. \end{aligned} \quad (5.16)$$

The discrepancy between the two values can be explained with the higher column density and tritium purity in the KNM2 measurement compared to KNM1 (cf. caption of Fig. 5.14). As for the KNM2 measurement, the column density can be determined with an uncertainty below 1% following a proper calibration against a WGTS pressure sensor, which was conducted by F. Block, C. Köhler and A. Marsteller for this specific setting¹¹. Also, the column density stability at this campaign was better and the results show a higher statistical significance. Consequently, only the KNM2 result is used for the following calculations.

Determination of the number of tritium atoms inside the first DPS dipole electrode potential from KNM2 results

In general, the FPD rate R and the number of tritium atoms N_T inside a starting potential U are linked via

$$R = c \cdot N_T \cdot (E_0 - eU_{\text{ana}} - eU)^3 \cdot \frac{1 - \cos(\theta)}{2} \quad (5.17)$$

¹¹F. Block, C. Köhler, A. Marsteller and P. Filip, KATRIN KNM2 Reference Report - Systematic Uncertainty of Column Density / Column Density Times Inelastic Scattering Cross-Section, internal report, 2020.

with a constant c , the β -spectrum endpoint E_0 , the elementary charge e , the absolute MS analyzing plane retarding voltage U_{ana} and the maximum pitch angle θ . Here, the β -spectrum shape is approximated by the cubic term $(E_0 - eU_{\text{ana}} - eU)^3$. The term $(1 - \cos(\theta))/2 = (1 - \cos(\arcsin(\sqrt{B/B_{\text{max}}})))/2$ represents the probability of a β -electron reaching the FPD without getting reflected magnetically, which was already introduced in Eq. 4.2 of section 4.5 for $^{83\text{m}}\text{Kr}$ conversion electrons.

Using Eq. 5.17, the relative number of tritium atoms inside the potential of the first dipole electrode $N_{\text{T,dipole1}}$ can be derived from the rate R_{dipole1} stated in Eq. 5.16. It is given by

$$\frac{N_{\text{T,dipole1}}}{N_{\text{T,WGTS}}} = \frac{R_{\text{dipole1}} \cdot (E_0 - eU_{\text{ana,WGTS}} - eU_{\text{WGTS}})^3 \cdot (1 - \cos(\theta_{\text{WGTS}}))}{f \cdot R_{\text{WGTS}} \cdot (E_0 - eU_{\text{ana,dipole1}} - eU_{\text{dipole1}})^3 \cdot (1 - \cos(\theta_{\text{dipole1}}))}. \quad (5.18)$$

Here, $N_{\text{T,WGTS}}$ is the number of tritium atoms contained inside the potential $U_{\text{WGTS}} = 0$ V of the WGTS. The corresponding FPD rate R_{WGTS} was measured at equal tritium purity and column density right after R_{dipole1} . The parameter values stated in Tab. 5.4 are plugged into Eq. 5.18. In addition, the correction factor f can be used in order to take into account the spatially inhomogeneous volume-weighted pressure pV , electric potential U and maximum pitch angle θ distributions inside the 134 T cm^2 flux tube of the first dipole electrode. Spatially homogeneous distributions of $pV = \text{const.}$, $U = -350$ V and $\theta = 77.4^\circ$ are given for $f = 1$. In this case, the resulting ratio of tritium atoms is given by

$$\frac{N_{\text{T,dipole1}}}{N_{\text{T,WGTS}}}(f = 1) = (7.00 \pm 0.44) \times 10^{-7}. \quad (5.19)$$

In reality, all three distributions are rather inhomogeneous, which is modeled by dedicated MolFlow+, KEMField and KASSIOPEIA simulations. A correction factor

Table 5.4: List of KNM2 parameters for the determination of the relative number of tritium atoms inside the potential of the first DPS dipole electrode. Shown are the FPD rates R measured at the absolute MS analyzing plane retarding voltages U_{ana} , at maximum pitch angles θ with a β -spectrum endpoint E_0 . The retarding voltage U_{ret} applied to the MS is effectively reduced by $\Delta U_{\text{ret}} = 2.15$ V in the analyzing plane, which is derived from a dedicated simulation by F. Glück. The analyzing plane retarding voltage is thus given by $U_{\text{ana}} = U_{\text{ret}} - \Delta U_{\text{ret}}$. The maximum pitch angles are calculated by $\theta = \arcsin(\sqrt{B/B_{\text{max}}})$ with the WGTS and the DPS dipole 1 magnetic field, $B_{\text{WGTS}} = 2.52$ T and $B_{\text{dipole1}} = 4.0$ T, respectively, and the maximum magnetic field $B_{\text{max}} = 4.2$ T at the pinch magnet.

Parameter	Value
R_{WGTS} in cps	107378 ± 59
R_{dipole1} in cps	0.160 ± 0.010
$eU_{\text{ana,WGTS}}$ in eV	$18227.01 - 2.15$
$eU_{\text{ana,dipole1}}$ in eV	$18577.01 - 2.15$
eU_{WGTS} in eV	0
eU_{dipole1} in eV	-350
θ_{WGTS} in $^\circ$	50.77
θ_{dipole1} in $^\circ$	77.4
E_0 in eV [AAA+19c]	18573.7 ± 0.1

$f = 0.54$ is derived as described in the appendix chapter 8. The result for the ratio of tritium atoms is then

$$\frac{N_{\text{T,dipole1}}}{N_{\text{T,WGTS}}}(f = 0.54) = (1.288 \pm 0.080) \times 10^{-6}. \quad (5.20)$$

It should be noted that both f and $N_{\text{T,dipole1}}$ are dependent on the considered volume of the 134 T cm^2 flux tube inside the dipole electrode geometry. The result of $f = 0.54$ was determined by taking all simulated values within the length of the dipole electrode $l = 0.84\text{ m}$ into account. Along the central z -axis the electric potential U is reduced to 68% at both ends $z = \pm 0.42\text{ m}$ with respect to the center of the dipole electrode at $z = 0\text{ m}$. Even lower potential values can be neglected because of their minor contribution to the background rate, which is suppressed by the cubic term $(E_0 - eU_{\text{ana,dipole1}} - eU)^3$.

Comparison to pressure gauge measurements

The result for the ratio of tritium atoms in Eq. 5.20 was derived by combining the results of a FPD rate measurement and several numerical simulations. It can be converted into a tritium density in the first dipole electrode in order to compare it to measurements of the MKS[®] 423 cold cathode vacuum pressure sensors mounted in PP0 and PP1 of the DPS.

First, the absolute number of T_2 molecules inside the dipole electrode 1 is determined:

$$\begin{aligned} N_{\text{T}_2,\text{dipole1}}(f = 0.54) &= \frac{N_{\text{T,dipole1}}}{N_{\text{T,WGTS}}}(f = 0.54) \cdot \epsilon_{\text{T}} \cdot \mathcal{N} \cdot A_{\text{WGTS}} \\ &= (2.83 \pm 0.18) \times 10^{13}. \end{aligned} \quad (5.21)$$

Here, $\epsilon_{\text{T}} = 98.4\%$ is the tritium purity, $\mathcal{N} = 4.2 \times 10^{17}\text{ molecules/cm}^2$ is the column density and $A_{\text{WGTS}} = 53.1\text{ cm}^2$ is the cross-sectional area of the 134 T cm^2 flux tube inside the WGTS. Further, the considered flux tube volume is given by

$$V_{\text{dipole1}} = 3765\text{ cm}^3. \quad (5.22)$$

Combining Eqs. 5.21 and 5.22 yields the mean number density of T_2 molecules inside the first dipole electrode as derived by a measurement of the corresponding FPD rate and dedicated simulations:

$$\begin{aligned} n_{\text{T}_2,\text{dipole1}}(f = 0.54) &= \frac{N_{\text{T}_2,\text{dipole1}}(f = 0.54)}{V_{\text{dipole1}}} \\ &= (7.52 \pm 0.47) \times 10^9 \frac{1}{\text{cm}^3}. \end{aligned} \quad (5.23)$$

At PP0 and PP1 pressure values of $8.4 \times 10^{-7}\text{ mbar}$ and $7.1 \times 10^{-8}\text{ mbar}$ were measured, respectively. The values were provided by A. Marsteller after applying correction factors for considering the gas type and the influence of the magnetic field on the pressure reading. The mean pressure $p = 4.6 \times 10^{-7}\text{ mbar}$ can be converted into a number density

$$\begin{aligned} n_{\text{T}_2,\text{dipole1}} &= \frac{p}{k_{\text{B}}T} \\ &= 1.1 \cdot 10^{10} \frac{1}{\text{cm}^3} \end{aligned} \quad (5.24)$$

with the Boltzmann constant k_B and the temperature $T = 293\text{ K}$. This number is in good agreement with the result stated in Eq. 5.23, considering the estimated uncertainty of $\sim 30\%$ ¹² on the measured pressure values after applying the gas type and magnetic field correction factors.

Determination of the systematic squared neutrino mass shift for KNM2

During neutrino mass measurements the first three DPS dipole electrodes are operated at negative voltages. Consequently, all three of them contribute to the background by tritium decay inside negative potentials along the beam line and effectively distort the measurement by shifting the best-fit result of the squared neutrino mass $m_{\bar{\nu}_e}^2$. In [Kle19] maximum set points of $(-5\text{ V}/-15\text{ V})$, $(-5\text{ V}/-35\text{ V})$ and $(-5\text{ V}/-85\text{ V})$ were theoretically derived for the lower/upper half-shells of dipole electrode 1, 2 and 3, respectively. For these voltages the expected systematic shift $\Delta m_{\bar{\nu}_e}^2$ is determined in this paragraph based on the ratio of tritium atoms in dipole electrode 1 and in the WGTS (cf. Eq. 5.20). The final result for $\Delta m_{\bar{\nu}_e}^2$ was simulated by L. Köllenberger with the Kafit software [Kle14] using Monte Carlo methods.

The software generates a β -spectrum based on the implemented model of β -decay and transmission of β -electrons from the source towards the FPD. Four simulations were performed in order to generate the signal WGTS spectrum and the three DPS dipole electrode background spectra. All four spectra were combined by stacking and fitted with the function given in Eq. 2.8. The best-fit result for $m_{\bar{\nu}_e}^2$ was then compared to the analogous result determined in an exclusive fit of the signal WGTS β -spectrum. Subtracting both results yields the expected shift $\Delta m_{\bar{\nu}_e}^2$.

The signal WGTS spectrum was simulated with the parameters $E_0 = 18\,573.7\text{ eV}$ [AAA+19c], $m_{\bar{\nu}_e}^2 = 0\text{ eV}^2/c^4$ and the amplitude corresponding to the nominal KNM2 β -activity. For the dipole electrode background spectra, endpoints of $E_{0,\text{dipole1}} = E_0 + 15\text{ V}$, $E_{0,\text{dipole2}} = E_0 + 35\text{ V}$ and $E_{0,\text{dipole3}} = E_0 + 85\text{ V}$ corresponding to their respective maximum bias voltage were assumed. The neutrino mass was likewise set to zero. The amplitudes are defined by the respective number of tritium atoms inside each dipole electrode potential. For dipole electrode 1 this number was determined from the ratio stated in Eq. 5.20, while for the dipole electrodes 2 and 3 the number was reduced by a factor of 10 and 100, respectively.

Spatially inhomogeneous distributions of the volume-weighted pressure pV , the electric potential U and the maximum pitch angle θ were not implemented in the Kafit simulation. However, especially the distribution of U is important to consider since all three dipole electrodes are operated in dipole mode so their effective potentials are reduced significantly compared to monopole mode operation. Therefore, for each dipole electrode $i \in (1,2,3)$ the rate $R_i(U_{\text{ana}})$ simulated at an analyzing plane retarding voltage U_{ana} had to be scaled by a dipole mode correction factor $f_{D,\text{dipole}i}(U_{\text{ana}}) < 1$. The derivation of $f_{D,\text{dipole}i}(U_{\text{ana}})$ from numerical simulation results is presented in the appendix chapter 8 for each of the three electrodes. Like for the correction factor f used for calculating the result of Eq. 5.20, it is important to emphasize that the results for $f_{D,\text{dipole}i}(U_{\text{ana}})$ are dependent on the considered volume of the 134 T cm^2 flux tube inside the dipole electrode geometry. Only the simulated pV , U and θ values within the length of the dipole electrode $l = 84\text{ m}$ were taken into account.

¹²Personal correspondence with A. Marsteller, 2020.

The resulting shift of the squared neutrino mass is then given by

$$\Delta m_{\nu_e}^2 = -6.1 \times 10^{-3} \frac{\text{eV}^2}{c^4} \quad (\text{preliminary}), \quad (5.25)$$

which would be negligible for KNM2. However, it is currently still preliminary because it was produced just before the completion of this thesis. Furthermore, at the moment there is some tension between this result and the one obtained in analogous Monte Carlo simulations with the Fitrium software [Kar18], which yield a larger value slightly above $1 \times 10^{-2} \text{eV}^2/c^4$.¹³ In any case, the systematic effect is probably negligible for KNM2, but a re-evaluation is necessary for future measurement campaigns.

5.3.5 Optimum ring and dipole electrode voltage settings

After the investigations described in the three preceding sections, the optimum electrode operational voltages during neutrino mass measurements can be defined. A short summary of the relevant findings is given in the following.

- The results stated in section 5.3.2 revealed that there is an optimum tradeoff between a voltage setting where ions from WGTS might pass and voltages where the Penning ion rate is elevated. At a column density on the order of 60% of the design value, these tradeoff voltages were determined to be 50 V for PS1, 26 V for DPSa and 24 V/19 V for DPS dipole electrode 4. For lower column densities the values are slightly higher.
- In addition, the effect of blocking voltage neutralization (cf. section 5.3.3) has to be considered. In principle, the results indicate that this process is negligible for a time scale of several weeks under nominal KATRIN conditions. Nevertheless, applying rather high voltages is advised. The linear increase of the Penning ion rate is acceptable, since the PS1 rate is rather low and residual gas Penning ions are not harmful for the MS background. Penning ions produced in the DPS could in principle contain a small fraction of tritium but those ions are blocked at the PS entrance by the PS1 ring electrode. On top of that, the fourth dipole electrode is operated in dipole mode with a positive blocking field acting as a non-neutralizable barrier. With three properly working blocking electrodes in place, it is reasonable to put the DPSb ring electrode to a rather low voltage of 5 V because its Penning ion rate is the highest of all electrodes as found in STSIIIa.
- In section 5.3.4 the influence of the tritium content of the first three DPS dipole electrodes was determined. It was found that the number of tritium atoms affected by the first dipole electrode potential is on the order of 10^{-6} compared to the WGTS. This number was assumed to be further reduced by a factor of 10 for the second and a factor of 100 for the third dipole electrode. The preliminary systematic shift $\Delta m_{\nu_e}^2 = -6.1 \times 10^{-3} \text{eV}^2/c^4$ (cf. Eq. 5.25) was determined for voltages of $(-5 \text{ V}/-15 \text{ V})$, $(-5 \text{ V}/-35 \text{ V})$ and $(-5 \text{ V}/-85 \text{ V})$ applied to the lower/upper half-shells of the dipole electrodes 1, 2 and 3, respectively. For KNM2 this preliminary shift would be negligible. When the

¹³L. Köllenberger, Influence of residual gas in the DPS on the neutrino mass, Talk at internal meeting, 2020.

Table 5.5: Overview of the beam line electrodes' optimum voltage settings.

Shown are the recommended set voltages based on systematic characterization measurements detailed in the sections 5.3.2 to 5.3.4. It is important to emphasize that the optimum values stated for the dipole electrodes 1 to 3 are preliminary, because they are valid for KNM2 but not necessarily for future campaigns in which the neutrino mass sensitivity will be much larger.

Dipole electrode	1	2	3	4
Optimum setting	(−5 V/−15 V)	(−5 V/−35 V)	(−5 V/−85 V)	(+25 V/+20 V)
Ring electrode	DPSa	DPSb	PS1	
Optimum setting	+40 V	+5 V	+200 V	

ultimate neutrino mass sensitivity is targeted in future campaigns, the shift induced by this effect probably has to be re-evaluated and either has to be taken into account in the fitting model or the voltages have to be reduced in order to mitigate the background contribution.

Taking all the above arguments into account leads to the optimum set voltages given in Tab. 5.5, which have been applied during KATRIN neutrino mass measurement runs up to now. With these settings the tritium ion flux is successfully blocked from the spectrometer section, as demonstrated by the measurements presented in the next section.

5.3.6 Residual tritium ion flux into the pre-spectrometer

An ion flux into the PS has to fulfill the limit of $\phi_{\text{CPS} \rightarrow \text{PS}} < 1 \times 10^4 \text{ T}_3^+$ ions/s according to Eq. 3.9 in order to meet the KATRIN background requirements. Dedicated ion flux measurements with both of the two ion detection techniques in the PS (cf. section 5.1.2) were performed at the ring and dipole electrode voltage settings stated in Tab. 5.5. While the PS current was monitored continuously throughout the months of operation, the ICE method requires special SDS settings and was only applied in between β -scanning runs on a regular basis.

ICE method measurements

At the beginning of each campaign the PS was operated in the ICE mode providing information about the ion flux into the PS during the ramp-up of the WGTS tritium column density with maximum sensitivity. Afterwards, regular measurements were carried out for monitoring the long-term performance of ion blocking. The results for KNM1 and KNM2 are shown in Fig. 5.15. The measured rates can be converted to the corresponding ion flux into the PS via dividing by the calibration factor $C_{\text{ICE}} = (2.771 \pm 0.095) \times 10^{-3} \text{ counts/ion}$ (cf. Eqs. 5.3 and 5.11). For both campaigns an upper limit of $\phi_{\text{CPS} \rightarrow \text{PS}} < 3 \times 10^3 \text{ ions/s}$ can be stated. This is more than a factor of 3 below the required upper limit.

In Fig. 5.15b a measurement of the background rate is included for which the beam line valve V2 between DPS and CPS was closed, so neither ions nor β -electrons were able to reach the PS. The difference between a background rate of around 0.3 cps and a signal rate of a few cps at opened V2 could in principle be caused by a tritium ion flux into the PS. However, it is more likely that the difference is attributed to non-tritiated residual gas Penning ions produced from trapped electrons inside

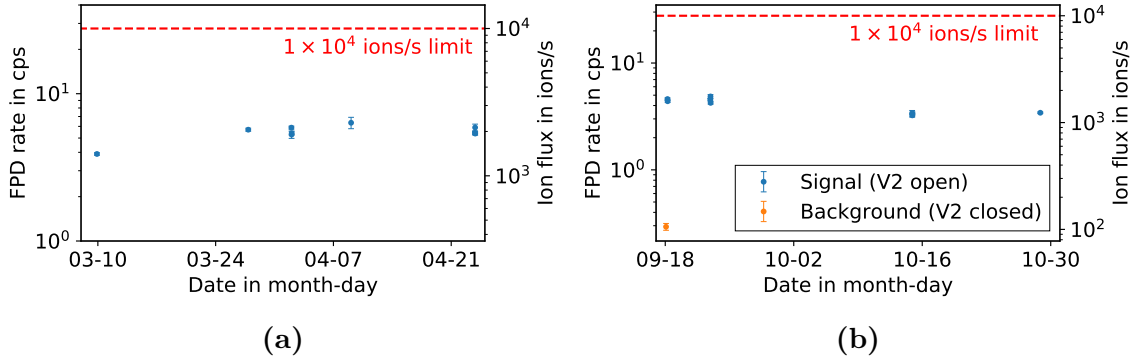


Figure 5.15: KNM1 and KNM2 ICE method measurements of the tritium ion flux into the PS. The FPD rate as measured by the ICE method is shown over a time of about one and a half months for KNM1 (a) and KNM2 (b), respectively. All beam line blocking and drifting electrodes are actively operated at nominal settings. The PS1 ring electrode is set to +200 V for KNM1 and to +60 V for KNM2 measurements in order to reduce the Penning ion contribution to the rate. For the KNM2 background measurement the beam line valve V2 between DPS and CPS was shut. In both campaigns the obtained values are significantly below the required limit of about 28 cps corresponding to $\phi_{\text{CPS} \rightarrow \text{PS}} = 1 \times 10^4$ ions/s.

the PS1 ring electrode¹⁴ (cf. section 5.3.2). Consequently, the true tritium ion flux into the PS is probably even lower than the upper limit of 3×10^3 ions/s stated above.

PS current measurements

Long-term measurements of the PS cone current were performed over the whole course of KNM1 and KNM2. No significant current increase was measured. In Fig. 5.16 current data of a 2019 (see Fig. 5.16a) and a 2020 (see Fig. 5.16b) WGTS column density ramp-up is plotted. The first was done in May 2019 over the course of the KNM1 campaign up to a fraction of about 88% of the design column density. To date, this is the highest ever achieved tritium density. The second one was executed one year later in May 2020 with the WGTS beam tube operated at a temperature $T \approx 80$ K at roughly 40%¹⁵ of the design column density. Both data sets were measured during nominal PS operation with voltages of -10 kV applied to the vessel and -10.5 kV applied to the inner electrodes.

Averaging the current values before and after the ramp-up yields no significant deviation from the dark current after tritium injection. These results support the complementary findings with the ICE method. An upper limit of the ion flux can be derived from the KNM1 measurement where the current after the WGTS ramp-up is slightly increased by $I_{\text{cone,down}} = (6.3 \pm 3.1)$ fA. Dividing this number by the overall calibration factor for the nominal PS setting $C(\text{nominal}) = (2.09 \pm 0.56) \times 10^{-19}$ C (cf. Eqs. 5.2 and 5.8), yields the corresponding ion flux

¹⁴Exact and generally valid numbers for the expected Penning rates at the PS1 voltages of +200 V (KNM1) and +60 V (KNM2) cannot be stated. One reason is that they depend on the column density, which makes it hard to distinguish between rates induced by WGTS ions and Penning ions. Further, the measured rate depends on the efficiency of the "conditioning" of the PS prior to the measurement (cf. section 5.1.2). The longer this preconditioning lasts, the lower is the Penning ion background rate measured in the ICE mode.

¹⁵Personal correspondence with C. Röttele, 2020.

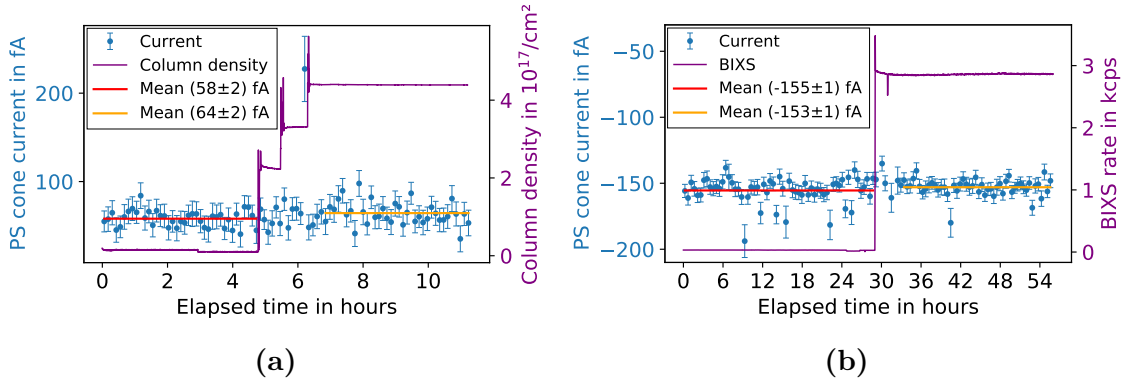


Figure 5.16: PS cone current measurements during WGTS tritium column density ramp-up. PS cone current data and a column density ramping curve are shown over time for one measurement in May 2019 (a) and one in May 2020 (b), respectively. Before and after the ramp-up the PS current data is averaged by calculating the arithmetic mean. No significant current increase is observed. In (a) the column density values as derived from throughput sensor data are plotted for illustrating the WGTS ramp-up. The spikes at the beginning of each step are artifacts caused by over-regulation of the throughput sensor. In (b) the WGTS is operated in krypton mode at $T \approx 80$ K and the column density ramp-up is indicated by the time-dependent count rate of one of the two BIXS detectors. The stable count rate after the ramp-up corresponds to roughly 40% of the nominal design column density.

into the PS $\phi_{\text{CPS} \rightarrow \text{PS}} \leq (3.0 \pm 1.7) \times 10^4$ ions/s.

5.3.7 Conclusion

Both dipole and ring electrodes were operated successfully over the course of two neutrino mass measurement campaigns. Various characterization measurements revealed the optimum voltage settings for each electrode, which can be found in Tab. 5.5. At these settings, tritium ions are successfully blocked from the SDS part, which was validated independently by both PS detection methods.

The blocking electrodes show reliable long-term performance since their blocking potentials are not neutralized by low-energy electrons on a time-scale of weeks or less. It was nevertheless decided to empty them by inverting their polarity on a weekly basis in between β -scanning runs.

Positive tritium ions were successfully drifted by the DPS dipole electrodes inducing a column density-dependent current. Also, the amount of tritium atoms inside the first dipole electrode could be determined. This is an important information necessary for modeling the corresponding energy-dependent background rate which distorts the WGTS T_2 signal spectrum. First Monte Carlo simulations were performed in order to quantify the expected shift of the best-fit squared neutrino mass value.

5.4 Summary

In KATRIN various experimental methods exist for blocking, removing and detecting tritium ions. These methods have been characterized in the STSIIIa campaign

and used for tritium ion monitoring in the PS during the neutrino mass measurements in KNM1 and KNM2.

For both the PS current and the ICE detection method the corresponding calibration factors could be determined experimentally. A current of 1 fA measured at the PS downstream cone electrode at a voltage of -10.5 kV is equivalent to $(4.8 \pm 1.3) \times 10^3$ ions/s flowing into the PS. As for the ICE method, a rate of 1 cps measured at the FPD corresponds to (361 ± 12) ions/s. Obviously, the ICE sensitivity is sufficient to assess values well below the required upper limit of $\phi_{\text{CPS} \rightarrow \text{PS}} = 1 \times 10^4 \text{ T}_3^+$ ions/s.

In the neutrino mass measurement campaigns KNM1 and KNM2 the two ion detection methods were applied. It could be validated that $\phi_{\text{CPS} \rightarrow \text{PS}}$ is more than a factor of 3 below the required upper limit and therefore a significant contribution to the MS background rate is excluded. This can be attributed to the properly working ion blocking and removing electrodes along the beam line.

Optimum operational voltage settings for minimizing the ion-induced MS background were found in dedicated in-situ studies and subsequently applied throughout the entire β -scanning runs of KNM1 and KNM2. Over longer periods of time the blocking performance in principle could be affected by the accumulation of low-energy electrons inside the electrode which would effectively neutralize the blocking potential. However, there was no noteworthy deterioration of the blocking electrode potentials observed on time scales relevant for KATRIN. Several months of tritium operation without any ion-related issues support that.

A different type of background contribution arises from the decay of neutral tritium gas inside the electric potentials of the three negatively biased DPS dipole electrodes. The negative dipole electrode voltages shift the β -electrons to higher energies which leads to an energy-dependent background spectrum superimposed to the original WGTS T_2 signal spectrum. In a dedicated measurement the tritium fraction contained in DPS dipole electrode 1 relative to the WGTS could be determined to be $(1.288 \pm 0.080) \times 10^{-6}$. By assuming the amount of tritium inside the dipole electrodes 2 and 3 to be 10 and 100 times lower, respectively, a preliminary result for the systematic shift of the squared neutrino mass of $\Delta m_{\bar{\nu}_e}^2 = -6.1 \times 10^{-3} \text{ eV}^2/c^4$ was determined in Monte Carlo simulations assuming bias voltages of $(-5 \text{ V}/-15 \text{ V})$, $(-5 \text{ V}/-35 \text{ V})$ and $(-5 \text{ V}/-85 \text{ V})$ applied to the lower/upper half-shells of the dipole electrodes 1, 2 and 3, respectively.

This chapter was mainly devoted to the ion-induced effects in the DPS and the SDS. For KATRIN, in addition, the effects induced by ions and electrons in the WGTS are of major importance. These systematic effects might have a direct impact on the neutrino mass result (cf. section 3.1.5) and are not yet implemented in the fitting model. The first-ever experimental studies of these effects are presented in the next chapter.

6. Experimental investigations of the WGTS tritium plasma

The WGTS gas contains neutral hydrogen isotopologues, electrons and both negative and positive ions. Those particles form a plasma which could induce systematic effects during the neutrino mass determination. These effects could be due to spatial inhomogeneities or temporal variations of the plasma potential, as well as effective changes of the kinetic energy of the β -electrons by high-frequency plasma instabilities (for details see section 3.1.5). From these considerations, objectives for the plasma investigations of this thesis were formulated in section 3.3. Those objectives are pursued in this chapter.

Plasma effects can be studied using small admixtures of gaseous $^{83\text{m}}\text{Kr}$ added to the tritium gas. The drawback of this method is that the WGTS operation mode has to be changed significantly with respect to the nominal one. First of all, the temperature has to be increased from $T = 30\text{ K}$ to $T = (80 - 100)\text{ K}$ in order to prevent krypton freeze-out. Second, a different gas circulation mode is required, in which the gas pumped out differentially is directly re-injected into the beam line without any purification¹. Because of these differences, further diagnostic tools are required which allow to characterize the source plasma at identical measurement conditions at which the neutrino mass runs take place. In the course of this thesis, such methods have been developed and applied in the KATRIN campaigns KNM1 and KNM2.

In this chapter detailed investigations of the WGTS plasma effects using non-krypton characterization methods are presented. The primary aim of the investigations is to improve the understanding of the interplay between the plasma and various beam line hardware devices defining its boundary conditions. Especially interesting is the influence of the rear wall surface potential on the plasma potential as dedicated

¹During the writing process of this thesis a new loop circulation mode for the krypton operation at $T = (80 - 100)\text{ K}$ was established in order to make it more comparable to the nominal mode [Mar]. In this novel approach the gas stream in the loop system is split into two parts. One part is directly fed back into the WGTS without filtering the impurities and the other part is purified by the permeator, like in the nominal mode. On this way, column density values and gas purities comparable to the nominal mode can be maintained. The drawback is a highly reduced $^{83\text{m}}\text{Kr}$ activity inside the WGTS.

simulations [Kuc16] indicate that this is the key parameter in establishing a homogeneous starting potential distribution for the β -electrons. Further, the stability of the plasma potential has to be investigated in the long-term (due to plasma instabilities or possible drifts of the boundary potentials) and on the sub-second scale (due to possible high-frequency plasma instabilities). Corresponding studies with $^{83\text{m}}\text{Kr}$ can be found in [Ost20, Mac].

At first, the WGTS plasma is introduced as a special case within the general plasma physics framework in section 6.1. Then, different methods for plasma characterization are explained in detail in section 6.2 and applied during KNM1 and KNM2 in section 6.3. The most important findings of this chapter are summarized in section 6.4.

6.1 The plasma in the KATRIN tritium source

Most of the baryonic matter in the visible universe exists in the form of a plasma. The term was used for the first time by I. Langmuir in 1928 describing a "region containing balanced charges of ions and electrons" [Lan28]. Plasma phenomena are complex and of importance for various physics disciplines so that the specific field of plasma physics has been developed. In this section some basic concepts are introduced which are relevant for a detailed understanding of the WGTS plasma. The description of the general fundamentals is based on [Bit04, Str18].

6.1.1 Key concepts of plasma physics

A plasma is characterized mainly by two parameters: the density of charge carriers n and its temperature T . A substance is referred to as plasma if n is sufficiently high so that a collective behavior due to long-range electric and magnetic forces is established. However, the transition into the plasma state is continuous because there is no definite threshold value. The most prominent examples of a plasma created in a laboratory are the ones present inside a thermonuclear fusion reactor at $T \sim 10^8$ K and $n \sim 10^{14}$ cm $^{-3}$. Compared to this, the WGTS plasma is extremely cold with $T = 30$ K and exhibits a very low density of $n = 10^5$ cm $^{-3}$ to 10^6 cm $^{-3}$ [KAT05, Kuc16]. As shown in Fig. 6.1, the WGTS plasma parameters are indeed different from basically all other plasmas commonly known. Another rather special feature is the high magnetization of the WGTS plasma. Magnetic fields of up to $B = 3.92$ T constrain the mobility of charge carriers perpendicular to the field lines significantly. Despite these rather uncommon properties, the WGTS gas column nevertheless fulfills the necessary criteria defined for the plasma state, which will be demonstrated in the next paragraph.

Plasma criteria

In general four criteria are defined when classifying a plasma. One important effect is the shielding of electric fields inside the plasma over a characteristic distance of [Bit04]

$$\lambda_D = \sqrt{\frac{\epsilon_0 k_B T}{n_e e^2}} \quad (6.1)$$

which is called the Debye length. Here, ϵ_0 is the vacuum permittivity, k_B is the Boltzmann constant, T is the temperature, n_e is the electron number density and

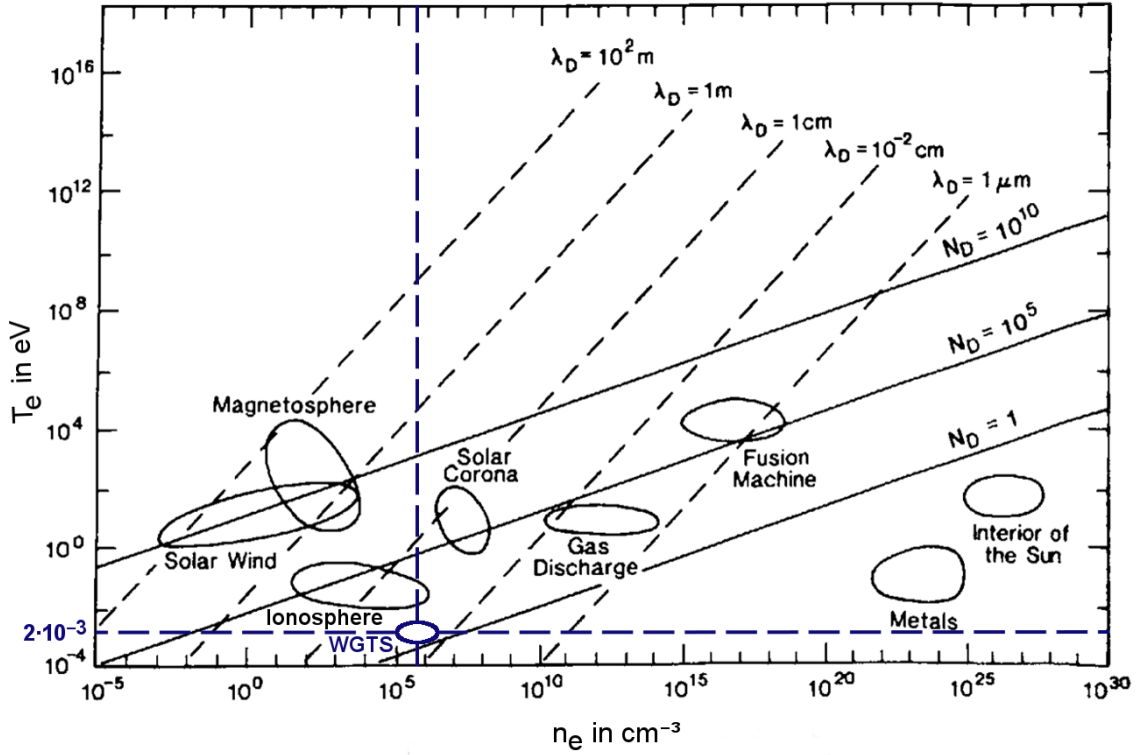


Figure 6.1: Temperature and charge carrier density for the WGTS plasma and other common plasmas. The solid and dashed lines indicate different values for the Debye length λ_D and the plasma parameter $N_D = 4/3\pi n\lambda_D^3$, respectively. The figure is taken from [Gal12] and inspired by [Kuc16].

e is the elementary charge. A sphere of radius λ_D within the plasma is referred to as Debye sphere. The influence of a charged particle's Coulomb potential on other particles is restricted to distances below the Debye length. The same is true for the influence of a boundary surface which is maintained on a constant potential. A layer of width λ_D called plasma sheath between surface and plasma is established within which the perturbation is effectively shielded. This is illustrated in Fig. 6.2.

From the concept of the Debye length necessary conditions for the plasma state can be derived.

- First, the macroscopic dimension L of the plasma has to be much larger than one Debye length $L \gg \lambda_D$ providing sufficient space for the shielding effect. As for the WGTS, L is on the order of 10 m. This value exceeds λ_D , which is in the range between $\sim 1 \times 10^{-3}$ m and $\sim 4 \times 10^{-4}$ m for $T = 30$ K, by many orders of magnitude.
- Second, the quasi-neutrality condition $n_e \approx Z_i \cdot n_i$, with the density of electrons n_e , ions n_i and their charge numbers Z_i , has to be fulfilled on distances larger than λ_D , provided that there are no external disturbances. Within the small Debye sphere $4/3\pi\lambda_D^3$ quasi-neutrality is necessarily violated. This requirement is fulfilled for the source plasma. Only for certain boundary conditions, which can be viewed as external disturbances, quasi-neutrality is violated (see section 6.1.3 for details). E.g. for high positive bias voltages applied to the RW the macroscopic positive ion density will exceed the electron density.
- Third, a large number of electrons inside a Debye sphere $n_e\lambda_D^3 \gg 1$ is required.

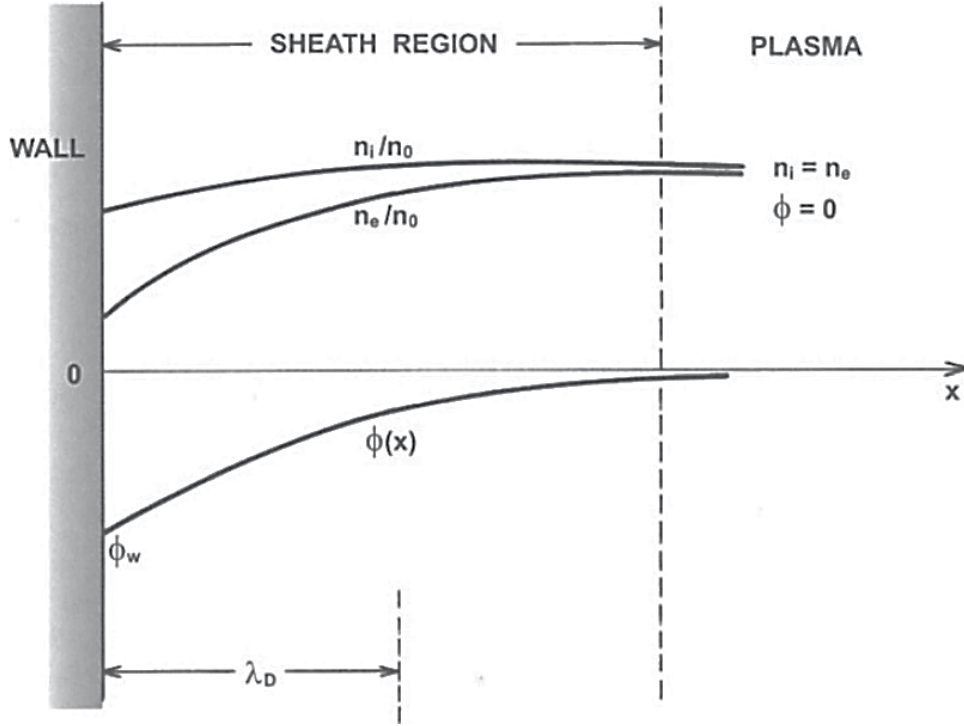


Figure 6.2: Trend of the electric potential and the charge carrier densities in the plasma sheath between an infinite plane wall and a plasma. Inside the plasma bulk quasi-neutrality holds since the ion density $n_i(x)$ is approximately equal to the electron density $n_e(x)$ at each position x . The ion excess grows as the distance to the wall decreases. At the same time the electric potential $\phi(x)$ is approaching the potential at the wall ϕ_w . It is $\phi_w < \phi = 0$ V since the wall is on a lower potential ϕ_w than the plasma bulk ϕ . The figure is taken from [Bit04] with permission from Springer Nature®.

This parameter is on the order of $n_e \lambda_D^3 \sim 100$ in case of the WGTS beam tube operated at $T = 30$ K.

- A final fourth criterion is the existence of a plasma oscillation with frequency $\omega_{\text{pl},e}$ for electrons, which should satisfy $\omega_{\text{pl},e} \tau > 1$ with τ being the average time between two collisions of an electron and a neutral particle. This requirement is necessary to maintain the basic property of any plasma to tend to stay at its equilibrium state of quasi-neutrality. It might happen that an external force causes a separation of charged particles, which leads to a temporal disturbance of the quasi-neutrality on a microscopic scale. As soon as the separation starts, internal electric fields are created which counteract it. Electrons react quite fast to these fields because of their low mass m_e . The electrons tend back to the equilibrium state but because of their inertia they move beyond it. After passing it they are slowed down and reverse their motion. Effectively, a periodic electron movement with the plasma frequency [Bit04]

$$\omega_{\text{pl},e} = \sqrt{\frac{n_e e^2}{m_e \epsilon_0}} \quad (6.2)$$

is established. Because of this fast reaction to the external perturbation the macroscopic quasi-neutrality is always maintained. To first order ions only

have a negligible contribution to this process. Nevertheless, they likewise perform oscillations but at a smaller frequency

$$\omega_{\text{pl},i} = \sqrt{\frac{n_i(Z_i e)^2}{m_i \epsilon_0}} \quad (6.3)$$

due to their large masses m_i . If the oscillations of electrons are completely damped by collisions between electrons and neutral particles, there would be no tendency towards the equilibrium state of quasi-neutrality. In this case, the fourth criterion would not be fulfilled and the substance could not be called a plasma. In the WGTS the electron plasma frequency is in the range between ~ 18 MHz and ~ 56 MHz, depending on the value of the electron number density. For an average time $\tau = (0.5 \times 10^{-6})$ s it follows that $\omega_{\text{pl},e}\tau$ lies in the range between 10 and 31.

Plasma instabilities

A plasma instability is a turbulent and chaotic motion of charge carriers due to small perturbations of the equilibrium state. Possible examples for a perturbation could be internal interactions of plasma particles with each other or fluctuations of external parameters like the magnetic field, density or boundary electric potential. Such perturbations are rather small in the first place but they are growing in case of unstable equilibrium states. This results in an effective separation of charges and the subsequent creation of time-dependent electric fields.

If plasma instabilities are present in the WGTS plasma, they can occur over a wide range of frequencies. Basically all of them are relevant for KATRIN, since they will induce changes of the WGTS plasma potential which leads to a systematic shift of the best-fit neutrino mass result. High-frequency (\gtrsim MHz) plasma instabilities could additionally lead to a distortion of the measured β -spectrum by effectively changing the kinetic energy of a traversing β -electron. This latter effect is increased for longer path lengths through the plasma, i.e. for a larger pitch angle θ . Beta-electrons created at the WGTS front end or in the DPS possess the largest pitch angles of up to $\theta_{\text{max}} = 77^\circ$ because of the high magnetic fields of up to $B = 4.0$ T (cf. Eq. 2.6). Moreover, according to the literature [GS62, Sch64], in these low-density regions the occurrence of plasma instabilities is more likely.

The Langmuir probe

The Langmuir probe concept has been developed by I. Langmuir and H. M. Mott-Smith in 1926 [MSL26]. It is a conducting electrode which allows to measure the temperature and number densities of electrons. After inserting the probe into a plasma different potentials can be applied to it, while the current flowing through the probe is measured. A sheath between probe and plasma is established.

For a planar Langmuir probe the characteristic curve is shown in Fig. 6.3. Ion and electron currents through the probe have negative and positive sign, respectively. If no external potential is applied, the floating potential ϕ_w would be established at the probe. In this equilibrium state the ion and electron flux through the probe would be identical resulting in a net current of zero. The floating potential is negative because of the higher average thermal velocity of electrons due to their lower mass. A further decrease of the potential will raise the repulsive force for electrons so for very negative potentials the electron contribution is minimized and the maximal ion current density J_i is measured. If the potential is instead increased above

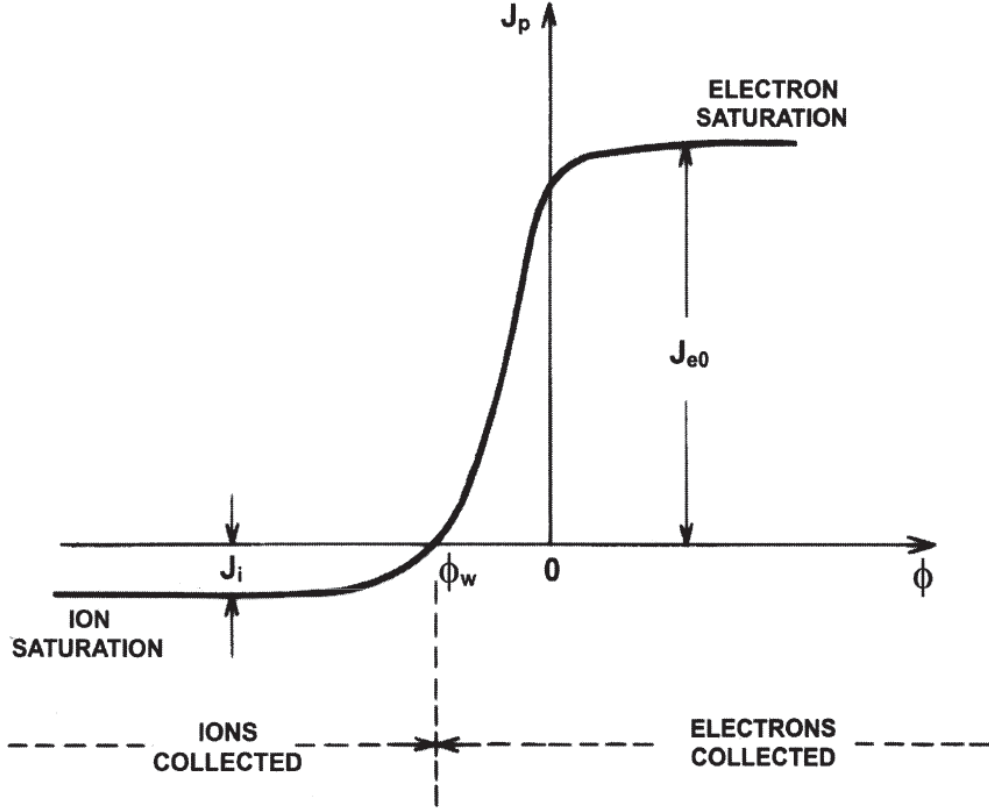


Figure 6.3: Schematic drawing of the characteristic curve of a plane Langmuir probe. Shown is the current density J_p versus the electric potential ϕ of the probe. A potential of $\phi = 0$ corresponds to the plasma potential. Ions and electrons induce a current density J_i and J_{e0} , respectively. The floating potential is denoted with ϕ_w . The figure is taken from [Bit04] with permission from Springer Nature®.

ϕ_w , more electrons than ions arrive per unit time so the current increases up to the saturation level at which all ions are repelled and electrons are the only remaining contribution. At $\phi = 0$ the probe potential is equal to the plasma potential and an electron current density J_{e0} is measured. Both the electron number density n_e and the electron temperature T_e can be derived from the characteristic curve by [Bit04]

$$T_e = \frac{e}{k_B} \frac{1}{\frac{d}{d\phi} (\ln(J_p + J_i))} \quad (6.4)$$

$$n_e = \frac{J_{e0}}{e} \sqrt{\frac{2\pi m_e}{k_B T_e}}$$

with the probe current density $J_p = J_{e0} \exp(e\phi/(k_B T_e)) - J_i$ for $\phi < 0$ and the saturation ion current density J_i .

6.1.2 The WGTS plasma

The WGTS plasma is created via β -decay and subsequent ionizations of gas molecules by β -electrons (cf. section 3.1). Molecular ions (T_2^+ , T_3^+ etc.) and ion clusters (T_5^+ , T_7^+ etc.) are formed and positive ions recombine with secondary electrons or negative ions. An ion-electron pair density on the order of 10^5 cm^{-3} to 10^6 cm^{-3} is

established in the steady-state. Comparable plasma densities can also be found in specific layers of the Earth's ionosphere.

By frequent scattering off gas molecules, both ions and secondary electrons are cooled down to the source temperature of $T = 30$ K in nominal mode or up to $T = 100$ K in krypton mode. For electrons, this process is much slower than for ions, as they have to undergo a factor of $\sim 10^3$ more scatterings in order to thermalize [Mes10]. Taking the nominal temperature and electron density into account, a WGTS Debye length between $\lambda_D = 1 \times 10^{-3}$ m and $\lambda_D = 4 \times 10^{-4}$ m can be calculated.

Per design, it is assumed that positive space charge potentials occurring along the source tube are efficiently compensated by electrons because of their high longitudinal mobility [KAT05]. Further, it is assumed that a longitudinal inhomogeneity of the plasma potential on the order of a few times the mean electron energy $3/2k_B T = 3.9$ meV remains. However, this is strongly dependent on the boundary conditions which will be covered in the next section 6.1.3.

Simulations in [Kuc16] indicate that quasi-neutrality is not fulfilled a priori for certain extreme boundary conditions which can lead to a net loss of charge carriers.

Motion of plasma particles

On a microscopic level the motion of charge carriers inside the WGTS plasma can be described by the Boltzmann equation. In this full kinetic approach the plasma is viewed as a Gibbs ensemble with a phase space distribution function $f(\vec{r}, \vec{v}, t)$ representing the probability density of finding any particle with velocity \vec{v} at the location \vec{r} at time t . Solving the Boltzmann equation for the WGTS plasma is rather complex due to the large number of particles and their interactions with each other. In first approximation the problem can be simplified drastically by assuming that the particle velocities follow a Maxwell-Boltzmann distribution. Then, starting from the Boltzmann equation two analytic expressions for the particle flux $\vec{\Gamma}$ can be derived [Bit04, Kuc16]²:

$$\frac{dn}{dt} + \vec{\nabla} \vec{\Gamma} = R, \quad (6.5)$$

$$\vec{\Gamma} = -D \vec{\nabla} n + n \mathcal{M} \vec{E} + n \vec{v}_g. \quad (6.6)$$

Here, n is the particle number density, R is the charged particle creation rate, D is the diffusion coefficient, \mathcal{M} is the mobility, \vec{E} is the electric field and \vec{v}_g is the velocity of the neutral gas flow pointing from the WGTS center towards its ends. Both Eqs. 6.5 and 6.6 have to be solved for ions, electrons and neutral gas particles, respectively. The individual sets of equations can not be treated independently but are coupled via collisions and the electric field. It is important to note that Eqs. 6.5 and 6.6 are only approximately valid in an environment with large collision rates such as the WGTS center. They are a reasonable simplification for the following rather qualitative discussions but for an exact treatment, however, they are not necessarily sufficient, depending on the desired degree of accuracy.

The different terms of Eq. 6.6 describe different physical transport mechanisms. The first term describes diffusion, the second term represents particle drift in an electric field and the third term stands for the interaction with the gas flow. Diffusion

²The third term of Eq. 6.6 representing the neutral gas flow was taken from "Electric fields in WGTS tubes I", an internal report written by F. Glück in 2002.

coefficient and mobility are linked via the Einstein relation [Bit04]:

$$D = \frac{k_B T}{e} \mathcal{M} \quad (6.7)$$

with the Boltzmann constant k_B , the temperature T and the elementary charge e . Further, the charged particle motion inside the beam line is restricted by boundary walls and potentials. Due to their different masses, charge signs and energies the motions of ions, secondary electrons and β -electrons are quite different.

The strong axial magnetic field leads to a high axial and low radial mobility of the electrons. In rear direction electrons are absorbed or backscattered at the RW, while they are reflected by the negatively biased DPS dipole electrodes in front direction. High-energy β -electrons are able to overcome the dipole electrode potentials and are ultimately reflected at the PS or MS negative high voltage. To first order, the RW is the only possibility for electrons to leave the source due to their low radial mobility. The neutral gas flow from the center towards both ends of the WGTS provides the same longitudinal energy for the ions and electrons (cf. Eq 6.6). However, the longitudinal mobility of the ions is more restricted than for electrons because of their much higher masses and thus lower thermal velocities. Therefore, they effectively move in the direction of the neutral gas flow. The ion flux can be terminated at the RW or reflected at the DPS electrodes. Positive ions are reflected at the blocking electrodes and negative ions at the negatively biased dipole electrodes, where some of the positive ions are removed. Radially, the ion confinement by the magnetic field is less than for electrons [Kuc16]. For certain voltage settings ions can leave the source via radial movement towards the beam tube surface where they are neutralized.

Beam line instrumentation

There are several hardware devices located along the beam line which have an influence on the WGTS plasma (see Fig. 6.4).

All field lines of the sensitive magnetic flux tube are terminated on the RW gold surface on the rear side. A bias voltage can be applied to the unit and the current flowing through the disk towards ground is measured with a picoammeter. The RW has a major influence on the WGTS plasma potential distribution which is discussed in detail in the next section. Also, it can be operated as a source of photoelectrons by homogeneously illuminating it with a Cermax[®] xenon UV lamp.

In the DPS beam line four dipole electrodes and two ring electrodes are mounted (cf. section 5.1.1). A negative dipole field is applied to the dipole elements 1, 2 and 3, which leads to an $E \times B$ drift of positive ions in radial direction until they are neutralized on metal lobes attached to one half-shell of each electrode. The corresponding neutralization current is measured by a picoammeter. By applying higher dipole fields more ions can be removed per unit time. Thus, the voltage settings at the dipole electrodes have an important influence on the number density of positive ions. Withdrawing positive ions from the plasma decreases the recombination rate. This could lead to a higher density of negative ions since they can not recombine anymore at a large rate with the positive ones, e.g. by the process described in Eq. 3.7. A possible consequence would be the amplification of negative space charges which would broaden the spatial plasma potential distribution.

Dipole element number 4 is operated at positive polarity with voltages (+25 V/+20 V). This positive dipole field both blocks positive ions and removes electrons possibly

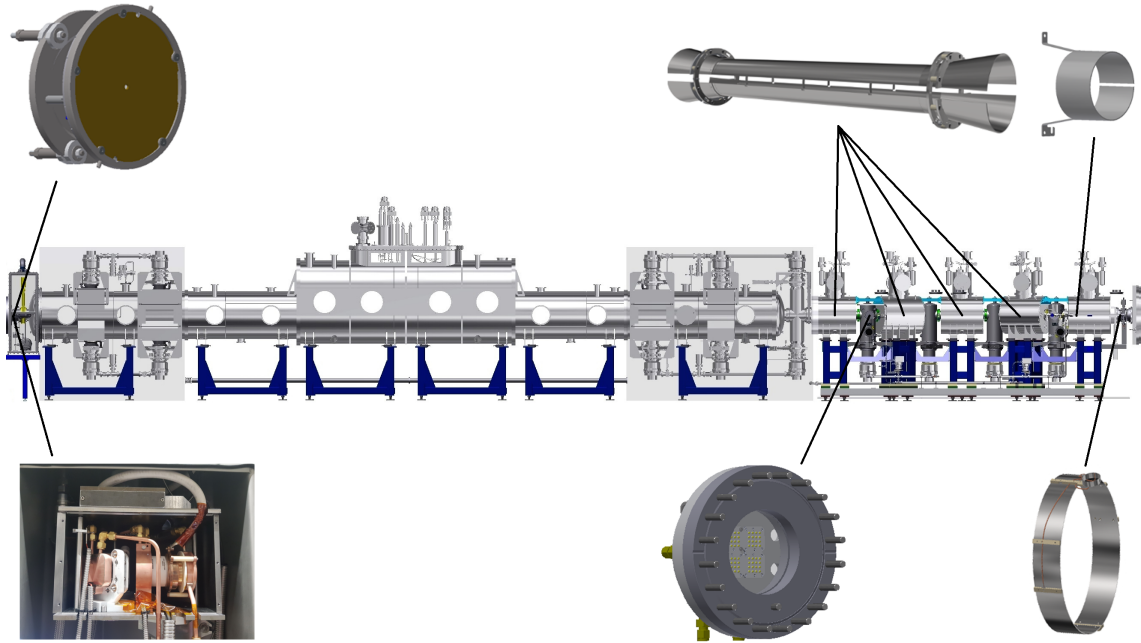


Figure 6.4: Locations of the individual beam line hardware devices influencing the WGTS plasma. On the bottom the optical setup of the Cermax[®] UV lamp, the DPS infrared illumination flange and the DPSb ring electrode and on the top the RW, the DPS dipole electrodes and the DPSa ring electrode are shown from left to right. The photograph of the Cermax[®] setup is taken from [Ful20].

stored between the negative potentials of the DPS and the PS, which could otherwise neutralize the ion blocking ring electrodes. The ring electrodes DPSa and DPSb are set on positive voltages of 40 V and 5 V, respectively. Positive ions can not overcome these electrostatic barriers and are reflected back towards the WGTS. Negative ions are reflected by the negative fields of the first three dipole electrodes. At the first DPS pump port an OSLO[®] 16 PowerCluster infrared (IR) illumination system consisting of four 4x4 LED arrays is mounted on the beam line facing side of a flange. The idea is to eliminate negative ions originating from the WGTS front end in order to reduce the impact of negative space charges on the plasma potential inhomogeneity. During nominal operation the illumination system is turned off and the negative ions are blocked by the first dipole electrode before they reach the pump port. For a proper operation the dipole element number 1 has to be switched off which enables negative ion transmission up to the first DPS pump port permitting an interaction with the IR photons.

6.1.3 Boundary conditions for the WGTS plasma potential

There are two boundaries constraining the plasma potential. In radial direction this is the grounded stainless steel beam tube surface at a bias voltage $U_{BT} = 0$ V. In axial direction it is the RW gold surface terminating the sensitive magnetic flux tube on the rear side. It is operated at a bias voltage U_{RW} .

The voltage setup is shown in Fig. 6.5³. An iseg[®] DPr 05 power supply provides a

³Strictly speaking, the setup shown in Fig. 6.5 is only valid after the 15.10.2019. Before, the RW power supply and the WGTS beam tube ground potential were not connected properly which lead to an offset of ~ 42 mV between both. This issue was fixed on 15.10.2019.

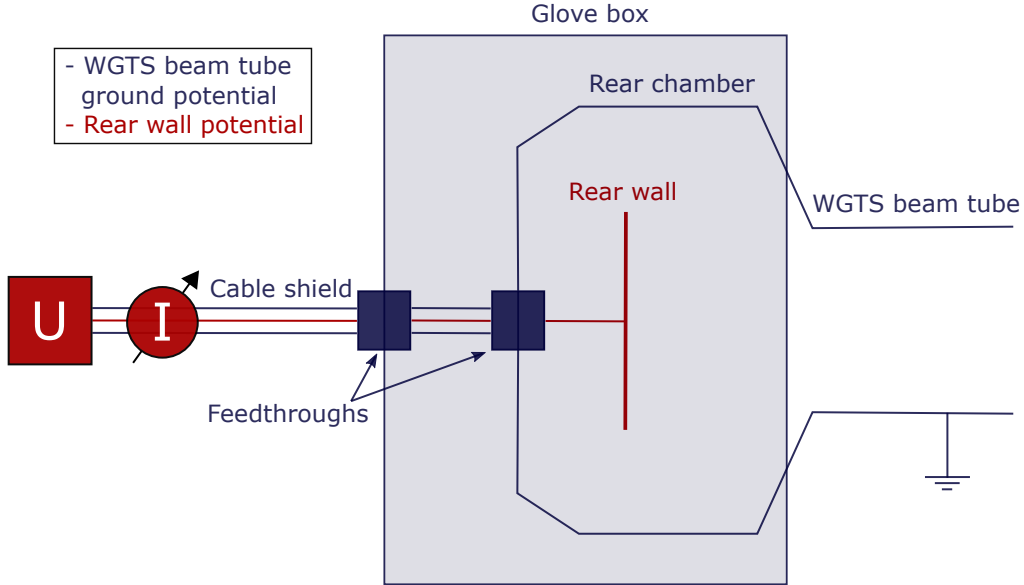


Figure 6.5: Schematic drawing of the RW and WGTS voltage setup. Shown are the power supply (iseg[®] or Agilent[®] function generator) and the picoammeter connected to the RW via a shielded triaxial cable. The power supply reference potential is defined by the KATRIN ground potential on which the WGTS beam tube, the rear chamber and the surrounding glove box are operated.

bias voltage of up to ± 500 V and the current flowing through the RW towards ground can be measured by a 9103 picoammeter from RBD instruments[®]. Alternatively, an Agilent[®] 33250A function generator can be deployed in order to apply voltages in a range of ± 10 V⁴.

Both boundaries each possess a surface potential defined as

$$\begin{aligned} V_{\text{BT}} &= U_{\text{BT}} - \frac{\Phi_{\text{BT}}}{e}, \\ V_{\text{RW}} &= U_{\text{RW}} - \frac{\Phi_{\text{RW}}}{e}. \end{aligned} \quad (6.8)$$

Here, U is the external bias voltage applied to the respective material and Φ is the absolute value of its intrinsic work function. The work function is the minimum energy required to move an electron out of a solid metal and is a characteristic property for each material [Kit13]. It is expected that the work functions of the beam tube and the RW differ by a few 100 meV [Bab14]. Also, variations over the respective surfaces can occur due to impurities, surface defects, adsorption of tritiated molecules and other effects influencing the physical surface properties [Bab14, Kuc16].

Coupling between rear wall and plasma bulk

In the KATRIN setup the single parameter of Eq. 6.8 that can be adjusted on purpose is the RW bias voltage U_{RW} . Thus, it is the only possibility to manipulate the starting potential distribution of the β -electrons. The impact of a certain change of

⁴The RW voltage setup described here is only valid in the scope of this thesis because afterwards it was modified. All three devices were replaced by a single Keithley[®] 6487/E picoammeter with an integrated power supply covering the three voltage ranges ± 10.1 V, ± 50.5 V and ± 505 V.

the RW voltage ΔU_{RW} on the plasma potential ΔV_{P1} is quantified by the empirical parameter labeled "coupling strength"⁵ c , which is defined by

$$c = \frac{\Delta V_{\text{P1}}}{\Delta U_{\text{RW}}}. \quad (6.9)$$

This parameter plays a major role for the investigations described in this chapter. At $c = 1$ the plasma would be maximally "coupled" to the RW and it would be $\Delta U_{\text{RW}} = \Delta V_{\text{P1}}$. Compensation currents would flow out of the plasma on a very short time scale and the plasma potential would rapidly adjust to the given RW surface potential. For $V_{\text{RW}} > V_{\text{P1}}$ a current of electrons and for $V_{\text{RW}} < V_{\text{P1}}$ a current of positive ions flows from the plasma towards the RW. At $c = 0$ the plasma would be "decoupled" from the RW and its potential could not be varied by changing the RW bias voltage. For some reason, in this configuration no sufficiently high compensation current can flow out of the plasma bulk, so an adjustment of potentials would be prevented. In between those two extremes at $0 < c < 1$ a change in the RW voltage would only partly be transferred to the plasma.

Simulations using a two-dimensional axially symmetric fluid model

Initially, it was assumed that the RW surface potential solely determines the plasma bulk potential ($c = 1$) due to the high longitudinal conductivity of the plasma [KAT05]. However, the first quantitative results for the spatial plasma potential distribution and the influence of boundary surfaces on it were provided by detailed simulations by L. Kuckert [Kuc16]. They are based on a two-dimensional axially symmetric three-particle fluid model. The most important results are summarized in the following since they are the basis for further studies. In fact, the assumption of a perfect coupling between RW and plasma was found to be only true if certain boundary conditions are fulfilled.

Four different scenarios can be identified by introducing the potential difference $\Delta = V_{\text{RW}} - V_{\text{BT}}$. For standard KATRIN conditions, a critical value $\Delta_C \approx -40$ mV can be calculated from theoretical considerations in order to separate the four scenarios explained below. In all of them homogeneous surface potential distributions were assumed neglecting variations of the respective work functions.

- **RW and beam tube on almost the same surface potential** ($|\Delta| \leq 10$ mV)
Thermal electrons can only leave the WGTS via the RW while ions leave it both at the RW and at the beam tube. Sheaths form between the boundaries and the plasma bulk, respectively. Quasi-neutrality is fulfilled for the bulk but not in the sheaths. The resulting WGTS potential inhomogeneity is expected to be minimal with a value below 10 mV.
- **RW biased more negative than beam tube** ($\Delta < \Delta_C \approx -40$ mV)
The plasma potential is settled in between the RW and the beam tube surface potential $V_{\text{RW}} < V_{\text{P1}} < V_{\text{BT}}$. Therefore, electrons are blocked from the RW and positive ions are blocked from the beam tube. There is no radial ion motion which results in radial electric fields building up. The plasma potential is determined by the beam tube, not by the RW, so the coupling strength is $c \approx 0$. A rather large plasma potential inhomogeneity of more than 100 mV is present.

⁵"Coupling strength" is here not used as a term of plasma physics, but as an empirical parameter.

- RW biased more positive than beam tube ($\Delta \gg \Delta_C \approx -40$ mV)**
 The plasma potential is settled in between the beam tube and the RW surface potential $V_{BT} < V_{PI} < V_{RW}$. Thus, electrons can leave the plasma via the RW and ions via the beam tube. The RW determines the plasma potential, while the beam tube potential is completely shielded from the plasma bulk within 1 cm above the surface. However, the coupling to the RW decreases with the distance, so it is $0 < c < 1$, which leads to a monotonously declining electric potential along the z -axis. At some point, a decoupling ($c \approx 0$) for very positive Δ is expected, although this case was not explicitly simulated. Overall, the inhomogeneity is on the order of several hundreds of mV and quasi-neutrality is violated.
- RW biased only slightly more positive than beam tube (50 mV $\gtrsim \Delta > \Delta_C \approx -40$ mV)**
 This configuration is similar to the $\Delta \gg \Delta_C$ case. The plasma potential is determined by the RW ($c \approx 1$). Further, the plasma potential inhomogeneity below 20 mV is close to the aspired optimum.

Besides these different scenarios also the influence of work function variations over the boundary surfaces has been investigated. Potential variations over the surface of up to 40 mV for the RW and between -100 mV and 500 mV for the beam tube were assumed. As for the RW, it was found that small-scale work function inhomogeneities are washed out in the immediate vicinity and do not penetrate deep into the plasma bulk. Thus, the influence on the longitudinal plasma potential inhomogeneity is minor. As for the beam tube, larger work function inhomogeneities than for the RW were assumed in the simulations. As long as $\Delta > \Delta_C$ is fulfilled, this inhomogeneous beam tube potential profile is not penetrating into the plasma bulk and thus does not influence the plasma potential inhomogeneity.

In summary, by applying the two-dimensional axially symmetric fluid approach it could be shown that potential variations of reasonable size over the RW or beam tube surface are not directly transferred to the plasma potential profile. Instead, the plasma potential homogeneity is determined by the Δ parameter which can be tuned by changing the RW bias voltage U_{RW} as the beam tube is fixed at ground potential. At $\Delta = 0$ mV the difference in the work functions $\Delta\Phi = \Phi_{RW} - \Phi_{BT}$ is exactly compensated by U_{RW} . It is recommended to set the RW on a voltage corresponding to a region -40 mV $\lesssim \Delta \lesssim 50$ mV in order to minimize the plasma potential inhomogeneity to values below the required upper limit of 10 mV. Both too high and too low RW voltages result in potential variations far beyond the design limit. Also, at $\Delta < \Delta_C$ the coupling strength is $c \approx 0$, which means that the RW is not influencing the plasma potential anymore. Instead, the beam tube potential is penetrating into the plasma bulk.

Implications for experimental plasma investigations

In this thesis the focus is on experimental studies of the influence of boundary conditions on the plasma and its potential. However, at KATRIN the plasma potential can not be measured directly. Instead, its impact on the β -spectrum can be determined. A shift of the mean WGTS plasma potential $\pm\Delta V_{PI}$ directly leads to a shift $\mp\Delta E_0$ of the β -spectrum endpoint which is proportional to the shift of the FPD

count rate $\mp \Delta R(U_{\text{ret}})$ measured at a fixed MS retarding potential:

$$\pm \Delta V_{\text{Pl}} = \mp \Delta E_0 \propto \mp \Delta R(U_{\text{ret}}). \quad (6.10)$$

This relation is the the basis for most of the measurements described in the succeeding sections. It is expected that the findings of the simulations described above are reflected in the results of a dedicated measurement. For the scope of this thesis, the implications derived from the simulations are summarized graphically in Fig. 6.6. Four different voltage regions can be identified. For $\Delta < \Delta_C$ there is $c = 0$, so the plasma potential and thus the FPD rate distribution is flat for different RW set points. In the central region at $-40 \text{ mV} \lesssim \Delta \lesssim 50 \text{ mV}$ the coupling strength is maximized so the FPD rate exhibits a linear drop in dependence of U_{RW} . For $\Delta > \Delta_C$ the absolute slope of the curve decreases with some coupling remaining. Finally, c is approaching zero for even more positive values of Δ .

6.1.4 Systematic plasma effects for neutrino mass determination and objectives of the experimental investigations

As for the KATRIN neutrino mass determination, the relevant plasma effects can be grouped in three different categories. For more details the reader is referred to section 3.1.5.

- **Spatial plasma potential inhomogeneity:** For an accurate measurement of the β -electron energy the WGTS plasma potential is equally important as

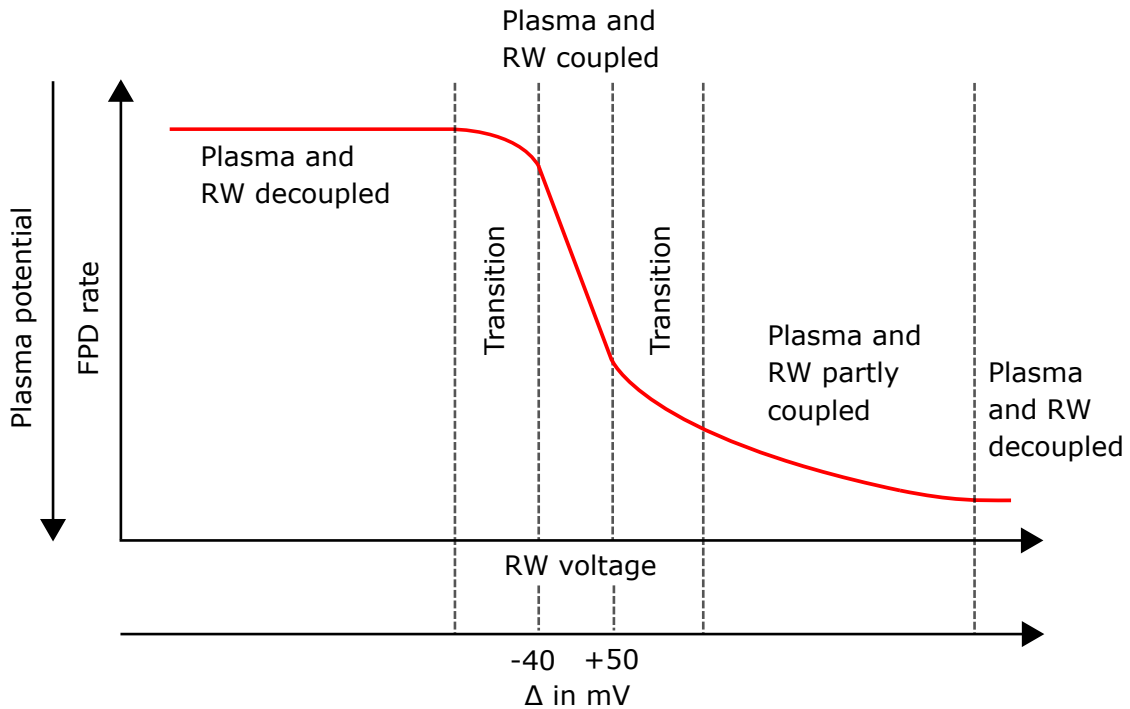


Figure 6.6: Schematic drawing of the expected impact of the RW set point on the plasma potential based on simulations using the two-dimensional axially symmetric fluid model. Shown are the expected dependence between the RW bias voltage/surface potential difference $\Delta = V_{\text{RW}} - V_{\text{BT}}$ and the FPD rate/plasma potential.

the MS retarding potential. Any spatial inhomogeneity of the plasma potential is directly influencing the energy scale of the experiment and effectively shifts the best-fit value of $m_{\nu_e}^2$. In order to fulfill KATRIN design requirements, an upper limit of 10 meV for the WGTS plasma potential variations was defined in [KAT05].

- **Time-dependent plasma potential:** Variations of the absolute plasma reference potential or its spatial distribution in time can either be induced by plasma instabilities or by changes in the boundary conditions like the RW or beam tube surface potentials. This would introduce a systematic effect to the final neutrino mass result obtained by combining data from different runs measured at different points in the KATRIN live time.
- **Change of β -electron energy by high-frequency plasma instabilities:** Short-term instabilities in the WGTS electric fields would affect the energy of a passing β -electron and thereby distort the energy measurement.

Measurements dedicated to the investigation of effects of each category are presented in this chapter pursuing the main objectives defined in section 3.3. They are shortly summarized in the following.

- Investigation of the influence of various hardware devices, especially the RW, on the WGTS plasma.
- Investigation of the coupling between RW surface potential and plasma potential.
- Determination of the optimum set point of the RW bias voltage for neutrino mass measurements.
- Monitoring of plasma observables over time.
- Investigation of plasma instabilities.

The determination of an optimum RW set point was especially relevant for both KNM1 and KNM2, as it is an important prerequisite before the scanning of the β -spectrum endpoint region can start.

6.2 Experimental methods for plasma investigation

The experimental methods applied in KNM1 and KNM2 are custom-made for the KATRIN apparatus and therefore require a detailed introduction. Each of them provides insights about one or more of the previously described plasma effects.

- The "plasma rear wall optimization at KATRIN" ("PRO KATRIN") method explained in section 6.2.1 yields the radial plasma potential distribution inferred from the β -spectrum endpoint measured at different FPD pixel rings. Furthermore, the coupling of the RW surface potential to the plasma potential is deduced in dependence of the bias voltage U_{RW} .
- A modified version of PRO KATRIN discussed in section 6.2.2 is solely sensitive to the front part of the WGTS, which reveals how the RW-plasma coupling is maintained at large distances.

- A characteristic curve of the RW current versus the RW bias voltage can be measured via the voltage sweep described in section 6.2.3.
- Finally, high-frequency plasma instabilities and the impact of high-frequency AC voltages applied to the RW can be investigated with the methods discussed in the sections 6.2.4 and 6.2.5, respectively.

6.2.1 PRO KATRIN

"PRO KATRIN" is short for "plasma rear wall optimization at KATRIN". The basic idea initially brought up by M. Babutzka is to exploit the relation stated in Eq. 6.10 in order to infer information about the plasma potential from measuring the FPD rate.

Motivation

A neutrino mass measurement run requires the optimization of the measurement conditions before it starts. As for the plasma, one important approach to do so is the PRO KATRIN method. A major boundary condition is the RW bias voltage as it mainly determines the starting potential distribution of the β -electrons inside the WGTS. If ignored, a non-optimized RW setting comes along with the risk that the data collected over several months of β -spectrum scanning might be affected by an inhomogeneous reference potential. Consequently, KNM1 and KNM2 measurements implied to define an optimum set point prior to data-taking.

In principle, the radial variation of the plasma potential could be inferred directly from the data obtained in the β -spectrum scanning. However, observing a significant effect would require several weeks of accumulating statistics. Therefore, a faster method is needed for studying the RW-plasma interplay systematically. With the PRO KATRIN method it is possible to study both the RW-plasma coupling and the radial homogeneity of the plasma potential within a measurement time on the order of 1-2 days.

Measurement procedure

The PRO KATRIN method consists of three individual voltage scans each serving a different purpose. The measurement principle is illustrated in Fig. 6.7.

- **RW scan:** The FPD rate originating from WGTS β -decays is measured for different U_{RW} at fixed U_{ret} by step-wise scanning of RW set points.
- **MS scan:** The dependence between the rate and the MS retarding voltage is deduced from a step-wise variation of U_{ret} . Then, this dependence is compared to the dependence between rate and RW voltage obtained in the RW scan. This allows to disentangle the effect of the coupling between RW and plasma from the shape of the β -spectrum. For both the RW and the MS scan it is assumed that neither the column density nor the tritium purity is changing significantly during the measurements.
- **Deep MS scan:** A scan deep into the β -spectrum is done by lowering U_{ret} in certain steps. Subsequently applying a fit to the obtained data provides the radial endpoint distribution at a fixed U_{RW} . By combining these results with the results of the RW scan, the radial endpoint distribution is determined for every RW set point applied.

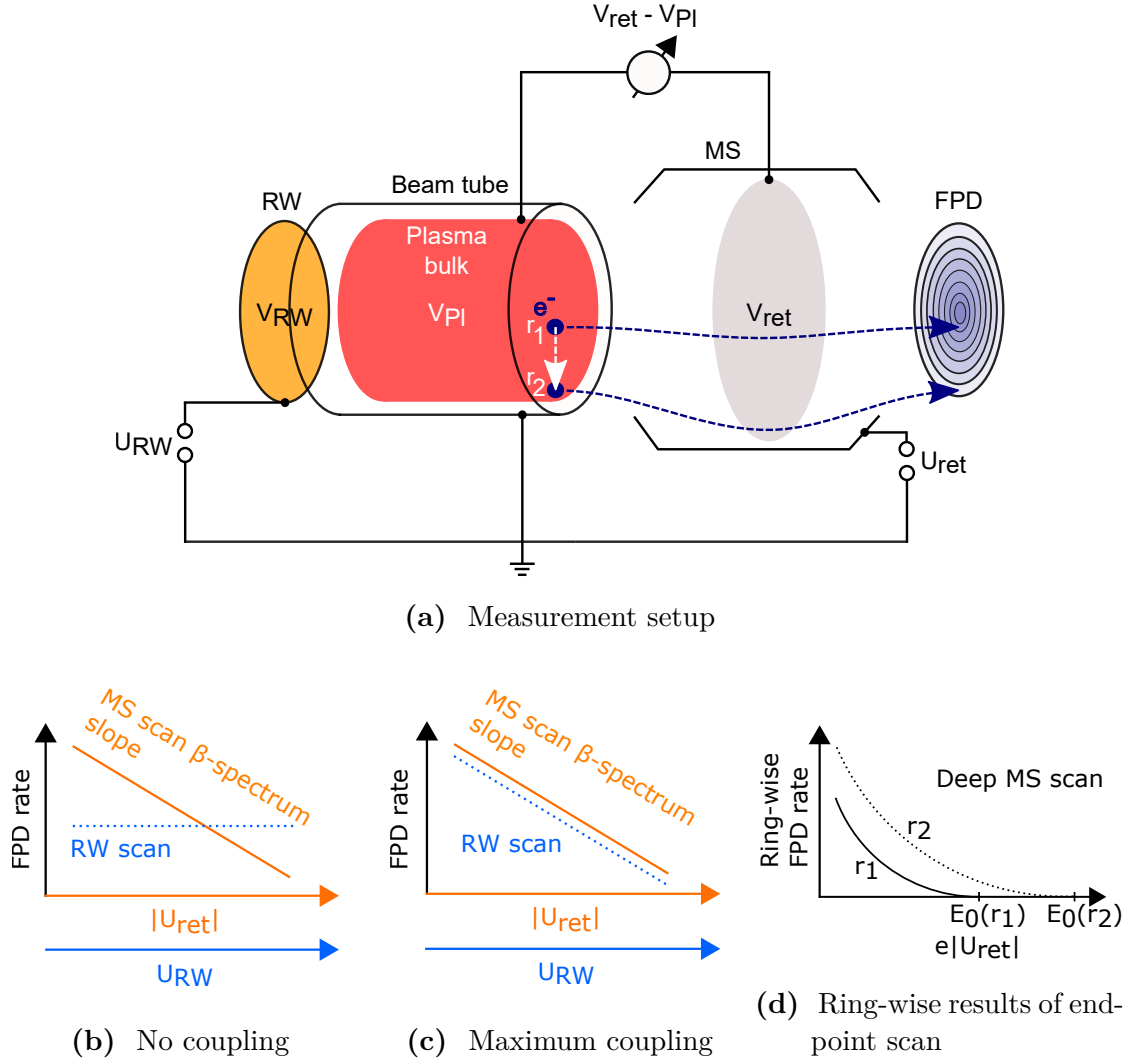


Figure 6.7: Schematic drawing of the PRO KATRIN measurement principle.

In (a) a sketch of the measurement setup is shown. Beta-electrons originating from different locations from inside the WGTS plasma bulk are counted by the FPD if they overcome the potential difference $V_{\text{ret}} - V_{\text{PI}}$. A sensitivity to radial effects is provided by the ring-wise segmentation of the FPD wafer. Sketches of exemplary measurement results are shown below. One goal is to find out how efficiently a change of the RW bias voltage is translated into a change of the plasma potential. Two extreme cases are illustrated on the left. In (b) the case of zero coupling between RW and plasma is shown. The β -electron rate measured in the RW scan is not changing with U_{RW} . For maximum coupling on the other hand, the FPD rate is expected to be linearly dependent on the RW voltage as shown in (c). The slope of this linear function is equal to the one of the β -spectrum measured in the MS scan by changing U_{ret} . In this scenario, changing U_{RW} at the RS and changing $|U_{\text{ret}}|$ at the MS have an identical impact on the measured rate. A second goal is to determine the radial distribution of the plasma potential. Therefore, a deep MS scan is performed at fixed U_{RW} . Ring-wise results for two different radii r_1 and r_2 are depicted in (d). If there is a radial dependence, the endpoints measured at different FPD rings are expected to differ (cf. Eq. 6.10).

According to Eq. 6.10, differences in the endpoint are equal to differences of the plasma potential. Consequently, PRO KATRIN ultimately provides the radial slope of V_{Pl} in dependence of U_{RW} .

Investigation of the coupling strength between plasma and rear wall

As seen in the previous section relevant plasma effects influencing the neutrino mass result can be as low as 10 mV, so a high sensitivity is needed in order to assess the rate shift. The sensitivity is increasing deep in the β -spectrum where the rate is high. Therefore, PRO KATRIN measurements are done several hundreds of eV below the tritium endpoint at a set point $U_{\text{ret}} = U_{\text{PK}}$ (in most cases at $U_{\text{PK}} = -17900.0$ V). Measuring deep in the spectrum in principle bears the risk for β -electrons to move non-adiabatically through the MS on rather chaotic trajectories without reaching the FPD [GGB⁺05]. This effect scales with the surplus energy of the β -electrons with respect to the MS retarding energy $E_{\text{sur}} = E_{\beta} - qU_{\text{ret}}$ and is dependent on their pitch angles and radial positions at which they enter the MS volume [Hub]. If necessary, this effect can be mitigated by increasing the magnetic field in the MS analyzing plane using the air-coil system. The measurements based on the PRO KATRIN method are performed at the nominal analyzing plane magnetic field of 0.63 mT. Dedicated simulations [Hub] for $E_{\text{sur}} = 1.6$ keV show that at this magnetic field the fraction of β -electrons not transmitted to the FPD is $< 1 \cdot 10^{-4}$ for the bull's eye up to pixel ring 10. Thus, at the surplus energies of PRO KATRIN (typically $E_{\text{sur}} \approx 700$ eV), non-adiabatic effects can be neglected.

FPD rates on the order of 1 Mcps are measured, which makes it necessary to record the data in the histogram mode (cf. section 2.4). The coupling between RW and plasma is inferred from two separate parts of the measurement: the RW scan and the MS scan.

- **MS scan**

In the MS scan the MS retarding voltage U_{ret} is varied within a range of $\pm \Delta U_{\text{ret}}$ while the RW voltage is fixed at $U_{\text{RW}} = 0$ V. Changing the absolute MS retarding potential is equivalent to changing the plasma potential because the true retarding potential felt by the β -electrons is given by $V_{\text{ret}} - V_{\text{Pl}}$. Therefore, the MS scan is a reference measurement for the subsequent RW scan.

The FPD rate $R(U_{\text{ret}})$ is measured at three distinct set points $U_{\text{ret},1} = U_{\text{PK}} - \Delta U_{\text{ret}}$, $U_{\text{ret},2} = U_{\text{PK}}$ and $U_{\text{ret},3} = U_{\text{PK}} + \Delta U_{\text{ret}}$ with $\Delta U_{\text{ret}} = 4$ V. This yields the shape of the integral WGTS T_2 β -spectrum. Because of the small scan interval this spectrum can in leading order be modeled by a linear function

$$R(U_{\text{ret}}) = a_{\text{MS}} \cdot U_{\text{ret}} + b_{\text{MS}}. \quad (6.11)$$

A linear fit to the data points yields a_{MS} and b_{MS} . In order to minimize systematic effects by column density or tritium purity drifts, the FPD rates are measured once in an upward scan at voltages $U_{\text{ret},i}$ with $i \in (1,2,3)$ and then in a downward scan at voltages $U_{\text{ret},i}$ with $i \in (3,2,1)$. Before applying the linear fit the mean FPD rates $R(U_{\text{ret},i})$ are calculated.

- **RW scan**

Throughout the RW scan U_{RW} is varied within a range of $(U_{\text{RW,min}}; U_{\text{RW,max}})$, while the MS retarding voltage is fixed at $U_{\text{ret}} = U_{\text{PK}}$. The FPD rate $R(U_{\text{RW}})$ is measured at each RW set point. If the rate-voltage dependence is similar to the result of the MS scan, the RW is defining the plasma potential with $c \approx 1$.

Otherwise, if the rate distribution is rather flat, there is no coupling between RW and plasma potential and it is $c = 0$. Like in the MS scan the data points are measured in consecutive upward and downward scans for compensating possible column density or tritium purity drifts. In the analysis the different data points at identical RW voltage set points are averaged in order to obtain the final result.

Measuring count rates with the FPD for both RW and MS scan also provides radial information since the analysis can be done for each of the twelve pixel rings and the central bull's eye separately.

In Fig. 6.8 the results of both scans are plotted together for a measurement in mid-September 2019 at the beginning of KNM2 at a column density $\mathcal{N} = 4.2 \times 10^{17}$ molecules/cm² ($\hat{=}$ 84% of the design value) and a tritium purity $\epsilon_T = 98.4\%$. The curve measured in the RW scan has the following characteristic features.

- For very negative RW bias voltages $U_{RW} \ll 0$ V, positive ions are attracted and leave the plasma over the RW. A higher ion removal current would correspond to a more negative plasma potential. However, the FPD rate distribution is rather flat, so the plasma potential is not influenced by the RW surface potential. This decoupling indicates that the ion current starts to saturate. This would mean that the current increase for a growing potential difference

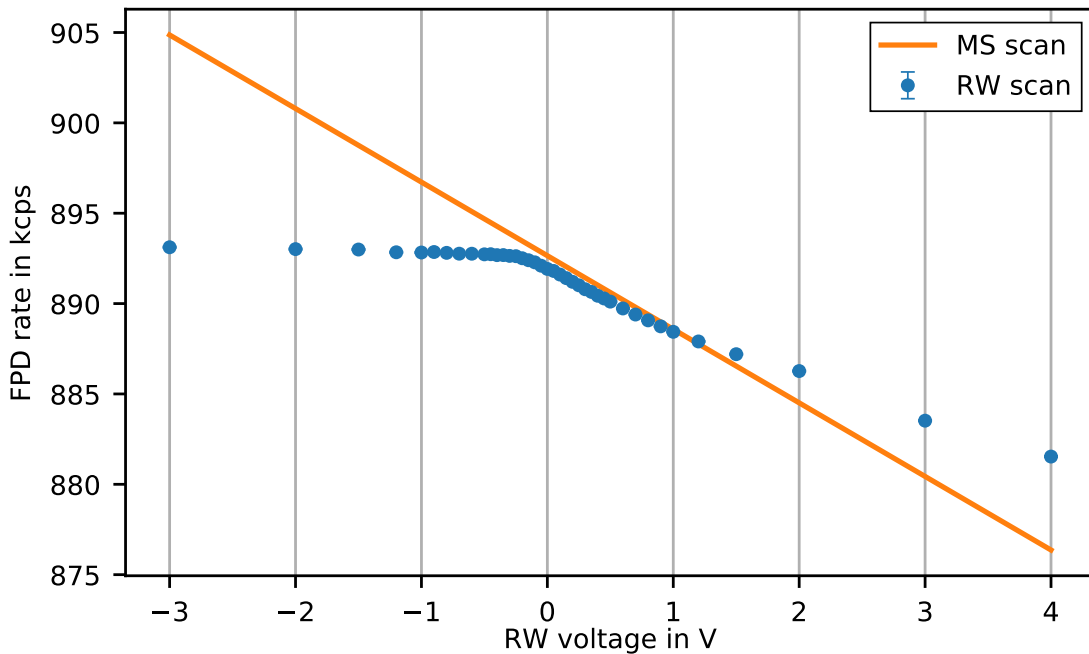


Figure 6.8: PRO KATRIN result measured in KNM2 on 19.09.2019. Shown is the total FPD rate versus the RW bias voltage for the data obtained in the RW scan. For comparison the linear reference slope of the β -spectrum as measured in the MS scan is superimposed. The measurements are carried out at $\mathcal{N} = 4.2 \times 10^{17}$ molecules/cm² and $\epsilon_T = 98.4\%$. Since the MS scan is performed at a RW voltage $U_{RW} = 0$ V, the MS scan line and the RW scan data points should meet at this specific set point. However, due to a minor drift in the column density there is a small offset in between.

between plasma and RW is not high enough in order to maintain an efficient assimilation of their respective potentials.

- In the central region around $U_{\text{RW}} = 0 \text{ V}$ the FPD rate is very sensitive to the RW voltage. A linear dependence is observed, which corresponds to the reference slope of the β -spectrum as measured in the MS scan. A change of the RW voltage is identical to an equivalent change of the MS retarding voltage. Here, the coupling between the plasma and the RW is maximized. In this region sufficiently high compensation currents can flow out of the plasma without any disturbance.
- In a third region at $U_{\text{RW}} \gg 0 \text{ V}$, electrons are attracted by the RW and the coupling diminishes. The FPD rate is still changing with the RW voltage but the slope is significantly reduced compared to the region of maximal coupling. This is probably due to the starting saturation of the compensation current of electrons flowing from the plasma bulk towards the RW.

Those three voltage regions can be classified by their respective coupling strength c (cf. section 6.1.3):

$$\begin{aligned} c &= 0 \text{ for } U_{\text{RW}} \ll 0 \text{ V} : \text{decoupled region,} \\ 0 < c < 1 &\text{ for } U_{\text{RW}} \gg 0 \text{ V} : \text{partly-coupled region,} \\ c &= 1 \text{ for } U_{\text{RW}} \approx 0 \text{ V} : \text{maximally-coupled region.} \end{aligned} \quad (6.12)$$

In principle, a fourth region with $c = 0$ for even higher positive voltages is expected. Indeed, this was observed in measurements of the KNM3 campaign after the work on this thesis has been completed. Furthermore, a fourth coupling region was found in measurements in the WGTS krypton mode at the end of KNM2 (see section 6.3.5). The curves shown in Fig. 6.8 can also be determined for different FPD pixel rings. In each of the three voltage regions one can fit the ring-wise data using an ad hoc model consisting of three linear functions⁶

$$R(U_{\text{RW}}) = \begin{cases} a_{\text{RW},0} \cdot U_{\text{RW}} + b_{\text{RW},0} & U_{\text{RW}} < U_{\text{RW}}^{\text{start}} \\ a_{\text{RW},1} \cdot U_{\text{RW}} + b_{\text{RW},1} & U_{\text{RW}}^{\text{start}} \leq U_{\text{RW}} < U_{\text{RW}}^{\text{end}} \\ a_{\text{RW},2} \cdot U_{\text{RW}} + b_{\text{RW},2} & U_{\text{RW}} \geq U_{\text{RW}}^{\text{end}} \end{cases} \quad (6.13)$$

with the kink positions $U_{\text{RW}}^{\text{start}}$ and $U_{\text{RW}}^{\text{end}}$ marking the start and the end of the maximum coupling region, respectively. An average radius r can be assigned to each ring for taking into account that the outer rings have a lower radial extension than the inner ones. The RW-plasma coupling strength is then given by

$$c(r) = \frac{a_{\text{RW}}(r)}{a_{\text{MS}}(r)}. \quad (6.14)$$

Here, a_{MS} is the slope of the β -spectrum as measured by the MS scan and a_{RW} is the slope of the RW scan curve in one of the three linear regions. The relation between the parameter $c(r)$ and the radial plasma potential $V_{\text{P1}}(r)$ can be derived as follows

$$\begin{aligned} V_{\text{P1}}(r) &= \Delta V_{\text{P1}}(r) + V_0(r) \\ &\approx \Delta V_{\text{P1}}(r) \\ &= c(r) \cdot \Delta U_{\text{RW}}. \end{aligned} \quad (6.15)$$

⁶This analysis procedure was mainly developed by M. Klein.

Here, a flat offset potential $V_0(r)$ is assumed⁷. Due to the linear dependence between $c(r)$ and $V_{\text{P1}}(r)$ a fit function

$$c(r) = A \cdot \left(1 - \left(\frac{r}{r_{\text{max}}} \right)^x \right) \quad (6.16)$$

with the free parameters A , r_{max} and x can be applied to the ring-wise coupling strength data. The parametrization of this fit function is based on the electric potential $V(r) \propto r^2$ of a charge homogeneously distributed inside a cylinder geometry. Plugging the fitted $c(r)$ values into Eq. 6.15 yields the radial distribution $V_{\text{P1}}(r)$, which was used as an input for dedicated plasma simulations by F. Glück (see section 6.3.3).

Investigation of the radial homogeneity of the plasma potential

Besides the investigation of the coupling between the RW and the plasma also the β -spectrum endpoint $E_0(U_{\text{RW}}; \text{ring})$ can be determined as a function of the FPD pixel ring and the RW voltage. According to Eq. 6.10, any variation of the endpoint is directly related to a corresponding change of the plasma potential V_{P1} . E.g. if E_0 is increased by ΔE_0 from one ring to another, the plasma potential is decreased by $-\Delta E_0$. Thus, the RW voltage at which the ring-wise slope of the endpoint distribution vanishes corresponds to a radially homogeneous plasma potential in the WGTS. Furthermore, as the plasma fluid model simulations by L. Kuckert indicate, the set point of radial homogeneity corresponds to the one of optimal longitudinal homogeneity [Kuc16]. Thus, applying this optimum set point throughout the neutrino mass runs provides ideal starting conditions for the β -electrons.

The ring-wise distribution is obtained by scanning deep into the β -spectrum at a single fixed reference set point $U_{\text{RW,ref}}$ and fitting the endpoint $E_0(U_{\text{RW,ref}}; \text{ring})$ for each ring individually. For all other RW voltages the MS scan and RW scan results are used for calculating an endpoint shift relative to the one at $U_{\text{RW,ref}}$.

The details of the deep scan into the β -spectrum are summarized in the following.

- **Deep MS scan**

The WGTS β -spectrum is scanned by varying the MS retarding voltage from the endpoint region down to about 500 eV below it, at a fixed reference RW voltage $U_{\text{RW,ref}}$. Such a deep scan is improving the sensitivity on the aspired best-fit result for $E_0(U_{\text{RW,ref}}; \text{ring})$. An analyzing plane magnetic field of 0.63 mT is applied. As discussed in the previous paragraph, dedicated simulations [Hub] show that systematic effects induced by non-adiabatic motion of β -electrons through the MS are negligible at these settings.

However, compared to a scan restricted to the last 30 eV of the spectrum, the deep MS scan nevertheless suffers from additional systematic effects not considered in the fitting model, like e.g. additional energy levels of the excited daughter molecule of the β -decay. A dedicated analysis by W. Choi showed

⁷The two-dimensional axially symmetric fluid model simulations by L. Kuckert [Kuc16] show that the plasma potential settles in between the RW and beam tube surface potentials. Thus, the inequality $0 \leq |V_{\text{P1}} - V_{\text{BT}}| \leq |V_{\text{RW}} - V_{\text{BT}}|$ is always valid. At the point of equal beam tube and RW surface potentials, it follows that $V_{\text{P1}} = V_{\text{BT}} = V_{\text{RW}}$. At this point the radial distribution of the plasma potential is necessarily flat.

that, at least for $(E_0 - E) > 100$ eV, the fitted ring-wise endpoint slopes are independent of the energy interval considered for the fit. Thus, the ring-wise E_0 slopes determined in the deep MS scan are considered to be unbiased by any systematic effect. However, the influence of these systematic effects is not investigated in full detail as of completion of this thesis.

The MS retarding voltage is changed in steps of 50 V far away from the endpoint and of 5 V to 10 V close to it. At each step the corresponding FPD rate is measured. Plotting the voltage-dependent rates yields the integral β -spectrum, which is fitted with the function stated in Eq. 2.8 using the KaFit software [Kle14] while keeping the $m_{\nu_e}^2$ parameter at zero.

Similar to the MS and RW scans explained above, consecutive upward and downward MS retarding voltage scans are alternated and the obtained data is stacked before fitting. The deep MS scan result obtained in the course of the PRO KATRIN measurement at the beginning of KNM2 in mid-September 2019 at $U_{\text{RW,ref}} = -0.15$ V is illustrated in Fig. 6.9a for the integral FPD. The corresponding ring-wise distribution $E_0(U_{\text{RW,ref}}; \text{ring})$ is shown in Fig. 6.9b together with a linear fit for determining the slope.

The endpoint shift $\Delta E_0(U_{\text{RW,ref}}; U_{\text{RW,i}})$ for changing the RW voltage from $U_{\text{RW,ref}}$ to any other set point $U_{\text{RW,i}}$ can be deduced from the MS and RW scan results. It is

$$\Delta E_0(U_{\text{RW,ref}}; U_{\text{RW,i}}) = \frac{R(U_{\text{RW,i}}) - R(U_{\text{RW,ref}})}{|a_{\text{MS}}|} \quad (6.17)$$

with the FPD rates $R(U_{\text{RW,ref}})$ and $R(U_{\text{RW,i}})$ measured in the RW scan and the β -spectrum slope a_{MS} measured in the MS scan. Thus, a rate shift $(R(U_{\text{RW,i}}) - R(U_{\text{RW,ref}})) > 0$ cps results in an increase of the endpoint.

Eq. 6.17 only provides relative information about what happens to E_0 for a certain change of the RW voltage. The deep MS scan provides the absolute endpoint $E_0(U_{\text{RW,ref}}; \text{ring})$ for each ring. Combining both results yields the absolute ring-wise

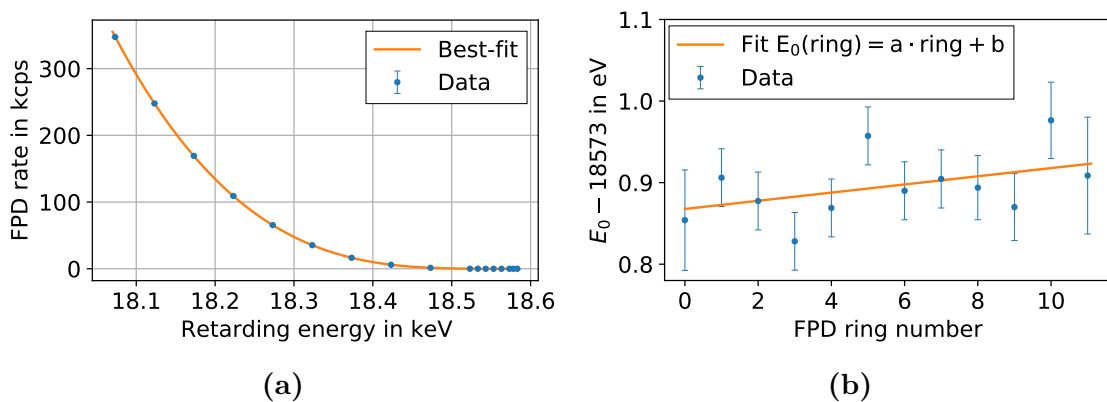


Figure 6.9: Results of the deep MS scan for the KNM2 PRO KATRIN measurement from 19.09.2019. In (a) the FPD rate versus the MS retarding energy measured at $U_{\text{RW,ref}} = -0.15$ V is shown together with the best-fit curve. A ring-wise analysis yields the best-fit result for $E_0(U_{\text{RW,ref}}; \text{ring})$ plotted in (b). A linear fit $E_0(U_{\text{RW,ref}}; \text{ring}) = a \cdot \text{ring} + b$ is applied to the data yielding $a = (5 \pm 4)$ meV/ring and $b = (18573.87 \pm 0.02)$ eV. The figures are based on data provided by W. Choi.

endpoint distribution for each RW scan set point $U_{\text{RW},i}$ by calculating

$$E_0(U_{\text{RW},i}; \text{ring}) = E_0(U_{\text{RW,ref}}; \text{ring}) + \Delta E_0(U_{\text{RW,ref}}; U_{\text{RW},i}; \text{ring}) \quad (6.18)$$

where $\Delta E_0(U_{\text{RW,ref}}; U_{\text{RW},i}; \text{ring})$ can be evaluated using Eq. 6.17.

Summary

PRO KATRIN consists of three individual measurements: RW, MS and deep MS scan. A total measurement time on the order of two days is necessary in order to accumulate a sufficiently high number of detector counts for each pixel ring. A combined analysis yields RW voltage-dependent information about the RW-plasma coupling and the radial distribution of the plasma potential. For the KNM1 and KNM2 β -scanning runs the RW voltage setting were mainly chosen based on these information. Results can be found in sections 6.3.1 and 6.3.2. Also, repeated PRO KATRIN measurements over the course of KNM2 revealed a drift of the plasma characteristic observables with time, as shown in section 6.3.4.

6.2.2 PRO KATRIN with ions

The insights about ions gained in chapter 5 can be used in order to develop an alternative version of the original PRO KATRIN method, in which tritium ions are used as plasma messenger particles instead of β -electrons. Those ions are created in the WGTS front end via molecular dissociation, where they are able to leave with eV-energies without being thermalized. By applying this novel method, the coupling between the RW and the plasma located about 16 m away from it can be investigated. Contributions from the central part of the WGTS and from the DPS can be neglected.

Measurement procedure

Tritium ions originating from the WGTS front end are detected in the PS by the ICE method, which was introduced in section 5.1.2. In analogy to the RW and MS scans of the original PRO KATRIN method, there are two distinct voltage scans. But instead of the MS, the DPSa ring electrode is used for scanning the energy spectrum of the messenger particles. All other ion blocking electrodes are fixed at reduced voltages below 20 V in order to enable ion transmission up to the PS.

- **RW scan:** The ICE rate $R_{\text{ICE}}(U_{\text{RW}})$, which is proportional to the flux of positive ions into the PS (cf. Eq. 5.3), is measured at different RW voltages U_{RW} at a fixed blocking voltage U_{DPSa} .
- **DPSa scan:** While keeping the RW voltage U_{RW} fixed, the ICE rate $R_{\text{ICE}}(U_{\text{DPSa}})$ is measured for different U_{DPSa} . This allows to disentangle the effect of the RW-plasma coupling from the ion energy spectrum. The data obtained for $R_{\text{ICE}}(U_{\text{DPSa}})$ is fitted with the exponential function

$$R_{\text{ICE}}(U_{\text{DPSa}}) = a_1 \cdot \exp(-a_2(U_{\text{DPSa}} - a_3)) + a_4 \quad (6.19)$$

where a_1 , a_2 , a_3 and a_4 are the fit parameters.

Throughout the entire measurement, the DPSa ring electrode voltage was never reduced below 19 V. This limits the ion flux into the PS and thereby assures that the

MS background is not significantly affected. Further, it is guaranteed that only ions originating from the low-density WGTS front end contribute, because there they can escape the source gas without losing significant amounts of their energy (cf. section 3.1.1). Other WGTS regions are not contributing at all, which is a unique feature of this approach. Ions from the DPS do contribute, but only to a minor extent due to the small gas density and thus small ion creation rate.

It should be noted that "PRO KATRIN with ions" is no high-precision measurement as the original version is. The FPD rate is rather low on the order of 100 cps, which is four orders of magnitude lower than the β -electron rate deep in the spectrum. Higher rates could only be achieved if the ion flux into the PS $\phi_{\text{CPS} \rightarrow \text{PS}}$ would be increased, which is not recommended because tritium ions induce background in the SDS. Even ICE rates of 100 cps are only acceptable for a short amount of time on the order of 1 h during the measurement, but not throughout an entire neutrino mass run over days and weeks. Furthermore, the DPSa ring electrode is not a MAC-E filter, so the energy measurement suffers from the rather bad energy resolution as there is no adiabatic collimation.

Investigation of the coupling strength between rear wall and plasma at the front end of the WGTS

The "PRO KATRIN with ions" investigations gives results for the front part of the WGTS, which can be compared to the findings of the original PRO KATRIN method in which the rate contribution over the whole WGTS is measured. A different coupling would indicate that the front part either decouples earlier or later than the entire WGTS.

The results of a measurement at the end of September 2019 can be seen in Fig. 6.10. Those can be compared to the results obtained with the original PRO KATRIN method. While in the plot in Fig. 6.8 a higher RW voltage leads to a lower FPD rate, the opposite is true for the curve in Fig. 6.10. This is because of the different charge signs of the messenger particles of the two methods. Positive tritium ions gain energy from a positive plasma potential while β -electrons lose it.

The RW scan curve is flat with an exponential dependence around $U_{\text{RW}} = 0\text{V}$. The coincidence with the shape of the reference spectrum indicates good coupling. This means that even the plasma at the far away front end of the WGTS is still following the RW surface potential although they are separated by about 16 m. However, at very positive voltages $U_{\text{RW}} \gg 0\text{V}$ the curve is flat again. For the same voltage region between $\sim 1\text{V}$ and $\sim 5\text{V}$, still a partly-coupled plasma was observed with the original PRO KATRIN method.

6.2.3 Characteristic current-voltage curves (I-U curves)

Plasma parameters can be derived from the characteristic current-voltage (I-U) curve of a Langmuir probe (cf. section 6.1.1). Such a curve can also be obtained with the RW voltage setup (cf. Fig. 6.5). A continuous voltage sweep can be applied while the current of impinging charge carriers is measured simultaneously. This procedure is referred to as I-U scan.

Comparison between an ideal Langmuir probe and the RW

The RW has some similarities to a Langmuir probe. It is directly exposed to the plasma and can be biased in order to attract or repel positive and negative charge

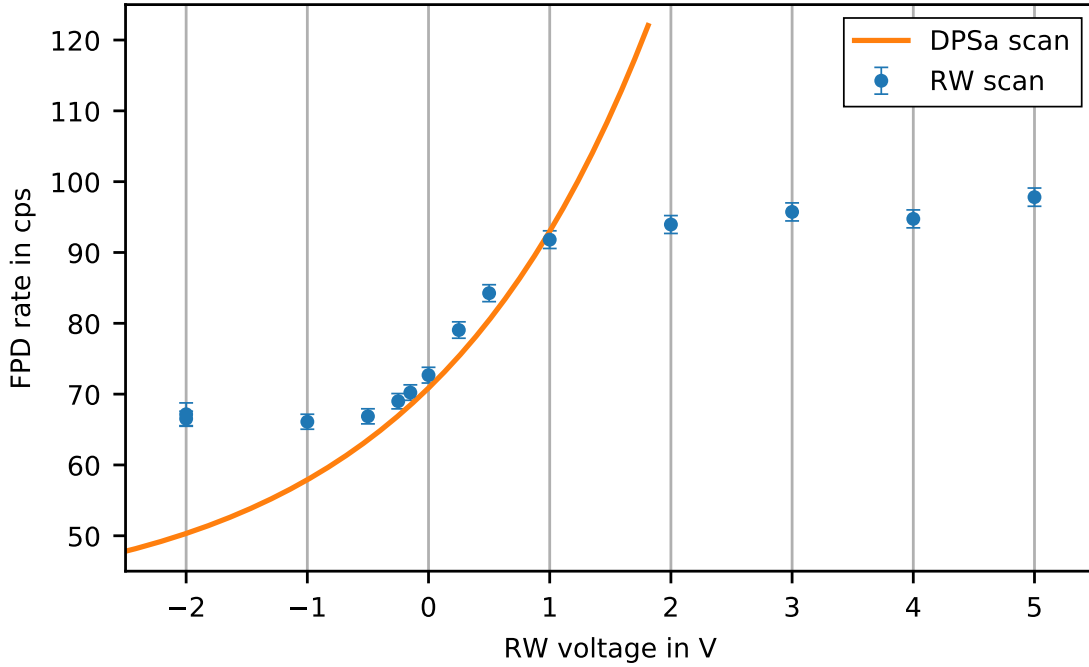


Figure 6.10: "PRO KATRIN with ions" result measured in KNM2 on 26.09.2019. The FPD rate captures the ion energy spectrum via the ICE method. It is shown versus the RW bias voltage. For comparison, the exponential reference curve of the dissociative ion spectrum (cf. Eq. 6.19) measured throughout the ring electrode DPSa scan at a RW voltage $U_{RW} = -150$ mV is superimposed. The reference spectrum $R_{ICE}(U_{RW})$ is mirrored ($U_{RW} \rightarrow -U_{RW}$), so that it matches the sign of the RW scan. The measurements are carried out at $\mathcal{N} = 4.2 \times 10^{17}$ molecules/cm² and $\epsilon_T = 98.7\%$.

carriers of the plasma. Also, the basic Langmuir probe theory explained in section 6.1.1 can be extended to include effects of highly magnetized plasmas. On the other hand, a Langmuir probe usually has small dimensions and represents only a minor perturbation with little influence on the global plasma. The comparably large-scale RW ($d = 145$ mm) is however designed to control the plasma. Currently, it is still a matter of debate which parts of the Langmuir probe theory can be applied to the RW.

Measurement procedure

Using the Agilent[®] function generator connected to the RW a triangular voltage modulation can be applied. The voltage U_{RW} is thereby continuously ramped over the range $(U_{RW,\min}; U_{RW,\max})$ while the current I_{RW} flowing through the RW towards ground is measured simultaneously. Typically, the voltage range is about ± 5 V and the period length of a full triangular cycle is 1 h.

During the I-U scan the DPS dipole electrodes 1-3 are operated in dipole mode at negative polarity DC voltages of $(-5$ V/ -15 V), $(-5$ V/ -35 V) and $(-5$ V/ -85 V) at their lower and upper half-shells, respectively. Thus, positive ions entering the DPS are removed via $E \times B$ drift.

Current observables

Charge carriers of any type such as β -electrons, secondary electrons, positive and

negative ions can contribute to the RW current I_{RW} . Positive currents represent incoming negative charge carriers while negative currents represent incoming positive ions. The currents I_{dipole1} , I_{dipole2} and I_{dipole3} measured at the three dipole electrodes are induced by the removal of positive ions. At the nominal voltage setting the dipole electrode currents are always negative, which corresponds to incoming positive ions. The total DPS current is defined as $I_{\text{DPS}} = I_{\text{dipole1}} + I_{\text{dipole2}} + I_{\text{dipole3}}$. The sum of the total DPS current and the RW current yields the total measured current $I_{\text{meas,tot}} = I_{\text{DPS}} + I_{\text{RW}}$. Overall, there are six parameters: I_{RW} , I_{dipole1} , I_{dipole2} , I_{dipole3} and the therefrom derived I_{DPS} and $I_{\text{meas,tot}}$. Any single parameter shows its own characteristic voltage-dependency.

A seventh parameter - the total current I_{tot} which is defined by the sum of the RW, the total DPS and the beam tube current - is not directly measured, but a basic assumption is that in steady state it has to satisfy⁸

$$I_{\text{tot}} = I_{\text{RW}} + I_{\text{DPS}} + I_{\text{BT}} = 0 \text{ A}. \quad (6.20)$$

Consequently, a measurement of $I_{\text{meas,tot}} = I_{\text{RW}} + I_{\text{DPS}} \neq 0 \text{ A}$ implies that the current towards the WGTS beam tube is given by $-I_{\text{meas,tot}}$.

Outlook on results

Characteristic I-U curves measured in KNM2 are shown in section 6.3.3. In the course of the campaign I-U scans were performed on a regular basis. For the RW set point $U_{\text{RW}}(I_{\text{meas,tot}} = 0 \text{ A})$, at which the total measured current vanishes, the same long-term drift as found with the PRO KATRIN method was observed (see section 6.3.4). Furthermore, I-U scans were carried out at different boundary conditions and WGTS operation modes during KNM1 and KNM2. The influence of various source settings on the shape of the characteristic I-U curve is discussed in section 6.3.5.

6.2.4 Search for high-frequency plasma instabilities with the egun

If the source plasma was exposed to high-frequency plasma instabilities, they would change the energy of a traversing β -electron. One could consider the (purely hypothetical) example of an electron with a kinetic energy of 18.6 keV and a corresponding velocity of about $v = 1/4c$ passing a 1 m long instability region in a time of approximately 12 ns. Then, frequencies above 80 MHz would be relevant.

One way to investigate this time-of-flight effect possibly induced by high-frequency plasma instabilities directly is to use electrons with defined energy E , pitch angle θ and radial off-axis shift Δr provided by the RS egun. A narrow beam of 18.6 keV electrons is shot through the WGTS and the whole KATRIN apparatus until it is finally detected at the FPD bull's eye. The electron path length through the plasma is enhanced for higher values of θ . As described in section 2.3.2, both the energy distribution $\eta(E)$ and the angular distribution $\zeta(\theta)$ of the egun electrons have a tiny but non-zero spread. Thus, the egun characteristic transmission function through

⁸This assumption is only valid if secondary electrons ejected from the RW or beam tube surfaces are neglected. This is justified because the ejection of secondary electrons is a second-order effect.

the MS differs from the ideal one stated in Eq. 2.5. It is given by [BRB⁺17]

$$T(E, U_{\text{ana}}) = \frac{dN_0}{dt} \cdot \int_E^\infty \eta(\epsilon) \int_0^{\theta_{\text{max}}(\epsilon, U_{\text{ana}})} \zeta(\theta) d\theta d\epsilon + \frac{dN_B}{dt} \quad (6.21)$$

where U_{ana} is the MS analyzing plane retarding voltage, dN_0/dt the amplitude of the signal, dN_B/dt the background rate and θ_{max} the maximum pitch angle at which electrons are still transmitted. This transmission function can be measured by stepping through the MS retarding voltage U_{ret} while the FPD rate is measured. The data can be fitted with an error function defined as [Sac20]

$$\frac{1}{2} \cdot \frac{dN_0}{dt} \cdot \left(1 + \frac{2}{\pi} \int_0^{\frac{e(U_{\text{sur}} - \mu)}{\sqrt{2}\sigma_E}} \exp(-\epsilon^2) d\epsilon \right) + \frac{dN_B}{dt} \quad (6.22)$$

with the mean voltage μ and the surplus voltage $U_{\text{sur}} = U_{\text{egun}} - U_{\text{ret}}$, where U_{egun} is the egun voltage which defines the electron energy $E = eU_{\text{egun}}$.

The observable for investigating plasma effects is the width of the fitted function σ_E . If the electron energy indeed is influenced by plasma instabilities, the transmission function width should be different compared to the case of an empty source tube without any plasma effects.

It is important to emphasize that the transmission function can only be modeled with an error function in case of Gaussian distributed $\eta(E)$ and $\zeta(\theta)$. This requirement is not perfectly fulfilled for the egun. However, the deviations are small and the fit with an error function is known from experience to apply well.

Results measured in KNM2 for various RW voltages can be found in section 6.3.6.

6.2.5 High-frequency sinusoidal voltage modulation at the rear wall

The guiding question of this approach is whether a high-frequency variation of the RW voltage has a significant influence on the plasma potential V_{P1} . If the answer is yes, high-frequency noise at the RW will eventually introduce a systematic effect for the neutrino mass determination.

A definite explanation of the underlying mechanism is currently pending. One hypothesis is related to the characteristics of the RW-plasma coupling. The coupling strength changes with the RW voltage, so an alternating RW voltage can not be translated to the plasma potential one-to-one, without any distortion. The coupling then acts similar to a rectifier and the mean value of the plasma potential is shifted, whereas the mean voltage at the RW is not affected at all by a symmetric oscillation. The remaining modulation of the plasma potential is likewise asymmetric.

Measurement procedure in nominal WGTS mode

According to Eq. 6.10 a variation of the plasma potential can be determined by measuring the β -spectrum endpoint shift ΔE_0 or equivalently a shift of the measured FPD rate ΔR . Consequently, the FPD rate is measured for different frequencies applied to the RW using an Agilent[®] 33220A function generator which is normally used at the egun. Throughout the measurements the waveform, offset and amplitude are kept constant. The sensitivity is increased by measuring deep in the spectrum at the same MS retarding voltage U_{PK} as in the PRO KATRIN approach. In order to handle the high rates, the FPD histogram mode is used for data acquisition.

It should be noted that at high frequencies exceeding 1 MHz the voltage amplitude set at the Agilent® function generator is not transported to the RW with 100% efficiency due to some damping in the supply cable. This is illustrated in Fig. 6.11, which shows a measurement of the effectively transmitted voltage amplitudes for different frequencies. AC voltages with frequencies of 3 MHz or beyond are damped by almost 100% and are not at all transported to the RW. This has to be considered for a correct interpretation of the measured data.

The obtained rate shift $\Delta R = R(\text{DC}) - R(f_i)$ between measurements at a RW DC voltage and an AC voltage with frequency f_i can be converted into a shift of the plasma potential ΔV_{Pl} via

$$\Delta V_{\text{Pl}}(\text{DC}, f_i) = \frac{R(\text{DC}) - R(f_i)}{a} \quad (6.23)$$

where a is the linear slope of the β -spectrum at the MS retarding potential U_{PK} as measured with the PRO KATRIN method.

Measurement procedure in WGTS krypton mode

Alternatively, an analogous measurement can be done in the WGTS krypton mode with $^{83\text{m}}\text{Kr}$ gas admixed to the plasma. At a MS retarding potential corresponding to the L_3 -32 line energy of $(30472.2 \pm 0.5) \text{ eV}$ [VSD⁺18] the sensitivity is maximized because even a tiny variation in energy results in a large shift of the rate. This is due to the narrow line width, which is measured integrally. An analytical integration of

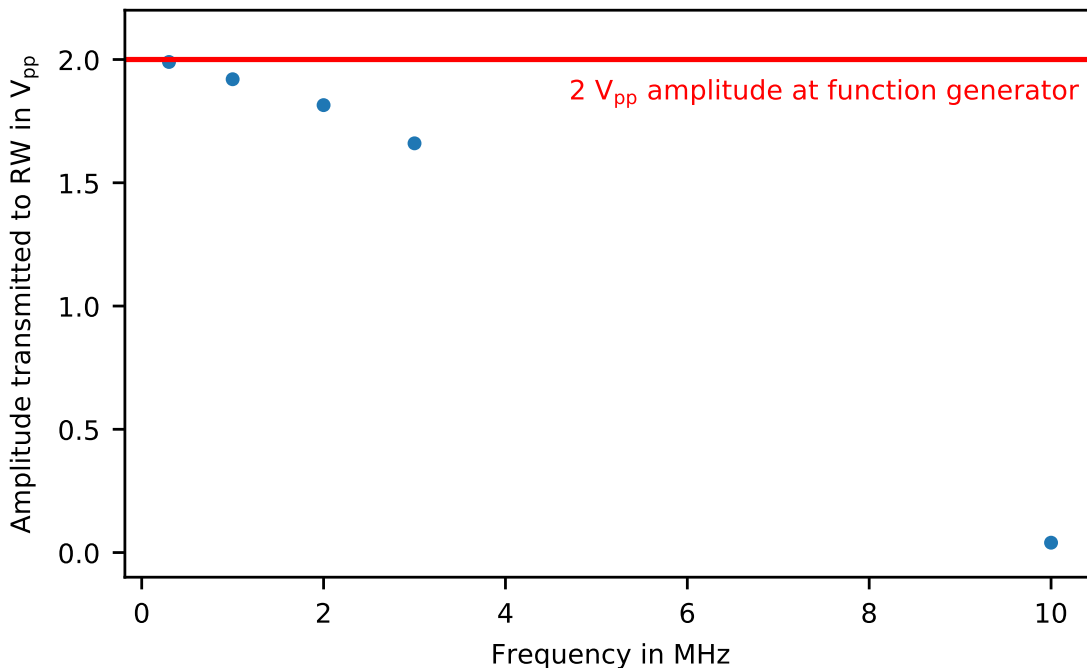


Figure 6.11: Frequency dependence of the peak-to-peak amplitudes transmitted from the function generator to the RW. A sinusoidal AC voltage was applied to the RW using the Agilent® function generator. The effectively transmitted voltage amplitudes were measured with an oscilloscope attached to a redundant cable connected to the RW.

the Lorentzian line profile (cf. Eq. 4.3) yields [Mac16]

$$R(E_{\text{ret}}) = A \left(\frac{1}{2} - \frac{1}{\pi} \arctan\left(\frac{2}{\Gamma}(E_{\text{ret}} - E_0)\right) \right) \approx A \left(\frac{1}{2} - \frac{2}{\pi\Gamma} \cdot (E_{\text{ret}} - E_0) \right) \quad (6.24)$$

with the FPD rate R , the MS retarding energy E_{ret} , the line position E_0 and the line width Γ . Taking the difference of two rates measured at two different retarding potentials results in $\Delta R = 2Ae\Delta U_{\text{ret}}/(\pi\Gamma)$. As for the measured FPD rate, a variation of the MS retarding potential is equivalent to a change of the plasma potential V_{Pl} so the formula can be used in order to convert a rate shift into a plasma potential shift via

$$\Delta V_{\text{Pl}}(\text{DC}, f_i) = \frac{\pi\Gamma}{2eA} \cdot (R(\text{DC}) - R(f_i)) \quad (6.25)$$

with the elementary charge e , the line width Γ , the line amplitude A , and the FPD rates $R(\text{DC})$ and $R(f_i)$ measured at a RW DC voltage and AC voltage with frequency f_i , respectively. Resolving Eq. 6.24 yields the line amplitude

$$A = \frac{R}{\left(\frac{1}{2} - \frac{2}{\pi\Gamma} \cdot (E_{\text{ret}} - E_0)\right)} \quad (6.26)$$

which can be calculated with the rate R and the retarding energy E_{ret} obtained in a dedicated reference run. The line position E_0 and width Γ are known from the analysis of the L₃-32 line, which is measured several times during the ^{83m}Kr campaign at the end of KNM2.

6.3 Plasma investigations during the KATRIN neutrino mass runs 1 and 2

Besides the β -spectrum scans to assess the neutrino mass scale, a significant number of systematic measurements were performed both over the KNM1 and KNM2 campaigns (cf. section 3.2). Investigation of plasma effects was a top priority. One of the main goals was to find a proper RW setting to apply throughout the neutrino mass runs. Therefore, several days before and in between the neutrino mass runs were used in order to perform plasma measurements based on the PRO KATRIN, I-U scan and other methods described in the previous section.

The results for both KNM1 and KNM2 are presented in this section. The main focus is on the investigations in the KNM2 nominal mode since it is close to the design configuration and most of the plasma measurements were conducted in this setting. As for the WGTS, the nominal mode is mainly characterized by the beam tube temperature $T_{\text{WGTS}} = 30$ K, the column density of 84% with respect to the design value $\mathcal{N} = 5 \times 10^{17}$ molecules/cm² and the tritium purity $\epsilon_T > 95\%$.

Unless otherwise noted, column density values stated in the text are derived from the results of several accurate egun calibration measurements performed by F. Block, C. Köhler and A. Marsteller^{9,10}. In this way absolute uncertainties of 1% and 0.6%

⁹F. Block, F. Glück, C. Köhler and A. Marsteller, KATRIN KNM1 Reference Report - Systematic Uncertainty of Column Density / Column Density Times Inelastic Scattering Cross-Section, internal report, 2019.

¹⁰F. Block, C. Köhler, A. Marsteller and P. Filip, KATRIN KNM2 Reference Report - Systematic Uncertainty of Column Density / Column Density Times Inelastic Scattering Cross-Section, internal report, 2020.

are achieved for the KNM1 and KNM2 column density values, respectively. All measurements were performed within the KATRIN (non-krypton) plasma team mainly consisting of F. Glück, M. Klein and M. Schlösser. Also, W. Choi provided important fit results. It will be denoted whenever an explicit contribution from one of them is depicted in the text.

First, in section 6.3.1 the coupling of the RW surface potential to the WGTS plasma is studied with the PRO KATRIN and the "PRO KATRIN with ions" method, respectively. Combining the PRO KATRIN data with the ring-wise analysis of an MS scan deep into the β -spectrum in section 6.3.2 leads to the ring-wise distribution of the end point or, correspondingly, the plasma potential. Characteristic I-U curves of the RW are shown and interpreted in section 6.3.3. In KNM2 different analyses of PRO KATRIN and I-U scan results reveal a linear drift of the observables, which is covered in section 6.3.4. Those methods were also applied in investigations of the influence of different WGTS parameters on the plasma, which is discussed in section 6.3.5. Further, measurements targeted to study high-frequency plasma instabilities, plasma oscillations and the impact of high-frequency AC voltages applied to the RW are presented in sections 6.3.6, 6.3.7 and 6.3.8, respectively. At last, the influence of different DPS dipole electrode voltage settings (see section 6.3.9) and of the DPS infrared illumination (see section 6.3.10) on the plasma potential is analyzed.

6.3.1 Plasma coupling to rear wall

In this section the coupling between RW and plasma is investigated using the PRO KATRIN and the "PRO KATRIN with ions" method described in sections 6.2.1 and 6.2.2, respectively.

Motivation

Since all magnetic field lines of the 134 T cm^2 flux tube are terminated on a specific spot on the RW surface, the initial idea was that the electric potential at this spot is propagated along the complete distance in z -direction due to the high axial and negligible radial conductivity. It was expected that the plasma potential would be dominated by the RW potential, independent of its absolute value. The first detailed simulations by L. Kuckert [Kuc16] showed that both assumptions do not hold in all cases. However, the KNM1 and KNM2 campaigns provided the first opportunity to experimentally validate or falsify these initial ideas.

Coupling averaged over whole FPD

In mid-September 2019 a PRO KATRIN measurement was performed in preparation for the KNM2 β -scans. The results analyzed for the integral FPD can be found in Fig. 6.8 of section 6.2.1. Ring-wise results are shown in Fig. 6.12 and will be discussed in the next paragraph. The overall shape of the RW scan curve is compatible to the expectation gained from the two-dimensional axially symmetric fluid model simulation (cf. Fig. 6.6 in section 6.1.3). For highly negative U_{RW} the FPD rate does not change with the RW voltage. This fits to the $\Delta < \Delta_C \approx -40 \text{ mV}$ scenario of the simulation where the RW is not anymore determining the plasma potential. At more positive U_{RW} there is a window of several hundreds of mV where the surface potentials of the RW and the beam tube are close and the coupling between RW and plasma is maximized. In this case, the plasma potential follows the RW bias

voltage and the slope of the curve is very close to the reference slope measured in the MS scan. For very positive U_{RW} it is $\Delta > \Delta_C$ and the coupling starts to diminish. Similar results were obtained by repeated measurements in KNM2, which will be discussed in section 6.3.4.

The underlying physical mechanisms responsible for the varying coupling strengths in the different regions can not be clearly identified from the measurement results. It is likely that both at very positive and very negative RW voltages the respective currents of electrons and ions flowing out of the plasma start to saturate, so the plasma can not efficiently adjust its potential anymore. In the fluid model simulations the decoupling for $\Delta < \Delta_C$ was due to the beam tube surface potential penetrating into the plasma bulk. For $\Delta > \Delta_C$, the diminishing coupling was because WGTS regions with a large distance to the RW were not influenced anymore by the RW setting. The PRO KATRIN method is not sensitive to these two processes, so they can not be validated. However, at least the coupling of the WGTS front part at $\Delta > \Delta_C$ can be investigated with the "PRO KATRIN with ions" method (see paragraph "longitudinal coupling" in this section).

Radial coupling

The RW scan curve can also be plotted for individual FPD pixel rings as it is done in Fig. 6.12 in order to derive radial patterns. While the overall shape of the curve is similar for different rings, there are significant differences in the absolute results.

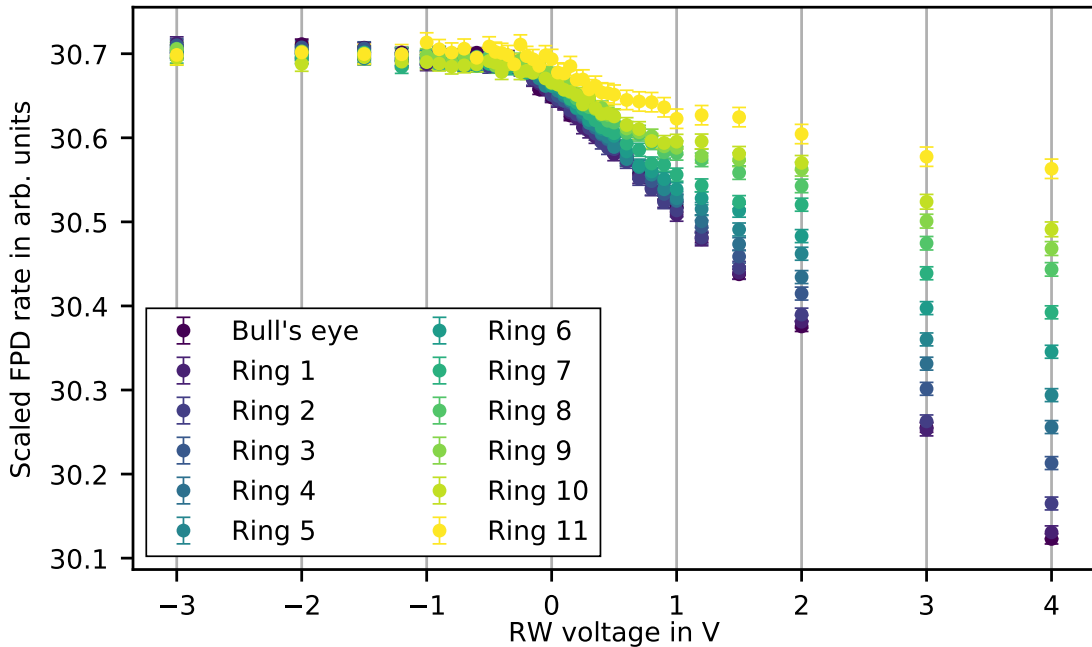


Figure 6.12: Ring-wise results of the PRO KATRIN RW scan measured in KNM2 on 19.09.2019. The measurements are carried out at $\mathcal{N} = 4.2 \times 10^{17}$ molecules/cm² and $\epsilon_T = 98.4\%$. For better comparison all curves are superimposed by scaling the ring-wise FPD rates. The scaling is done with a constant factor in such a way that the rates at $U_{RW} = -0.3$ V are all equal to the bull's eye rate. The ring numbers indicate the radial position starting from ring 1 closest to the bull's eye up to ring 11 which is the outermost one.

A change of the RW voltage induces a significantly higher change in the FPD rate measured at the central rings ($r \rightarrow 0$) compared to the outer rings ($r \rightarrow \max$). Consequently, at outer radii of the sensitive magnetic flux tube the coupling strength between RW and plasma is declining. It can be concluded that the plasma potential around $r = 0$ is closest to the RW surface potential, while for growing radii the difference between plasma bulk and RW boundary potential is increasing. At $U_{\text{RW}} \ll 0 \text{ V}$ the decoupling holds for all rings.

The data is fitted with the function stated in Eq. 6.13. The best-fit results for the rates at the bull's eye and three different FPD rings are shown in Figs. 6.13a to 6.13d. It can be seen that the first kink at $U_{\text{RW}}^{\text{start}}$ is prominently appearing in all rings, while the second kink at $U_{\text{RW}}^{\text{end}}$ becomes more pronounced at the outer rings.

In Fig. 6.13e the best-fit kink positions are plotted versus the average ring radius. It can be seen that the starting position of the region of maximum coupling stays rather constant with the radius, while the end position is decreasing. Consequently, the width of the maximally-coupled region is getting smaller for the outer rings.

In section 6.3.4 the starting point of the maximally-coupled region $U_{\text{RW}}^{\text{start}}$ determined for different KNM2 PRO KATRIN data sets is used as an important observable for investigating time-dependencies.

The coupling strength c is calculated in the maximally-coupled region for each FPD ring according to Eq. 6.14 and plotted in Fig. 6.14a. The result supports the diminishing coupling strength towards outer radii starting from approximately $c = 1$ at the central bull's eye and decreasing to about $c = 0.5$ at ring 11. As for the partly-coupled region at $U_{\text{RW}} \gg 0 \text{ V}$, a similar drop can be seen in Fig. 6.14b. To both data sets a fit using the model stated in Eq. 6.16 is applied, yielding the results given in Tab. 6.1. These quantitative results validate that at outer radii the plasma potential is only loosely coupled to the RW surface potential. A reasonable explanation could be the influence of the WGTS beam tube surface potential which grows as a function of the radius. For the partly-coupled region, this would however disagree with the simulations of L. Kuckert (cf. section 6.1.3), because for $\Delta \gg \Delta_C \approx -40 \text{ mV}$ a complete shielding of the beam tube surface potential is expected. An alternative explanation formulated by G. Drexlin could be the presence of negative blocking potentials of up to several hundreds of mV at large radii in front of the RW surface. These would prevent the flow of electron currents out of the plasma, which would be required for a good coupling. Furthermore, this mechanism could also be responsible for the radial independence of $U_{\text{RW}}^{\text{start}}$ (cf. Fig. 6.13e). At $U_{\text{RW}}^{\text{start}}$ positive ions start to flow towards the RW. This current would not be affected by negative blocking potentials, so it could flow undisturbed at all radii.

In both the maximally-coupled and partly-coupled region the radial coupling strength data provides the radial plasma potential distributions by making use of Eq. 6.15, which serve as an input for advanced simulations by F. Glück (see section 6.3.3).

Influence of the UV RW illumination

As found in dedicated analyses by A. Fulst [Ful20], the voltage interval of maximal RW-plasma coupling can be significantly widened by illuminating the RW with the Cermax[®] UV lamp. This can be attributed to the higher number of eV-energy electrons with a high longitudinal mobility. A ring-wise analysis shows that the coupling strength is increased for all rings likewise. However, this comes at the expense of a negative space charge potential.

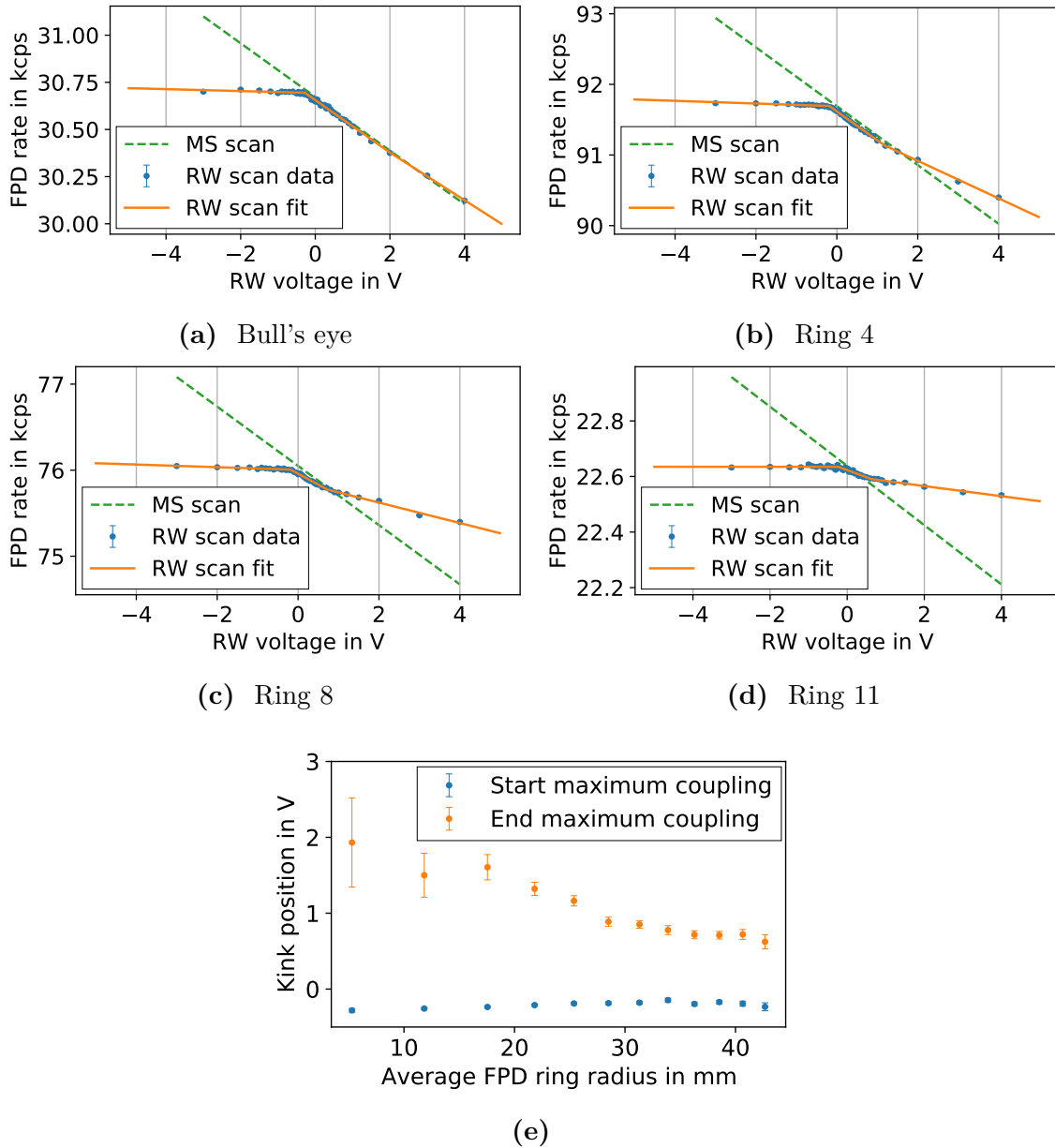


Figure 6.13: Triple linear fit of the ring-wise PRO KATRIN results measured in KNM2 on 19.09.2019. The triple linear model stated in Eq. 6.13 is fitted to the PRO KATRIN data of the FPD bull's eye (a), ring 4 (b), ring 8 (c) and ring 11 (d). The different absolute rates can be attributed to the smaller area of the bull's eye (172 mm^2) compared to one of the other pixel rings (516 mm^2) and to the exclusion of certain pixels from the analysis. These pixels are either noisy or the electron transmission is disturbed by beam line obstacles. There are no pixels excluded for the the bull's eye and ring 4, while 2 and 9 out of 12 pixels are excluded for the rings 8 and 11, respectively. For each ring the linear reference slope of the β -spectrum as measured in the MS scan is superimposed. In (e) the best-fit kink positions $U_{\text{RW}}^{\text{start}}$ and $U_{\text{RW}}^{\text{end}}$ are plotted versus the average FPD ring radius. The plots are produced using an analysis source code provided by M. Klein.

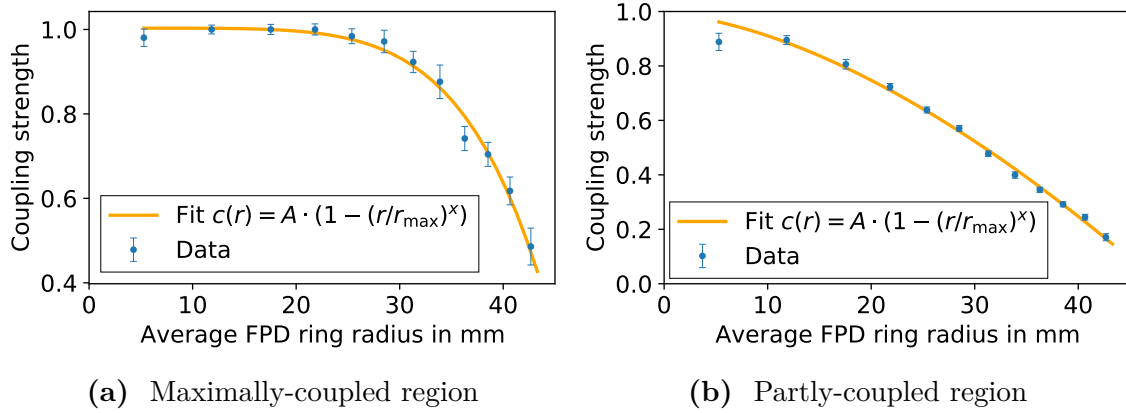


Figure 6.14: Ring-wise coupling strength results for the KNM2 PRO KATRIN measurement from 19.09.2019. The radial evolution of the coupling strength $c(r)$ (cf. Eq. 6.14) is shown in (a) for the maximally-coupled region and in (b) for the partly-coupled region together with a best-fit curve. The plots are produced using an analysis source code provided by M. Klein.

Table 6.1: Best-fit results for the radial dependence of the coupling strength between RW and plasma. Shown are the values obtained from fitting the function $c(r) = A \cdot (1 - (r/r_{\max}))^x$ to data obtained in a PRO KATRIN measurement in KNM2 from 19.09.2019.

RW voltage region	A	r_{\max} in mm	x
Maximally-coupled region	1.003 ± 0.006	47.7 ± 0.8	5.7 ± 0.5
Partly-coupled region	0.99 ± 0.03	47.8 ± 0.6	1.6 ± 0.1

Longitudinal coupling

In addition to the radial coupling dependence there is also the possibility to deduce information about the longitudinal behavior. The coupling of the plasma located at the front end of the WGTS can be inferred using the "PRO KATRIN with ions" method (cf. section 6.2.2).

The result of a measurement at the beginning of KNM2 was already shown in Fig. 6.10 in section 6.2.2. For $U_{\text{RW}} \geq 1$ V a decoupling is observed whereas in the original PRO KATRIN approach, in which the average over the entire WGTS is taken, there is still a partly-coupled plasma. This means that at very positive RW voltages the WGTS front part is decoupling while the rear part closer to the RW is still coupled. In fact, this fits to the outcome of the two-dimensional axially symmetric fluid model simulation for the $\Delta > \Delta_C$ case (cf. section 6.1.3). If $\Delta > \Delta_C$ is fulfilled, the simulations predict that the RW surface potential will determine the plasma potential, while the beam tube potential will be completely shielded. The coupling will get worse for larger distances to the RW.

It has to be emphasized that at even more positive RW voltages beyond those measured in KNM2 a complete decoupling between RW and plasma is expected. In this fourth coupling region the plasma potential is not anymore determined by the RW. In fact, this was observed in measurements in the WGTS krypton mode (see section 6.3.5) and in the KNM3 campaign after completion of this thesis.

Conclusion

The RW-plasma coupling strength was found to be highly dependent on the applied RW bias voltage. While for negative U_{RW} the coupling strength is minimal with $c \approx 0$, there is a window of several hundreds of mV around $U_{\text{RW}} = 0$ V in which it is $c = 1$. For $U_{\text{RW}} \gg 0$ V, however, the coupling strength decreases but does not vanish completely within the voltage range ≤ 4 V covered in KNM2. Measurements during KNM3 and in the WGTS krypton mode (see section 6.3.5) in fact show that the plasma completely decouples from the RW eventually. The decoupling at extreme RW set points is likely caused by saturating currents flowing out of the plasma bulk during the process of potential adjustment.

The results deviate for different radii. A trend of weaker coupling strengths for larger radii can be observed. Possible explanations are either the growing influence of the beam tube surface potential or the presence of negative blocking potentials at large radii in front of the RW.

As found by A. Fulst, both the coupling strength and the RW voltage interval of maximal coupling can be significantly enhanced by producing eV-scale photoelectrons using the Cermax[®] UV lamp. This applies to all radii likewise.

The coupling characteristics of the front end of the WGTS are compatible with the central part, with an exception at $U_{\text{RW}} \geq 1$ V where a decoupling was observed. In this voltage domain, parts further away from the RW decouple while closer regions are still coupled. This finding is in good agreement with simulations.

Considering the entirety of results, it can be stated that the initial ideas about the role of the RW stated in [KAT05] need to be modified.

6.3.2 Radial endpoint homogeneity: determination of the optimum rear wall set voltage for neutrino mass measurements

Results for the radial endpoint distribution of the β -spectrum are presented in this section. They were determined by combining results of the RW and the deep MS scan, which are both part of the PRO KATRIN method (cf. section 6.2.1).

Motivation

For neutrino mass measurements a flat radial distribution is optimal, since it corresponds to a homogeneous plasma potential profile. It is expected that there is a certain RW set point where this flat distribution is realized (cf. section 6.1.3). Based on the simulation results of L. Kuckert [Kuc16], the radial homogeneity is expected to correlate with longitudinal homogeneity, which is the actual optimization criterion for the RW voltage. Thus, before the official start of KNM1 and KNM2 β -scanning, the optimum RW voltage had to be found.

Radial endpoint slopes for different RW voltages

The PRO KATRIN RW and MS scans are supplemented by a deep MS scan up to 500 V below the β -spectrum endpoint E_0 . Using the relation between MS retarding voltage and FPD rate from Eq. 2.8, the data for each FPD ring is fitted individually¹¹, yielding the ring-wise endpoint $E_0(U_{\text{RW,ref}}; \text{ring})$ at a fixed RW voltage $U_{\text{RW,ref}}$. Only the signal amplitude, the background rate and the endpoint are

¹¹The fits were carried out by W. Choi.

free parameters of the fit, while the squared neutrino mass $m_{\nu_e}^2$ parameter is fixed to zero. The result of a measurement performed in mid-September 2019 was already given in Fig. 6.9. Combining the results of the RW, the MS and the deep MS scan by evaluating Eq. 6.18 yields the ring-wise distribution of the absolute endpoint $E_0(U_{\text{RW},i}; \text{ring})$ at any RW voltage $U_{\text{RW},i}$. This distribution can in turn be fitted with a linear function in order to deduce the radial slope of the endpoint.

For different RW voltages the ring-wise endpoint slopes are plotted in Fig. 6.15. At $U_{\text{RW}} \ll 0 \text{ V}$ the slope is slightly negative, while a steep rise to positive values is visible for $U_{\text{RW}} \gg 0 \text{ V}$. A possible explanation is the following. According to the findings of the previous section, the plasma observed with the inner rings couples strongly to the RW, while the coupling strength decreases at the outer rings. Thus, for large positive RW voltages the potential of the inner plasma part is highly positive, too. But the outer parts do not follow the RW, so there the potential stays at a smaller value. This leads to a lower endpoint in the inner rings and a higher endpoint at the outer rings (cf. Eq. 6.10), which explains the highly positive slope. Similar arguments can be applied to the negative RW voltage region.

Overall, it should be emphasized that the observed characteristics of the endpoint slope pattern are in good agreement with the results of the simulations using the two-dimensional axially symmetric three-particle fluid model [Kuc16].

At the point of zero slope the plasma potential is independent of the radius. At this optimum point no radial electric field is present and the radial and presumably also

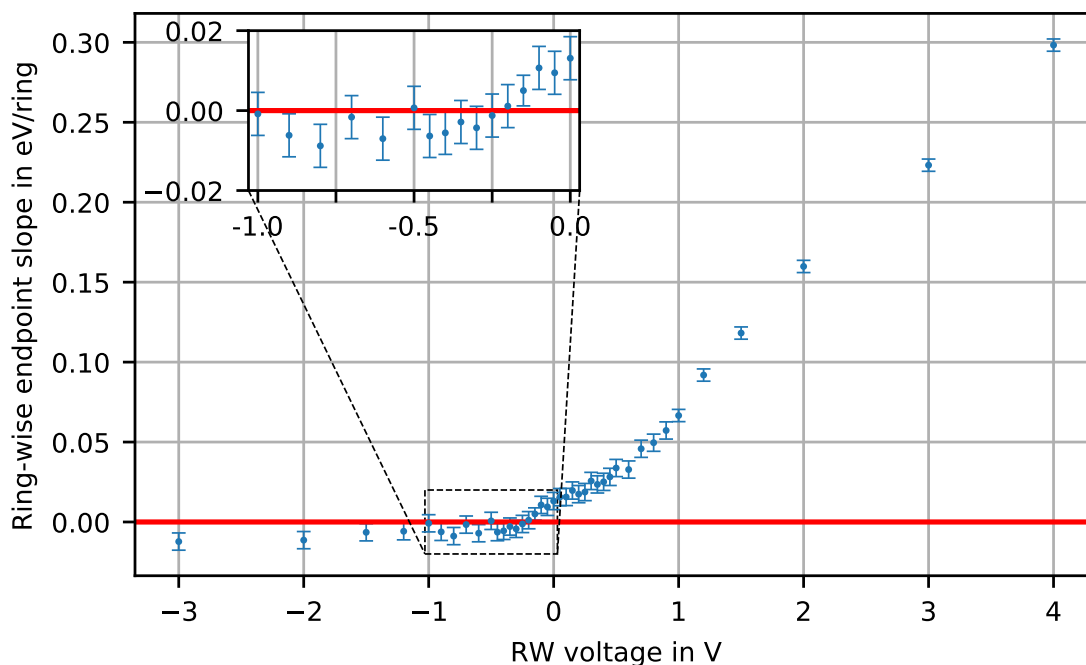


Figure 6.15: PRO KATRIN result for the ring-wise β -spectrum endpoint slope as a function of the RW voltage measured in KNM2 on 19.09.2019. Shown are the best-fit results of the ring-wise β -spectrum endpoint slope for different RW bias voltages. A slope of zero represents a flat endpoint distribution and is indicated by the red horizontal line. This point of zero slope is assumed to be the optimal setting for neutrino mass measurements. Thus, the corresponding RW voltage determined in dedicated PRO KATRIN measurements was applied during KNM1 and KNM2 β -scanning.

longitudinal homogeneity of the plasma potential is maximized. Both in KNM1 and in KNM2 the RW voltages applied throughout the entire neutrino mass measurement were chosen based on this criterion. As for KNM1, the optimum set point was found to be $U_{\text{RW}} = -0.15 \text{ V}$ [AAA+19c]. In KNM2 a long-term drift of the curve shown in Fig. 6.15 required adjusting the RW setting over time. Three different optimum voltages $U_{\text{RW}} = -0.05 \text{ V}$ ¹², $U_{\text{RW}} = -0.008 \text{ V}$ and finally $U_{\text{RW}} = +0.2 \text{ V}$ were determined in repeated measurements and each applied for several weeks over the course of the campaign. The various results obtained with the PRO KATRIN method at different points in time during KNM2 will be presented in section 6.3.4. There, the zero radial slope point is used as a reference point in order to quantify the long-term drift.

Conclusion

The ring-wise endpoint slopes for different RW voltages exhibit some characteristic features, which can be understood with the insights gained in the previous section about the RW-plasma coupling. At $U_{\text{RW}} \gg 0 \text{ V}$ the plasma potential at inner radii is highly positive while at outer radii less positive plasma potentials are established. Thus, the radial endpoint slope is positive since it is anticorrelated to the corresponding plasma potential slope. The absolute slope is growing if U_{RW} is increased. At $U_{\text{RW}} \ll 0 \text{ V}$ there is no coupling, so there is no effect of the RW voltage on the radial plasma potential slope. The point of zero ring-wise slope corresponds to a radially homogeneous plasma potential and was defined the top criterion for choosing the RW set point to apply for the first neutrino mass measurements in KNM1 and KNM2.

6.3.3 Measurement of characteristic I-U curves via rear wall voltage sweeps

During measurements of the characteristic I-U curve of the RW a triangular voltage modulation is applied (cf. section 6.2.3). Moreover, the currents at the DPS dipole electrodes are measured simultaneously. Across repeated measurements a characteristic curve can be observed, which has been reproduced many times. The features of this curve reveal important insights about the plasma.

Motivation

Before the start of KNM1 the currents generated by ions and electrons were not considered as a possible observable for plasma characterization. This is why before the development of this thesis there were no plasma simulation results for the RW current available. In the course of the first PRO KATRIN measurements the RW and DPS dipole electrode currents were measured simultaneously and the idea of dedicated voltage scans was developed. Since then the I-U scan results have evolved to an important plasma simulation benchmark and provided major insights about the motion of electrons and ions within the WGTS.

Currents measured at different RW voltages

The characteristic I-U curves measured in KNM2 in mid-October 2019 at a column

¹²The choice of $U_{\text{RW}} = -0.05 \text{ V}$ was based on a faulty analysis of the PRO KATRIN data and after the application of this voltage the analysis turned out to be wrong. The true optimum was rather between $U_{\text{RW}} = -0.25 \text{ V}$ and $U_{\text{RW}} = -0.2 \text{ V}$ as one can see in Fig. 6.15.

density $\mathcal{N} = 4.2 \times 10^{17}$ molecules/cm² and a tritium purity $\epsilon_T = 98.6\%$ can be seen in Fig. 6.16. Plots for all of the six relevant observables are shown.

- **RW current I_{RW} :** At first glance the RW characteristic I-U curve looks similar to a typical Langmuir probe curve (cf. Fig. 6.3). At highly positive voltages the electron current is asymptotically approaching its saturation value of about 300 nA, while at highly negative voltages the current induced by

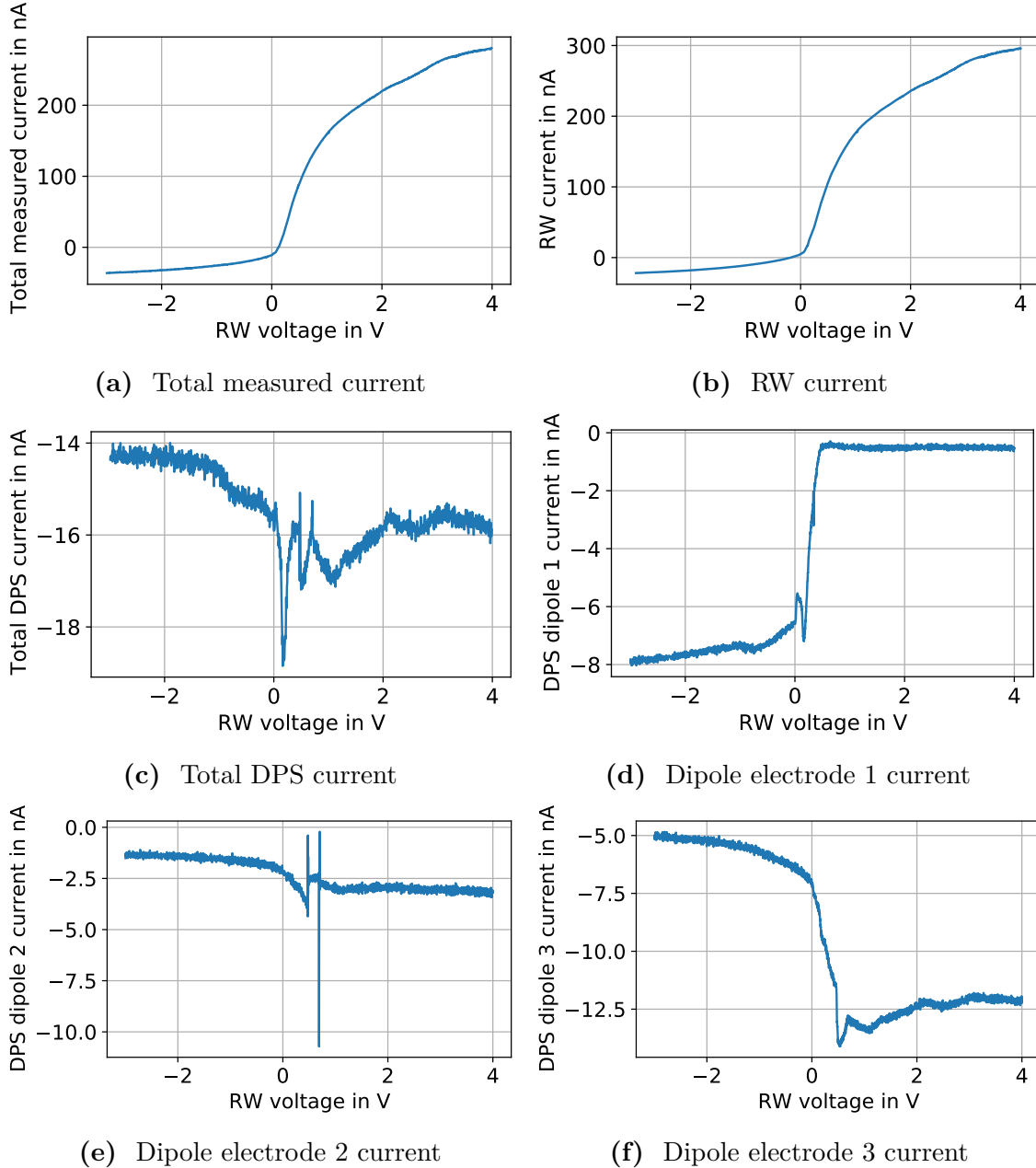


Figure 6.16: I-U scan results measured in KNM2 on 16.10.2019. Shown are the currents $I_{\text{meas,tot}}$ (a), I_{RW} (b), I_{DPS} (c), I_{dipole1} (d), I_{dipole2} (e) and I_{dipole3} (f) versus the applied RW voltage. The data is measured at $\mathcal{N} = 4.2 \times 10^{17}$ molecules/cm² and $\epsilon_T = 98.6\%$ in a continuous voltage sweep in downward direction starting at the maximum positive value and ending at the minimum negative value. The plots are produced using an analysis source code provided by M. Klein.

positive ions is maximized.

- **Dipole electrode currents I_{dipole1} , I_{dipole2} , I_{dipole3} :** Below $U_{\text{RW}} \approx 0$ V a rather constant current of positive ions is measured at the first dipole electrode, while above this threshold value the current drops by roughly one order of magnitude. The complete opposite is true for dipole elements 2 and 3 where the current steeply rises as soon as the threshold value is exceeded. Apparently, positive ions are blocked from reaching the DPS elements 2 and 3 below a certain threshold value. Once this value is exceeded, a higher positive plasma potential provides the positive ions with sufficient energy to overcome this barrier and reach the dipole elements located further downstream. The blocking barrier is likely caused by work function differences of roughly 150 mV between the DPS beam tube elements 1 and 2.
- **Total DPS current I_{DPS} :** The sum of all three dipole electrode currents stays rather constant over the entire voltage range, which indicates that a constant flux of positive ions is entering the DPS independent of the plasma potential.
- **Total measured current $I_{\text{meas,tot}}$:** The sum of all measured currents exhibits a similar shape as the stand-alone RW current. In the steady state, however, the sum of all currents out of the plasma is required to be zero (cf. Eq. 6.20). Thus, a measured value below zero implies an undetected current of negatively charged particles towards the beam tube. The same applies to values above zero, which imply undetected currents of positively charged particles. In principle, these currents could be due to magnetic field line collisions with the beam tube but this effect is considered minor. The only remaining possibility for charge carriers to leave the WGTS without contributing either to I_{RW} or I_{DPS} is to move perpendicularly to the magnetic field lines and to eventually neutralize on the beam tube.

Possible interpretations of I-U scan results

There are different possibilities for explaining the characteristic shape of the I-U curves. However, the details are still a matter of debate and discussing all of them is beyond the scope of this thesis. In the following some important, but not yet validated, ideas are summarized briefly.

In the classic Langmuir probe theory the ratio of positive ion and electron saturation currents is given by $I_{i,\text{sat}}/I_{e,\text{sat}} \propto \sqrt{m_e/m_i}$ with the mass of an electron m_e and a positive ion m_i [Str18]. It is $I_{i,\text{sat}} \ll I_{e,\text{sat}}$ because the thermal velocity of ions is much smaller than the one of electrons. This would be in agreement with the shape of the RW I-U curve shown in Fig. 6.16b.

Furthermore, the effect of the strong axial magnetic field have to be taken into account. First efforts have been made by F. Glück who performed simulations based on a drift-diffusion fluid approach. This was only possible by using the radial dependence of the coupling and the ring-wise endpoint slopes gained from the PRO KATRIN measurements (cf. sections 6.3.1 and 6.3.2) as an input for the simulations. Quantitative results were obtained only for the $\Delta > 0$ V case, in which the RW surface potential is more positive than the one of the beam tube. Based on the ring-wise endpoint slopes (cf. Fig. 6.15) it would follow that a positive transversal electric field would be present for $\Delta > 0$ V, which would drift positive ions in transversal direction (cf. Eq. 6.6 of section 6.1.2). The relative shape of this radial electric field

is taken from the radial coupling strength results (cf. Eq. 6.15 and Fig. 6.14). According to the simulation results, for $\Delta > 0$ V the dominant mechanism for generating the characteristic I-U curve of the RW would be the movement of positive ions perpendicular to the magnetic field lines. This transversal motion is also present in the simulation results described in 6.1.3 for the $\Delta > \Delta_C$ case.

As for $\Delta < 0$ V, the radial electric fields would be negative (cf. Fig. 6.15) and a negative current would be measured at the RW. Thus, negative charge carriers would be lost to the beam tube. Due to the low amount of negative ions the electrons are assumed to dominantly contribute to this drift current. However, they have a few orders of magnitude lower transversal mobility than ions, which would agree with the significantly lower absolute RW saturation current measured at $U_{RW} \ll 0$ V compared to the saturation current at $U_{RW} \gg 0$ V. Nevertheless, the transversal electron mobility induced by the drift due to the observed radial electric field would be too low, so the underlying mechanism responsible for the transversal electron movement would have to be something unconsidered yet. A possible explanation could be the so-called anomalous radial electron transport induced by plasma instabilities (see e.g. [Bal05]). In this scenario azimuthal time-dependent electric fields would lead to an $E \times B$ drift in radial direction. These electric fields could be induced by cross field instabilities (see e.g. [Cap76]). However, this idea could not yet be validated by simulations.

Systematic effects

The I-U scan results shown in Fig. 6.16 were obtained in a single downward sweep in which the voltage is decreased from the most positive to the most negative set point. During this process systematic effects are introduced which distort the measured curves. This can for example be seen from the plots of Fig. 6.17 in which a hysteresis effect is observed if both scanning directions are considered. The curves measured consecutively are shifted by up to 70 mV with respect to each other. This applies to all six current parameters likewise. Furthermore, during consecutive sweeps the I-U curves drift to more positive voltages. Such effects induced by variations of the volt-

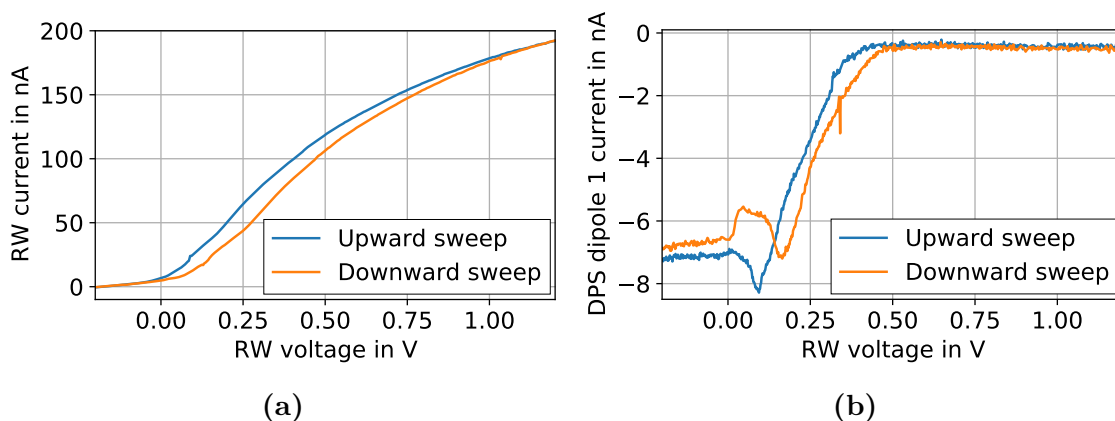


Figure 6.17: Asymmetry between a downward and an upward RW voltage sweep measured in KNM2 on 16.10.2019. Shown are the RW current I_{RW} (a) and the DPS dipole electrode 1 current I_{dipole1} (b) versus the applied RW voltage for a continuous voltage sweep in upward and downward direction. The plots are produced using an analysis source code provided by M. Klein.

age are commonly observed in plasma measurements using a Langmuir probe (see e.g. [D'A74]). Both effects and their underlying physical mechanisms are described more elaborately in the next section.

Conclusion

Characteristic patterns were observed for the I-U curve of the RW, the DPS dipole electrodes and different combinations of those four. However, the measurement procedure suffers from some intrinsic systematic effects, which are commonly observed in similar plasma measurements. The physical processes responsible for the characteristic shape of the I-U curves are currently still a matter of debate. One hypothetical explanation is that the loss of positive ions (for $U_{\text{RW}} \gg 0 \text{ V}$) and electrons (for $U_{\text{RW}} \ll 0 \text{ V}$) to the beam tube would be the main mechanism. Based on this assumption, the current-voltage pattern at $U_{\text{RW}} \gg 0 \text{ V}$ could be reproduced in dedicated simulations by F. Glück, taking into account the large transversal mobilities of positive ions. However, the radial electron mobility is so low that in this model another mechanism would have to be responsible for the measured current at negative RW voltages. A promising candidate for the latter case would be the anomalous radial transport of electrons induced by cross field plasma instabilities. If this assumption is validated in the future, it will be the first-ever experimental hint towards the presence of plasma instabilities in the WGTS.

6.3.4 Study of time dependencies of the RW voltage reference points

Both short-term and long-term effects were observed in KNM2 with the PRO KATRIN method and in I-U scans. In this context, short-term refers to a time-scale of hours to days where a single plasma measurement is performed. Furthermore, a long-term drift over almost two months was observed.

Motivation

In order to perform neutrino mass measurements with minimum systematic uncertainties, the characteristic RW voltage points determined with the I-U scan and PRO KATRIN methods have to be stable over time. A monitoring of possible long-term trends can be done by performing periodic measurements. Short-term effects occurring during these measurements would indicate that those are not performed at stable conditions and that the results might be influenced due to intrinsic systematic effects.

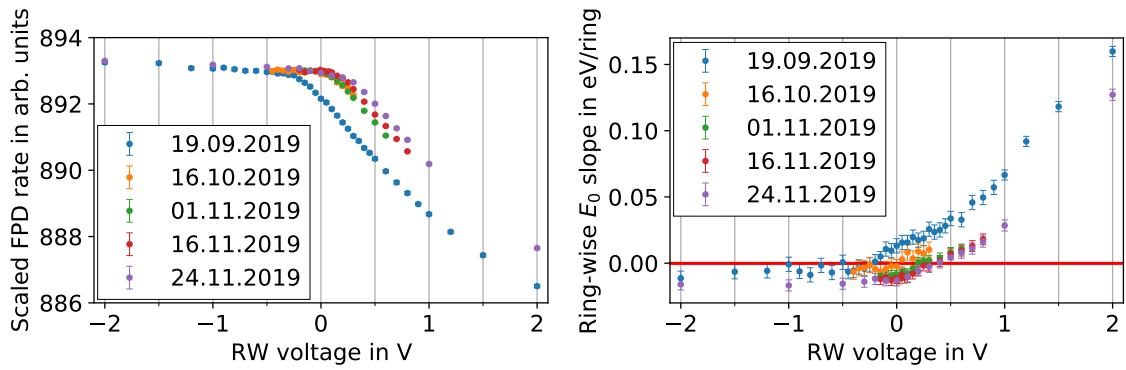
Long-term drift

Over the course of KNM2 the PRO KATRIN and I-U scan measurements were performed repeatedly on a regular basis which enables a combined analysis. As can be seen in Fig. 6.18 the obtained curves are systematically shifted towards higher RW voltages over the time scale of the campaign. The shift along the RW voltage was quantified with four different methods.

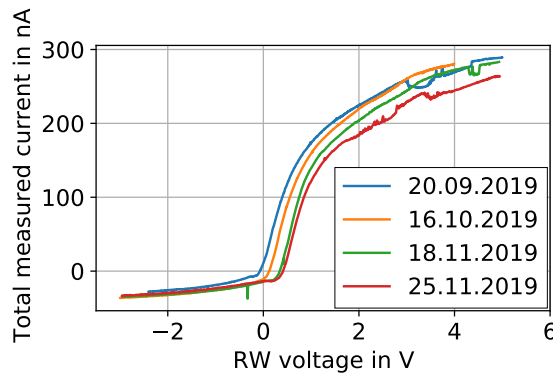
- **Start of maximally-coupled region $U_{\text{RW}}^{\text{start}}$:** The first kink in the PRO KATRIN RW scan plot (cf. Fig. 6.18a) represents the start of the region of maximal coupling between RW and plasma. It is a free parameter derived in the fit of the three linear functions model (cf. Eq. 6.13) to the ring-wise data. For each measurement the ring-wise best-fit values are averaged.

- **RW set point of vanishing ring-wise endpoint slope**
 $U_{\text{RW}}(dE_0/dr = 0 \text{ eV/ring})$: For each PRO KATRIN measurement the RW voltage showing a slope of zero for the ring-wise endpoint (cf. Fig. 6.18b) is determined.
- **RW set point of vanishing total measured current**
 $U_{\text{RW}}(I_{\text{meas,tot}} = 0 \text{ A})$: For each characteristic I-U curve the RW voltage where the line of the total measured current crosses 0 A (cf. Fig. 6.18c) is determined.
- **Shift of entire I-U curve**: A voltage shift of the entire I-U curve is derived by interpolating the data points, calculate the shift of each point with respect to the measurement on 20.09.2019 and finally take the average.

These reference voltages are evaluated for different KNM2 plasma measurements and plotted versus time (see Fig. 6.19). A drift of several mV per day towards more positive U_{RW} is observed in all four observables over a time of about two months. Applying a linear fit to each data set provides the drift rates stated in Tab. 6.2. It



(a) PRO KATRIN RW scans

(b) PRO KATRIN ring-wise E_0 slopes

(c) Total measured current curves

Figure 6.18: PRO KATRIN and I-U scan results over the course of KNM2.

Shown are the PRO KATRIN RW scans (a), ring-wise endpoint slopes (b) and the $I_{\text{meas,tot}}$ curves each measured in a downward sweep of the RW voltage (c) for different points in time during KNM2. All results are obtained during nominal WGTS operation at a column density $\mathcal{N} = 4.2 \times 10^{17} \text{ molecules/cm}^2$ and comparable tritium purities $\epsilon_{\text{T}} > 95\%$. The plot in (c) is produced using an analysis source code provided by M. Klein.

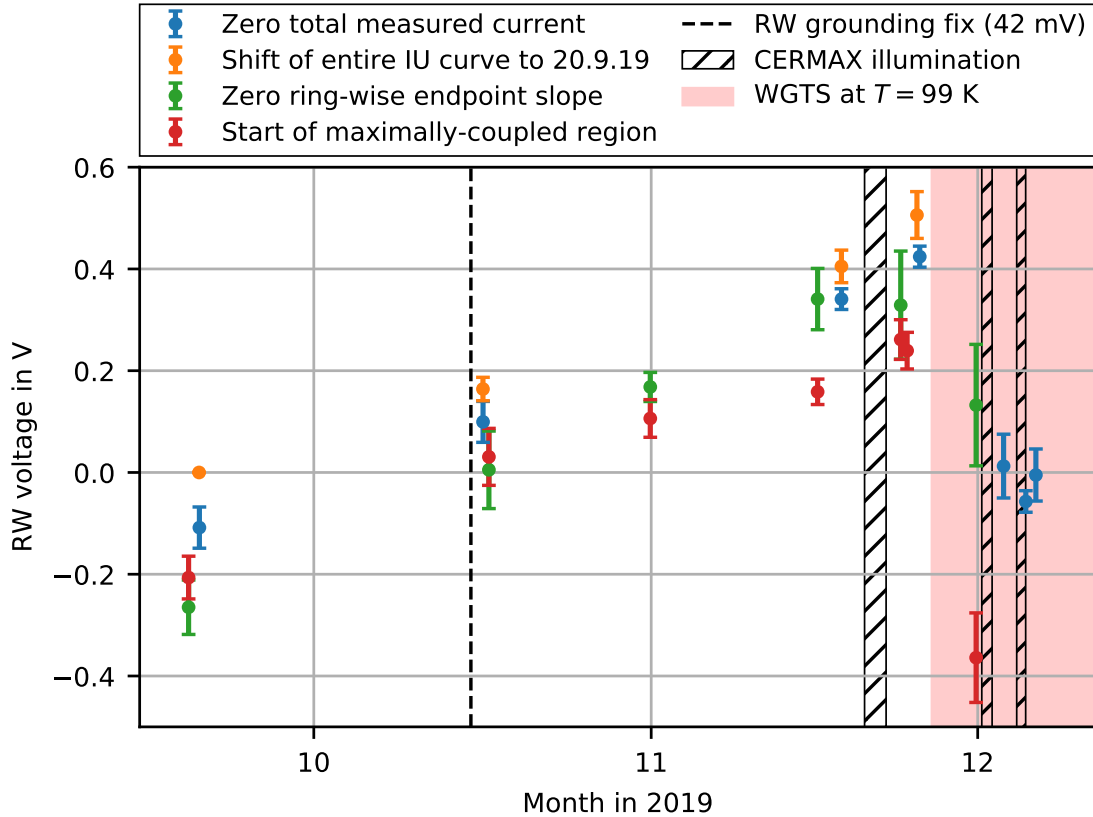


Figure 6.19: KNM2 long-term drift of RW reference set points. Four different RW voltage reference point data sets are plotted over time. Those were determined by applying the four methods described in the text. Furthermore, important changes in the RW and WGTS boundary conditions are illustrated. On 15.10.2019 the reference ground of the RW power supply was properly connected to the WGTS beam tube ground and the previously existing offset of 42 mV was thereby removed. At 26.11.2019 the WGTS temperature was increased to $T = 99$ K for the $^{83\text{m}}\text{Kr}$ campaign which took place at the end of KNM2. The RW was illuminated with the Cermax[®] UV lamp once at the end of November for about two days, and two times at the beginning of December in the krypton campaign for about one day each. The plot is produced using an analysis source code provided by M. Klein.

has to be noted that on 15.10.2019 the RW voltage setup was modified because an offset of ~ 42 mV between the RW power supply and the WGTS beam tube ground potential was discovered. Therefore, a step of 42 mV is included in the linear fit. At the end of November 2019 the drift was reset by changing the operational mode of the WGTS from nominal mode at a beam tube temperature $T = 30$ K to krypton mode at $T = 99$ K. Drops of the RW voltage reference set points of several hundreds of mV were observed both with the I-U scan and the PRO KATRIN method.

It is important to emphasize that the observed long-term drift of the RW voltage reference points can not necessarily be equated with a drift of the source potential. Both are different parameters. Nevertheless, a drift of the RW voltage reference points is an important systematic effect of the KNM2 β -scanning, especially be-

Table 6.2: KNM2 long-term drift rates of selected plasma observables. Shown are the values obtained from a linear fit to each of the four different reference values versus time. The linear function includes a step of +42 mV at the 15.10.2019 for considering the proper grounding of the RW power supply. A common fit including all four data sets is not applied. This is due to the fact that the two I-U scan as well as the two PRO KATRIN results are correlated because they are derived from the same underlying data set, respectively.

Measurement method	Reference	Drift in mV/day
I-U scan	RW set point of vanishing $I_{\text{meas,tot}}$	7.4 ± 0.5
I-U scan	Shift of entire I-U curve	6.9 ± 0.8
PRO KATRIN	RW set point of vanishing dE_0/dr	9.3 ± 0.5
PRO KATRIN	Start of maximally-coupled region $U_{\text{RW}}^{\text{start}}$	6.0 ± 0.5

cause the optimum RW set point $U_{\text{RW}}(dE_0/dr = 0 \text{ eV/ring})$ is not stable over the time of the neutrino mass measurement.

Such a long-term effect cannot be caused by the plasma itself, for example by a slow equilibration, because typically the plasma frequencies are MHz and higher. But both the RW and the beam tube boundary are prone to long-term surface effects, which would be transferred to the potential of the enclosed plasma. The two most probable causes of the drift are sorption processes on the surface, resulting in a change of the work function, and charging of insulating patches on the surface, likewise changing the effective surface potential.

In order to mitigate possible adsorption effects on the RW, in between the last and second to last PRO KATRIN measurement in nominal WGTS mode, the RW was illuminated with the Cermax[®] UV lamp for about two days (cf. Fig. 6.19). However, no significant impact on the trend of the drift was observed. The fact that the drift was reset at elevated temperature $T = 99 \text{ K}$ is in favor of the hypothesis of sorption processes on the beam tube. At $T = 30 \text{ K}$, β -decay-induced processes lead to the adsorption of carbonic molecules like CT_4 and CO on stainless steel surfaces, which was observed at the inlet capillary of the loop system in KNM1 [Mar]. Back then, this was the reason for the large drift of the column density (cf. section 3.2). Presumably, CT_4 and CO molecules were desorbed as soon as the temperature increased, which lead to a sudden change of the work function and thereby to the drop of the RW voltage reference set points. Further, the results of the $^{83\text{m}}\text{Kr}$ campaign at the end of KNM2 indicated that there may be no long-term drift at elevated temperature, which could in turn be explained by the absence of adsorption of carbonic molecules. This was one of the main reasons to increase the WGTS temperature from $T = 30 \text{ K}$ to about $T = 80 \text{ K}$ during the follow-up campaign KNM3. However, during the writing process of this thesis the KNM3 data was analyzed and it was found that there is also a long-term drift of several mV per day present at elevated source temperature.

Short-term effects

In repeated upward and downward RW voltage sweeps one can identify short-term variations. A data set with a high number of sweeps was produced in the PRO KATRIN measurement at the beginning of KNM2 in mid-September 2019 (cf. sections 6.2.1 and 6.3.1). During this measurement the RW voltage was ramped up and down over many cycles. This was performed not continuously but in discrete

steps of 100 s each, while the RW current was measured simultaneously to the FPD rate. The curves shown in Fig. 6.20 were obtained. Two different effects shift the individual I-U curves.

- **Hysteresis:** There is a shift of about 20 mV to 40 mV observed comparing consecutive upward and downward sweeps. I-U curves obtained during downward sweeps are consistently shifted to more positive RW voltages compared to preceding upward sweeps. Correspondingly, curves measured during upward sweeps are shifted to more negative RW voltages. This hysteresis effect is reversible. After one complete run the initial state is re-established.
- **Short-term drift:** The second effect superimposed to the first one is a con-

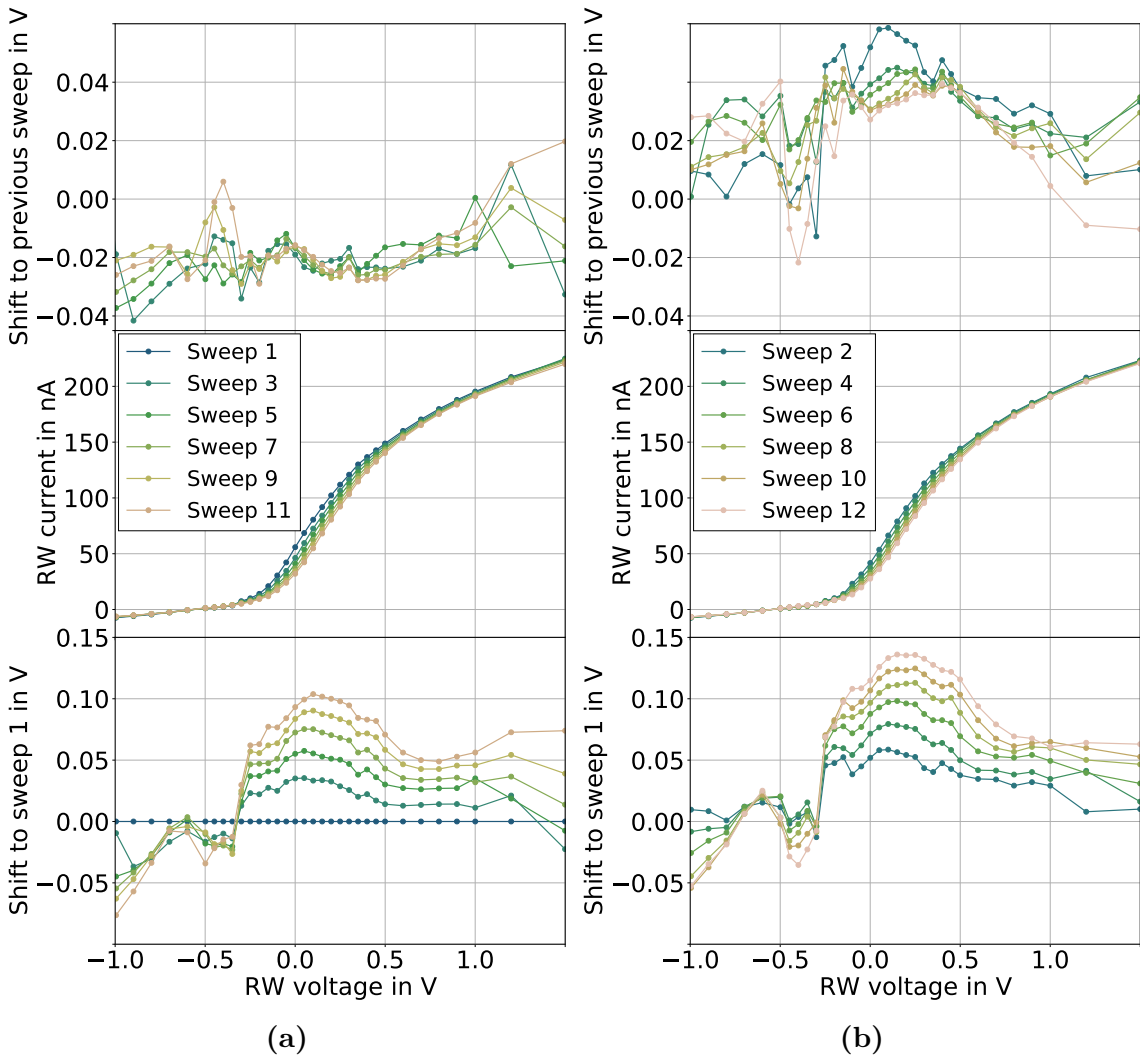


Figure 6.20: Results for RW I-U curves measured consecutively throughout the PRO KATRIN measurement in KNM2 on 19.09.2019. In (a) the RW voltage is ramped step-wise in upward direction while in (b) it is done in downward direction. The measurements are carried out at $\mathcal{N} = 4.2 \times 10^{17}$ molecules/cm² and $\epsilon_T = 98.4\%$. In both figures the middle plot shows the obtained characteristic I-U curves. On top the voltage shift of sweep n is plotted relative to the previous sweep $n - 1$. On the bottom the total voltage shift with respect to the very first sweep is given. The plot is produced using an analysis source code provided by M. Klein.

tinuous drift leading to a growing shift of the I-U curves over time. In total this adds up to ~ 100 mV comparing the curves obtained in the very last and the very first sweep, respectively. A time of ~ 14 h elapsed in between. Thus, the drift amounts to roughly 200 mV per day, which is almost two orders of magnitude higher than the long-term drift of (6 - 9) mV per day described previously. However, it should be noted that the shift between consecutive sweeps in the same direction decreases over time. This can be seen from comparing the individual curves in the two bottom plots of Fig. 6.20. Other measurements confirmed that and revealed that after some time the shift reaches a saturation level.

The observed short-term effects only occur while ramping the RW voltage. They are typical for such type of measurements [D'A74] and can likely be attributed to the charging of dielectric spots on the RW surface. During an upward sweep electrons are attracted and accumulate in this insulating layer. Thereby, the effective surface potential of the RW is reduced. In the subsequent downward sweep more positive bias voltages need to be applied in order to compensate the negative potential on the surface. This is why the I-U curves obtained in downward sweeps are systematically shifted to more positive U_{RW} . During such a downward sweep, the negatively charged particles accumulated on the surface are not entirely removed or compensated by an equal number of positive ions, so after one complete run the initial surface potential is not exactly reached again, which is the reason for the short-term drift superimposed to the hysteresis effect.

Such systematic effects were also found in measurements during the KNM3 campaign, which strongly indicates a drift of the boundary conditions induced by changes of the RW voltage.

In summary, a RW voltage-dependent effect, such as the charging of insulating surface patches, explains the short-term drift and the hysteresis alike and is probably also contributing to the long-term drift.

Conclusion

A systematic long-term drift of the PRO KATRIN and I-U scan plasma observables over almost two months was found in KNM2 at nominal WGTS operation at $T = 30$ K. The optimum set point of the RW voltage, at which the plasma potential is radially homogeneous, was drifting to ever more positive values. Thus, it was concluded that the plasma boundary conditions are not stable, which is possibly related to charging effects or adsorption processes on the RW or beam tube surfaces. As a consequence, it was decided to operate the WGTS at $T = 80$ K for the subsequent KNM3 campaign in order to mitigate possible sorption processes on the beam tube and investigate if the long-term drift persists at elevated temperature. Unfortunately, results from KNM3 measurements revealed that it does.

On top of that, during sweeps of the RW voltage two short-term effects were found to shift the characteristic I-U curve of the RW. The most reasonable explanation for this is the charging of insulating patches on the RW surface, which reduces the effective surface potential.

6.3.5 Influence of different WGTS operation modes on plasma measurement results

Two different methods were used in the investigations of the influence of different source conditions. The characteristic I-U curve of the RW can be measured within a comparably short time. One up and down sweep of the RW voltage is done within 1 h. This enables multiple measurements at different WGTS boundary conditions in a rather short time compared to e.g. the PRO KATRIN method which requires at least one day to reach reasonable statistical sensitivity.

The influence of the Cermax[®] RW illumination on the plasma - especially with regards to the RW-plasma coupling - is published in [Ful20] and not further discussed here.

Motivation

During KNM1 and KNM2 different WGTS operation modes were realized regarding temperature, column density, and magnetic field. Especially relevant for KATRIN is a comparison between the nominal mode at $T = 30$ K and the krypton mode at elevated temperature $T = 99$ K. The tritium gas is circulated differently in the loop system during krypton mode operation in order to obtain a large count rate of krypton conversion electrons. It is not purified by the permeator but directly fed back into the WGTS center after it is pumped out by the differential pumping sections. The column density established inside the WGTS is therefore different to the nominal mode.

High-precision plasma measurements with gaseous $^{83\text{m}}\text{Kr}$ can only be done in the krypton mode. Thus, a method applicable in both modes is beneficial when transferring the results to a different temperature regime. Also, results obtained at different source conditions can serve as a benchmark to validate future simulation efforts.

Magnetic field

One possible reason for the observed shape of the characteristic I-U curve of the RW is the transversal mobility of ions and electrons (cf. section 6.3.3), which is a function of the WGTS magnetic field B_{WGTS} . For lower magnetic fields the radial mobility increases. As for the characteristic I-U curve of the RW, it is therefore expected that the rise in between the electron and positive ion saturation level is getting steeper.

On the other hand, the role of the RS magnet is to map the electrons and ions from the plasma onto the RW, where the corresponding current is measured. An exclusive reduction of the RS magnetic field strength B_{RS} at constant B_{WGTS} would widen the magnetic flux tube. This would possibly lead to a mapping of the outer rim of the flux tube onto the stainless steel beam tube surface behind the RW, where it would not contribute to the measured current anymore. In order to avoid this systematic effect in a measurement at different magnetic fields, the relative reduction of B_{RS} must not exceed the one of B_{WGTS} . Then, the total amount of mapped plasma particles is not affected by a change of the RS field.

KNM1 and KNM2 results are shown in Fig. 6.21 for changing the WGTS magnetic field from 70% to 57% and from 70% to 35% of the design value $B_{\text{WGTS}} = 3.6$ T, respectively. In the latter case the RS magnet was ramped simultaneously from 85% to 43% of the design value $B_{\text{RS}} = 4.7$ T. In both cases the same amount of plasma particles is mapped onto the RW. All other source parameters are kept stable on a

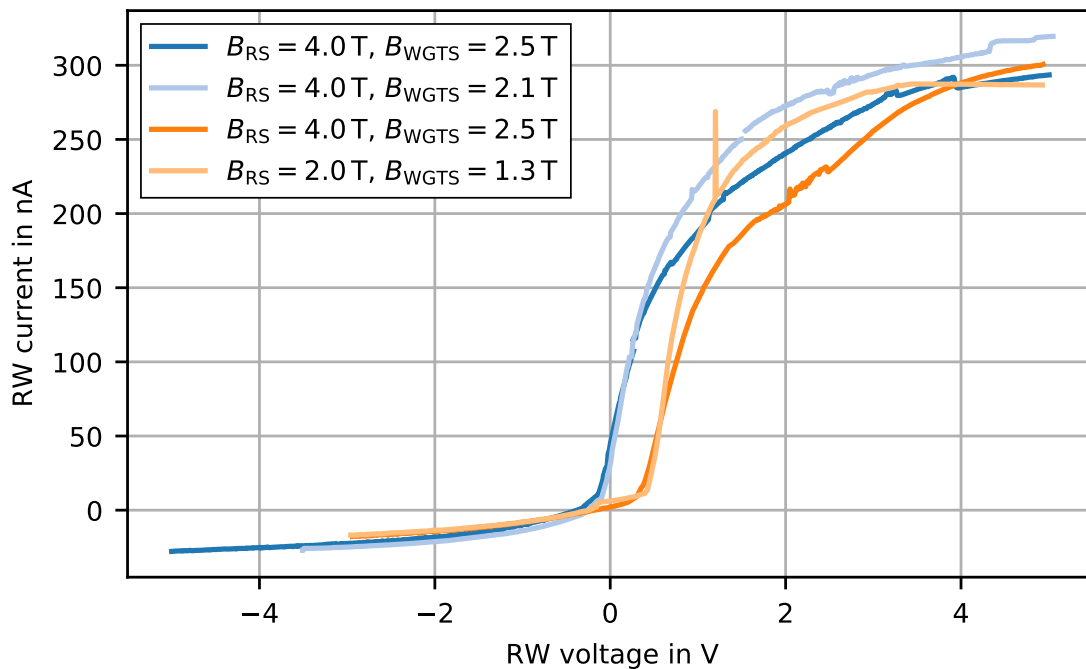


Figure 6.21: Characteristic RW I-U curves for different WGTS and RS magnetic fields. The blue curves were measured in KNM1 on 20.05. and 21.05.2019, while the orange curves were measured in KNM2 on 25.11. and 26.11.2019. All results are obtained in upward sweeps of the RW voltage during nominal WGTS operation at comparable column densities between $\mathcal{N} = 4.0$ and 4.2×10^{17} molecules/cm² and tritium purities $\epsilon_T > 95\%$. The plot is produced using an analysis source code provided by M. Klein.

comparable level in between two measurements.

The KNM2 curves are shifted with respect to the ones measured in KNM1 because of the long-term drift described in the previous section. For lower magnetic fields the current increase with the voltage steepens, as expected.

Measurements based on the PRO KATRIN method were carried out at different magnetic fields in the KNM3 campaign following up the investigations presented in this thesis.

Column density

Over the course of KNM1 a high number of different column densities was established inside the WGTS. The ion and secondary electron creation rate both increase quadratically with the column density. Thus, it is expected to measure higher saturation currents at $U_{RW} \ll 0$ V and $U_{RW} \gg 0$ V, respectively.

Measurements of the characteristic I-U curve of the RW at different column density set points (see Fig. 6.22) confirm this assumption. Evaluating the dependence of the current at a fixed RW voltage for different column densities yields a quadratic increase of the RW current and a linear increase of the DPS dipole electrode currents as described in section 5.3.1 (cf. Fig. 5.10). The linear dependence of the dipole electrode currents is due to the larger recombination probability of positive ions and electrons at larger column densities. This leads to a reduced number of positive ions flowing towards the DPS compared to the number one would expect from the quadratically increasing creation rate.

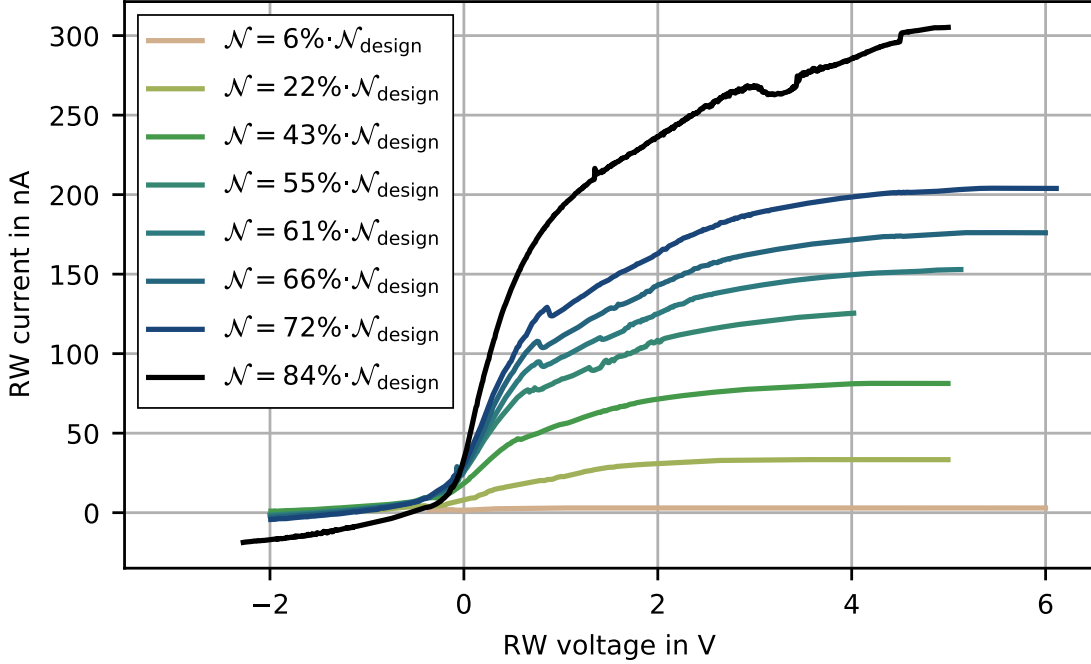


Figure 6.22: Characteristic RW I-U curves for different column densities. All curves were measured in upward sweeps of the RW voltage during KNM1 with the one exception of $\mathcal{N} = 84\% \cdot \mathcal{N}_{\text{design}}$ which is a KNM2 measurement. The column density values are stated as fractions of the design column density $\mathcal{N}_{\text{design}} = 5 \times 10^{17}$ molecules/cm². Most of these values were calculated with a systematic uncertainty of +3%/-4% by using a model from [Hei19] provided by A. Marsteller and applying it to data of the throughput sensor attached to the inlet capillary at the WGTS center. In case of $\mathcal{N} = 22\% \cdot \mathcal{N}_{\text{design}}$ and $\mathcal{N} = 84\% \cdot \mathcal{N}_{\text{design}}$ the values were determined with uncertainties of 1% and 0.6%, respectively, by using the results of dedicated calibration measurements with the egun as it is usually done for column density values stated in this chapter. The plot is produced using an analysis source code provided by M. Klein.

WGTS nominal versus krypton mode

Both in KNM1 and in KNM2 the PRO KATRIN method was applied in the WGTS nominal as well as in the krypton mode. The results for the integral FPD rate are given in Fig. 6.23. The source conditions are quite different for each measurement. Besides the WGTS temperature, the most important difference is the column density with values of $\mathcal{N} = 1.1 \times 10^{17}$ molecules/cm² (KNM1 nominal mode), $\mathcal{N} \approx 1.6 \times 10^{17}$ molecules/cm² (KNM1 krypton mode), $\mathcal{N} = 4.2 \times 10^{17}$ molecules/cm² (KNM2 nominal mode) and $\mathcal{N} \approx 1.6$ to 1.8×10^{17} molecules/cm² (KNM2 krypton mode)¹³. Comparing KNM1 and KNM2 the shape of the RW scan curves differ significantly. As for KNM1, the regions of decoupling, maximum coupling and partly coupling are less pronounced. This applies to both WGTS operation modes and makes a quantitative analysis difficult.

As for KNM2, the different regions are very distinct. In fact, in the KNM2 krypton mode even a fourth region can be identified which is not present in the nominal

¹³The krypton mode values are rough estimates provided by A. Marsteller in a personal correspondence in 2020.

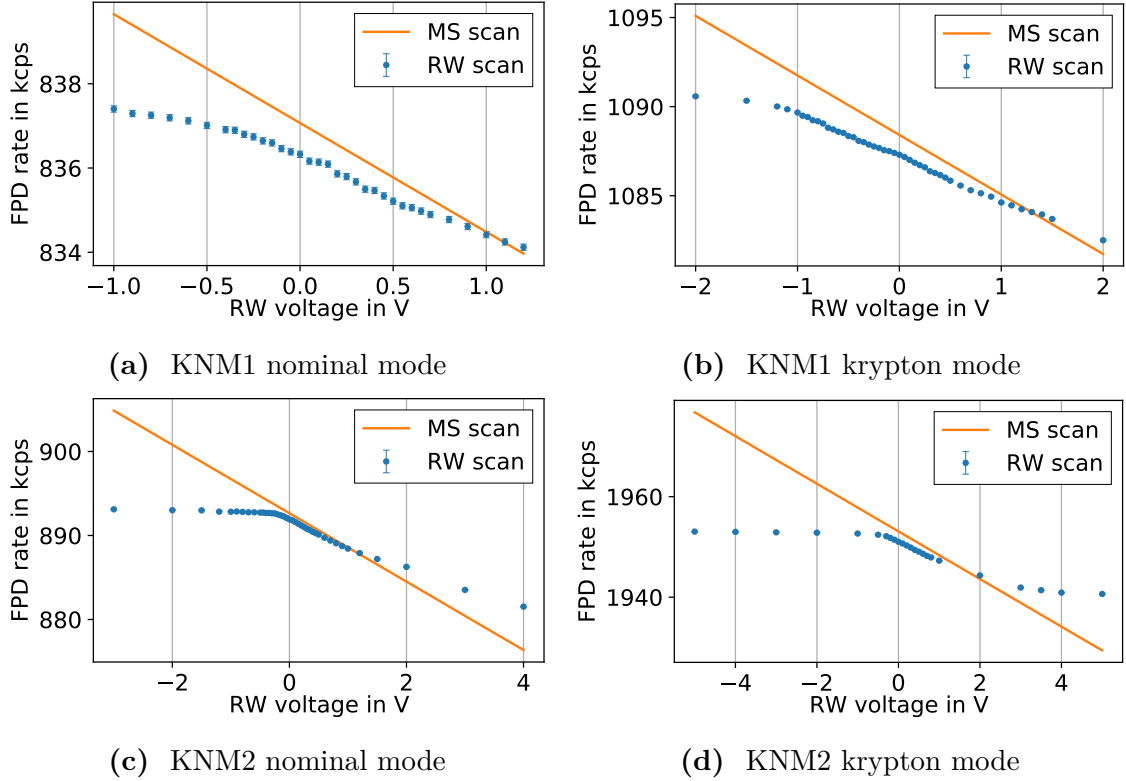


Figure 6.23: PRO KATRIN results for KNM1 and KNM2 obtained in the WGTS nominal and krypton mode. Shown are the results of the RW and the MS scan for the total FPD rate versus the applied RW voltage. The measurements were performed on 28.03.2019 in KNM1 nominal mode at $U_{\text{ret}} = -17.6$ keV, $\mathcal{N} = 1.1 \times 10^{17}$ molecules/cm², $\epsilon_T = 96.5\%$ (a); on 29.05.2019 in KNM1 krypton mode at $U_{\text{ret}} = -17.6$ keV, $\mathcal{N} \approx 1.6 \times 10^{17}$ molecules/cm² (b); on 19.09.2019 in KNM2 nominal mode at $U_{\text{ret}} = -17.9$ keV, $\mathcal{N} = 4.2 \times 10^{17}$ molecules/cm², $\epsilon_T = 98.4\%$ (c) and in KNM2 krypton mode at $U_{\text{ret}} = -17.4$ keV, $\mathcal{N} \approx 1.6 \times 10^{17}$ to 1.8×10^{17} molecules/cm² (d). The curves of the MS and the RW scan do not cross at $U_{\text{RW}} = 0$ V, where the MS scan was performed, due to small drifts in the column density in between both measurements.

mode. For highly positive RW voltages the curve becomes flat. This feature can be attributed to the higher temperature of the krypton mode since it has not been observed at different column densities. At higher temperatures the recombination probability of positive ions and electrons is smaller, which presumably leads to a saturation of the electron current flowing out of the plasma already at smaller RW voltages¹⁴. This could be the reason for the decoupling between RW and plasma observed in this fourth region. In this case a quadruple linear fit model can be applied to the data:

$$R(U_{\text{RW}}) = \begin{cases} a_{\text{RW},0} \cdot U_{\text{RW}} + b_{\text{RW},0} & U_{\text{RW}} < U_{\text{RW}}^{\text{start}} \\ a_{\text{RW},1} \cdot U_{\text{RW}} + b_{\text{RW},1} & U_{\text{RW}}^{\text{start}} \leq U_{\text{RW}} < U_{\text{RW}}^{\text{end}} \\ a_{\text{RW},2} \cdot U_{\text{RW}} + b_{\text{RW},2} & U_{\text{RW}}^{\text{end}} \leq U_{\text{RW}} < U_{\text{RW}}^{\text{start,decoupling}} \\ a_{\text{RW},3} \cdot U_{\text{RW}} + b_{\text{RW},3} & U_{\text{RW}} \geq U_{\text{RW}}^{\text{start,decoupling}} \end{cases} \quad (6.27)$$

¹⁴Personal correspondence with G. Drexlin, 2020.

with the kink positions $U_{\text{RW}}^{\text{start}}$, $U_{\text{RW}}^{\text{end}}$ and $U_{\text{RW}}^{\text{start,decoupling}}$ marking the start and the end of the maximum coupling region and the start of the decoupled region at highly positive RW set points, respectively. For the KNM2 nominal mode data the triple linear model stated in Eq. 6.13 is fitted.

The ring-wise best-fit results are given in Fig. 6.24a for the nominal and in Fig. 6.24b for the krypton mode. In the krypton mode the voltage interval of the maximum coupling region defined by $U_{\text{RW}}^{\text{end}} - U_{\text{RW}}^{\text{start}}$ is significantly increased for the bull's eye and rings 1 to 4 compared to the nominal mode. Probably, this can again be attributed to the smaller recombination rate at increased temperature, which increases the number of electrons with large longitudinal mobility. However, rings 5 to 11 exhibit rather comparable widths of the maximum coupling region. The radial evolution of $U_{\text{RW}}^{\text{start,decoupling}}$ is similar as for $U_{\text{RW}}^{\text{end}}$, since both are decreasing at the outer radii. However, the voltage interval of the partly-coupled region is wider at the outer rings.

Besides the different coupling characteristics, switching from nominal to krypton mode did have a significant impact on the long-term drift of the RW voltage reference points (cf. section 6.3.4). As soon as the WGTS mode was switched, this long-term trend was reset (cf. Fig. 6.19), presumably because molecules desorbing from the beam tube at increased temperature lead to a sudden change of the work function. Furthermore, as analyzes of KNM3 measurements indicate, the drift rate seems to be smaller than in nominal mode.

Conclusion

The major source parameters are the column density, magnetic field and temperature. All of them have a significant influence on the results of the PRO KATRIN and I-U scan method. Lower magnetic fields induce steeper RW I-U curves. For higher column densities the ion and electron saturation currents increase. While the

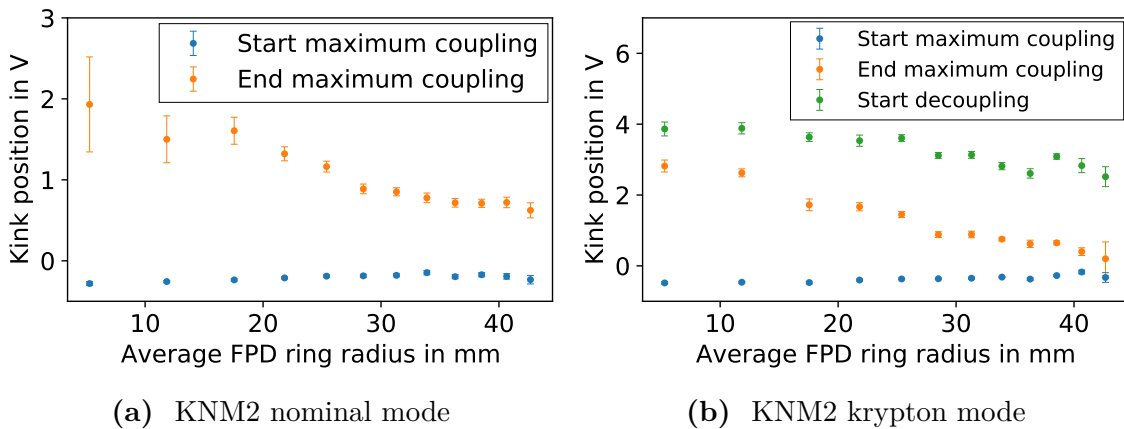


Figure 6.24: KNM2 WGTS nominal and krypton mode results for the best-fit kink positions marking the different coupling regions. Shown are the kink positions $U_{\text{RW}}^{\text{start}}$, $U_{\text{RW}}^{\text{end}}$ and $U_{\text{RW}}^{\text{start,decoupling}}$ as a function of the average ring radius. The results are determined by fitting the triple and quadruple linear model (cf. Eqs. 6.13 and 6.27) to the data measured during nominal WGTS operation (a) and in krypton mode (b), respectively. The plots are produced using an analysis source code provided by M. Klein.

RW current at a fixed RW voltage increases quadratically with the column density, a linear dependence was found for the DPS dipole electrode currents.

Comparing the WGTS nominal with the krypton mode reveals that the shape of the PRO KATRIN RW scan curves are rather similar for both. This applies to KNM1 as well as KNM2. However, between both campaigns the curve shapes are significantly different which is not understood as of now.

In the case of KNM2 krypton operation, a decoupling between RW and plasma was identified for very positive RW voltages, which might be explained by the smaller recombination rate at increased temperature. Furthermore, switching from nominal to krypton mode resets the long-term drift of the RW voltage reference points and changes the drift rate.

6.3.6 Measurements of the rear section egun transmission function width in order to investigate high-frequency plasma instabilities

In section 6.2.4 a method to investigate high-frequency plasma instabilities was described. It was applied in the course of KNM2 yielding the results summarized in the following.

Motivation

As already described in section 6.3.3, the occurrence of cross field instabilities would be a possible explanation of the transversal electron movement at negative RW voltages. This finding, if verified, would point towards the presence of plasma instabilities inside the WGTS. If these indeed exist, they will distort the measured β -spectrum systematically either by changing the WGTS starting potential or, if they are high-frequent, by changing the kinetic energy of β -electrons in flight. The latter effect can be investigated by measuring the rear section egun transmission function width.

Measurements of the rear section egun transmission function width

The egun transmission function $T(E, U_{\text{ana}})$ (cf. Eq. 6.21) was measured at two different source conditions. One measurement was performed at an empty WGTS beam tube without the presence of a plasma yielding a reference value. In addition, measurements at different RW bias voltages were carried out at a high column density where a significant plasma density is maintained. Plasma instabilities could only occur in the latter case. So in this case, provided that they have a significant impact, they would induce a change of the transmission function width σ_E .

In between the empty source reference and the high column density measurements at $\mathcal{N} = 4.2 \times 10^{17}$ molecules/cm² and $\epsilon_T = 98.5\%$ there was a time gap of about one week due to organizational issues. In order to assure the comparability of the results, parameters like electron energy, pitch angle, radial off-axis shift and so on were the same. However, different MS analyzing plane magnetic fields of 0.63 mT in the reference and 0.14 mT in the high column density measurements were set by mistake. For the 18.6 keV energy egun electrons this directly leads to different MS energy resolutions of $\Delta E = 2.8$ eV and $\Delta E = 0.62$ eV, respectively (cf. Eq. 2.4). According to calculations by L. Schimpf, this causes a systematic shift $\Delta\sigma_E \approx +0.0079$ eV of the reference value of σ_E . The egun electrons were produced with a pitch angle $\theta = 0^\circ$ close to the central z -axis at a radial off-axis shift $\Delta r = 0$ mm.

Both the performance of the measurements and the data analysis were intensively supported by the KATRIN egun team, especially by L. Schimpf.

While the reference measurement was performed at an arbitrary fixed RW bias voltage of 0.3 V, the measurements at high column density were done at twelve different set points. For each voltage value the transmission function was scanned during a 15 min long run. The RW voltages were applied consecutively until one cycle including twelve runs was completed. Then, the whole procedure was repeated in another cycle. In total, the combined measurement time adds up to ~ 12 h for almost four complete RW voltage cycles.

In the analysis, the data is fitted with the error function given in Eq. 6.22. This is shown in Fig. 6.25a for the reference run and in Fig. 6.25b for one selected run at high column density. For each run a best-fit value of the transmission function width σ_E is determined. Values obtained at the same RW set point are averaged and plotted in Fig. 6.26.

Applying different RW voltages has no significant effect on the σ_E parameter. Thus, if high-frequency plasma instabilities contribute to the measured transmission function width, they are not affected by the RW voltage.

In general, at high column density the best-fit values of σ_E are smaller by about 5 meV to 9 meV compared to the reference value obtained with an empty source. This can likely be attributed to the two different MS analyzing plane magnetic field settings of 0.14 mT and 0.63 mT, respectively. Those can be taken into account by subtracting $\Delta\sigma_E \approx 0.0079$ eV from the reference width. After that, there is no significant difference left between the results of the reference and the high column density measurements. This would mean that high-frequency plasma instabilities do not have a significant impact on the electron energy. In order to get unbiased results, however, this measurement has to be repeated while making sure that the

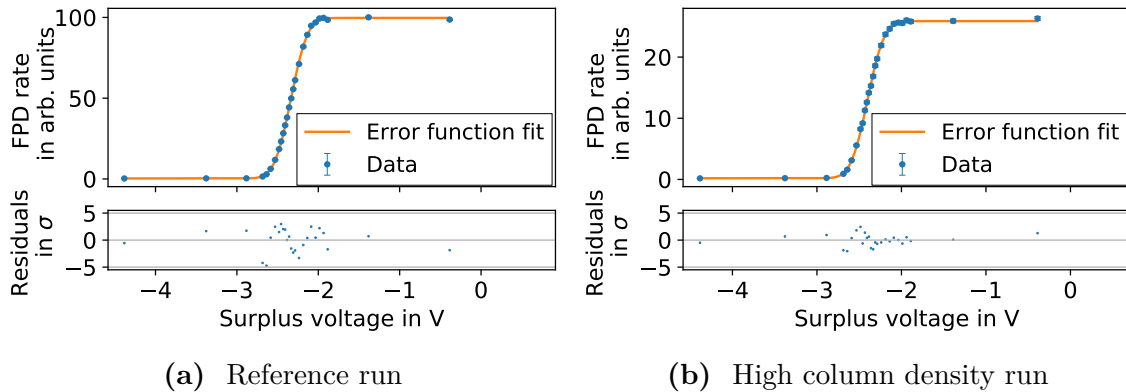


Figure 6.25: Exemplary KNM2 results of the egun transmission function scans.

Shown is the FPD rate versus the surplus voltage $U_{\text{sur}} = U_{\text{egun}} - U_{\text{ret}}$ with the applied error function fit and the corresponding residuals normalized to the uncertainty σ of the data points. The transmission is proceeding at $U_{\text{sur}} < -2$ V because the voltage in the MS analyzing plane U_{ana} is effectively lower than the applied retarding voltage U_{ret} . The data set shown in (a) was measured with an empty WGTS in order to determine the reference width $\sigma_{E,\text{ref}}$ for scans like the one shown in (b) performed at $U_{\text{RW}} = -0.15$ V in WGTS nominal mode at a column density $\mathcal{N} = 4.2 \times 10^{17}$ molecules/cm² and a tritium purity $\epsilon_{\text{T}} = 98.5\%$. The measurement data and the corresponding fit parameters were provided by L. Schimpf.

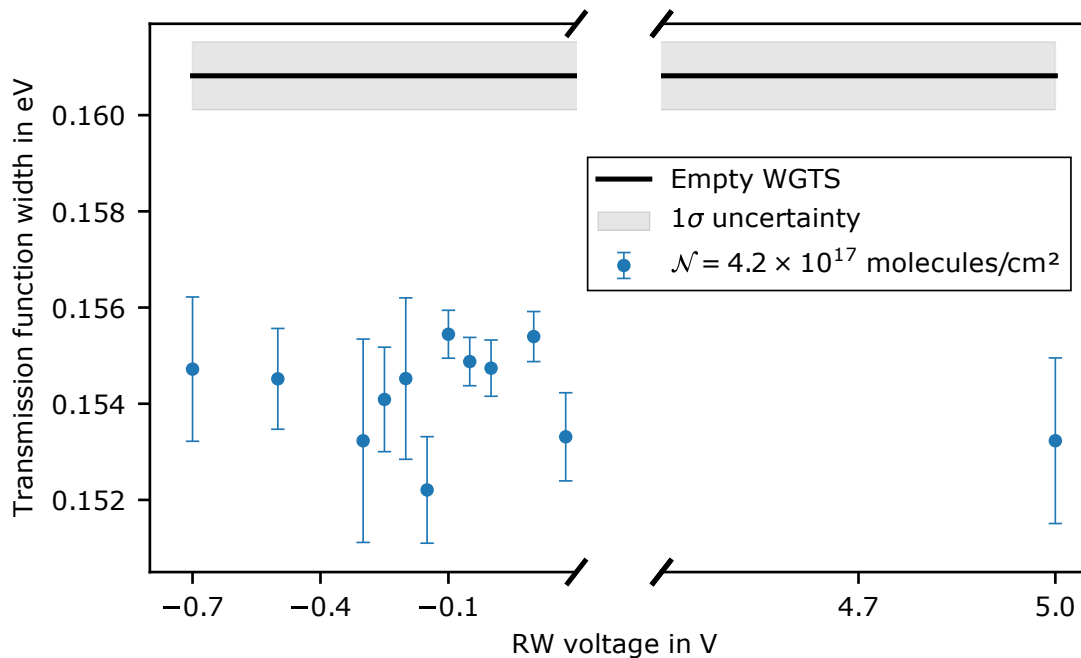


Figure 6.26: KNM2 results of the egun transmission function width for different RW voltages. Shown are the best-fit σ_E results for different RW voltages with an electron pitch angle of 0° at a column density $\mathcal{N} = 4.2 \times 10^{17}$ molecules/cm² and a tritium purity $\epsilon_T = 98.5\%$. The reference width is determined at an empty WGTS beam tube without any plasma present.

MS analyzing plane magnetic field is kept constant throughout the duration of the measurements.

Conclusion

The width of the egun transmission function is a sensitive probe, which can be used to detect high-frequency plasma instabilities which would change the kinetic energy of β -electrons in flight. Measurements were carried out at an empty WGTS beam line and at nominal KNM2 column density. Changing the RW bias voltage in the latter measurements did not result in any significant change of the egun transmission function width. The reference and nominal mode measurements were performed at different MS analyzing plane magnetic fields of 0.63 mT and 0.14 mT, respectively, which introduces a systematic broadening of the reference transmission function on the order of $\Delta\sigma_E \approx +0.0079$ eV. This is probably the explanation for the larger best-fit value determined for the reference width. After reducing this value by $\Delta\sigma_E$ there is no significant deviation left between the results obtained with and without a source plasma. Consequently, the change of the electron energy by high-frequency instabilities seems to be negligible. In the future both parts of the measurement procedure should be performed at equal magnetic field settings in order to confirm these initial results.

6.3.7 Search for plasma eigenfrequencies in the FPD rate data

The measurements described in this section aim for the determination of the frequencies imposed on the FPD rate data by plasma oscillations.

Motivation

The phenomenon of plasma oscillations was described in section 6.1.1 as a periodic movement of electrons and ions, respectively. Plasma oscillations are the response of a plasma to disturbances of the equilibrium state. In the case of the WGTS plasma, eigenfrequencies of several tens of MHz are expected for electrons while ions oscillate with smaller frequencies scaling with $1/\sqrt{m_i}$, depending on their mass m_i (cf. Eq. 6.3).

Fourier spectra of the FPD rate data

The imprint of plasma eigenfrequencies could be seen from periodic patterns in the FPD rate versus time, which can be analyzed for example by a fast Fourier transformation (FFT). Discrete peaks in the Fourier spectrum reveal the frequency composition of the data set.

This procedure is illustrated in Fig. 6.27, which shows the results of a test measurement at a MS retarding voltage of $U_{\text{ret}} = -17.573 \text{ kV}$ where an AC voltage with a sine waveform, a peak-to-peak amplitude of 4 V, a DC offset of 0 V and a frequency of 50 mHz was applied to the RW using the Agilent[®] function generator. Apparently, the modulation of the RW voltage is directly transferred to the measured FPD rate (see Fig. 6.27a). However, from the results of the PRO KATRIN measurements it is known that the coupling between RW and plasma at $|U_{\text{RW}}| \gtrsim 0.5 \text{ V}$ is limited (cf. Fig. 6.8). The rate modulation is clearly visible from the main peak at 50 mHz and its harmonics at 100 mHz and 150 mHz in the FFT spectrum (see Fig. 6.27b).

If the RW voltage is not modulated but kept at a constant DC voltage, an analogous analysis should reveal frequency patterns induced by low-frequency plasma

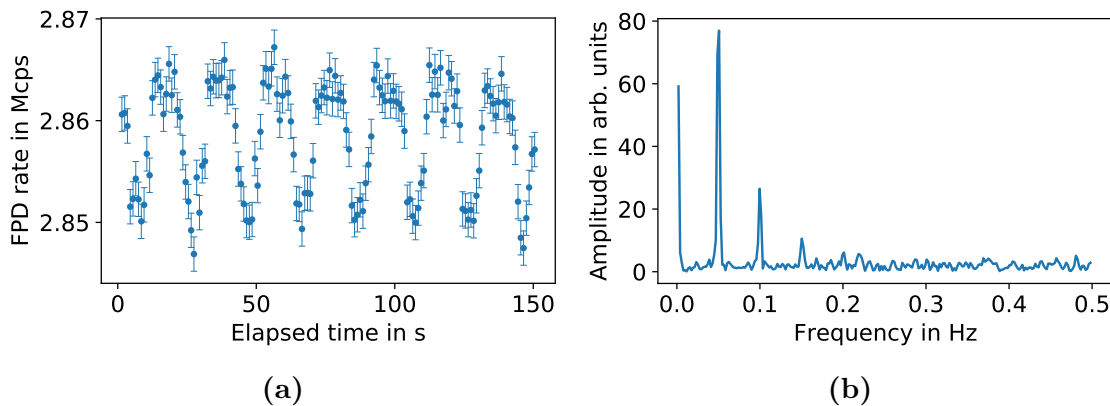


Figure 6.27: Modulation of the FPD rate for a low-frequency AC voltage applied to the RW. The FPD rate data shown in (a) is obtained at $U_{\text{ret}} = -17.573 \text{ kV}$ while applying a sinusoidal voltage modulation around 0 V with a peak-to-peak amplitude of 4 V and a frequency of 50 mHz to the RW. Column density and tritium purity are $4.2 \times 10^{17} \text{ molecules/cm}^2$ and 98.5%, respectively. In (b) the corresponding FFT spectrum is plotted. The peak amplitudes A_i are damped with a logarithmic decrement $\Lambda = \ln(A_i/A_{i+1}) \approx 1$.

oscillations. In a dedicated KNM2 measurement cycle different DC voltages were applied to the RW. At each set point the FPD rate of 2.87 Mcps was measured at a MS retarding voltage $U_{\text{ret}} = -17.573$ kV while the WGTS was operated at a column density $\mathcal{N} = 4.2 \times 10^{17}$ molecules/cm² and a tritium purity $\epsilon_{\text{T}} = 98.6\%$. The FPD rate was measured for 15 different RW voltages in the range of -1000 mV to $+300$ mV, each applied for 60 min. The data was recorded in histogram mode so as to limit the size of the output files. In histogram mode only very low frequencies ≤ 1 Hz are accessible in the analysis because of the default binning of the data into 1 s bins. In addition, three 15 min long runs were performed at RW voltages of -0.3 V, -0.15 V and $+3$ V in energy mode. In this mode the data for each individual event is stored, so it is sensitive to higher frequencies ≥ 1 Hz.

An exemplary FFT spectrum for $U_{\text{RW}} = -150$ mV is shown in Fig. 6.28. It does not feature any distinct peaks. There is no obvious frequency pattern distinguishable. The same applies to all the other RW voltages covered in the measurement cycle.

Conclusion

Measurements of the FPD rate at different RW voltages both in histogram and in energy mode did not show any periodic pattern. Thus, there are no low-frequency plasma oscillations observed with this method.

6.3.8 Plasma potential change for a high-frequency sinusoidal voltage modulation at the rear wall

The impact of applying different AC voltages to the RW using an Agilent[®] function generator was investigated in the course of KNM2 both in the nominal WGTS mode and in the krypton mode with active ^{83m}Kr gas circulation.

Motivation

In the course of a modification of the RW voltage setup in mid-October 2019, it was

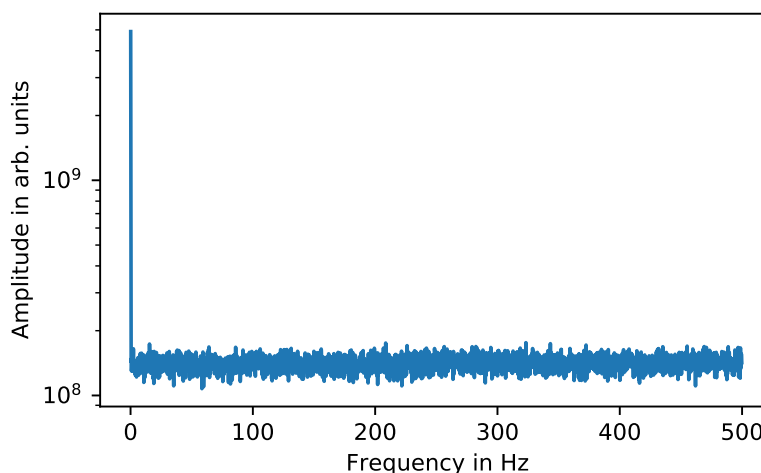


Figure 6.28: Exemplary FFT spectrum of the FPD rate at a DC voltage of -150 mV applied to the RW in KNM2. The spectrum originates from an energy mode run measured for 15 min at a MS retarding voltage $U_{\text{ret}} = -17.573$ kV, a column density $\mathcal{N} = 4.2 \times 10^{17}$ molecules/cm² and a tritium purity $\epsilon_{\text{T}} = 98.6\%$.

found that the picoammeter from RBD instruments[®] did impose high-frequency noise at the RW. Consequently, it was removed. Possibly, such a noise-induced high-frequency modulation of the RW voltage can cause an absolute shift of the plasma potential and thereby shift the endpoint (cf. section 6.2.5 for details). This hypothesis was tested in KNM2.

Measurement at nominal WGTS operation

In the nominal WGTS mode at a temperature of $T_{\text{WGTS}} = 30\text{ K}$ the FPD rate was measured deep in the β -spectrum at a column density of 4.2×10^{17} molecules/cm² and a tritium purity of 98.2%. The MS was operated at the same retarding voltage as in the PRO KATRIN method $U_{\text{ret}} = U_{\text{PK}} = -17\,900.01\text{ V}$.

At the RS, sinusoidal AC voltages with peak-to-peak amplitudes of 2 V and offsets of 0 V were applied to the RW. Frequencies $f_i \in (1, 0.1, 10, 3, 0.3)\text{ MHz}$ were applied in this order, while the FPD rate was measured in 10 min long runs. Before each of those measurements, a 5 min long FPD run with a DC voltage of 0 V applied to the RW was recorded in order to obtain a reference rate. In total this adds up to ten FPD runs.

In the analysis a reference rate $R_i(\text{DC})$ is determined for each frequency f_i applied in a run j by averaging the rates measured in the run before ($j - 1$) and after ($j + 1$). As for the very last run $j = 10$, there is no run number $j + 1$, so in this case only the run $j - 1$ is taken as a reference.

By calculating the rate shift $\Delta R(\text{DC}, f_i) = R_i(\text{DC}) - R(f_i)$ the impact of the voltage frequency f_i on the rate is quantified. This rate difference is finally converted to a corresponding shift of the plasma potential $\Delta V_{\text{Pl}}(\text{DC}, f_i)$ according to Eq. 6.23. The required slope of the β -spectrum a was measured in a PRO KATRIN MS scan two days before this frequency study at comparable source conditions.

The results for the shift of the FPD rate and the plasma potential can be found for the whole FPD in Fig. 6.29a and for individual pixel rings in Fig. 6.29b. The following statements can be made.

- For frequencies $f_i \leq 1\text{ MHz}$ a shift of the rate on the order of $\Delta R(\text{DC}, f_i) = -500\text{ cps}$ corresponding to a rise of the plasma potential by about $\Delta V_{\text{Pl}}(\text{DC}, f_i) = 120\text{ mV}$ is observed. This amounts to a shift of $\sim 0.5\%$ relative to the total FPD rate of about 900 kcps.
- Applying higher frequencies of 3 MHz and 10 MHz has no significant impact on the measured rate. The reason for this remains unknown but can at least partly be attributed to the damping effect of the voltage in the RW supply cable which was described in section 6.2.5. At a frequency of 3 MHz only about 83% of the voltage amplitude is effectively transported from the Agilent[®] function generator to the RW while at a frequency of 10 MHz there is no transmission at all. So at least for $f_i = 10\text{ MHz}$ the measured rate shift of zero is an artifact of the hardware setup.
- The rate shifts measured for $f_i \leq 1\text{ MHz}$ are compatible within the uncertainties, so there seems to be no frequency-dependence.
- As for the ring-wise analysis, the data suffers from rather large uncertainties which hinders a conclusive judgment on the observed effects. Nevertheless, at the frequencies 100 kHz and 1 MHz a ring-dependency can be identified. The plasma potential shifts on the order of 200 mV for the inner rings diminish to-

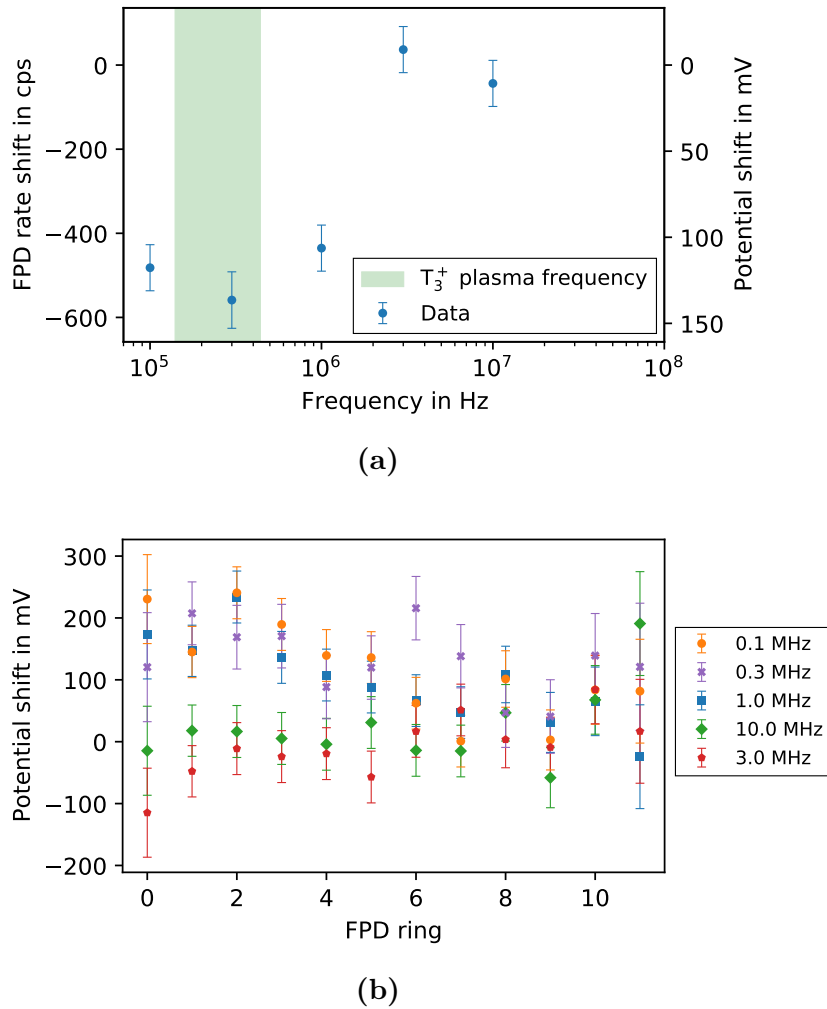


Figure 6.29: Frequency-dependent shifts of the β -spectrum FPD rate and the plasma potential for applying a sinusoidal voltage to the RW during nominal WGTS operation. The measurements were performed with the WGTS operated in nominal mode at $T = 30$ K, a column density $\mathcal{N} = 4.2 \times 10^{17}$ molecules/cm² and a tritium purity $\epsilon_T = 98.2\%$. At the RW five different AC voltages with a peak-to-peak amplitude of 2 V and an offset of 0 mV were applied. The measured FPD rate shifts plotted in (a) are calculated by taking the difference of the rate measured with an AC and a 0 V DC voltage applied to the RW. For comparison the plasma frequency of T_3^+ oscillations (cf. Eq. 6.3) is illustrated. The true frequency value depends on the unknown number density of charged particles $n = 10^5$ cm⁻³ to 10^6 cm⁻³ and lies in the range indicated by the green area. Ring-wise results are given in (b). The bull's eye is denoted by ring number 0.

wards zero for the outer rings. This is probably related to the better coupling between the RW and the plasma found for the inner radii in other measurements (cf. section 6.3.1). As for the other frequencies the distributions are rather flat.

The data definitely show a significant effect on the plasma potential induced by high-frequency voltages at the RW. However, more precise results would be bene-

ficial especially for the analysis of radial effects. Such results were obtained in the WGTS krypton mode.

Measurement at WGTS krypton mode operation

In KNM2 krypton mode the WGTS was operated at a temperature $T_{\text{WGTS}} = 99$ K. Krypton gas was actively circulated so the WGTS was filled with a mixture of tritium and small traces of $^{83\text{m}}\text{Kr}$ ¹⁵. In this configuration the sharp lines of the krypton spectrum provide the opportunity to measure any change of the rate with a high sensitivity.

Due to the different circulation mode of the loop system the stability of the WGTS $^{83\text{m}}\text{Kr}$ activity is on the level of 0.5% which is worse than the 0.1% stability of the tritium activity during nominal operation. Also, the tritium column density is reduced to a value in the range between 32% and 36% of the nominal design value¹⁶. The FPD rate was measured near the L₃-32 line position at a MS retarding voltage $U_{\text{ret}} = -30\,473.17$ V. A magnetic field of 0.27 mT in the MS analyzing plane provides a high energy resolution.

Again, 0 V DC voltages as well as sinusoidal AC voltages with an offset of 0 V were applied to the RW, but with a different peak-to-peak amplitude of 200 mV. Frequencies of $f_i \in (1, 0.1, 10, 3, 0.3)$ MHz were applied in this order with DC reference runs in between. This time, one reference run is added at the end of the measurement cycle so in total it consists of eleven runs. Each run lasted 60 s. For each frequency f_i applied in a run j a reference rate $R_i(\text{DC})$ is determined by averaging the rates measured in the run before ($j - 1$) and after ($j + 1$).

The conversion of the rate difference to the corresponding shift of the plasma potential $\Delta V_{\text{P1}}(\text{DC}, f_i)$ is done by using Eq. 6.25. For this the L₃-32 line position E_0 , width Γ and amplitude A have to be known. The L₃-32 line position $E_0 = (30472.0258 \pm 0.0008)$ eV and width $\Gamma = (1.168 \pm 0.005)$ eV are best-fit results obtained in the analysis of a measurement on the day before the frequency investigations by R. Ostertag. With these values at hand the amplitude A is determined by plugging in the rate R and MS retarding energy E_{ret} of the first FPD run into Eq. 6.26. Finally, the plasma potential shift $\Delta V_{\text{P1}}(\text{DC}, f_i)$ can be inferred.

The whole measurement procedure is carried out twice back-to-back, which results in a total number of $2 \times 11 = 22$ FPD runs. The redundant data sets of the runs 12-22 increase the confidence that the measured rate shifts are indeed due to the high-frequency AC voltage applied to the RW and are not an artifact of the fluctuation of the WGTS $^{83\text{m}}\text{Kr}$ activity.

The obtained rate and plasma potential shifts for each of the two measurement cycles are illustrated in Fig. 6.30a for the integral FPD. In Fig. 6.30b a ring-wise analysis is shown. In the latter the results from the two back-to-back cycles are averaged in order to obtain one $\Delta V_{\text{P1}}(\text{DC}, f_i)$ value for each frequency f_i . Several conclusions can be drawn from the obtained data.

- Significant rate shifts $\Delta R(\text{DC}, f_i)$ on the order of -1 kcps are observed for all applied frequencies except for the highest frequency of 3 MHz. At a total measured rate on the order of 100 kcps this corresponds to an effect of about 1%. A conversion into potential shifts yields results on the order of 10 mV.

¹⁵The total number of krypton atoms is at least six orders of magnitude below the total number of tritium molecules [Mac16].

¹⁶Personal correspondence with A. Marsteller, 2020.

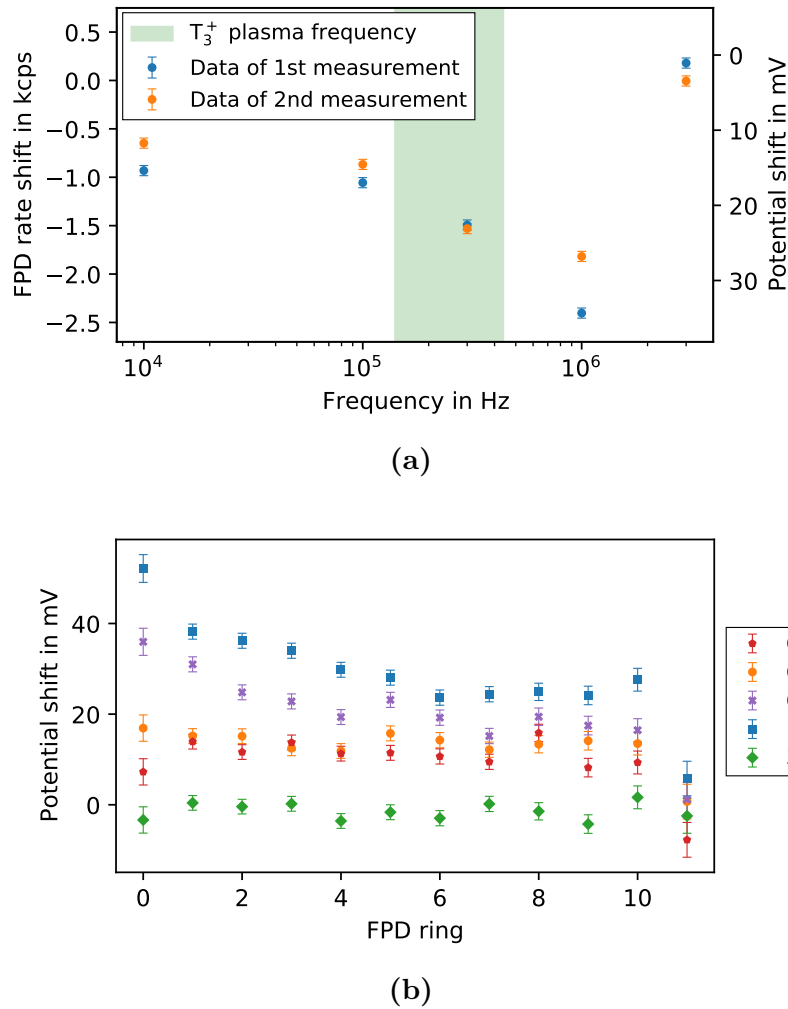


Figure 6.30: Frequency-dependent shifts of the L₃-32 FPD rate and the plasma potential for applying a sinusoidal voltage to the RW during WGTS krypton mode operation. The measurements were performed with the WGTS operated in krypton mode at $T = 99$ K at a column density in the range between 32% and 36% of the nominal design value. At the RW five different AC voltages with a peak-to-peak amplitude of 200 mV, an offset of 0 mV and frequencies 10 kHz, 100 kHz, 300 kHz, 1 MHz and 3 MHz were applied. Every frequency was set twice within two redundant back-to-back measurement cycles. The measured FPD rate shifts plotted in (a) are calculated by taking the difference of the rate measured with an AC and a 0 V DC voltage applied to the RW. For comparison the plasma frequency of T_3^+ oscillations (cf. Eq. 6.3) is illustrated. The true frequency value depends on the unknown number density of charged particles $n = 10^5 \text{ cm}^{-3}$ to 10^6 cm^{-3} and lies in the range indicated by the green area. Ring-wise results are given in (b) by averaging the two data points redundantly measured at the same frequency. The bull's eye is denoted by ring number 0.

This is in good agreement with the tritium mode data considering the ten times lower amplitude of the RW AC voltages.

- The absolute rate shift increases with the applied frequency. An exception is

the measurement at 3 MHz, where the shift is not significantly different from zero.

- The rate shifts $\Delta R(\text{DC}, f_i)$ obtained in two redundant measurement cycles differ significantly, which is due to instabilities of the $^{83\text{m}}\text{Kr}$ activity. These large systematic uncertainties cannot be quantified, however. Nevertheless, in both cycles significant rate shifts are observed and the size of the obtained potential shifts are in good agreement.
- The ring-wise analysis yields much more significant results than in tritium mode. A non-zero plasma potential shift is observed for ring numbers 0 (bull's eye) to 10 for all frequencies except for 3 MHz. Independent of the frequency the outermost ring number 11 shows no response at all. For the frequencies 0.3 MHz and 1.0 MHz the inner rings exhibit a larger potential shift than the outer ones. This only partially agrees with the tritium mode data because there the 0.3 MHz frequency did not result in a radial dependence. However, this could be attributed to the larger uncertainties hiding the effect. The negative slope of the ring-wise potential shifts supports the idea of a better RW-plasma coupling at inner radii compared to outer ones (cf. section 6.3.1). For the lower frequencies 10 kHz and 100 kHz the radial distribution is rather flat.

Conclusion

Investigations done at different WGTS operation modes both with T_2 and $^{83\text{m}}\text{Kr}$ show that high-frequency noise in the range between 10 kHz and 1 MHz picked up by the RW can have a significant effect on the FPD rate and therefore on the β -spectrum shape obtained during neutrino mass measurements. Depending on the RW voltage frequency, amplitude and the analyzed pixel ring the plasma potential can effectively be shifted by up to several hundreds of mV. A definite reason for the frequency-dependence can not be given as of now. The effect on the plasma potential increases for larger frequencies, up to a cut-off frequency at 3 MHz, which is not fully transmitted from the function generator to the RW due to damping in the supply cable.

It is recommended to operate the RW in a low-noise environment and to remove any hardware device potentially acting as a source of high-frequency noise in the first place. One consequence from these considerations was to modify the RW voltage setup after the KNM2 campaign was completed (for details see section 6.1.3).

6.3.9 Influence of the DPS dipole electrode voltages on the plasma potential

Positive tritium ions are continuously removed from the plasma via the three DPS dipole electrodes operated in dipole mode (cf. section 6.1.2). In this section, a measurement to investigate the influence of the removal rate on the plasma potential by applying different electrode settings is described.

Motivation

The ion removal rate at the DPS dipole electrodes increases with the dipole field, which is tunable by varying the applied half-shell voltages. For a higher removal rate a lower recombination rate of negative ions, e.g. by the process stated in Eq. 3.7, is

expected. Possibly, this could lead to negative space charges inducing a measurable shift of the plasma potential towards more negative values.

Measurement procedure

A shift of the plasma potential can be investigated in a straightforward manner by measuring the FPD rate deep in the β -spectrum for a certain time at two extremely different dipole electrode voltage settings. Any shift in the FPD rate would correspond to a shift of the plasma potential. The measurement was carried out in KNM2 at a RW voltage $U_{\text{RW}} = -150$ mV, a MS retarding voltage $U_{\text{ret}} = -17\,573.00$ V, a column density $\mathcal{N} = 4.2 \times 10^{17}$ molecules/cm² and a tritium purity $\epsilon_{\text{T}} = 98.7\%$. Two consecutive 60 min long runs were performed at significantly different voltages applied to the dipole electrodes 1, 2 and 3. In run 1 the dipole fields were reduced to a minimum while in run 2 nominal settings were applied:

$$\begin{aligned} \text{Run 1: } & (-0.5 \text{ V}/-5.0 \text{ V}), (-0.5 \text{ V}/-5.0 \text{ V}), (-0.5 \text{ V}/-5.0 \text{ V}), \\ \text{Run 2: } & (-5 \text{ V}/-15 \text{ V}), (-5 \text{ V}/-35 \text{ V}), (-5 \text{ V}/-85 \text{ V}). \end{aligned} \quad (6.28)$$

Results

The integral FPD rate R is received for combining all pixel rings. In order to estimate the fluctuation of the tritium activity, the mean BIXS rate R_{BIXS} is determined for each run. The measured rates are given by

$$\begin{aligned} \text{Run 1: } & R = (2869075 \pm 28) \text{ cps}, R_{\text{BIXS}} = (6753.0 \pm 1.4) \text{ cps}, \\ \text{Run 2: } & R = (2869231 \pm 28) \text{ cps}, R_{\text{BIXS}} = (6751.6 \pm 1.4) \text{ cps}. \end{aligned} \quad (6.29)$$

Reducing the dipole fields to a minimum in run 1 results in a tiny shift of the integral FPD rate $\Delta R = (R(\text{run 1}) - R(\text{run 2})) / \bar{R} = (-0.005 \pm 0.001)\%$ with respect to the nominal setting in run 2, normalized to the mean rate of both runs \bar{R} . This is far below the stability of the tritium activity and could in principle be due to a fluctuation of the source density. However, considering the uncertainties of the mean BIXS rates, the shift of the integral FPD rate can not be clearly assigned either to a source density fluctuation or to a plasma effect.

This distinction is done in a more sensitive way by taking a closer look at individual FPD pixel ring rates. The rate is measured simultaneously at each ring, so differences between individual rings are independent of any fluctuation of the source activity. A ring-wise evaluation of $\Delta R_{\text{ring}} = (R_{\text{ring}}(\text{run 1}) - R_{\text{ring}}(\text{run 2})) / \bar{R}_{\text{ring}}$ yields the results shown in Fig. 6.31. A linear fit applied to the data reveals a significantly larger rate shift at the outer rings compared to the inner ones. This points towards a plasma effect. For the inner rings lower rates are observed with the minimum compared to the nominal voltage setting. This corresponds to a more positive plasma potential, which fits to the expectation that for lower dipole fields negative space charges are reduced.

An accurate conversion of the rate shift into a corresponding plasma potential shift is not possible for this specific measurement due to the lack of a reference measurement of the β -spectrum slope. The measurements were performed 1 kV below the β -spectrum endpoint, so the slope is much higher than the slope at the PRO KATRIN set point which is measured about 700 V deep in the spectrum. Thus, the slope obtained for the integral FPD in the PRO KATRIN MS scan has to be scaled accordingly. Then, one finds that a shift of the integral rate of about $\Delta R = -0.005\%$ would correspond to a shift of the plasma potential on the order of ~ 10 mV, provided that it is a pure plasma effect and not induced by source activity fluctuations.

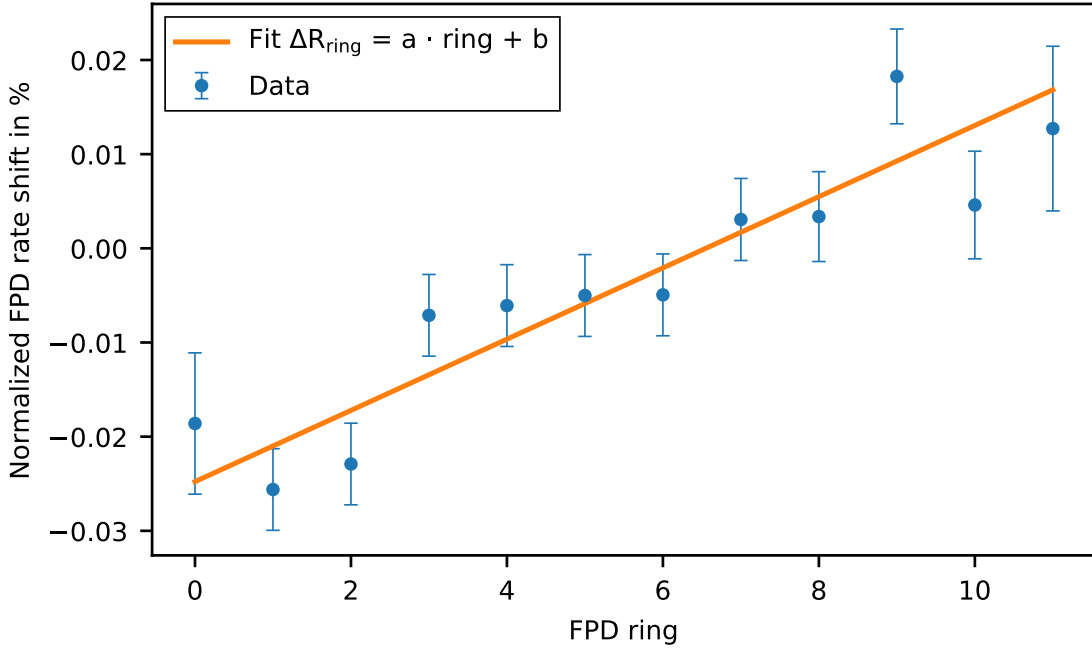


Figure 6.31: Results of the relative ring-wise shift of the FPD rate for two different DPS dipole voltage settings measured in KNM2. The ring-wise shift $\Delta R_{\text{ring}} = (R_{\text{ring}}(\text{run 1}) - R_{\text{ring}}(\text{run 2})) / \bar{R}_{\text{ring}}$ is calculated as a rate difference between run 1 performed at a minimum voltage setting and run 2 performed at the nominal voltage setting (cf. Eq. 6.28), which is normalized to the average rate of the respective ring. Both runs were executed at a MS retarding voltage $U_{\text{ret}} = -17\,573.00$ V, a column density $\mathcal{N} = 4.2 \times 10^{17}$ molecules/cm² and a tritium purity $\epsilon_{\text{T}} = 98.7\%$. A linear fit $\Delta R_{\text{ring}} = a \cdot \text{ring} + b$ is applied to the data yielding $a = (0.0038 \pm 0.0005)\%/\text{ring}$ and $b = (-0.025 \pm 0.003)\%$. The bull’s eye is denoted by ring number 0.

The differences of the shifts observed for the inner with respect to the outer rings correspond to several tens of mV. Thus, the ring-wise analysis yields a significant shift induced by the different dipole electrode voltage settings.

Possible interpretation of the results

A possible explanation for the ring-dependent shifts of the plasma potential was formulated by F. Glück and is summarized in the following.

Negative ions are stored at the front end of the WGTS. In upstream direction their motion is restricted by the WGTS neutral gas flow, while in downstream direction they are blocked by the negative fields of the dipole electrodes. At the front end of the WGTS the negative ions recombine with positive ones. The number of positive ions is reduced for higher dipole fields. So for higher fields, the number of negative ions increases and negative space charge potentials can form. Consequently, the plasma potential is shifted to more negative values compared to the case of lower dipole fields.

For the inner pixel rings the shift is expected to be higher than for the outer rings

because of the following considerations¹⁷. The negative space charge leads to a longitudinal electric field between the WGTS center and its front end. At some point, this electric field counterbalances the negative ion flow in downstream direction. The electric field strength is proportional to the neutral gas flow velocity, which is radially dependent. At smaller radii, the neutral gas flow velocity is higher than at larger radii. Therefore, at smaller radii one can expect a higher longitudinal electric field and thereby a more negative space charge potential.

This explanation fits to the observed pattern as shown in Fig. 6.31. The minimal dipole fields applied in run 1 correspond to smaller amounts of negative ions located at the front end of the WGTS, while the higher fields applied in run 2 come along with a higher number of negative ions. Thus, in run 2 higher FPD rates, corresponding to more negative space charge potentials, are expected for the inner rings, where the neutral gas flow velocity is high.

Conclusion

The FPD rate was measured at minimum voltages applied to the first three dipole electrodes and compared to the rate measured at the nominal setting. A ring-wise analysis reveals a significant plasma potential shift of several tens of mV measured for the bull's eye and the inner rings 1 and 2. The plasma potential is more negative for the nominal setting than for the minimum voltage setting.

This could be explained by negative space charges induced by the accumulation of negative ions at the front end of the WGTS. The higher the dipole fields are, the higher is the amount of negative ions. If this is the correct interpretation, it is advised to reduce the dipole electrode voltages during future neutrino mass measurements. Further, the settings should be kept constant throughout neutrino mass runs. Only those runs performed at comparable dipole electrode settings should be considered for the final analysis.

6.3.10 Influence of the DPS infrared illumination on the plasma potential

The procedure described in the previous section was executed in an analog way to test the influence of the DPS IR illumination (cf. section 6.1.2) on the plasma potential.

Motivation

As discussed in the previous section, the plasma potential is shifted to more negative values if the dipole electrodes are operated at high dipole fields. This shift could be induced by negative ions located at the front end of the WGTS. The purpose of the IR illumination inside the first DPS pump port is to neutralize negative ions and thereby reduce the influence of negative space charges inside the WGTS. If this is indeed accomplished, a significant change of the plasma potential will be observable

¹⁷A parameter which is neglected in these considerations is the removal efficiency of positive ions by the dipole electrodes. It is expected to exhibit a radial dependence too, which would in turn affect the radial number density of negative ions. However, an analytical estimation of the radial dependence is not straightforward since the removal efficiency not only depends on the radial position but also on the distance to the metal lobe at which the ions are neutralized. In order to gain a quantitative understanding, dedicated numerical simulations of the ring-wise impact of the removal efficiency are required.

by the measurement procedure described in the following.

Measurement procedure

Two consecutive runs were performed at a RW voltage $U_{\text{RW}} = -150$ mV, a MS retarding voltage $U_{\text{ret}} = -17\,573.00$ V, a column density $\mathcal{N} = 4.2 \times 10^{17}$ molecules/cm² and a tritium purity $\epsilon_{\text{T}} = 98.7\%$. In run 1 the IR illumination was actively operated, while in run 2 it was turned off.

The two dipole elements 1 and 2, in between which the IR illumination is located, were operated in monopole mode at positive voltages. In this way, negative ion transmission up to the first DPS pump port, where they could interact with the IR photons, was enabled. The voltage settings for both runs were +0.5 V/+0.5 V, +0.5 V/+0.5 V and -5 V/-85 V for dipole electrodes 1, 2 and 3, respectively.

Results

Results both for the integral FPD and BIXS rate, R and R_{BIXS} , are given by

$$\begin{aligned} \text{Run 1: } R &= (2868762 \pm 28) \text{ cps, } R_{\text{BIXS}} = (6755.5 \pm 1.4) \text{ cps,} \\ \text{Run 2: } R &= (2869458 \pm 28) \text{ cps, } R_{\text{BIXS}} = (6753.8 \pm 1.4) \text{ cps.} \end{aligned} \quad (6.30)$$

The stability of the WGTS activity was well below the design value of 0.1%, which provides good boundary conditions for measuring plasma effects. The integral FPD rate R was shifted by $\Delta R = (R(\text{run 1}) - R(\text{run 2})) / \bar{R} = (-0.024 \pm 0.001)\%$ relative to the mean rate of both runs \bar{R} when the IR illumination was active. In principle, this could either be due to a plasma effect or to fluctuations of the WGTS activity. Differences in the normalized ring-wise results as shown in Fig. 6.32 are insensitive to WGTS activity fluctuations as the data is recorded simultaneously for all rings. Similar to the previously discussed results for the different dipole electrode voltage settings, the inner rings exhibit a larger absolute rate shift than the outer ones. However, the results are far less significant. A linear fit applied to the data results in a positive slope compatible with zero within 2σ . The absolute deviation from zero for all rings can not be clearly assigned to an effect induced by the IR illumination because the deviation is compatible with the WGTS activity fluctuations as measured with BIXS.

Conclusion

Active operation of the DPS IR illumination system did not result in a significantly different FPD rate. Therefore, no conclusive quantitative statement about the effect of the IR illumination on the plasma potential can be made. From the results it can be inferred that any possibly existing effect is restricted to a conservative upper limit of 100 mV. If there will be a demand for removing negative ions in the future, dedicated measurements to characterize the IR illumination system have to be performed.

6.4 Summary

Various investigations of WGTS plasma effects were performed during the first two neutrino mass measurement campaigns KNM1 and KNM2. The main focus was on the study of the interplay between plasma and its boundary conditions. All these investigations were based on two observables only: the RW current and the FPD

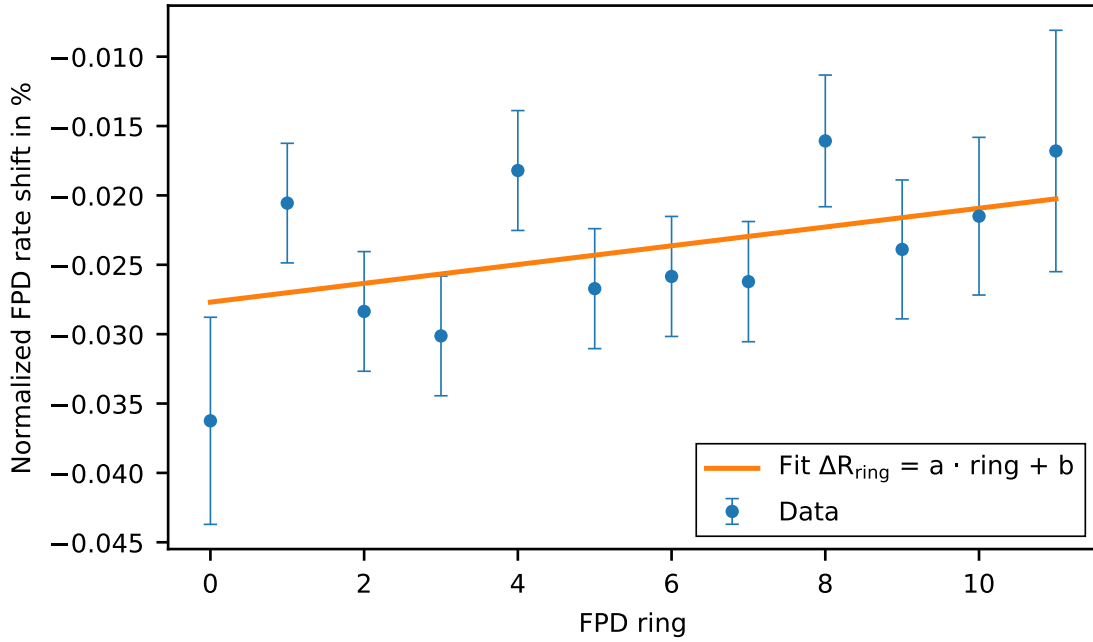


Figure 6.32: Results of the relative ring-wise shift of the FPD rate obtained by operating the DPS IR illumination system in KNM2. The shift $\Delta R_{\text{ring}} = (R_{\text{ring}}(\text{run 1}) - R_{\text{ring}}(\text{run 2})) / \bar{R}_{\text{ring}}$ is calculated as a rate difference between run 1 performed with an actively operated IR illumination and run 2 performed without, which is normalized to the average rate of the respective ring \bar{R}_{ring} . Both runs were executed at a MS retarding voltage $U_{\text{ret}} = -17573.00 \text{ V}$, a column density $\mathcal{N} = 4.2 \times 10^{17} \text{ molecules/cm}^2$ and a tritium purity $\epsilon_{\text{T}} = 98.7\%$. A linear fit $\Delta R_{\text{ring}} = a \cdot \text{ring} + b$ is applied to the data yielding $a = (0.00068 \pm 0.0005)\%/\text{ring}$ and $b = (-0.028 \pm 0.003)\%$. The bull's eye is denoted by ring number 0.

rate. Except for two single measurements (cf. sections 6.2.2 and 6.2.4), the FPD rate was always induced by β -decays of tritium molecules inside the plasma. Provided that the β -activity and the MS retarding potential remain constant, a change of this rate is directly related to a corresponding variation of the plasma potential.

The influence of the RW bias voltage U_{RW} on the plasma potential V_{P1} was thoroughly examined. Both parameters are coupled to each other, which is quantified by the effective coupling strength c . A change of the RW bias voltage induces compensation currents of electrons and ions flowing out of the plasma. The plasma potential follows the RW bias voltages most efficiently in the central voltage region around $U_{\text{RW}} \approx 0 \text{ V}$, where the RW-plasma coupling is maximized with $c \approx 1$. At slightly more positive RW voltages, the coupling starts to diminish with $0 < c < 1$, so a voltage change at the RW is only partly transferred to the plasma potential. In this region, results of a measurement of the FPD rate induced by tritium ions from the WGTS front end indicate that the coupling diminishes along the z -axis, so the parts of the source far away from the RW are somewhat decoupled, while the regions close to it still exhibit a large coupling strength. Eventually, at very large absolute voltages, $|U_{\text{RW}}| \gg 0 \text{ V}$, the plasma fully decouples from the RW with $c \approx 0$, most likely because of a saturation of the compensation currents. Due to the limited RW voltage range $U_{\text{RW}} \leq 4 \text{ V}$ during KNM2 measurements, the decoupling at very

positive voltages was however only observed at elevated temperature $T = 99$ K in the WGTS krypton mode. At increased temperature the plasma already decouples at $U_{\text{RW}} \approx 3$ V, which can probably be explained by the lower recombination rate of positive ions with secondary electrons, which in turn leads to a saturation of the compensation currents already at smaller RW voltages.

The coupling strength exhibits a radial dependence and diminishes at outer radii. Currently, the reason for this is still a matter of debate. In one view negative blocking potentials of several hundreds of mV at outer radii in front of the RW would prohibit an undisturbed flow of electron currents. In a second scenario, the influence of the beam tube surface potential could grow at outer radii.

The RW voltage region of maximal coupling can be broadened for all radii likewise by illuminating the RW with the Cermax[®] UV lamp [Ful20]. Thereby, eV-energy photoelectrons are produced and contribute to the compensation currents. The drawback of this procedure is the creation of a rather large negative space charge.

As predicted by earlier plasma simulations [Kuc16], U_{RW} is the key parameter for reducing the spatial inhomogeneity of V_{P1} for neutrino mass measurements. Both for KNM1 and KNM2, optimum RW set points were determined, at which the radial distribution of the endpoint is rather flat. This corresponds to a radially and presumably also longitudinally homogeneous plasma potential. These set points are among the most important results of this thesis as they have provided an important prerequisite in the measurement of the neutrino mass. For KNM1, the optimum voltage was determined to be $U_{\text{RW}} = -0.15$ V. For KNM2, however, a long-term drift of this reference parameter of (9.3 ± 0.5) mV/day was found. Therefore, three different voltages $U_{\text{RW}} = -0.05$ V, $U_{\text{RW}} = -0.008$ V and $U_{\text{RW}} = 0.2$ V were applied each for several weeks in different phases of the campaign.

This drift is probably either induced by sorption processes or charging of dielectric patches on the boundary surfaces, which both would change the respective surface potentials over time. Several observations favor the hypothesis of adsorption of carbonic molecules on the WGTS beam tube. The adsorption of CT_4 and CO was already observed at the beginning of KNM1 in the inlet capillary of the loop system [Mar]. Further, the long-term drift was reset as soon as the WGTS beam tube temperature was increased from 30 K to 99 K.

If the RW voltage is varied during a measurement, systematic effects are introduced, which was shown by measuring the characteristic I-U curve of the RW. Interestingly, one observes a hysteresis between curves obtained in consecutive upward and downward sweeps of U_{RW} . On top of that, the curves are drifted continuously towards more positive RW voltages at a rate of ~ 200 mV/day. Both effects are commonly observed in Langmuir probe measurements and can likely be attributed to the charging of dielectric spots on the RW surface. This effect probably also contributes to the long-term drift.

The long-term drift was also observed in I-U scans. Over the period of KNM2 the obtained current-voltage curves were shifted to more positive RW voltages by (6.9 ± 0.8) mV/day. The I-U curve of the RW has a characteristic pattern similar to the one of a Langmuir probe, with large electron saturation currents of up to ~ 300 nA and ion saturation currents of up to ~ 20 nA at a column density $\mathcal{N} = 4.2 \times 10^{17}$ molecules/cm². Different curve shapes were found for different

WGTS magnetic field strengths and different column densities. Larger magnetic fields induce a steeper rise in between ion and electron saturation currents. An increased column density comes along with larger saturation currents due to the higher creation rate of ions and secondary electrons. First simulation efforts indicate that the shape of the characteristic I-U curve could be induced by the transversal motion of electrons (for $U_{\text{RW}} \ll 0 \text{ V}$) and ions (for $U_{\text{RW}} \gg 0 \text{ V}$) towards the beam tube. In case of transversal electron motion this would require the existence of cross field plasma instabilities.

To date, there is however no direct evidence for the occurrence of plasma instabilities in general. A dedicated search for high-frequency plasma instabilities did not show any significant effect on the energy of 18.6 keV electrons from an electron gun. However, it should be mentioned that these measurements were systematically biased due to a change of the MS analyzing plane magnetic field, which is why it should be repeated.

Furthermore, no low-frequency plasma oscillations were found by applying a fast Fourier transformation to the FPD rate data measured at a fixed RW voltage.

Applying sinusoidal AC voltages with frequencies between 10 kHz and 1 MHz to the RW induces significant shifts of the plasma potential of up to several hundreds of mV, depending on the applied amplitude, frequency and the FPD pixel ring at which the shift is measured. At frequencies $\geq 3 \text{ MHz}$, the plasma potential is not changed significantly, which is however at least partly due to a damping of the applied voltage in the RW supply cable.

Further, the influence of the DPS instrumentation was tested. The nominal dipole voltages of $(-5 \text{ V}/-15 \text{ V})$, $(-5 \text{ V}/-35 \text{ V})$ and $(-5 \text{ V}/-85 \text{ V})$ applied to the first three electrodes were found to shift the plasma potential at inner radii by several tens of mV with respect to the outer ones compared to settings with much smaller dipole voltages. This could be interpreted as radially-dependent creation of negative space charge potentials by negative ions accumulating at the WGTS front end. The number of negative ions and thereby the negative space charge would be increased at higher dipole fields because of the larger removal rate of positive ions which could recombine with the negative ones. Provided that this is the correct interpretation, the dipole electrode voltages should be reduced in future campaigns.

A countermeasure against negative ions could be to operate the IR illumination system at the first DPS pump port. However, first measurements did not show any significant impact on the plasma potential so further investigations are required for a proper characterization.

7. Conclusion and outlook

In order to achieve the targeted neutrino mass sensitivity, both a low background rate and a stable and homogeneous β -electron starting potential are mandatory for the KATRIN experiment. The two requirements could potentially be impacted in a negative way by the creation of ions and secondary electrons at a rate of 10^{12} s^{-1} , forming a plasma inside the beam tube of the windowless, gaseous tritium source (WGTS). If tritium ions would be allowed to propagate along the differential and cryogenic pumping sections (DPS and CPS) to eventually enter the pre-spectrometer (PS) located right before the main spectrometer (MS), they would induce a significant increase of the MS background rate. Further, as the plasma potential governs the starting potential of the β -electrons, spatial or temporal variations would significantly affect the measured spectrum.

Measurements to investigate these systematic effects were performed at four different KATRIN campaigns: the first operation of the KATRIN apparatus with $^{83\text{m}}\text{Kr}$ gas in July 2017, the STSIIIa commissioning campaign with inactive D_2 gas in the fall of 2018 and the first two neutrino mass measurement campaigns KNM1 in spring 2019 and KNM2 in fall 2019, with column densities of 22% and 84% of the design value $\mathcal{N} = 5 \times 10^{17} \text{ molecules/cm}^2$, respectively.

Contributions to the $^{83\text{m}}\text{Kr}$ July 2017 measurements

A unique method to directly measure spatial plasma potential variations is to admix small amounts of $^{83\text{m}}\text{Kr}$ to the T_2 carrier gas. The decay spectrum of $^{83\text{m}}\text{Kr}$ conversion electrons exhibits sharp lines, which are shifted in case of changing plasma potentials. Moreover, these lines will be broadened in case of more inhomogeneous plasma potential distributions. Although the analysis of krypton lines is discussed in other publications, the first-ever operation of the KATRIN apparatus with gaseous krypton in July 2017 was supported by performing dedicated gas flow and electromagnetic field simulations and compare them to the results of the measurements in order to validate the underlying models.

- It was found that the simulated effective distribution of krypton decays along the beam line is in good agreement with results obtained by measuring the FPD rate of the $\text{L}_3\text{-32}$ line.

Minimization of ion-induced background

A variety of ring and dipole electrodes is operated in the DPS to block and remove ions. Two different approaches for ion detection have been applied in order to validate that the residual ion flux ϕ into the PS is below the required upper limit of $\phi = 1 \times 10^4$ ions/s. Both methods were calibrated in STSIIIa using deuterium ions. Following this, the two techniques were applied over the course of the KNM1 and KNM2 campaigns, with ring and dipole electrodes being continuously operated at the voltage settings stated below.

- In KNM1 and KNM2 an upper limit of $\phi < 3 \times 10^3$ ions/s was determined. This is more than a factor of three below the required upper limit of $\phi = 1 \times 10^4$ ions/s.
- Three ring electrode elements called DPSa, DPSb and PS1 were operated at voltages of +40 V, +5 V and +200 V, respectively. These blocking voltage values are an optimum tradeoff between lower voltages, which would allow tritium ions created in the WGTS to pass, and higher voltages, where the rate of Penning ions generated by trapped electrons would increase. In addition, voltages of (+25 V/+20 V) are applied to the lower/upper half-shell of the last of the four dipole electrodes. This dipole field can not be neutralized by trapped electrons.
- Beta-electrons from tritium decays inside the volume of the dipole electrode potentials are shifted in energy compared to the ones created inside the grounded WGTS beam tube. Thus, each of the dipole electrodes acts as a source of energy-dependent background. This effect was quantified for the three negatively biased dipole electrodes, which are currently operated at voltages of (−5 V/−15 V), (−5 V/−35 V) and (−5 V/−85 V). First Monte Carlo simulations yield a preliminary shift of $\Delta m_{\nu_e}^2 = -6.1 \times 10^{-3} \text{ eV}^2/c^4$ imposed on the best-fit value of the squared neutrino mass. If genuine, this is considered to be negligible at the current neutrino mass sensitivity, but a re-evaluation is required when the ultimate sensitivity is targeted.

Experimental investigations of the WGTS plasma effects

Plasma effects were studied during KNM1 and KNM2 at several configurations of the rear wall (RW), a gold-coated disk mounted at the rear end of the WGTS on which the magnetic flux tube is mapped. Further, the influence of the operation of the UV illumination system of the RW, and, at the other end of the source, the dipole electrodes and the IR illumination system at the DPS were investigated.

- The plasma potential V_{P1} is influenced by its boundaries: the RW and the beam tube surface potential. Since the beam tube is grounded, the RW bias voltage U_{RW} is a central parameter to control V_{P1} . If U_{RW} is chosen in an optimum narrow range, the work function differences between RW and beam tube are compensated, and a spatially homogeneous V_{P1} is expected to be established.
- The impact of a change of U_{RW} onto V_{P1} is quantified by the effective parameter of the "coupling strength" $c \in [0,1]$. It is close to zero in case of very extreme voltages $|U_{RW}| \gg 0 \text{ V}$, and maximized around $U_{RW} = 0 \text{ V}$, while it is small at slightly positive voltages above 0 V. At larger radii, c is reduced, which could be explained by a growing influence of the WGTS beam tube surface potential. Another effect could come from the occurrence of negative blocking

potentials on the outer edge in front of the RW, which would disturb the flow of electron compensation currents. At slightly positive RW voltages, the diminished overall coupling strength was found to be due to the fully decoupled ($c \approx 0$) WGTS front part.

- The RW voltage interval where c is maximized can be increased by illuminating the RW with UV light and, at least for the inner radii, by increasing the WGTS beam tube temperature. In both cases the reason presumably is a higher number of meV-scale electrons with large longitudinal mobility.
- For both KNM1 and KNM2 the optimum RW set points corresponding to a radially and presumably also longitudinally homogeneous plasma potential were determined. This was achieved by measuring the radial distribution of E_0 in tritium operation and choosing the value of U_{RW} where radial inhomogeneities are minimal. For KNM1, an optimum value $U_{RW} = -0.15$ V was found and set throughout the neutrino mass measurements. For KNM2, with its much larger tritium throughput, a long-term drift of the optimum set point towards more positive voltages of (9.3 ± 0.5) mV/day made it necessary to adjust U_{RW} over time. Three different voltages $U_{RW} = -0.05$ V, $U_{RW} = -0.008$ V and $U_{RW} = 0.2$ V were set, each for several weeks during KNM2 neutrino mass measurements.

The long-term drift was also found to shift the current-voltage (I-U) curve of the RW to more positive voltages. There are several possible explanations of the underlying physics mechanism. The drift can not be caused by the plasma itself because it equilibrates on short time scales of 10^{-6} s. Instead, sorption or charging processes on the boundary surfaces have to be responsible. One scenario is based on the adsorption of molecules like CT_4 and CO from radiochemical processes at the surface of the WGTS beam tube. These would effectively change the beam tube work function over long-term tritium circulation.

- As found in measurements of the I-U curves, systematic effects are introduced whenever the RW voltage is varied during an investigation. The I-U curve of the RW exhibits a hysteresis-like behavior when comparing curves obtained in consecutive upward and downward voltage sweeps. Further, a fast drift of ~ 200 mV/day was observed, which shifts the I-U curves towards more positive RW voltages. The drift does not evolve at constant rates but is saturating at some point. Both the hysteresis and the short-term drift could be explained by charging of dielectric parts on the RW surface. This would be a typical systematic effect observed in similar plasma measurements with Langmuir probes. Possibly, this effect also contributes to the long-term drift.
- In case that U_{RW} is modulated by applying a sinusoidal AC voltage, the plasma potential can be effectively shifted by up to several hundreds of mV, depending on the parameters.
- The currently applied dipole electrode voltages to eliminate ions from the beam line could possibly be too large. The results of a specific measurement can be interpreted in such a way that they lead to a significant radial inhomogeneity of V_{p1} due to negative ions accumulating at the front end of the WGTS. Consequently, it is advised to perform further measurements and, if necessary,

reduce the dipole electrode voltages during future neutrino mass measurement campaigns.

- The IR illumination system to influence tritium anions was found to have no significant impact on the plasma potential.
- Measurements with 18.6 keV-energy electrons provided by the electron gun attached to the rear end of KATRIN did not detect significant effects induced by high-frequency plasma instabilities. For an ultimate conclusion, the results however are not yet sufficiently precise because they are systematically biased due to a change of the MS energy resolution during the measurements.

Outlook

The investigations focused on ion-induced background in this thesis can be viewed as a conclusion of the topic. However, given the complex nature of the topic, many open questions remain regarding the scale and relevance of plasma effects. The underlying physical mechanisms responsible for the observed effects are currently still a matter of debate and no plasma model has been set up yet. A large step towards a better understanding of the experimental observations presented in this thesis will be provided by results of detailed plasma simulations based on a particle-in-cell approach, which are currently in development.

One of the main consequences from the investigations described in this thesis was to perform neutrino mass measurements in the subsequent KNM3 campaign at a temperature of about $T = 80$ K instead of the anticipated design value $T = 30$ K. The two main advantages are the expected mitigation of CT₄ and CO adsorption on the beam tube potentially leading to a more stable plasma configuration and the possibility to perform ^{83m}Kr spectroscopy at identical conditions as the neutrino mass measurements to quantify the properties of the plasma potential.

Future tasks are focused on investigations of plasma instabilities together with further measurements to characterize the influence of the DPS dipole electrode voltages and the DPS IR illumination system.

8. Appendix: Calculation of correction factors for the determination of the background contribution by tritium decay inside the DPS dipole electrodes

In section 5.3.4 the shift $\Delta m_{\bar{\nu}_e}^2$ of the best-fit squared neutrino mass result induced by tritium decays inside the DPS dipole electrodes was determined. Two correction factors had to be applied in order to obtain the final result.

- **Monopole mode correction factor f :** This correction factor is necessary for deriving the number of tritium atoms N_T inside the negative electric potential U of the first dipole electrode from dedicated measurements of the FPD rate R during monopole mode operation of the electrode. Both a lower electric potential U and a lower maximum pitch angle θ at the decay location would result in a higher number of tritium atoms for a given measured FPD rate. In addition, the distribution of the pressure times volume pV has to be taken into account as U and θ values located in a lower pV region contribute less than the same values in a higher pV region.

The factor f includes all effects induced by spatially inhomogeneous distributions of U , pV and θ . Thus, the number of tritium atoms N_T determined by assuming perfectly homogeneous electric potential, pressure and maximum pitch angle distributions can be divided by f in order to get the corresponding number for the true distributions, which are approximated by numerical simulations.

- **Dipole mode correction factor f_D :** During nominal neutrino mass measurements the dipole electrodes are operated in dipole mode at two different voltages applied to their respective lower and upper half-shells. Further, the β -

electrons are born at different locations with different maximum pitch angles, which affects their transmission towards the FPD. In the Kafit simulations described in section 5.3.4, however, a constant potential and maximum pitch angle was assumed for each dipole electrode. Thus, the rate $R_i(U_{\text{ana}})$ simulated at an analyzing plane retarding voltage U_{ana} for a dipole electrode i has to be multiplied by the correction factor $f_D(U_{\text{ana}})$ in order to get the corresponding rate one would receive during dipole mode operation with spatially inhomogeneous distributions of the electric potential and maximum pitch angle.

Determination of the monopole mode correction factor f

Different simulations similar to the ones described in section 5.2.4 were performed in order to determine the dipole electrode 1 electric potential, pressure and pitch angle distributions.

- At first, the magnetic field line tracks of the 134 T cm^2 flux tube were simulated with KASSIOPEIA for a magnetic field $B = 4.0 \text{ T}$ at the first DPS superconducting magnet. At each tracking position j on the field lines, the corresponding electric potential U_j was simulated with KEMField assuming monopole mode operation of the dipole electrode at $U_{\text{dipole1}} = -350 \text{ V}$. The corresponding magnetic field strength B_j was simulated with KASSIOPEIA.
- The distribution of the pressure p along the central z -axis was simulated with MolFlow+. A stand-alone DPS beam line model was used in which the TMPs were modeled by surfaces with a sticking probability $\alpha = 0.25$ corresponding to the pumping speed for T_2 according to a model developed by O. B. Malyshev [Mal07].

From these simulation results the correction factor f is determined by

$$f = \frac{\sum_j p_j V_j \cdot \frac{1 - \cos(\theta_j)}{2} \cdot (E_0 - eU_{\text{ana,dipole1}} - eU_j)^3}{\sum_j (p_j V_j) \cdot \frac{1 - \cos(\theta_{\text{dipole1}})}{2} \cdot (E_0 - eU_{\text{ana,dipole1}} - eU_{\text{dipole1}})^3} = 0.54. \quad (8.1)$$

Here, p_j is the pressure, V_j is the volume approximated by $r_j^2 = x_j^2 + y_j^2$, $(1 - \cos(\theta_j))/2 = (1 - \cos(\arcsin(\sqrt{B_j/B_{\text{max}}})))/2$ is the probability of full transmission of a β -electron towards the FPD for a maximum pitch angle θ_j and magnetic field $B_{\text{max}} = 4.2 \text{ T}$, $E_0 = (18573.7 \pm 0.1) \text{ eV}$ [AAA+19c] is the endpoint, e is the elementary charge, $U_{\text{ana,dipole1}}$ is the analyzing plane retarding voltage during the measurement with dipole electrode 1, U_j is the electric potential, and $\theta_{\text{dipole1}} = 77.4^\circ$ and $U_{\text{dipole1}} = -350 \text{ V}$ are the maximum pitch angle and the maximum electric potential of dipole electrode 1. It is important to note that only positions j within a distance of $|z| \leq 0.42 \text{ m}$ from the dipole electrode center at $z = 0 \text{ m}$ are considered for the final calculation of f . This cut corresponds to the geometrical length of the dipole electrode. Cuts at higher z -values would result in higher values of f . However, it is expected that tritium decays located further away from the dipole electrode are not contributing significantly to the measured background rate since the rate is suppressed by $(E_0 - eU_{\text{ana,dipole1}} - eU)^3$. The resulting factor $f = 0.54$ is plugged into Eq. 5.18 in order to obtain the result stated in Eq. 5.20.

Determination of the dipole mode correction factor f_D

The systematic shift $\Delta m_{\nu_e}^2$ of the best-fit squared neutrino mass result was determined by simulating the β -spectrum originating from each of the three dipole electrodes with Kafit. In the simulation constant values were assumed for the maximum

pitch angle $\theta_{\text{dipole}i} = 77.4^\circ$ of each dipole electrode $i \in (1,2,3)$. Further, the end-points of the dipole electrode background spectra were set to $E_{0,\text{dipole}1} = E_0 + 15 \text{ V}$, $E_{0,\text{dipole}2} = E_0 + 35 \text{ V}$ and $E_{0,\text{dipole}3} = E_0 + 85 \text{ V}$ with $E_0 = 18573.7 \text{ eV}$ [AAA+19c]. Before those spectra could be compared to the WGTS signal spectrum, the rates $R_i(U_{\text{ana}})$ from a dipole electrode i simulated at an analyzing plane retarding voltage U_{ana} each had to be scaled by a dipole mode correction factor $f_{D,\text{dipole}i}(U_{\text{ana}}) < 1$. This correction factor is given by

$$f_{D,\text{dipole}i}(U_{\text{ana}}) = \frac{\sum_j p_j V_j \cdot \frac{1 - \cos(\theta_j)}{2} \cdot (E_0 - eU_{\text{ana}} - eU_j^{i,\text{dipole}})^3}{\sum_j (p_j V_j) \cdot \frac{1 - \cos(\theta_{\text{dipole}i})}{2} \cdot (E_0 - eU_{\text{ana}} - eU^{i,\text{monopole}})^3} \quad (8.2)$$

with the simulated values for the pressure p_j , the volume V_j and maximum pitch angle θ_j which were already used in Eq. 8.1. The electric potential values $U_j^{i,\text{dipole}}$ were simulated with KEMField for the respective dipole electrode i operated in dipole mode with voltages of $-5 \text{ V}/-15 \text{ V}$ for $i = 1$, $-5 \text{ V}/-35 \text{ V}$ for $i = 2$ and $-5 \text{ V}/-85 \text{ V}$ for $i = 3$ applied to their lower/upper half-shells. In the denominator the maximum pitch angle $\theta_{\text{dipole}i} = 77.4^\circ$ is the same for all dipole electrodes. The electric potentials are given by $U^{1,\text{monopole}} = -15 \text{ V}$, $U^{2,\text{monopole}} = -35 \text{ V}$ and $U^{3,\text{monopole}} = -85 \text{ V}$. The results for $f_{D,\text{dipole}i}(U_{\text{ana}})$ can be found in Fig. 8.1 for analyzing plane retarding voltages up to 90 eV below the WGTS signal β -spectrum endpoint. Like for the determination of f in the previous paragraph, only positions j within a distance of $|z| \leq 0.42 \text{ m}$ from the dipole electrode center at $z = 0 \text{ m}$ were taken into account.

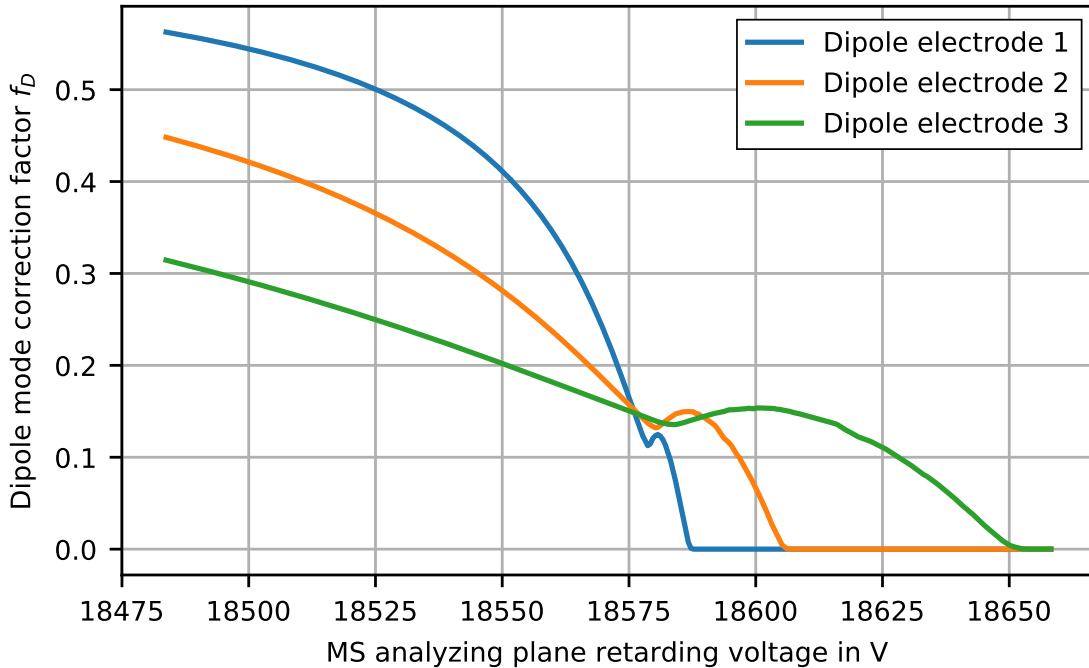


Figure 8.1: Simulated dipole mode correction factor $f_{D,\text{dipole}i}(U_{\text{ana}})$ for different analyzing plane retarding voltages and dipole electrodes. The values expand from 90 V below the endpoint E_0 of the WGTS signal spectrum up to the endpoint of the third dipole electrode $E_{0,\text{dipole}3} = E_0 + 85 \text{ V}$.

List of Acronyms

2dFGRS	2-degree-Field Galaxy Redshift Survey
ADEI	Advanced Data Extraction Infrastructure
AGS	Alternating Gradient Synchrotron
BEANS	Building Analysis Sequence
CC	Charged Current
CMB	Cosmic Microwave Background
CNGS	CERN to Gran Sasso
CPS	Cryogenic Pumping Section
cps	counts per second
DPS	Differential Pumping Section
ES	Elastic Scattering
FBM	Forward Beam Monitor
FFT	Fast Fourier Transformation
FPD	Focal Plane Detector
FT-ICR	Fourier-Transform Ion Cyclotron Resonance
GUI	Graphical User Interface
HDM	Hot-Dark-Matter
HV	High Voltage
IR	Infrared
KATRIN	Karlsruhe Tritium Neutrino Experiment
KIT	Karlsruhe Institute of Technology

KNM1 **K**ATRIN **N**eutrino **M**ass **R**un **1**
LEP **L**arge **E**lectron **P**ositron **C**ollider
MAC-E **M**agnetic **A**diabatic **C**ollimation with **E**lectrostatic filter
MoS **M**onitor **S**pectrometer
MS **M**ain **S**pectrometer
MSW **M**ikheyev-**S**mirnov-**W**olfenstein
NC **N**eutral **C**urrent
NPI **N**uclear **P**hysics **I**nstitute
ORCA **O**bject-oriented **R**eal-time **C**ontrol and **A**cquisition
PCS7 **S**iemens **S**IMATIC **P**rocess **C**ontrol **S**ystem **7**
PRO KATRIN **P**lasma **R**ear **W**all **O**ptimization at **K**ATRIN
PS **P**re-**S**pectrometer
RS **R**ear **S**ection
RW **R**ear **W**all
SDS **S**pectrometer and **D**etector **S**ection
SDSS **S**loan **D**igital **S**ky **S**urvey
see **s**econdary **e**lectron **e**mission
SLC **S**LAC **L**inear **C**ollider
STS **S**ource and **T**ransport **S**ection
TLK **T**ritium **L**aboratory **K**arlsruhe
TMP **T**urbo**M**olecular **P**ump
TPMC **T**est **P**article **M**onte **C**arlo
TRIMS **T**ritium **R**ecoil-**I**on **M**ass **S**pectrometer
UHV **U**ltra-**H**igh **V**acuum
WGTS **W**indowless **G**aseous **T**ritium **S**ource
ZEUS **Z**entrale **D**atenerfassung **U**nd **S**teuerung

List of Figures

1.1	Historical measurement result for the β -decay energy spectrum of radium E (today known as bismuth-210).	2
1.2	Weak standard model interactions of neutrinos.	4
1.3	Transition probabilities for a two flavor oscillation.	7
1.4	First Super-Kamiokande results of atmospheric neutrino zenith angle distributions.	11
1.5	Models showing the influence of different sums of neutrino mass eigenvalues on cosmological spectra.	19
1.6	Effective Majorana mass constraints on the lightest neutrino mass and double β -decay energy spectra.	21
1.7	Energy spectrum of tritium β -decay and influence of the electron neutrino mass on the shape close to the endpoint.	23
2.1	Illustration of the KATRIN measurement principle.	28
2.2	Electron movement along magnetic field lines and the definition of the pitch angle θ	29
2.3	Illustration of the KATRIN response function.	32
2.4	Simulation of the integral β -spectrum close to the endpoint for a neutrino mass of $0.350 \text{ eV}/c^2$ and comparison with the theoretical model expectations.	33
2.5	Anticipated uncertainties and sensitivity over time for a 36 months long measurement of the β -spectrum endpoint region.	35
2.6	Engineering drawing of the global KATRIN setup.	36
2.7	Engineering drawing of the 16 m WGTS cryostat in a three quarter section view.	37
2.8	Schematic drawing of the WGTS two-phase neon cooling system.	38
2.9	Simplified schematic drawing of the WGTS loop system.	38
2.10	Engineering drawing of the rear section.	40
2.11	Engineering drawing of the rear chamber with a view inside and photograph of the isolated rear wall mount.	40
2.12	Engineering drawing of the DPS in a half to three-quarter section view.	42
2.13	Engineering drawing of the CPS in a three-quarter section view.	43
2.14	Engineering drawing of the spectrometer and detector section.	44
2.15	Engineering drawing of the focal plane detector system.	46
3.1	Simulated neutral gas density distribution along the WGTS z-axis.	54
3.2	Simulated longitudinal ion density distribution in the front half of the WGTS.	55

3.3	Illustrative plot showing the influence of an exemplary energy-dependent background β -spectrum on the effectively measured spectrum.	57
3.4	KNM1 measurement and best-fit result of the integral beta-spectrum.	63
4.1	Decay scheme of $^{83\text{m}}\text{Kr}$	70
4.2	MolFlow+ beam line geometry model for krypton gas flow simulations.	73
4.3	KASSIOPEIA simulation results for the outermost field lines of the sensitive magnetic flux tube mapped onto the FPD in the July 2017 krypton campaign.	75
4.4	Simulated longitudinal distributions of $^{83\text{m}}\text{Kr}$ decays in the July 2017 campaign.	77
4.5	Simulated electric potential distribution at the DPS $^{83\text{m}}\text{Kr}$ decay locations for all four dipole electrodes operated in monopole mode at $U = -350\text{ V}$	78
5.1	Locations of the beam line electrodes for tritium ion blocking and removing.	83
5.2	Engineering drawing of the pre-spectrometer inner electrode system in nominal setting during neutrino mass measurements in a half section view.	86
5.3	Engineering drawing of the pre-spectrometer inner electrode system in the ICE setting in a half section view.	88
5.4	STSIIIa Penning ion creation at DPS dipole electrode 1.	92
5.5	Blocking of photoelectrons from the RW with negative voltages applied to the beam line electrodes.	93
5.6	KEMField simulation of the electric potential distribution inside the sensitive magnetic flux tube volume of the first DPS dipole electrode.	99
5.7	MolFlow+ simulation of the longitudinal D_2 pressure profile in the first DPS beam tube element.	100
5.8	Pressure dependence of the ICE method.	102
5.9	KNM1 measurement of the DPS dipole electrode currents during step-wise tritium column density ramp-up.	106
5.10	KNM1 measurement of the RW and DPS dipole electrode currents versus the column density during step-wise ramp-up.	106
5.11	KNM1 ion energy spectrum measurements with DPS electrodes during tritium operation.	108
5.12	KNM1 ion energy spectrum measurement during tritium operation with ring electrode PS1.	109
5.13	KNM1 ion energy spectrum measurements with ring electrode DPSa for different tritium column densities.	110
5.14	KNM1 and KNM2 measurements of the FPD background rate originating from tritium inside the first DPS dipole electrode.	113
5.15	KNM1 and KNM2 ICE method measurements of the tritium ion flux into the PS.	119
5.16	PS cone current measurements during WGTS tritium column density ramp-up.	120
6.1	Temperature and charge carrier density for the WGTS plasma and other common plasmas.	125

6.2	Trend of the electric potential and the charge carrier densities in the plasma sheath between an infinite plane wall and a plasma.	126
6.3	Schematic drawing of the characteristic curve of a plane Langmuir probe.	128
6.4	Locations of the individual beam line hardware devices influencing the WGTS plasma.	131
6.5	Schematic drawing of the RW and WGTS voltage setup.	132
6.6	Schematic drawing of the expected impact of the RW set point on the plasma potential based on simulations using the two-dimensional axially symmetric fluid model.	135
6.7	Schematic drawing of the PRO KATRIN measurement principle.	138
6.8	PRO KATRIN result measured in KNM2 on 19.09.2019.	140
6.9	Results of the deep MS scan for the KNM2 PRO KATRIN measurement from 19.09.2019.	143
6.10	"PRO KATRIN with ions" result measured in KNM2 on 26.09.2019.	146
6.11	Frequency dependence of the peak-to-peak amplitudes transmitted from the function generator to the RW.	149
6.12	Ring-wise results of the PRO KATRIN RW scan measured in KNM2 on 19.09.2019.	152
6.13	Triple linear fit of the ring-wise PRO KATRIN results measured in KNM2 on 19.09.2019.	154
6.14	Ring-wise coupling strength results for the KNM2 PRO KATRIN measurement from 19.09.2019.	155
6.15	PRO KATRIN result for the ring-wise β -spectrum endpoint slope as a function of the RW voltage measured in KNM2 on 19.09.2019.	157
6.16	I-U scan results measured in KNM2 on 16.10.2019.	159
6.17	Asymmetry between a downward and an upward RW voltage sweep measured in KNM2 on 16.10.2019.	161
6.18	PRO KATRIN and I-U scan results over the course of KNM2.	163
6.19	KNM2 long-term drift of RW reference set points.	164
6.20	Results for RW I-U curves measured consecutively throughout the PRO KATRIN measurement in KNM2 on 19.09.2019.	166
6.21	Characteristic RW I-U curves for different WGTS and RS magnetic fields.	169
6.22	Characteristic RW I-U curves for different column densities.	170
6.23	PRO KATRIN results for KNM1 and KNM2 obtained in the WGTS nominal and krypton mode.	171
6.24	KNM2 WGTS nominal and krypton mode results for the best-fit kink positions marking the different coupling regions.	172
6.25	Exemplary KNM2 results of the egun transmission function scans.	174
6.26	KNM2 results of the egun transmission function width for different RW voltages.	175
6.27	Modulation of the FPD rate for a low-frequency AC voltage applied to the RW.	176
6.28	Exemplary FFT spectrum of the FPD rate at a DC voltage of -150 mV applied to the RW in KNM2.	177
6.29	Frequency-dependent shifts of the β -spectrum FPD rate and the plasma potential for applying a sinusoidal voltage to the RW during nominal WGTS operation.	179

6.30	Frequency-dependent shifts of the L ₃ -32 FPD rate and the plasma potential for applying a sinusoidal voltage to the RW during WGTS krypton mode operation.	181
6.31	Results of the relative ring-wise shift of the FPD rate for two different DPS dipole voltage settings measured in KNM2.	184
6.32	Results of the relative ring-wise shift of the FPD rate obtained by operating the DPS IR illumination system in KNM2.	187
8.1	Simulated dipole mode correction factor $f_{D,dipolei}(U_{ana})$ for different analyzing plane retarding voltages and dipole electrodes.	197

List of Tables

1.1	Current best-fit values for all neutrino oscillation parameters.	13
3.1	Overview of the systematic effects on the neutrino mass determination induced by tritium ions and plasma effects.	52
4.1	Overview of important conversion electron properties of the $^{83\text{m}}\text{Kr}$ 32.2 keV transition.	71
4.2	MolFlow+ simulation results for the krypton July 2017 campaign. . .	74
5.1	Overview of important parameters of the ring electrodes DPSa, DPSb and PS1.	83
5.2	Overview of PS high voltage settings.	94
5.3	STSIIIa measurement and simulation results for determining the deuterium ion flux into the PS as measured by PULCINELLA in dependence of the MS retarding voltage.	100
5.4	List of KNM2 parameters for the determination of the relative number of tritium atoms inside the potential of the first DPS dipole electrode.	114
5.5	Overview of the beam line electrodes' optimum voltage settings. . . .	118
6.1	Best-fit results for the radial dependence of the coupling strength between RW and plasma.	155
6.2	KNM2 long-term drift rates of selected plasma observables.	165

Bibliography

- [A⁺06] M. H. Ahn et al. Measurement of neutrino oscillation by the K2K experiment. *Physical Review D*, 74:072003, 2006. doi:10.1103/PhysRevD.74.072003.
- [A⁺08] S. Abe et al. Precision measurement of neutrino oscillation parameters with KamLAND. *Physical Review Letters*, 100:221803, 2008. doi:10.1103/PhysRevLett.100.221803.
- [A⁺12a] Y. Abe et al. Reactor $\bar{\nu}_e$ disappearance in the Double Chooz experiment. *Physical Review D*, 86:052008, 2012. doi:10.1103/PhysRevD.86.052008.
- [A⁺12b] J. K. Ahn et al. Observation of Reactor Electron Antineutrinos Disappearance in the RENO experiment. *Physical Review Letters*, 108:191802, 2012. doi:10.1103/PhysRevLett.108.191802.
- [A⁺12c] F. P. An et al. Observation of Electron-Antineutrino Disappearance at Daya Bay. *Physical Review Letters*, 108:171803, 2012. doi:10.1103/PhysRevLett.108.171803.
- [A⁺13] P. Adamson et al. Measurement of neutrino and antineutrino oscillations using beam and atmospheric data in MINOS. *Physical Review Letters*, 110:251801, 2013. doi:10.1103/PhysRevLett.110.251801.
- [A⁺14] M. G. Aartsen et al. Letter of Intent: The Precision IceCube Next Generation Upgrade (PINGU). 2014, 1401.2046.
- [A⁺15] M. Antonello et al. A Proposal for a Three Detector Short-Baseline Neutrino Oscillation Program in the Fermilab Booster Neutrino Beam. 2015, 1503.01520.
- [A⁺16] Y. Abe et al. Measurement of θ_{13} in Double Chooz using neutron captures on hydrogen with novel background rejection techniques. *Journal of High Energy Physics*, 163, 2016. doi:10.1007/JHEP01(2016)163.
- [A⁺17] S. Ajimura et al. Technical Design Report (TDR): Searching for a Sterile Neutrino at J-PARC MLF (E56, JSNS2). 2017, 1705.08629.
- [A⁺18a] B. Abi et al. The DUNE Far Detector Interim Design Report Volume 1: Physics, Technology and Strategies. 2018, 1807.10334.
- [A⁺18b] N. Aghanim et al. Planck 2018 results. VI. Cosmological parameters. 2018, 1807.06209.

- [AAA⁺01a] Q. R. Ahmad, R. C. Allen, T. C. Andersen, et al. Measurement of the Rate of $\nu_e + d \rightarrow p + p + e^-$ Interactions Produced by ^8B Solar Neutrinos at the Sudbury Neutrino Observatory. *Physical Review Letters*, 87:071301, 2001. doi:10.1103/PhysRevLett.87.071301.
- [AAA⁺01b] S. H. Ahn, S. An, S. Aoki, et al. Detection of accelerator-produced neutrinos at a distance of 250 km. *Physics Letters B*, 511(2):178–184, 2001. doi:10.1016/S0370-2693(01)00647-5.
- [AAA⁺02] Q. R. Ahmad, R. C. Allen, T. C. Andersen, et al. Direct Evidence for Neutrino Flavor Transformation from Neutral-Current Interactions in the Sudbury Neutrino Observatory. *Physical Review Letters*, 89:011301, 2002. doi:10.1103/PhysRevLett.89.011301.
- [AAA⁺10] N. Agafonova, A. Aleksandrov, O. Altinok, et al. Observation of a first ν_τ candidate event in the OPERA experiment in the CNGS beam. *Physics Letters B*, 691(3):138–145, 2010. doi:10.1016/j.physletb.2010.06.022.
- [AAA⁺13] B. Aharmim, S. N. Ahmed, A. E. Anthony, et al. Combined analysis of all three phases of solar neutrino data from the Sudbury Neutrino Observatory. *Physical Review C*, 88:025501, 2013. doi:10.1103/PhysRevC.88.025501.
- [AAA⁺14a] K. Abe, J. Adam, H. Aihara, et al. Observation of Electron Neutrino Appearance in a Muon Neutrino Beam. *Physical Review Letters*, 112:061802, 2014. doi:10.1103/PhysRevLett.112.061802.
- [AAA⁺14b] P. Adamson, I. Anghel, A. Aurisano, et al. Combined Analysis of ν_μ disappearance and $\nu_\mu \rightarrow \nu_e$ Appearance in MINOS Using Accelerator and Atmospheric Neutrinos. *Physical Review Letters*, 112:191801, 2014. doi:10.1103/PhysRevLett.112.191801.
- [AAA⁺15] M. G. Aartsen, M. Ackermann, J. Adams, et al. Determining neutrino oscillation parameters from atmospheric muon neutrino disappearance with three years of IceCube DeepCore data. *Physical Review D*, 91:072004, 2015. doi:10.1103/PhysRevD.91.072004.
- [AAA⁺16] P. Adamson, C. Ader, M. Andrews, et al. First measurement of muon-neutrino disappearance in NOvA. *Physical Review D*, 93:051104, 2016. doi:10.1103/PhysRevD.93.051104.
- [AAA⁺18a] K. Abe, R. Akutsu, A. Ali, et al. Search for CP Violation in Neutrino and Antineutrino Oscillations by the T2K Experiment with 2.2×10^{21} Protons on Target. *Physical Review Letters*, 121:171802, 2018. doi:10.1103/PhysRevLett.121.171802.
- [AAA⁺18b] M. A. Acero, P. Adamson, L. Aliaga, et al. New constraints on oscillation parameters from ν_e appearance and ν_μ disappearance in the NOvA experiment. *Physical Review D*, 98:032012, 2018. doi:10.1103/PhysRevD.98.032012.
- [AAA⁺18c] N. Agafonova, A. Alexandrov, A. Anokhina, et al. Final Results of the OPERA Experiment on ν_τ Appearance in the CNGS

- Neutrino Beam. *Physical Review Letters*, 120:211801, 2018. doi:10.1103/PhysRevLett.120.211801.
- [AAA⁺19a] M. A. Acero, P. Adamson, L. Aliaga, et al. First measurement of neutrino oscillation parameters using neutrinos and antineutrinos by NOvA. *Physical Review Letters*, 123:151803, 2019. doi:10.1103/PhysRevLett.123.151803.
- [AAA⁺19b] M. Agostini, K. Altenmüller, S. Appel, et al. Simultaneous precision spectroscopy of pp , ${}^7\text{Be}$, and pep solar neutrinos with Borexino Phase-II. *Physical Review D*, 100:082004, 2019. doi:10.1103/PhysRevD.100.082004.
- [AAA⁺19c] M. Aker, K. Altenmüller, M. Arenz, et al. Improved Upper Limit on the Neutrino Mass from a Direct Kinematic Method by KATRIN. *Physical Review Letters*, 123:221802, 2019. doi:10.1103/PhysRevLett.123.221802.
- [AAA⁺20] M. Aker, K. Altenmüller, M. Arenz, W.-J. Baek, et al. First operation of the KATRIN experiment with tritium. *The European Physical Journal C*, 80(264), 2020. doi:10.1140/epjc/s10052-020-7718-z.
- [AAB⁺01] A. Aguilar, L. B. Auerbach, R. L. Burman, et al. Evidence for neutrino oscillations from the observation of $\bar{\nu}_e$ appearance in a $\bar{\nu}_\mu$ beam. *Physical Review D*, 64:112007, 2001. doi:10.1103/PhysRevD.64.112007.
- [AAB⁺18] D. Adey, F. P. An, A. B. Balantekin, et al. Measurement of the Electron Antineutrino Oscillation with 1958 days of operation at Daya Bay. *Physical Review Letters*, 121:241805, 2018. doi:10.1103/PhysRevLett.121.241805.
- [AAB⁺19a] M. Aker, M. Altenmüller, A. Beglarian, et al. Suppression of Penning discharges between the KATRIN spectrometers. 2019, 1911.09633.
- [AAB⁺19b] K. Altenmüller, M. Arenz, W.-J. Baek, et al. High-resolution spectroscopy of gaseous ${}^{83\text{m}}\text{Kr}$ conversion electrons with the KATRIN experiment. 2019, 1903.06452.
- [AABB⁺18] A. A. Aguilar-Arevalo, B. C. Brown, L. Bugel, et al. Significant Excess of Electronlike Events in the MiniBooNE Short-Baseline Neutrino Experiment. *Phys. Rev. Lett.*, 121:221801, 2018. doi:10.1103/PhysRevLett.121.221801.
- [AAKV88] E.N. Alexeyev, L.N. Alexeyeva, I.V. Krivosheina, and V.I. Volchenko. Detection of the neutrino signal from SN 1987A in the LMC using the INR Baksan underground scintillation telescope. *Physics Letters B*, 205(2):209–214, 1988. doi:10.1016/0370-2693(88)91651-6.
- [ABB⁺87] M. Aglietta, G. Badino, G. Bologna, et al. On the Event Observed in the Mont Blanc Underground Neutrino Observatory during the Occurrence of Supernova 1987a. *Europhysics Letters (EPL)*, 3(12):1315–1320, 1987. doi:10.1209/0295-5075/3/12/011.
- [ABB⁺00] M. Altmann, M. Balata, P. Belli, et al. GNO solar neutrino observations: results for GNO i. *Physics Letters B*, 490(1):16–26, 2000. doi:10.1016/S0370-2693(00)00915-1.

- [ABB⁺05] M. Altmann, M. Balata, P. Belli, et al. Complete results for five years of GNO solar neutrino observations. *Physics Letters B*, 616(3):174–190, 2005. doi:10.1016/j.physletb.2005.04.068.
- [ABB⁺08] C. Arpesella, G. Bellini, J. Benziger, et al. First real time detection of ^7Be solar neutrinos by Borexino. *Physics Letters B*, 658(4):101–108, 2008. doi:10.1016/j.physletb.2007.09.054.
- [ABB⁺11] V. N. Aseev, A. I. Belesev, A. I. Berlev, et al. Upper limit on the electron antineutrino mass from the Troitsk experiment. *Physical Review D*, 84:112003, 2011. doi:10.1103/PhysRevD.84.112003.
- [ABB⁺15] J. F. Amsbaugh, J. Barrett, A. Beglarian, et al. Focal-plane detector system for the KATRIN experiment. *Nuclear Instruments and Methods in Physics Research Section A: Accelerators, Spectrometers, Detectors and Associated Equipment*, 778:40–60, 2015. doi:10.1016/j.nima.2014.12.116.
- [ABB⁺16] M. Arenz, M. Babutzka, M. Bahr, et al. Commissioning of the vacuum system of the KATRIN Main Spectrometer. *Journal of Instrumentation*, 11:P04011, 2016, 1603.01014. doi:10.1088/1748-0221/11/04/P04011.
- [ABB⁺18a] M. Arenz, W.-J. Baek, M. Beck, et al. First transmission of electrons and ions through the KATRIN beamline. *Journal of Instrumentation*, 13(04):P04020, 2018. doi:10.1088/1748-0221/13/04/P04020.
- [ABB⁺18b] M. Arenz, W.-J. Baek, M. Beck, et al. Calibration of high voltages at the ppm level by the difference of $^{83\text{m}}\text{Kr}$ conversion electron lines at the KATRIN experiment. *The European Physical Journal C*, 78(5):368, 2018. doi:10.1140/epjc/s10052-018-5832-y.
- [ABB⁺18c] M. Arenz, W.-J. Baek, M. Beck, et al. The KATRIN superconducting magnets: Overview and first performance results. *Journal of Instrumentation*, 13(08):T08005, 2018. doi:10.1088/1748-0221/13/08/T08005.
- [ABH⁺18] K. Abe, C. Bronner, Y. Haga, et al. Atmospheric neutrino oscillation analysis with external constraints in Super-Kamiokande I-IV. *Physical Review D*, 97:072001, 2018. doi:10.1103/PhysRevD.97.072001.
- [AEE⁺05] T. Araki, K. Eguchi, S. Enomoto, et al. Measurement of Neutrino Oscillation with KamLAND: Evidence of Spectral Distortion. *Physical Review Letters*, 94:081801, 2005. doi:10.1103/PhysRevLett.94.081801.
- [AGG⁺09] J. N. Abdurashitov, V. N. Gavrin, V. V. Gorbachev, et al. Measurement of the solar neutrino capture rate with gallium metal. III. Results for the 2002–2007 data-taking period. *Physical Review C*, 80:015807, 2009. doi:10.1103/PhysRevC.80.015807.
- [AHH⁺92] P. Anselmann, W. Hampel, G. Heusser, et al. Implications of the GALLEX determination of the solar neutrino flux. *Physics Letters B*, 285(4):390–397, 1992. doi:10.1016/0370-2693(92)91522-B.
- [Ake] M. Aker. PhD thesis, Karlsruher Institut für Technologie (KIT). Forthcoming.

- [AVV02] J.N. Abdurashitov, E.P. Veretenkin, and V.M. et al. Vermul. Solar neutrino flux measurements by the Soviet-American gallium experiment (SAGE) for half the 22-year solar cycle. *Journal of Experimental and Theoretical Physics*, 95:181–193, 2002. doi:10.1134/1.1506424.
- [AW93] G. Audi and A. H. Wapstra. The 1993 atomic mass evaluation: (I) Atomic mass table. *Nuclear Physics A*, 565(1):1–65, 1993. doi:10.1016/0375-9474(93)90024-R.
- [AW03] G. Altarelli and K. Winter, editors. *Neutrino mass*, volume 190 of *Springer Tracts in Modern Physics*. Springer-Verlag, Berlin, Heidelberg, 1. edition, 2003. doi:10.1007/b13585.
- [Bab14] M. Babutzka. *Design and development for the Rearsection of the KATRIN experiment*. PhD thesis, Karlsruhe Institut für Technologie (KIT), 2014. doi:10.5445/IR/1000045598.
- [Bae17] W.-J. Baek. Investigation of background processes of ions and Rydberg atoms in the KATRIN spectrometers. Master’s thesis, Karlsruhe Institut für Technologie (KIT), 2017.
- [Bal05] R. Balescu. *Aspects of Anomalous Transport in Plasmas*. Series in Plasma Physics. Institute of Physics Publishing, Bristol and Philadelphia, 1. edition, 2005.
- [BBB⁺87] R. M. Bionta, G. Blewitt, C. B. Bratton, et al. Observation of a neutrino burst in coincidence with supernova 1987A in the Large Magellanic Cloud. *Physical Review Letters*, 58:1494–1496, 1987. doi:10.1103/PhysRevLett.58.1494.
- [BBB⁺12] M. Babutzka, M. Bahr, J. Bonn, et al. Monitoring of the operating parameters of the KATRIN Windowless Gaseous Tritium Source. *New Journal of Physics*, 14(10):103046, 2012. doi:10.1088/1367-2630/14/10/103046.
- [BBG⁺95] A.I. Belesev, A.I. Bleule, E.V. Geraskin, et al. Results of the troitsk experiment on the search for the electron antineutrino rest mass in tritium beta-decay. *Physics Letters B*, 350(2):263–272, 1995. doi:10.1016/0370-2693(95)00335-I.
- [BBS68] J. N. Bahcall, N. A. Bahcall, and G. Shaviv. Present Status of the Theoretical Predictions for the ³⁷Cl Solar-Neutrino Experiment. *Physical Review Letters*, 20:1209–1212, 1968. doi:10.1103/PhysRevLett.20.1209.
- [BBS⁺17] B. Bornschein, U. Besserer, M. Steidl, et al. The Five Phases to Standard Tritium Operation of KATRIN. *Fusion Science and Technology*, 71(3):231–235, 2017. doi:10.1080/15361055.2016.1273703.
- [BCJ⁺18] G. Bak, J. H. Choi, H. I. Jang, et al. Measurement of Reactor Antineutrino Oscillation Amplitude and Frequency at RENO. *Physical Review Letters*, 121:201801, 2018. doi:10.1103/PhysRevLett.121.201801.
- [BES80] J. R. Bond, G. Efstathiou, and J. Silk. Massive Neutrinos and the Large-Scale Structure of the Universe. *Physical Review Letters*, 45:1980–1984, 1980. doi:10.1103/PhysRevLett.45.1980.

- [BFL61] M. Bardon, P. Franzini, and J. Lee. Helicity of μ^- Mesons; Mott Scattering of Polarized Muons. *Physical Review Letters*, 7:23–25, 1961. doi:10.1103/PhysRevLett.7.23.
- [BG15] S. M. Bilenky and C. Giunti. Neutrinoless double-beta decay: A probe of physics beyond the Standard Model. *International Journal of Modern Physics A*, 30(04n05):1530001, 2015. doi:10.1142/S0217751X1530001X.
- [BGG⁺12] V. Barger, R. Gandhi, P. Ghoshal, et al. Neutrino Mass Hierarchy and Octant Determination with Atmospheric Neutrinos. *Physical Review Letters*, 109:091801, 2012. doi:10.1103/PhysRevLett.109.091801.
- [Bit04] J. A. Bittencourt. *Fundamentals of Plasma Physics*. Springer Science+Business Media, New York, 3. edition, 2004. doi:10.1007/978-1-4757-4030-1.
- [BMF⁺14] E. Bulbul, M. Markevitch, A. Foster, et al. Detection of an unidentified emission line in the stacked X-ray spectrum of galaxy clusters. *The Astrophysical Journal*, 789(1):13, 2014. doi:10.1088/0004-637x/789/1/13.
- [BPB01] J. N. Bahcall, M. H. Pinsonneault, and S. Basu. Solar Models: Current Epoch and Time Dependences, Neutrinos, and Helioseismological Properties. *The Astrophysical Journal*, 555(2):990–1012, 2001. doi:10.1086/321493.
- [BPT80] G. Beamson, H. Q. Porter, and D. W. Turner. The collimating and magnifying properties of a superconducting field photoelectron spectrometer. *Journal of Physics E: Scientific Instruments*, 13(1):64–66, 1980. doi:10.1088/0022-3735/13/1/018.
- [BR97] R. Brun and F. Rademakers. ROOT - An object oriented data analysis framework. *Nuclear Instruments and Methods in Physics Research Section A: Accelerators, Spectrometers, Detectors and Associated Equipment*, 389(1–2):81–86, 1997. doi:10.1016/S0168-9002(97)00048-X.
- [BRB⁺17] J. D. Behrens, P. C.-O. Ranitzsch, M. Beck, et al. A pulsed, mono-energetic and angular-selective UV photo-electron source for the commissioning of the KATRIN experiment. *The European Physical Journal C*, 77(6):410, 2017. doi:10.1140/epjc/s10052-017-4972-9.
- [Cap76] F. F. Cap. *Handbook on Plasma Instabilities: Volume 1*. Academic Press Rapid Manuscript Reproduction. Academic Press, New York, 1. edition, 1976.
- [CBKV10] S. Chilingaryan, A. Beglarian, A. Kopmann, and S. Vöcking. Advanced data extraction infrastructure: Web based system for management of time series data. *Journal of Physics: Conference Series*, 219(4):042034, 2010. doi:10.1088/1742-6596/219/4/042034.
- [CDD⁺98] B. T. Cleveland, T. Daily, R. Davis, et al. Measurement of the Solar Electron Neutrino Flux with the Homestake Chlorine Detector. *The Astrophysical Journal*, 496(1):505–526, 1998. doi:10.1086/305343.
- [Cer34] P. A. Cerenkov. Visible Emission of Clean Liquids by Action of γ Radiation. *Doklady Akadademii Nauk SSSR*, 2:451, 1934.

- [Cha14] J. Chadwick. Intensitätsverteilung im magnetischen Spektrum von β -Strahlen von Radium B+C. *Verhandlungen der Deutschen Physikalischen Gesellschaft*, 16:383–391, 1914.
- [CPP⁺05] S. Cole, W. J. Percival, J. A. Peacock, et al. The 2dF Galaxy Redshift Survey: power-spectrum analysis of the final data set and cosmological implications. *Monthly Notices of the Royal Astronomical Society*, 362(2):505–534, 2005, <https://academic.oup.com/mnras/article-pdf/362/2/505/6155670/362-2-505.pdf>. doi:10.1111/j.1365-2966.2005.09318.x.
- [Cre03] O. Cremonesi. Neutrinoless double beta decay: Present and future. *Nuclear Physics B - Proceedings Supplements*, 118:287–296, 2003. doi:10.1016/S0920-5632(03)01331-8. Proceedings of the XXth International Conference on Neutrino Physics and Astrophysics.
- [CRH⁺56] C. L. Cowan, F. Reines, F. B. Harrison, H. W. Kruse, and A. D. McGuire. Detection of the Free Neutrino: a Confirmation. *Science*, 124(3212):103–104, 1956. doi:10.1126/science.124.3212.103.
- [D'A74] R. J. D'Arcy. Dielectric impurities and surface instability in Langmuir probe plasma measurements. *Journal of Physics D: Applied Physics*, 7(10):1391–1401, 1974. doi:10.1088/0022-3727/7/10/312.
- [Dav64] R. Davis. Solar Neutrinos. II. Experimental. *Physical Review Letters*, 12:303–305, 1964. doi:10.1103/PhysRevLett.12.303.
- [Dav94] R. Davis. A review of the homestake solar neutrino experiment. *Progress in Particle and Nuclear Physics*, 32:13–32, 1994. doi:10.1016/0146-6410(94)90004-3.
- [Deb12] P. Debye. Zur Theorie der spezifischen Wärmen. *Annalen der Physik*, 344:789–839, 1912. doi:10.1002/andp.19123441404.
- [DGG⁺62] G. Danby, J-M. Gaillard, K. Goulianos, et al. Observation of High-Energy Neutrino Reactions and the Existence of Two Kinds of Neutrinos. *Physical Review Letters*, 9:36–44, 1962. doi:10.1103/PhysRevLett.9.36.
- [DHJ⁺17] G. Drexlin, F. Harms, A. Jansen, et al. Calculations and TPMC simulations of the reduction of radioactive decays of a noble gas by cryopanels. *Vacuum*, 138:165–172, 2017. doi:10.1016/j.vacuum.2016.12.013.
- [DHMW13] G. Drexlin, V. Hannen, S. Mertens, and C. Weinheimer. Current direct neutrino mass experiments. *Advances in High Energy Physics*, 2013:293986, 2013, 1307.0101. doi:10.1155/2013/293986.
- [Dir28] P. A. M. Dirac. The quantum theory of the electron. *Proceedings of the Royal Society of London A*, 117:610–624, 1928. doi:10.1098/rspa.1928.0023.
- [DK63] G. H. Dunn and L. J. Kieffer. Dissociative Ionization of h_2 : A Study of Angular Distributions and Energy Distributions of Resultant Fast Protons. *Physical Review*, 132:2109–2117, 1963. doi:10.1103/PhysRev.132.2109.

- [dSGM⁺18] P. F. de Salas, S. Gariazzo, O. Mena, C. A. Ternes, and M. Tórtola. Neutrino Mass Ordering from Oscillations and Beyond: 2018 Status and Future Prospects. *Frontiers in Astronomy and Space Sciences*, 5:36, 2018. doi:10.3389/fspas.2018.00036.
- [EB64] F. Englert and R. Brout. Broken Symmetry and the Mass of Gauge Vector Mesons. *Physical Review Letters*, 13:321–323, 1964. doi:10.1103/PhysRevLett.13.321.
- [EBB⁺14] M. Erhard, S. Bauer, A. Beglarian, et al. High-voltage monitoring with a solenoid retarding spectrometer at the KATRIN experiment. *Journal of Instrumentation*, 9(6):P06022, 2014. doi:10.1088/1748-0221/9/06/P06022.
- [EBB⁺18] M. Erhard, J. Behrens, S. Bauer, et al. Technical design and commissioning of the KATRIN large-volume air coil system. *Journal of Instrumentation*, 13(02):P02003, 2018. doi:10.1088/1748-0221/13/02/P02003.
- [EEF⁺03] K. Eguchi, S. Enomoto, K. Furuno, et al. First Results from KamLAND: Evidence for Reactor Antineutrino Disappearance. *Physical Review Letters*, 90:021802, 2003. doi:10.1103/PhysRevLett.90.021802.
- [EHM87] S. R. Elliott, A. A. Hahn, and M. K. Moe. Direct evidence for two-neutrino double-beta decay in ⁸²Se. *Physical Review Letters*, 59:2020–2023, 1987. doi:10.1103/PhysRevLett.59.2020.
- [Ell19] E. Ellinger. *Development and investigation of the Forward Beam Monitor for the KATRIN experiment*. PhD thesis, Bergische Universität Wuppertal (BUW), 2019. doi:10.25926/r160-7a40.
- [EW27] C. D. Ellis and W. A. Wooster. The average energy of disintegration of Radium E. *Proceedings of the Royal Society of London*, 117:109–123, 1927. doi:10.1098/rspa.1927.0168.
- [FBD⁺11] F. M. Fränkle, L. Bornschein, G. Drexlin, et al. Radon induced background processes in the KATRIN pre-spectrometer. *Astroparticle Physics*, 35(3):128–134, 2011. doi:10.1016/j.astropartphys.2011.06.009.
- [Fer34] E. Fermi. Versuch einer Theorie der β -Strahlen. *Zeitschrift für Physik*, 88(3–4):161–177, 1934. doi:10.1007/BF01351864.
- [FGT⁺17] D. Furse, S. Groh, N. Trost, et al. Kassiopeia: a modern, extensible C++ particle tracking package. *New Journal of Physics*, 19(5):053012, 2017. doi:10.1088/1367-2630/aa6950.
- [FHI⁺96] Y. Fukuda, T. Hayakawa, K. Inoue, et al. Solar Neutrino Data Covering Solar Cycle 22. *Physical Review Letters*, 77:1683–1686, 1996. doi:10.1103/PhysRevLett.77.1683.
- [FHI⁺98] Y. Fukuda, T. Hayakawa, E. Ichihara, et al. Evidence for Oscillation of Atmospheric Neutrinos. *Physical Review Letters*, 81:1562–1567, 1998. doi:10.1103/PhysRevLett.81.1562.

- [Fis14] S. Fischer. *Commissioning of the KATRIN Raman system and durability studies of optical coatings in glove box and tritium atmospheres*. PhD thesis, Karlsruher Institut für Technologie (KIT), 2014. doi:10.5445/IR/1000043697.
- [FRS⁺19] F. Friedel, C. Röttele, L. Schimpf, et al. Time-dependent simulation of the flow reduction of D₂ and T₂ in the KATRIN experiment. *Vacuum*, 159:161–172, 2019. doi:10.1016/j.vacuum.2018.10.002.
- [Ful20] A. Fulst. *A Novel Quasi-Differential Method for MAC-E Filters and Determination and Control of the Electric Potentials of the KATRIN Experiment with a Stabilized Condensed Krypton Source and a UV Illumination System*. PhD thesis, Westfälische Wilhelms-Universität Münster (WWU), 2020.
- [G⁺13] A. Gando et al. Reactor on-off antineutrino measurement with KamLAND. *Physical Review D*, 88:033001, 2013. doi:10.1103/PhysRevD.88.033001.
- [Gal12] P. T. Gallagher. Introduction to plasma physics (py5012) lectures 1 & 2: Basic concepts. Lecture slides, 2012. URL https://www.tcd.ie/Physics/people/Peter.Gallagher/lectures/PlasmaPhysics/Lecture1n2_basic_properties.pdf.
- [GBB⁺05] F. Glück, S. Baeßler, J. Byrne, et al. The neutron decay retardation spectrometer aSPECT: Electromagnetic design and systematic effects. *The European Physical Journal A - Hadrons and Nuclei*, 23:135–146, 2005. doi:10.1140/epja/i2004-10057-1.
- [GBB⁺18] S. Görhardt, J. Bonn, L. Bornschein, et al. Impact of a cryogenic baffle system on the suppression of radon-induced background in the KATRIN Pre-Spectrometer. *Journal of Instrumentation*, 13(10):T10004–T10004, 2018. doi:10.1088/1748-0221/13/10/t10004.
- [GBC⁺17] L. Gastaldo, K. Blaum, K. Chrysalidis, et al. The electron capture in ¹⁶³Ho experiment – ECHo. *The European Physical Journal Special Topics*, 226(8):1623–1694, 2017. doi:10.1140/epjst/e2017-70071-y.
- [GBD⁺14] L. Gastaldo, K. Blaum, A. Doerr, et al. The Electron Capture ¹⁶³Ho Experiment ECHo. *Journal of Low Temperature Physics*, 176:876–884, 2014. doi:10.1007/s10909-014-1187-4.
- [GBH⁺13] S. Grohmann, T. Bode, M. Hötzel, et al. The thermal behaviour of the tritium source in KATRIN. *Cryogenics*, 55-56(0):5–11, 2013. doi:10.1016/j.cryogenics.2013.01.001.
- [GBSS11] S. Grohmann, T. Bode, H. Schön, and M. Süßer. Precise temperature measurement at 30 K in the KATRIN source cryostat. *Cryogenics*, 51(8):438–445, 2011. doi:10.1016/j.cryogenics.2011.05.001.
- [GGH⁺16] A. Gando, Y. Gando, T. Hachiya, et al. Search for Majorana Neutrinos Near the Inverted Mass Hierarchy Region with KamLAND-Zen. *Physical Review Letters*, 117:082503, 2016. doi:10.1103/PhysRevLett.117.082503.

- [GGS58] M. Goldhaber, L. Grodzins, and A. W. Sunyar. Helicity of Neutrinos. *Physical Review*, 109:1015–1017, 1958. doi:10.1103/PhysRev.109.1015.
- [GHK64] G. S. Guralnik, C. R. Hagen, and T. W. B. Kibble. Global Conservation Laws and Massless Particles. *Physical Review Letters*, 13:585–587, 1964. doi:10.1103/PhysRevLett.13.585.
- [Gil72] A. Gilardini. *Low energy electron collisions in gases: swarm and plasma methods applied to their study*. Wiley series in plasma physics. A Wiley-Interscience publication. John Wiley and Sons, New York, London, Sydney, Toronto, 1972.
- [GJBG⁺08] S. Grohmann, B. Bornschein J. Bonn, R. Gehring, et al. Cryogenic design of the KATRIN source cryostat. *AIP Conference Proceedings*, 985:1277–1284, 2008. doi:10.1063/1.2908483.
- [GL10] C. Giunti and M. Laveder. Short-baseline electron neutrino disappearance, tritium beta decay, and neutrinoless double-beta decay. *Physical Review D*, 82:053005, 2010. doi:10.1103/PhysRevD.82.053005.
- [Gla61] S. L. Glashow. Partial-symmetries of weak interactions. *Nuclear Physics*, 22(4):579 – 588, 1961. doi:10.1016/0029-5582(61)90469-2.
- [Glü11] F. Glück. Axisymmetric Magnetic Field Calculation with Zonal Harmonic Expansion. *Progress In Electromagnetics Research B*, 32:351–388, 2011. doi:10.2528/PIERB11042108.
- [Gro15] S. Groh. *Modeling of the response function and measurement of transmission properties of the KATRIN experiment*. PhD thesis, Karlsruher Institut für Technologie (KIT), 2015. doi:10.5445/IR/1000046546.
- [GS62] G. Guest and A. Simon. Instability in Low-Pressure Plasma Diffusion Experiments. *The Physics of Fluids*, 5(5):503–509, 1962. doi:10.1063/1.1706650.
- [Har15] F. Harms. *Characterization and Minimization of Background Processes in the KATRIN Main Spectrometer*. PhD thesis, Karlsruher Institut für Technologie (KIT), 2015. doi:10.5445/IR/1000050027.
- [HCH⁺04] M. A. Howe, G. A. Cox, P. J. Harvey, et al. Sudbury neutrino observatory neutral current detector acquisition software overview. *IEEE Transactions on Nuclear Science*, 51(3):878–883, 2004. doi:10.1109/TNS.2004.829527.
- [Hei19] F. Heizmann. *Analysis tools and methods for tritium data taking with the KATRIN experiment*. PhD thesis, Karlsruher Institut für Technologie (KIT), 2019. doi:10.5445/IR/1000093536.
- [HHH⁺99] W. Hampel, J. Handt, G. Heusser, et al. GALLEX solar neutrino observations: results for GALLEX iv. *Physics Letters B*, 447(1):127–133, 1999. doi:10.1016/S0370-2693(98)01579-2.
- [Hig64] P. W. Higgs. Broken Symmetries and the Masses of Gauge Bosons. *Physical Review Letters*, 13:508–509, 1964. doi:10.1103/PhysRevLett.13.508.

- [HKK⁺87] K. Hirata, T. Kajita, M. Koshiba, et al. Observation of a neutrino burst from the supernova SN1987A. *Physical Review Letters*, 58:1490–1493, 1987. doi:10.1103/PhysRevLett.58.1490.
- [HNB⁺07] G. Hinshaw, M. R.olta, C. L. Bennett, et al. Three-Year Wilkinson Microwave Anisotropy Probe(WMAP) Observations: Temperature Analysis. *The Astrophysical Journal Supplement Series*, 170(2):288–334, 2007. doi:10.1086/513698.
- [HSM17] F. Heizmann and H. Seitz-Moskaliuk. The Windowless Gaseous Tritium Source (WGTS) of the KATRIN experiment. *Journal of Physics: Conference Series*, 888(1):012071, 2017. doi:10.1088/1742-6596/888/1/012071.
- [Hub] A. Huber. *Analysis of first KATRIN data and searches for keV-scale sterile neutrinos*. PhD thesis, Karlsruher Institut für Technologie (KIT). Forthcoming.
- [IR50] M. G. Inghram and J. H. Reynolds. Double Beta-Decay of Te¹³⁰. *Physical Review*, 78:822–823, 1950. doi:10.1103/PhysRev.78.822.2.
- [Jac06] J. D. Jackson. *Klassische Elektrodynamik*. Walter de Gruyter, Berlin, 4. edition, 2006.
- [Jou18] K. Jousten, editor. *Handbuch Vakuumtechnik*. Springer Reference Technik. Springer Vieweg, Wiesbaden, 12. edition, 2018.
- [Kar18] C. Karl. Analysis of First Tritium Data of the KATRIN Experiment. Master’s thesis, Technische Universität München (TUM), 2018.
- [KAT05] KATRIN collaboration. KATRIN design report. FZKA scientific report 7090, 2005. URL <http://bibliothek.fzk.de/zb/berichte/FZKA7090.pdf>.
- [KBB⁺05] C. Kraus, B. Bornschein, L. Bornschein, et al. Final results from phase II of the Mainz neutrino mass search in tritium β decay. *The European Physical Journal C - Particles and Fields*, 40:447–468, 2005. doi:10.1140/epjc/s2005-02139-7.
- [KBD⁺19] M. Kleesiek, J. Behrens, G. Drexlin, et al. β -Decay Spectrum, Response Function and Statistical Model for Neutrino Mass Measurements with the KATRIN Experiment. *The European Physical Journal C*, 79(204), 2019. doi:10.1140/epjc/s10052-019-6686-7.
- [KHD⁺18] L. Kuckert, F. Heizmann, G. Drexlin, et al. Modelling of gas dynamical properties of the KATRIN tritium source and implications for the neutrino mass measurement. *Vacuum*, 158:195–205, 2018. doi:10.1016/j.vacuum.2018.09.036.
- [KHH⁺10] F. Kaether, W. Hampel, G. Heusser, J. Kiko, and T. Kirsten. Reanalysis of the gallex solar neutrino flux and source experiments. *Physics Letters B*, 685(1):47 – 54, 2010. doi:https://doi.org/10.1016/j.physletb.2010.01.030.

- [Kim15] S.-B. Kim. New results from RENO and prospects with RENO-50. *Nuclear and Particle Physics Proceedings*, 265-266:93–98, 2015. doi:10.1016/j.nuclphysbps.2015.06.024. Proceedings of the Neutrino Oscillation Workshop.
- [Kit13] C. Kittel. *Einführung in die Festkörperphysik*. De Gruyter Oldenbourg, München, 15. edition, 2013. doi:10.1007/978-3-662-59335-6.
- [Kle14] M. Kleesiek. *A Data-Analysis and Sensitivity-Optimization Framework for the KATRIN Experiment*. PhD thesis, Karlsruher Institut für Technologie (KIT), 2014. doi:10.5445/IR/1000043301.
- [Kle19] M. Klein. *Tritium ions in KATRIN: blocking, removal and detection*. PhD thesis, Karlsruher Institut für Technologie (KIT), 2019. doi:10.5445/IR/1000093526.
- [KP09] R. Kersevan and J.-L. Pons. Introduction to MOLFLOW+: New graphical processing unit-based Monte Carlo code for simulating molecular flows and for calculating angular coefficients in the compute unified device architecture environment. *Journal of Vacuum Science & Technology A*, 27(4):1017–1023, 2009. doi:10.1116/1.3153280.
- [KUA⁺01] K. Kodama, N. Ushida, C. Andreopoulos, et al. Observation of tau neutrino interactions. *Physics Letters B*, 504(3):218–224, 2001. doi:10.1016/S0370-2693(01)00307-0.
- [KUA⁺08] K. Kodama, N. Ushida, C. Andreopoulos, et al. Final tau-neutrino results from the DONuT experiment. *Physical Review D*, 78:052002, 2008. doi:10.1103/PhysRevD.78.052002.
- [Kuc16] L. Kuckert. *The Windowless Gaseous Tritium Source of the KATRIN Experiment – Characterisation of Gas Dynamical and Plasma Properties*. PhD thesis, Karlsruher Institut für Technologie (KIT), 2016. doi:10.5445/IR/1000065077.
- [Lan28] I. Langmuir. Oscillations in Ionized Gases. *Proceedings of the National Academy of Sciences*, 14(8):627–637, 1928. doi:10.1073/pnas.14.8.627.
- [Lin19] Y.-T. Lin. *The Tritium Recoil-Ion Mass Spectrometer Experiment*. PhD thesis, University of Washington (UW), 2019.
- [LK05] C. H. Lefhalm and V. Krieger. A full featured monitoring, control and data management system for liquid metal coolant loops. In *14th IEEE-NPSS Real Time Conference, 2005.*, pages 570–573, 2005. doi:10.1109/RTC.2005.1547521.
- [LL02] T. J. Loredo and D. Q. Lamb. Bayesian analysis of neutrinos observed from supernova SN 1987A. *Physical Review D*, 65:063002, 2002. doi:10.1103/PhysRevD.65.063002.
- [Lod17] F. Di Lodovico. The Hyper-Kamiokande Experiment. *Journal of Physics: Conference Series*, 888:012020, 2017. doi:10.1088/1742-6596/888/1/012020.

- [LS85] V. M. Lobashev and P. E. Spivak. A method for measuring the electron antineutrino rest mass. *Nuclear Instruments and Methods in Physics Research Section A: Accelerators, Spectrometers, Detectors and Associated Equipment*, 240(2):305–310, 1985. doi:10.1016/0168-9002(85)90640-0.
- [LT15] A. V. Lokhov and F. V. Tkachov. Confidence intervals with a priori parameter bounds. *Physics of Particles and Nuclei*, 46(3):347–365, 2015. doi:10.1134/S1063779615030089.
- [Mac] M. Machatschek. *A Phenomenological Theory of KATRIN Source Potential Systematics and its Application in Krypton-83m Calibration Measurements*. PhD thesis, Karlsruher Institut für Technologie (KIT). Forthcoming.
- [Mac16] M. Machatschek. Simulation of the $^{83\text{m}}\text{Kr}$ Mode of the Tritium Source of the KATRIN Experiment. Master’s thesis, Karlsruher Institut für Technologie (KIT), 2016.
- [Mac20] P. A. N. Machado. Sterile Neutrino Global Picture. Talk at the XXIX International Conference on Neutrino Physics and Astrophysics, 2020. URL <https://conferences.fnal.gov/nu2020/>.
- [Mal07] O. B. Malyshev. Characterisation of a turbo-molecular pumps by a minimum of parameters. *Vacuum*, 81(6):752–758, 2007. doi:<https://doi.org/10.1016/j.vacuum.2005.11.055>. Proceedings of the European Vacuum Conference (EVC-9).
- [Mar] A. Marsteller. *Characterization and Optimization of the KATRIN Tritium Source*. PhD thesis, Karlsruher Institut für Technologie (KIT). Forthcoming.
- [Mar17] E. L. Martin. *Electron Detection Systems for KATRIN Detector and Spectrometer Section*. PhD thesis, University of Washington (UW), 2017.
- [MBB⁺20] A. Marsteller, B. Bornschein, L. Bornschein, et al. Neutral tritium gas reduction in the KATRIN differential pumping sections. 2020, 2009.10403.
- [McC15] E. A. McCutchan. Nuclear data sheets for $A = 83$. *Nuclear Data Sheets*, 125:201–394, 2015. doi:10.1016/j.nds.2015.02.002.
- [MDF⁺13] S. Mertens, G. Drexlin, F. M. Fränkle, et al. Background due to stored electrons following nuclear decays in the KATRIN spectrometers and its impact on the neutrino mass sensitivity. *Astroparticle Physics*, 41:52–62, 2013. doi:10.1016/j.astropartphys.2012.10.005.
- [Men20] Y. Meng. JUNO Status. Talk at the XXIX International Conference on Neutrino Physics and Astrophysics, 2020. URL <https://conferences.fnal.gov/nu2020/>.
- [Mes10] D. Meschede, editor. *Gerthsen Physik*. Springer, Berlin, Heidelberg, 24. edition, 2010. doi:10.1007/978-3-642-12894-3.

- [MFL⁺11] G. Mention, M. Fechner, Th. Lasserre, et al. Reactor antineutrino anomaly. *Physical Review D*, 83:073006, 2011. doi:10.1103/PhysRevD.83.073006.
- [MLG⁺15] S. Mertens, T. Lasserre, S. Groh, et al. Sensitivity of next-generation tritium beta-decay experiments for keV-scale sterile neutrinos. *Journal of Cosmology and Astroparticle Physics*, 2015(02):020, 2015. doi:10.1088/1475-7516/2015/02/020.
- [MNS62] Z. Maki, M. Nakagawa, and S. Sakata. Remarks on the Unified Model of Elementary Particles. *Progress of Theoretical Physics*, 28(5):870–880, 1962. doi:10.1143/PTP.28.870.
- [MO30] L. Meitner and W. Orthmann. Über eine absolute Bestimmung der Energie der primären β -Strahlen von Radium E. *Zeitschrift für Physik*, 60:143–155, 1930. doi:10.1007/BF01339819.
- [MS85] S. P. Mikheyev and A. Y. Smirnov. Resonance enhancement of oscillations in matter and solar neutrino spectroscopy. *Soviet Journal of Nuclear Physics*, 42(6):913–917, 1985.
- [MSL26] H. M. Mott-Smith and I. Langmuir. The Theory of Collectors in Gaseous Discharges. *Physical Review*, 28:727–763, 1926. doi:10.1103/PhysRev.28.727.
- [N⁺18] A. Nucciotti et al. Direct neutrino mass measurement by the HOLMES experiment. *Journal of Physics Conference Series*, 1056(1):012039, 2018. doi:10.1088/1742-6596/1056/1/012039.
- [Nuc12] A. Nucciotti. Neutrino mass calorimetric searches in the MARE experiment. *Nuclear Physics B - Proceedings Supplements*, 229-232:155–159, 2012. doi:10.1016/j.nuclphysbps.2012.09.025. Neutrino 2010.
- [OO19] L. Oberauer and J. Oberauer. *Neutrinophysik. Grundlagen, Experimente und aktuelle Forschung*. Springer Spektrum, Berlin, Heidelberg, 1. edition, 2019. doi:10.1007/978-3-662-59335-6.
- [Ost20] R. Ostertag. Investigation of Plasma Effects in the KATRIN Source with $^{83\text{m}}\text{Kr}$. Master’s thesis, Karlsruher Institut für Technologie (KIT), 2020.
- [PAB⁺75] M. L. Perl, G. S. Abrams, A. M. Boyarski, et al. Evidence for Anomalous Lepton Production in $e^+ - e^-$ Annihilation. *Physical Review Letters*, 35:1489–1492, 1975. doi:10.1103/PhysRevLett.35.1489.
- [Pau27] W. Pauli. Zur Quantenmechanik des magnetischen Elektrons. *Zeitschrift für Physik*, 43(9):601–623, 1927. doi:10.1007/BF01397326.
- [PBB⁺92] A. Picard, H. Backe, H. Barth, et al. A solenoid retarding spectrometer with high resolution and transmission for keV electrons. *Nuclear Instruments and Methods in Physics Research Section B: Beam Interactions with Materials and Atoms*, 63(3):345–358, 1992. doi:10.1016/0168-583X(92)95119-C.

- [Per09] D. H. Perkins. *Particle Astrophysics*. Oxford Master Series in Particle Physics, Astrophysics, and Cosmology. Oxford University Press, Oxford, 2. edition, 2009.
- [Pon58] B. Pontecorvo. Inverse beta processes and nonconservation of lepton charge. *Soviet Physics JETP*, 7:172–173, 1958.
- [PRS⁺15] B. Povh, K. Rith, C. Scholz, F. Zetsche, and W. Rodejohann. *Particles and Nuclei. An Introduction to the Physical Concepts*. Graduate Texts in Physics. Springer-Verlag, Berlin, Heidelberg, 7. edition, 2015. doi:10.1007/978-3-662-46321-5.
- [PS95] M. E. Peskin and D. V. Schroeder. *An Introduction To Quantum Field Theory*. Frontiers in Physics. Addison-Wesley Publishing Company, 1. edition, 1995.
- [PSB15] F. Priester, M. Sturm, and B. Bornschein. Commissioning and detailed results of KATRIN inner loop tritium processing system at Tritium Laboratory Karlsruhe. *Vacuum*, 116:42–47, 2015. doi:10.1016/j.vacuum.2015.02.030.
- [PW65] A. A. Penzias and R. W. Wilson. A Measurement of excess antenna temperature at 4080 Mc/s. *Astrophysical Journal*, 142:419–421, 1965. doi:10.1086/148307.
- [RB71] J. A. Ray and C. F. Barnett. Secondary Electron Emission of Metals Bombarded with 120-ev to 5-kev Protons. *Journal of Applied Physics*, 42(8):3260–3261, 1971. doi:10.1063/1.1660722.
- [RC53] F. Reines and C. L. Cowan. Detection of the Free Neutrino. *Physical Review*, 92:830–831, 1953. doi:10.1103/PhysRev.92.830.
- [RK88] R. G. H. Robertson and D. A. Knapp. Direct measurements of neutrino mass. *Annual Review of Nuclear and Particle Science*, 38(1):185–215, 1988. doi:10.1146/annurev.ns.38.120188.001153.
- [Röl15] M. Röllig. *Tritium analytics by beta induced X-ray spectrometry*. PhD thesis, Karlsruher Institut für Technologie (KIT), 2015. doi:10.5445/IR/1000054050.
- [Röt19] C. Röttele. *Tritium suppression factor of the KATRIN transport section*. PhD thesis, Karlsruher Institut für Technologie (KIT), 2019. doi:10.5445/IR/1000096733.
- [SAB⁺04] M. Sisti, C. Arnaboldi, C. Brofferio, et al. New limits from the Milano neutrino mass experiment with thermal microcalorimeters. *Nuclear Instruments and Methods in Physics Research Section A: Accelerators, Spectrometers, Detectors and Associated Equipment*, 520(1):125–131, 2004. doi:10.1016/j.nima.2003.11.273. Proceedings of the 10th International Workshop on Low Temperature Detectors.
- [Sac20] R. Sack. *Measurement of the energy loss of 18.6 keV electrons on deuterium gas and determination of the tritium Q-value at the KATRIN experiment*. PhD thesis, Westfälische Wilhelms-Universität Münster (WWU), 2020.

- [Sal68] A. Salam. Weak and Electromagnetic Interactions. *Conference Proceedings*, C680519:367–377, 1968. doi:10.1142/9789812795915_0034.
- [Sch64] F. Schwirzke. Diffusion of Charged Particles Across a Magnetic Field in "Short Circuiting Geometry". *The Physics of Fluids*, 7(2):311–318, 1964. doi:10.1063/1.1711200.
- [Sch13] M. Schlösser. *Accurate calibration of the Raman system for the Karlsruhe Neutrino Experiment*. PhD thesis, Karlsruher Institut für Technologie (KIT), 2013. doi:10.1007/978-3-319-06221-1.
- [Sch16] K. Schönung. *Development of a Rear Wall for the KATRIN Rear Section and investigation of tritium compatibility of Rear Section components*. PhD thesis, Karlsruher Institut für Technologie (KIT), 2016. doi:10.5445/IR/1000056077.
- [SDL⁺18] J. Sentkerestiová, O. Dragoun, O. Lebeda, et al. Gaseous $^{83\text{m}}\text{Kr}$ generator for KATRIN. *Journal of Instrumentation*, 13(04):P04018–P04018, 2018. doi:10.1088/1748-0221/13/04/p04018.
- [SM19] H. Seitz-Moskaliuk. *Characterisation of the KATRIN tritium source and evaluation of systematic effects*. PhD thesis, Karlsruher Institut für Technologie (KIT), 2019. doi:10.5445/IR/1000090748.
- [SRL⁺96] H. C. Straub, P. Renault, B. G. Lindsay, K. A. Smith, and R. F. Stebbings. Absolute partial cross sections for electron-impact ionization of H_2 , N_2 , and O_2 from threshold to 1000 eV. *Physical Review A*, 54:2146–2153, 1996. doi:10.1103/PhysRevA.54.2146.
- [Str18] U. Stroth. *Plasmaphysik : Phänomene, Grundlagen und Anwendungen*. SpringerLink. Springer Spektrum, Berlin, Heidelberg, 2. edition, 2018. doi:10.1007/978-3-662-55236-0.
- [Suz01] Y. Suzuki. Solar neutrino results from Super-Kamiokande. *Nuclear Physics B - Proceedings Supplements*, 91(1):29–35, 2001. doi:10.1016/S0920-5632(00)00919-1. Neutrino 2000.
- [THH⁺18] M. Tanabashi, K. Hagiwara, K. Hikasa, et al. Review of Particle Physics. *Physical Review D*, 98:030001, 2018. doi:10.1103/PhysRevD.98.030001. and 2019 update.
- [TMW09] T. Thümmler, R. Marx, and C. Weinheimer. Precision high voltage divider for the KATRIN experiment. *New Journal of Physics*, 11(10):103007, 2009. doi:10.1088/1367-2630/11/10/103007.
- [Tro19] N. R.-M. Trost. *Modeling and measurement of Rydberg-State mediated Background at the KATRIN Main Spectrometer*. PhD thesis, Karlsruher Institut für Technologie (KIT), 2019. doi:10.5445/IR/1000090450.
- [TW71] M. Troy and J. P. Wightman. Physisorption of Ar, Kr, CH_4 , and N_2 on 304 Stainless Steel at Very Low Pressures. *Journal of Vacuum Science and Technology*, 8(6):743–750, 1971. doi:10.1116/1.1315387.

- [UB02] A. Unsöld and B. Baschek. *Der neue Kosmos. Einführung in die Astronomie und Astrophysik*. Springer-Verlag, Berlin, Heidelberg, 7. edition, 2002. doi:10.1007/978-3-662-06529-7.
- [UDRL⁺09] M. Ubieto-Díaz, D. Rodríguez, S. Lukic, et al. A broad-band FT-ICR Penning trap system for KATRIN. *International Journal of Mass Spectrometry*, 288(1–3):1–5, 2009. doi:10.1016/j.ijms.2009.07.003.
- [Val11] K. Valerius. The wire electrode system for the KATRIN main spectrometer. *Progress in Particle and Nuclear Physics*, 64(2):291–293, 2011. doi:10.1016/j.pnpnp.2009.12.032. Neutrinos in Cosmology, in Astro, Particle and Nuclear Physics: International Workshop on Nuclear Physics, 31st course.
- [VH] A. P. Vizcaya Hernández. PhD thesis, Carnegie Mellon University (CMU). Forthcoming.
- [vM85] K. v. Meyenn, editor. *Wolfgang Pauli, Wissenschaftlicher Briefwechsel mit Bohr, Einstein, Heisenberg u.a. Band II: 1930–1939*, volume 6 of *Sources in the History of Mathematics and Physical Sciences*. Springer-Verlag, Berlin, Heidelberg, 1985. doi:10.1007/978-3-540-78801-0.
- [VSD⁺18] D. Vénos, J. Sentkerestiová, O. Dragoun, et al. Properties of $^{83\text{m}}\text{Kr}$ conversion electrons and their use in the KATRIN experiment. *Journal of Instrumentation*, 13(02):T02012, 2018. doi:10.1088/1748-0221/13/02/T02012.
- [WABHS75] D. Wischlitzi, R. Ahrens-Botzong, P. Hess, and K. Schäfer. Zur Adsorption von Xenon und Krypton an verschiedenen Oberflächen. *Berichte der Bunsengesellschaft für physikalische Chemie*, 79(4):348–352, 1975. doi:10.1002/bbpc.19750790407.
- [WAH⁺57] C. S. Wu, E. Ambler, R. W. Hayward, D. D. Hoppes, and R. P. Hudson. Experimental Test of Parity Conservation in Beta Decay. *Physical Review*, 105:1413–1415, 1957. doi:10.1103/PhysRev.105.1413.
- [Wan13] N. Wandkowsky. *Study of background and transmission properties of the KATRIN spectrometers*. PhD thesis, Karlsruher Institut für Technologie (KIT), 2013. doi:10.5445/IR/1000036631.
- [Was14] Center for Experimental Nuclear Physics and Astrophysics: Annual Report. University of Washington (UW), 2014.
- [Wei67] S. Weinberg. A model of Leptons. *Physical Review Letters*, 19:1264–1266, 1967. doi:10.1103/PhysRevLett.19.1264.
- [Wol78] L. Wolfenstein. Neutrino oscillations in matter. *Physical Review D*, 17:2369–2374, 1978. doi:10.1103/PhysRevD.17.2369.
- [Won11] Y. Y. Y. Wong. Neutrino Mass in Cosmology: Status and Prospects. *Annual Review of Nuclear and Particle Science*, 61(1):69–98, 2011. doi:10.1146/annurev-nucl-102010-130252.
- [WPB⁺93] C. Weinheimer, M. Przyrembel, H. Backe, et al. Improved limit on the electron-antineutrino rest mass from tritium β -decay. *Physics Letters B*, 300(3):210–216, 1993. doi:10.1016/0370-2693(93)90355-L.

-
- [WSH⁺20] S. Welte, M. Sturm, D. Hillesheimer, et al. Tritium Supply and Processing for the First KATRIN Tritium Operation. *Fusion Science and Technology*, 76(3):227–231, 2020. doi:10.1080/15361055.2019.1705681.
- [XZ11] Z.-Z. Xing and S. Zhou. *Neutrinos in Particle Physics, Astronomy and Cosmology*. Advanced Topics in Science and Technology in China. Springer-Verlag, Berlin, Heidelberg, 1. edition, 2011. doi:10.1007/978-3-642-17560-2.
- [Zub12] K. Zuber. *Neutrino Physics*. Series in High Energy Physics, Cosmology, and Gravitation. CRC Press, Boca Raton, Florida, 2. edition, 2012. doi:10.1201/b11065.

Acknowledgements

At this point I want to thank all those who supported me in my work on this thesis. Those were

- Prof. Dr. Guido Drexlin who gave me the opportunity to be a part of the KATRIN collaboration. Thank you for lots of discussions about plasma and supporting me throughout my graduation.
- Prof. Dr. Kathrin Valerius who took responsibility as a second reviewer and always had an open door for me.
- The whole ion and plasma team: Dr. Ferenc Glück, Ana Paula Vizcaya Hernández, Dr. Manuel Klein and Dr. Magnus Schlösser. I am very thankful for being part of such a great team, which was always motivated (even after 12 hours of work in the KATRIN control room), pushing things forward and having great expertise. Thank you also for countless helpful discussions and accurate proofreadings of my talks, papers and PhD thesis.
- Dr. Joachim Wolf with whom I shared an office and benefited from his great expertise and patient responding to all my questions (there were a lot of them).
- Judith Bast, Bernard Bender, Jörg Bohn, Rainer Gumbsheimer, Mareike Held, Monika Kaiser, Alan Kumb, Steffen Lichter, Klaus Mehret, Dr. Philipp Ranitzsch, Rolf Rinderspacher, Rudolf Sack, Dr. Klaus Schlösser, Dr. Kerstin Schönung and Alexander Verbeek who supported me in my lab work on the Kelvin probe.
- Dr. Alexander Jansen who organized the measurement campaigns and offered his help whenever needed.
- Armen Beglarian who supported me in all kinds of data acquisition problems and Christian Bettin, Arne Felden, Jürgen Grimm, Thomas Höhn and Dr. Sascha Wüstling who did the same regarding electrotechnical issues.
- Lutz Schimpf for being a friend and colleague from day one of our academic studies and many helpful discussions.

- All the other KATRIN scientists with which I worked together, had discussions and a nice time on conferences: Max Aker, Dr. Jan Behrens, Dr. Wonqook Choi, Marco Deffert, Martin Descher, Dr. Sanshiro Enomoto, Dr. Florian Fränkle, Alexander Fulst, Dr. Stephanie Hickford, Dr. Roman Hiller, Dominic Hinz, Leonard Köllenberger, Dr. Alexey Lokhov, Alexander Marsteller, Raphael Ostertag, Prof. Dr. Diana Parno, Caroline Rodenbeck, Dr. Carsten Röttele, Dr. Hendrik Seitz-Moskaliuk, Dr. Michael Sturm, Larisa Thorne, Dr. Thomas Thümmler, ...
- My bachelor students Christina Klauda and Emanuel Weiss who were very dedicated and supported me a lot in my work.
- Thomas Csabo who supplied me with a high-performance server for performing CPU-intensive MolFlow+ simulations.
- Marion Behecti, Katharina Fischer, Sylvia Krieger, Emma Malcherek and Eva Porter who supported me regarding administrative processes.
- My family, first and foremost my wife Katja Friedel, who provided me with a lot of moral support and backed me up by relieving me from a lot of everyday work.